Photocopy and Use Authorization

In presenting this thesis in partial fulfillment of the requirements for an advanced degree at Idaho State University, I agree that the Library shall make it freely available for inspection. I further state that permission for extensive copying of my thesis for scholarly purposes may be granted by the Dean of the Graduate School, Dean of my academic division, or by the University Librarian. It is understood that any copying or publication of this thesis for financial gain shall not be allowed without my written permission.

Signature ___________________________________

Date _______________________________________

Dismembering the Putnam Thrust: Miocene Extension Within the Foreland-Hinterland Transition of the Idaho-Wyoming Salient and a Revised Kinematic Model for the Putnam Thrust System

by

Andrew B. Yokel-Deliduka

A thesis

submitted in partial fulfillment

of the requirements for the degree of

Master of Science in the Department of Geosciences

Idaho State University

Spring 2023

Committee Approval

To the Graduate Faculty:

The members of the committee appointed to examine the thesis of Andrew Yokel-Deliduka find it satisfactory and recommend that it be accepted.

Dr. David M. Pearson
Major Advisor

Dr. Ryan B. Anderson
Committee Member

Dr. Colin Johnson
Graduate Faculty Representative

(Additional signature lines may be necessary in the case of dissertations and theses that involve committees of more than three faculty members.)

DEDICATION

This thesis is dedicated to my parents. Mom, you always supported me, even when I was still finding myself and figuring out who I was going to be. Thank you for encouraging me to take time to enjoy my youth and to follow my passions. I miss working in the garden with you. Dad, thank you for teaching me about hard work, and how to reach my goals by breaking them down into manageable pieces, and thank you for appreciating a good roadcut, I never knew how important those stops would be.

ACKNOWLEDGMENTS

This thesis could not have been possible without the support of Ryan Anderson and Dave Pearson. Thank you both for devoting time and energy to me and this project. I owe you each a debt of gratitude for believing in me, pushing me, and making me a better scientist and a better person.

A tremendous thanks goes out to Kawner Sistrunk, I could not have asked for a better field assistant. Never a complaint, always willing to go farther, take another sample, and offer any assistance whenever he could make the time. Your work ethic, curiosity, and intelligence will take you far. Thank you to my fellow students, both graduate and undergraduate. I would like to thank Matt Ruggiero for his invaluable insight into big picture concepts, and collaboration in developing structural models. This thesis wouldn't be where it is without your input. A huge thanks to Dr. Tyler Paladino for sharing an office with me and being a good friend.

I want to thank Kurt Sundell, Paul Link, Glenn Thackray, and any other Geoscience faculty who answered my random questions, lent me books, and took the time to help me work through the many facets of this project. Your willingness to offer help is part of what makes the Geoscience department so special. I owe a special thanks to those who helped get me to ISU. Thank you to Jeffrey Lee who changed my life with an undergraduate research project. Thank you to Kelsay Stanton for encouraging my interest in geology and pushing me to go farther. Thank you to all my family and friends who supported me through this journey, I can't wait to catch up with you all. This project was funded in large part by the EdMap grant #G22AC00216-00, as well as the Idaho State Geoscience Geslin award. Petroleum Experts provided Move kinematic modeling software.

TABLE OF CONTENTS

List of Figures ix

Abstract xi

Chapter I: Introduction 1

- Study Area 3

Chapter II: Geologic Background 6

- Introduction to the Geology of the Northern Portneuf Range 6
- Geologic History of Southeastern Idaho 6
  - Neoproterozoic-Paleozoic History 6
  - Neoproterozoic Rifting and the Paleozoic Passive Margin 6
  - Disruption of the Passive Margin 8
- Mesozoic History 10
  - Amalgamation of the North American Cordillera 10
  - Horizontal Crustal Shortening within the Idaho-Wyoming Salient 13
  - The Putnam Thrust Sheet 18
  - The Cache-Pocatello Culmination 22
- Cenozoic History 25
  - Eocene-Oligocene Extensional Collapse of the Cordilleran Orogen 26
  - Basin and Range Extension 27
  - The Yellowstone Volcanic System 32
  - Quaternary History 35
  - Previous Work 38

Chapter III: Methods 41

  - Field Mapping 41

Cartography 41
Cross Sections 42
Field Mapping 40
Stratigraphic Separation Diagrams 43
Sampling Strategy and Preparation 44
U-Th-Pb Geochronology 45
LA-ICP-MS 49
ID-TIMS 50
Data Analysis 51
Field Mapping 40
Chapter IV: Results 53
Mapping 53
Unit Descriptions 57
Quaternary System 59
Cenozoic System 60
Paleozoic System 61
Lower Cambrian and Neoproterozoic System 67
Structural Framework 70
Thrust Faults 70
Stratigraphic Separation Diagrams 72
Folds and Stereonets 75
Normal Faults 77
Cross Sections 80

Geochronology 83
LA-ICP-MS 83
ID-TIMS 89
Chapter V: Discussion 91
Cenozoic Deformation 93
Normal Faulting and Influence of the Yellowstone Hotspot 93
Significance of U-Pb Zircon Geochronologic Ages 96
Timing and Magnitude of Extension within the Portneuf Range 97
Regional Context of Extension within the Portneuf Range 102
Miocene Fault Block Rotation 104
Mesozoic Deformation 106
Bear Canyon-Toponce Thrust 106
Revised Kinematic Model for the Putnam Thrust System 111
Chapter VI: Conclusion 118
References 122
Appendices
Appendix A: LA-ICP-MS U-Pb Composition and Isotopic Ratios 137
Appendix B: LA-ICP-MS U-Pb Dates 142
Appendix C: LA-ICP-MS Trace Element Data 148
Appendix D: ID-TIMS Data 154
Appendix E: Structural Measurement and Locations 155
Appendix F: Locations of Samples 165
Appendix G: Cathodoluminescence Images of LA-ICP-MS Spot Analyses 166

Plates

Plate 1: Geologic Map of the Bear Camp Gulch 7.5-minite Quadrangle, Bannock and Caribou Counties, Idaho, by Andrew B. Yokel-Deliduka, Ryan B. Anderson, David M. Pearson, and Kawner F. Sistrunk

LIST OF FIGURES

Figure 2.1 Overview of North American Cordillera 13

Figure 2.2 Major Thrusts of Idaho-Wyoming Salient 14

Figure 2.3 Regional Cross Section 17

Figure 2.4 Conflicting Regional Cross Sections 20

Figure 2.5 Paleogeologic Map 23

Figure 2.6 Comparison of Cache-Pocatello Culmination and Wasatch Anticlinorium 25

Figure 2.7 Major Normal Faults of Pocatello Area 30

Figure 2.8 Spatial-Temporal Pattern of Extension 31

Figure 2.9 Major Eruptive Centers of Eastern Snake River Plain 34

Figure 2.10 Zones of Seismic Activity and Yellowstone Volcanic System 37

Figure 3.1 Example Concordia Diagram 49

Figure 4.1 Simplified Geologic Map of Bear Camp Gulch, Preliminary 55

Figure 4.2 Simplified Geologic Map of Bear Camp Gulch, new 56

Figure 4.3 Correlation Diagram of Geologic Units 58

Figure 4.4 Overturned Strata of Toponce Thrust 72

Figure 4.5 Stratigraphic Separation Diagram Map 73

Figure 4.6 Separation Diagram 74

Figure 4.7 Stereograms 77

Figure 4.8 Outcrop Photos of Starlight Formation 79

Figure 4.9 Cross Sections 81

Figure 4.10 Cross Section B-B’ 82

Figure 4.11 Results from Initial LA-ICP-MS Analysis 86

Figure 4.12 LA-ICP-MS Results for BCG-770 87

Figure 4.13 Cenozoic Basin Fill 88

Figure 4.14 ID-TIMS results for BCG-612 89

Figure 4.15 ID-TIMS results for BCG-770 90

Figure 5.1 Simplified Geologic Map of Bear Camp Gulch Quadrangle 92

Figure 5.2 Growth Strata 99

Figure 5.3 Regional Basin 100

Figure 5.4 Timing and Location of Extension in Southeastern Idaho 102

Figure 5.5 Restored Cross Section C-C’ 106

Figure 5.6 Restored Cross Section A-A’ 107

Figure 5.7 Simplified Toponce Thrust 108

Figure 5.8 Putnam Thrust Model 113

Figure 5.9 Putnam Thrust Model 114

Figure 5.10 Model for Bear Canyon Thrust 116

Dismembering the Putnam Thrust: Miocene Extension Within the Foreland-Hinterland Transition of the Idaho-Wyoming Salient and a Revised Kinematic Model for the Putnam Thrust System

Thesis Abstract — Idaho State University (2023)

In southeastern Idaho, the Sevier fold-thrust belt records the geometry, timing, and kinematics of contractional structures that accommodated horizontal crustal shortening during growth of the North American Cordillera. However, these structures have been intensely overprinted by Cenozoic extension and volcanism. Detailed geologic mapping and U-Pb zircon analysis of Miocene basin fill in the Portneuf Range has identified a phase of horizontal extension between 6.421 and 6.032 Ma, which was contemporaneous with extension observed south of the ESRP that may represent ongoing Basin and Range extension that was accelerated by passage of the Yellowstone volcanic system. The Putnam thrust sheet, a major Sevier-aged thrust fault that occurs near the foreland-hinterland transition of the fold-thrust belt, has been complexly dismembered by normal faulting, contributing to differing interpretations for its development. Restoration of slip along normal faults and construction of stratigraphic separation diagrams has allowed for a revised model for the Putnam sheet.

Key Words: Putnam thrust, Sevier orogeny, Bear Camp Gulch, Extension, Kinematic Model

CHAPTER 1: INTRODUCTION

In some ocean-continent subduction systems, plate convergence leads to horizontal shortening and crustal thickening of the overriding continental plate, generating major mountain belts. These mountain belts are important localities for understanding how continental crust accommodates horizontal shortening and are also the sites for many of Earth's mineral and energy resources. One such mountain belt is the Sevier fold-thrust belt of the North American Cordillera, which extends from Alaska to Mexico. The major components of a Cordilleran system consist of a subduction zone, volcanic arc, and a retro-arc fold-thrust belt. Retroarc fold-thrust belts are interpreted to be the result of horizontally-directed compressive stresses associated with subduction, and the transfer of stress from the subducting oceanic lithosphere to the overriding continental plate. The retroarc Sevier fold-thrust belt is one of the foremost localities for investigating the geometry, kinematics, and dynamics of ancient retroarc fold-thrust belts formed during plate convergence (e.g., Armstrong, 1968; Dahlstrom, 1969; Burchfiel et al., 1992, Dickinson, 2004; Yonkee and Weil, 2015). Horizontal contraction in the retroarc associated with the Cordilleran margin affected large tracts of upper-crustal rocks in North America during Mesozoic time (Burchfield and Davis, 1975; Dickinson, 2004; Yonkee and Weil, 2015). In North America, the maximum eastern extent of the Sevier fold-thrust belt is known as the Idaho-Wyoming salient, and is defined by an array of major, eastward transported, thrust fault-bound sheets of sedimentary rocks. Estimates for total horizontal slip within the Idaho-Wyoming salient range from 160-220 km (DeCelles, 2004; DeCelles and Coogan, 2006; Yonkee and Weil, 2015; Yonkee et al., 2019). The Idaho-Wyoming salient of the Sevier fold-thrust belt has been fundamental to the understanding of the kinematics, geometry, timing, and resource potential of continental-scale fold-thrust belts. Research conducted in the Idaho-

Wyoming salient of the Sevier fold-thrust belt provides the foundation for our understanding of continental fold-thrust belts around the world.

Good exposures, and a wealth of subsurface data has contributed greatly to the understanding of the kinematics and shortening estimates within the eastern portion of the Idaho-Wyoming salient (Royse et al., 1975; Coogan 1992). However, much of the presumably older western portion of the salient in southeastern Idaho, lacks published and proprietary subsurface data, and has been complexly overprinted by normal faulting and volcanic deposits related to the Yellowstone volcanic system (Armstrong and Oriel, 1965; Kellogg, 1992; Pierce and Morgan, 1992; Kellogg et al., 1999; Rodgers et al., 2002; Gentry et al., 2018). Therefore, reconstruction of these thrust systems relies heavily on detailed geologic mapping as a primary constraint. Without an improved understanding of the geometry and kinematics of western thrusts at these latitudes, the Mesozoic history of horizontal shortening within the greater Idaho-Wyoming salient remains unclear.

The Putnam thrust is the western most major thrust of the Idaho-Wyoming salient, and is an important Sevier-age structure that likely accommodated a significant amount of shortening early in the history of the Idaho-Wyoming salient. Being the western most major thrust structure, the Putnam system is likely one of the oldest thrusts within the Sevier belt and represents a critical transitional area between the foreland and hinterland of the Sevier fold-thrust belt. The Putnam thrust is likely a northern equivalent to the Paris thrust, and resides within the hanging wall of the Meade thrust (Royse et al., 1975; Coogan, 1992; Rodgers and Janecke, 1992; Yonkee and Weil, 2015). However, interpretations as to the internal geometry of the Putnam system are conflicting, and range from a foreland-dipping duplex (Kellogg et al., 1999) to a duplex (Rodgers and Long, 2012). At present, a viable kinematic model for the entire Putnam system does not exist (Kellogg et al., 1999; Rodgers and Long, 2012). Part of this disagreement stems from existing mapping in the Pocatello Range (Rodgers and Othberg, 1999; Rodgers et al., 2006) and the Portneuf Range to the east (Kellogg et al., 1989; Kellogg, 1990; Riesterer et al., 2000), which proposed differing interpretations of the observed structural geometry and sequence of deformation. Important hanging wall structures of the Putnam thrust exposed in the Portneuf Range of southeastern Idaho are essential for understanding the subsurface architecture and reconstructing a viable kinematic model of the thrust system; however, mapping for this area at a scale more detailed than 1:48,000 did not exist prior to this study.

Construction of detailed cross sections, and subsequent restoration of slip along Cenozoic normal faults permits the reconstruction of important Sevier-age thrust structures that were obscured by Cenozoic extension and volcanism. By doing so, we can better understand the degree to which thrust structures were modified and what their original geometries may have been prior to extensional overprinting. Understanding the pre-extension thrust geometries here can shed light on their correlation with structures of the central and eastern Sevier fold-thrust belt, and allow for the integration of these Sevier-age structures into a viable regional model which includes the foreland-hinterland transition of the Idaho-Wyoming salient.

Study Area

To better constrain the subsurface footwall geometry of the Putnam thrust sheet, additional hanging wall structures and subsidiary thrust faults need to be identified and mapped in detail. An existing transect of 1:24,000 scale quadrangles that encompass the Bannock, Pocatello, and Portneuf Ranges (Rodgers and Othberg, 1999; Riesterer et al., 2000; Rodgers et al., 2006) have identified many important structures within the Putnam sheet, but do not extend far enough east to capture any additional structural features in the immediate hanging wall of the Putnam thrust. Therefore, a major component of this project involved the 1:24,000 scale mapping of the Bear Camp Gulch 7.5-minute quadrangle on the eastern flank of the Portneuf Range in southeastern Idaho. Existing mapping for this area consisted of a compilation of unpublished preliminary mapping conducted at a scale of 1:48,000 (Corbett, 1978), which was partially reinterpreted and incorporated into the geologic map compilation of the Pocatello 30 x 60-minute quadrangle (Link and Stanford, 1999). This new mapping improves resolution of existing mapping, as well as highlights key thrust relationships, and the orientations of normal faults in the study area. Any attempts at understanding the contractional structures in this area must contend with the effects of Miocene extensional deformation, which are widespread (Pogue, 1984; Rodgers et al., 2002; Rodgers and Long, 2012). For example, many Mesozoic structures have been tilted and rotated by extension (Kellogg, 1992), and understanding the timing and magnitude of this deformation is key to reconstructing critical thrust relationships. Another component of this study was determining the extent and age of the Cenozoic basin fill. In this area, extension occurred in unison with development of the Yellowstone volcanic system and the formation of the eastern Snake River Plain, resulting in the deposition of the Miocene Starlight Formation, which consists of fluvial, lacustrine, volcanic, and volcaniclastic material that accumulated in developing basins (Trimble and Carr, 1976; Crane et al., 2000; Rodgers et al., 2002; Long et al., 2006). Samples were taken from key stratigraphic levels in the Starlight Formation and dated using U-Pb in zircon. Ages and structural attitudes of the Starlight Formation were combined in order to constrain the magnitude and timing of extension within the study area.

The overarching goal of this study is to conduct detailed mapping of Miocene normal faults and basin fill, as well as critical thrust structures in the Portneuf Range in order to constrain the timing and effects of Miocene extension in southeastern Idaho; these results will then help refine the existing kinematic model for the Putnam thrust system. New, high-resolution mapping will be a valuable resource for future work in this area and cross-sections can be used for framing future hypotheses focused on extension and contraction in the region and in other similar tectonic settings. Improving our understanding of the anatomy of the Putnam thrust system, and foreland-hinterland transition in the Idaho-Wyoming salient can further constrain estimates of crustal-shortening for the Sevier fold-thrust belt at these latitudes, and ultimately improve our understanding of deformation styles accommodated within Cordilleran retroarc fold-thrust belts.

CHAPTER 2: GEOLOGIC BACKGROUND

Introduction to the Geology of the Northern Portneuf Range

The geology of the northern Portneuf Range is dominated by thick successions of Neoproterozoic through Cambrian clastic and carbonate sedimentary rocks that were complexly deformed by Mesozoic thrusting and Cenozoic extension. These rocks and deformation within them record a diverse geologic history, including: 1) protracted Neoproterozoic to Cambrian rifting of Rodinia, 2) clastic and carbonate sedimentation during Paleozoic thermal subsidence of the rift margin and development of the Cordilleran passive margin sequence, 3) Mesozoic construction of the North American Cordillera, including horizontal crustal-shortening accommodated by the retroarc Sevier fold-thrust belt, 4) late Cenozoic extensional collapse of tectonically thickened crust, and 5) contemporaneous volcanism related to the passage of the Yellowstone volcanic system 50 km to the northwest. Presently, Mesozoic-age thrust structures are thoroughly overprinted by extensional deformation and hotspot related-volcanism, obscuring the pre-Cenozoic geologic record of the region.

Geologic History of Southeastern Idaho

Neoproterozoic-Paleozoic History

Neoproterozoic Rifting and the Paleozoic Passive Margin

The Cordilleran rift-margin is defined by Rb-Sr isotopic data ($^{87}Sr/^{86}Sr$) that mark the western extent of Laurentian crust, coarsening of sediments within thick clastic sedimentary packages that have been documented from southern California to Canada (Stewart, 1972), mafic volcanism, and variations in detrital zircon provenance that record shifts from distal to local sediment source areas as differential uplift of basement blocks during rifting disrupted continental-scale drainage networks (Crittenden et al., 1971; Armstrong et al., 1977, Link et al., 1987, Yonkee et al., 2014).

Development of the Laurentian rift margin occurred over a period of approximately 200 Myr, beginning with an initial episode of intracratonic basin formation and early volcanism from ~770 – 600 Ma (e.g., Dehler, 2010). Subsidence and final rifting occurred between ~660 and 520 Ma, with the quartzites of the lower Brigham Group recording broad subsidence along the margin (Yonkee et al., 2014). The completion of rifting is recorded by the Mutual Formation of the upper Brigham Group, and the transition to drift and a passive margin setting by the middle Cambrian Elkhead Limestone (Crittenden et al., 1971; Link et al., 1987; Smith et al., 1994).

The oldest exposed rocks in the study area belong to the Neoproterozoic and lower-Cambrian Brigham Group, which includes the Inkom, Mutual, Camelback Mountain Quartzite and Gibson Jack formations (Link et al.,1987). In southeastern Idaho, strata of the Brigham Group consist primarily of quartzites and conglomerates with subsidiary siltstones and shales, documenting a transition from a deep marine to a fluvial and shoreface depositional environment (Mansfield, 1927; Crittenden et al., 1971; Oriel and Armstrong, 1971; Oriel and Platt, 1980; Link et al., 1987). The generally coarse-grained nature and thickness of the Brigham Group (~4000 m) has led to the widespread interpretation that these rocks record terrigenous detrital input during and just after rifting of the supercontinent Rodinia (e.g., Yonkee et al., 2014). Chrono-and-lithostratigraphic equivalents to the Brigham Group have been described from the Yukon to southern California, recording the late Neoproterozoic-early Paleozoic rifting of the western margin of the ancestral North American continent Laurentia (Yonkee et al., 2014; Brennan et al., 2023).

Paleozoic carbonates and lesser siliciclastic rocks overlying the Brigham Group in southeastern Idaho record shallow-water or near-shore marine conditions during deposition of the Cordilleran passive margin sequence (Stewart, 1972; Bond et al. 1985; Yonkee et al., 2014). In the study area, these units include the Cambrian Elkhead, Bloomington, and Nounan formations; the Cambro-Ordovician St. Charles Formation; the Ordovician Swan Peak, Garden City, and Fish Haven formations; and the Silurian Laketown Dolostone. Aside from the Ordovician Swan Peak Quartzite, the Worm Creek Member of the Cambrian-Ordovician St. Charles Formation is the only other clastic lithology in this sequence, and contains ~500 Ma zircons associated with exhumation of the Beaverhead and Lemhi plutons to the north of the eastern Snake River Plain (Link et al., 2017). Deposition of carbonate-rich strata during Cambrian, Ordovician, and Silurian time occurred along the entire Cordilleran margin; this carbonate succesion thickens to as much as 8 km in western regions, but thins to the east toward the craton (Stewart, 1972; 1974; Yonkee et al., 2014). These sedimentary rocks were deposited primarily in shallow marine environments and carbonate platforms, onlapping onto the craton during transgressive events of the Sauk and Tippecanoe sequences (Sloss, 1963; Link et al., 1987; Yonkee et al., 2014).

Disruption of the Passive Margin

Continued sedimentation along the passive margin was periodically interrupted by tectonic activity along the western edge of North America. Though Devonian-Permian rocks are not present in the northern Portneuf Range, they are present in the footwall of the Putnam thrust as well as ranges both to the east and west (Oriel and Platt, 1980; Link and Stanford, 1999). In Late Devonian to Mississippian time, the Antler orogeny resulted from the oblique closure of a western basin outboard of the passive margin, and deformation of marginal marine and volcaniclastic sedimentary rocks in present-day central Idaho and Nevada (Burchfiel et al., 1992). In Nevada, this event is well-documented by the Roberts Mountain thrust and the adjacent Antler foreland basin clastic sequence consisting of the Chainman Shale and the Diamond Peak Formation (Burchfiel and Davis, 1972; Harbaugh, 1981; Speed and Sleep, 1982; Burchfiel et al., 1992; Cashman and Sturmer, 2023). However, in Idaho this event is more enigmatic. In central Idaho, Antler tectonism is evidenced by a thick succession of Mississippian marine rocks known as the Copper Basin Group, consisting largely of turbidite deposits, submarine fans, and deltaic deposits. The eastern boundary of the Copper basin is marked by a transition to shallow marine sediments and the appearance of reefal limestones (Paull et al., 1972; Wilson et al., 1994; Beranek et al., 2016). Based on rapid subsidence rates, sediment routing patterns, evidence for mafic volcanism and mineralization typical of extensional faulting, the tectonic setting of the Copper Basin Group was interpreted to be a transtensional pull-apart basin resulting from oblique plate convergence during Late-Devonian and Mississippian time (Link et al., 1996; Beranek et al., 2016). South of the Snake River Plain, orogenic detritus related to the Antler tectonism is lacking, and Devonian-Mississippian deposition was characterized instead by carbonate sedimentation along the slope and forebank of a prograding carbonate shelf (Skipp, et al., 1979). Accordingly, during Late Devonian and Mississippian time, southeastern Idaho was far enough east that it was the site of deposition of a cratonal platform carbonate bank in a zone of semi-restricted circulation represented by deposition of the Devonian Hyrum Dolomite and Beirdneau Formation, and a thick sequence of Mississippian limestone (Oriel and Platt, 1980). This semi-restricted marine depositional environment persisted into Pennsylvanian and Permian time in southeastern Idaho during development of the Ancestral Rocky Mountains (Geslin, 1998). Development of the Ancestral Rocky Mountains is exemplified by enigmatic basement-cored uplifts and adjacent rapidly subsiding basins across the western U.S. imparted by the combined collisional stresses from the Ouachita-Marathon belt and the Sonoran margin of Laurentia (Miller, et al., 1992; Leary et al., 2017). Pennsylvanian to Permian Rocks in southeastern Idaho were likely deposited in the eastern Wood River-Oquirrh Basin, which is interpreted to be a short-lived foreland basin that developed in response to reactivated Antler age structures farther to the west in Nevada (Geslin, 1998). Late Permian to Early Triassic time saw a similar series of events similar to the Antler orogeny, in which Permian deep marine and volcanic rocks deposited in a western basin were again thrust eastward during the Sonoma orogeny (Speed and Sleep, 1982; Dickinson, 2006).

Mesozoic History

Amalgamation of the North American Cordillera

By Early-to-Middle Triassic time, eastward subduction of oceanic lithosphere beneath western North America is suggested by the development of a nascent volcanic arc, although a series of island arcs and accompanying oceanic basins likely resided outboard of the subduction zone at this time (Burchfiel and Davis, 1972; Hamilton, 1969; Dickinson, 2006). In southeastern Idaho, Early and Middle Triassic time was characterized by a shallow-to non-marine depositional setting, with a package of sedimentary rocks thinning to the east with increasing proximity to the cratonal platform (Hamilton, 1969). Sedimentary rocks from this time are not present in most of the Portneuf Range, but are in nearby ranges to the east, and consist largely of limestones, siltstones, shales, and lesser sandstones of the Dinwoody Formation, Woodside Shale, and the Thaynes Limestone (Oriel and Platt, 1980). Upper Triassic rocks of southeastern

Idaho record the retreat of shallow seas and deposition of continentally-derived sandstones and conglomerates (McKee, 1951).

The Jurassic breakup of the supercontinent Pangea and opening of the Atlantic Ocean initiated a major episode of global tectonic reorganization, and facilitated the development of a coherent east-dipping subduction zone along with a well-established volcanic arc along the western margin of North America (Armstrong, 1968; Hamilton, 1969; Dewey and Bird, 1970; Burchfield and Davis, 1975; Coney and Evenchick, 1994; DeCelles, 2004). Accretion (Coney et al., 1980; Monger et al., 1982).

By mid-Jurassic time, east-dipping subduction along the continental margin of Laurentia and west-dipping subduction associated with fringing island arc complexes resulted in the complete subduction of the Mezcalera plate and the closure of these intervening intra-arc basins (Dickinson, 2006). Subsequent to this collision, east-dipping subduction of the Farallon plate was reestablished outboard of the accreted terranes along much the North American Cordilleran margin (Dickinson, 2006). Outboard of Idaho, accretion of the intra-oceanic island-arc Blue Mountain composite terrane along the Salmon River suture zone occurred in Early Cretaceous time, beginning around 130 Ma, and may have persisted until approximately 118 Ma when the oldest undeformed plutonism in the suture zone is observed. (McClelland, et al., 2000; Schwartz et al., 2014). This event was followed by the establishment of east-dipping subduction of the Farallon plate and activation of arc volcanism in the Idaho batholith at approximately 110 Ma (Gaschnig et al., 2011; 2017). This resulted in a coherent magmatic arc present along the margin of the Cordillera from Mexico to Alaska (Armstrong, 1974; Gaschnig et al., 2011).

Oblique convergence of the North American Plate with the eastward-dipping Farallon Plate resulted in development of a retroarc fold-thrust belt in the overriding continental plate, known as the Sevier fold-thrust belt, named for exposures of thrust structures in the Sevier desert of central Utah (Armstrong, 1968; Coney and Evenchick, 1994). During the interval from 140 to 55 Ma, Neoproterozoic-Paleozoic rift-related and passive margin strata were remobilized and transported eastward by north-south striking thrust faults, which exploited fine-grained siliciclastic units as major detachment horizons (Armstrong, 1968; DeCelles, 2004). This roughly 6000-km long belt of retroarc deformation was continuous from Alaska to Mexico (Fig. 2.1; Burchfiel and Davis, 1975; Dickinson, 1978; Coney and Evenchick, 1994; DeCelles, 2004) and is exemplified by thin-skinned folding, thrust faulting, and horizontal transport of long, thin thrust sheets of clastic and carbonate sedimentary rocks toward the continental interior.

In contrast, an episode of generally high-angle faulting, and thrust transport of crystalline basement rocks began in latest-Cretaceous and early Paleogene time, and briefly overlapped in time with earlier thin-skinned thrusting associated with the Sevier fold-thrust belt (Armstrong, 1968; Burchfiel and Davis, 1975; DeCelles, 2004). Deformation of this style also accommodated east-west to northeast-southwest crustal shortening, yet differed in structural style from that of the Sevier and occurred farther inboard of the zone of classic Sevier-style deformation (Armstrong, 1968). This region of deformation is known as the Laramide province and is characterized by a thick-skinned structural style; it was named for exposures in southern Wyoming (Coney, 1976; Dickinson and Snyder, 1978; Erslev, 1993). Most structures associated with Laramide-style deformation are located to the east of the study area (Fig. 2.1). This region of deformation has often been considered to have formed during a separate orogeny, and is traditionally been attributed to the subduction of an oceanic plateau that may have caused a shallower subduction angle and terminated arc magmatism in the Sierra Nevada (Lipman, 1971; Coney and Reynolds, 1977; Dickinson and Snyder, 1978; Livaccari et al., 1981; Saleeby, 2003).

However, other regions along the plate boundary likely did not experience shallow subduction and thus Laramide structures there may have developed in response to propagation of the fold-thrust belt into the continental interior (Parker and Pearson, 2021).

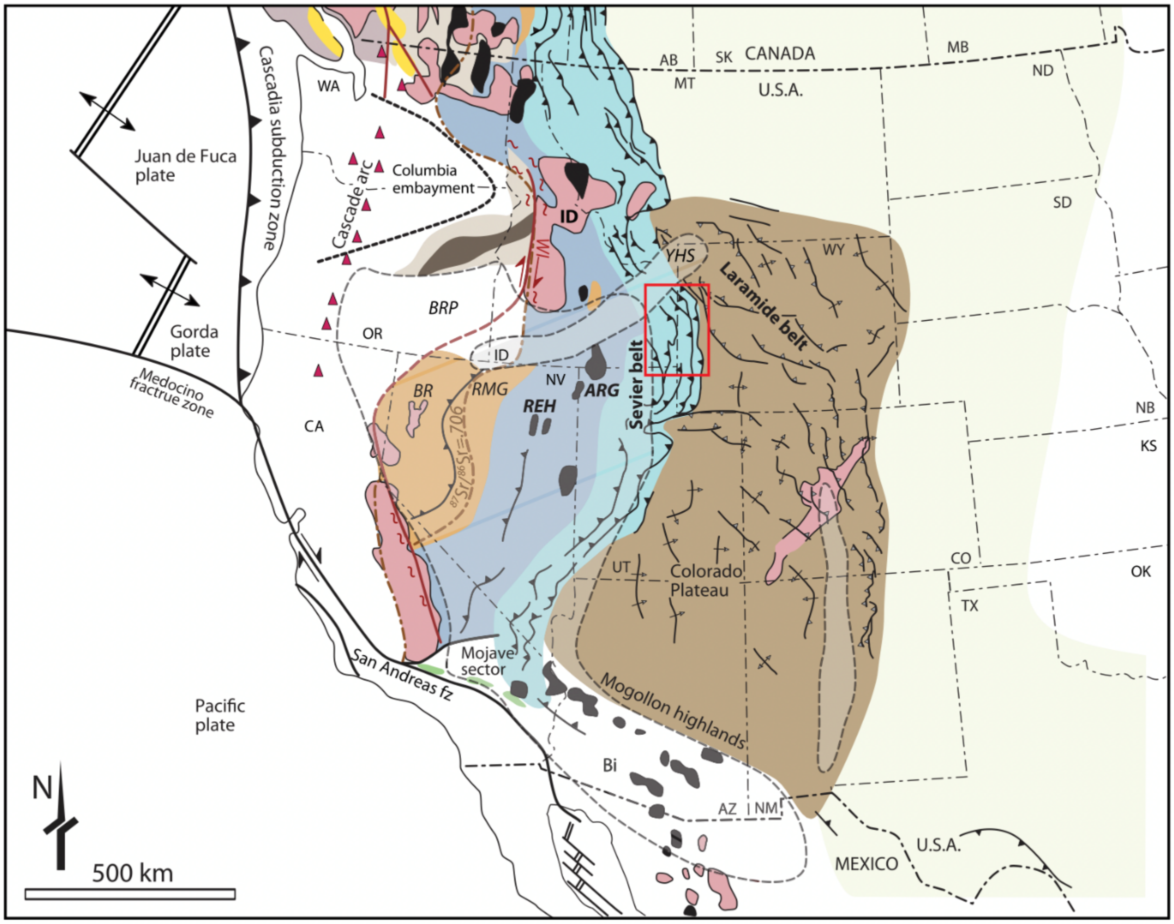

Figure 2.1 – Major geologic provinces of the North American Cordillera. Idaho-Wyoming salient outlined in red.

Horizontal Crustal Shortening within the Idaho-Wyoming Salient

In the southeastern Idaho-Wyoming portion of the Sevier fold-thrust belt, construction of the Cordilleran orogen is expressed by large, generally north-south striking thrust faults that accommodated tens of kilometers of offset, and bound major thrust sheets and structural culminations (Royse et al., 1975; Coogan, 1992; DeCelles, 2004; Yonkee and Weil, 2015). On the basis of propagation of the foreland basin toward the continental interior, the magnitudes of total horizontal crustal shortening range between 300 and 350 km for the latitude of the study area during Late-Jurassic to Eocene time (DeCelles and Coogan, 2006). However, balanced cross sections, which are generally constructed as minimum estimates of horizontal shortening, suggest 160-220 km, (DeCelles, 2004; DeCelles and Coogan, 2006; Yonkee and Weil, 2015; Yonkee et al., 2019). The Idaho-Wyoming salient contains eight major thrust fault systems (Fig. 2.2); from west to east, they are: The Paris, Willard, Meade, Crawford, Medicine Butte, Absaroka, Darby and Hogsback thrusts (Royse et al., 1975; Coogan, 1992; DeCelles, 2004; Yonkee and Weil, 2015). Near Pocatello, thrusts include the Putnam thrust, which is likely the northward continuation of the Paris thrust system (Rodgers and Janecke, 1992).

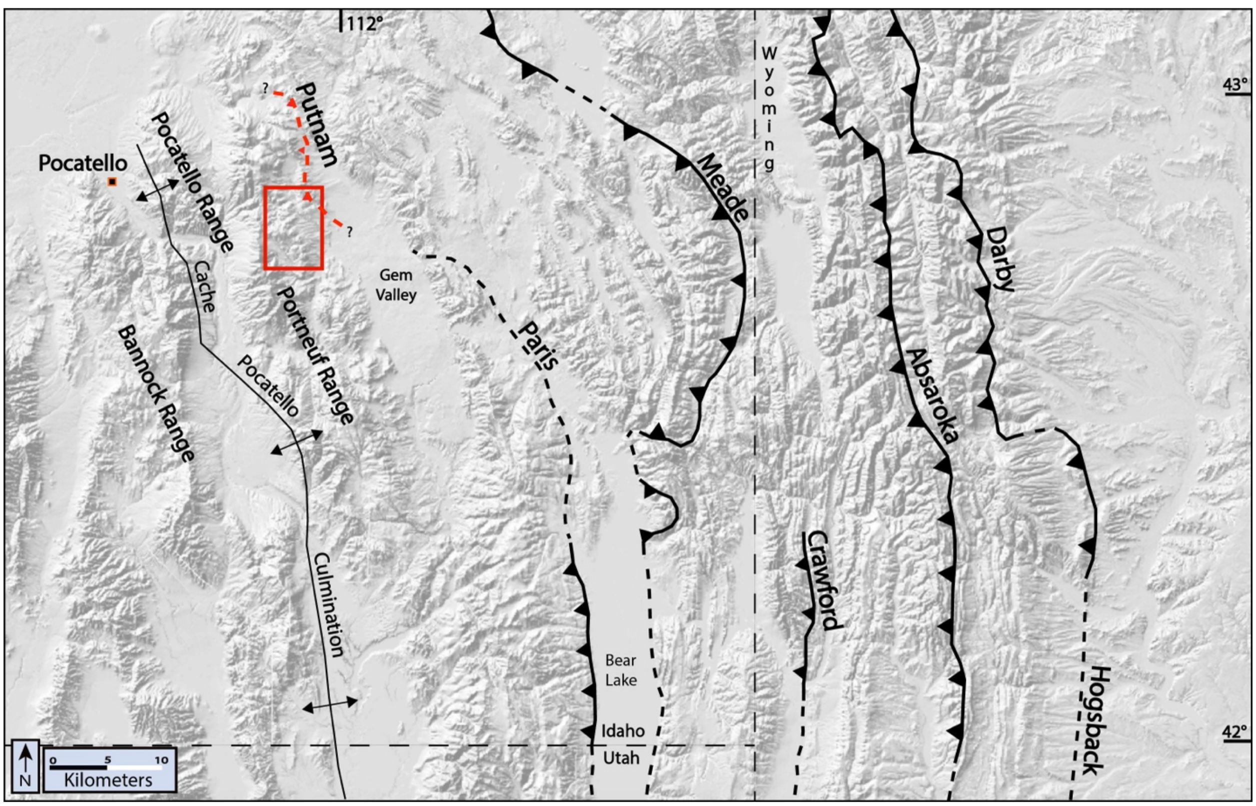

Figure 2.2 – Major thrust faults of the Idaho-Wyoming Salient. The Willard thrust is interpreted to be the along-strike equivalent to the Paris thrust and is exposed south of the map. Study area is shown by a solid rectangle and the trace of the Putnam thrust is shown by a dashed red line.

The Paris-Willard-Putnam system of southeastern Idaho is the western-most and likely the oldest major thrust of the Sevier belt, assuming deformation in the fold-thrust belt occurred primarily in-sequence (e.g., DeCelles and Mitra, 1995). As such, it is likely that the Putnam thrust contributed significantly to the total shortening budget of the Idaho-Wyoming salient, particularly in the early history of the Sevier fold-thrust (Gentry et al., 2018). In northern Utah, the Paris and Meade thrust systems were active from 125 to 96 Ma and accommodated 60-70 km of horizontal slip before transferring displacement to the thrust systems to the east. The Willard thrust is an along-strike equivalent to the Paris-Putnam thrusts, and was active between 125-90 Ma (Wiltschko and Dorr, 1983; Yonkee and Weil, 2015; Gentry et al., 2018; Yonkee et al., 2019). Slip rates during this time fluctuated between 1-3 km/m.y. from 125-92 Ma (Yonkee et al., 2019) with a period of increased slip occurring between 104-96 Ma, which coincided with an increase in deformation and subsidence rates along the Sevier belt from southern California to parts of Canada (Panã and van der Pluijm, 2015; Wells, 2016).

A regional kinematic model at the latitude of the study area does not yet exist for the Idaho-Wyoming salient that encompasses both the Paris and Putnam thrusts, as well as major thrust sheets to the east. The geometry and kinematics of major thrust sheets to the east of the Paris-Putnam thrust have been better constrained by an abundance of hydrocarbon exploration-related seismic and drill hole data from southeastern Idaho and western Wyoming (e.g., Royse et al., 1975; Dixon, 1982; Coogan, 1992). However, these data are limited within and west of the Putnam thrust, where rocks were too hot for hydrocarbon preservation (e.g., Harris et al., 1980) and thus were largely unexplored by the petroleum industry. This lack of seismic and well data, widespread structural complexities, and pervasive Neogene extensional dismemberment have hindered geologists from developing a viable structural model for the Putnam thrust sheet for almost a century. At present, the most complete cross-section for the area west of the trace of the Putnam thrust (Fig. 2.3) does not span far enough to the east to capture the hanging wall geometries necessary for deciphering critical subsurface features. Without a viable kinematic model and balanced cross section for the Paris-Putnam system, a total shortening magnitude for the Sevier belt at this latitude cannot be estimated. For this reason, the Bear Camp Gulch quadrangle was chosen for this study because it extends the existing mapping and cross-sections that encompass the Putnam thrust sheet, and likely contains structural elements essential to understanding subsurface geometries of the Putnam thrust sheet.

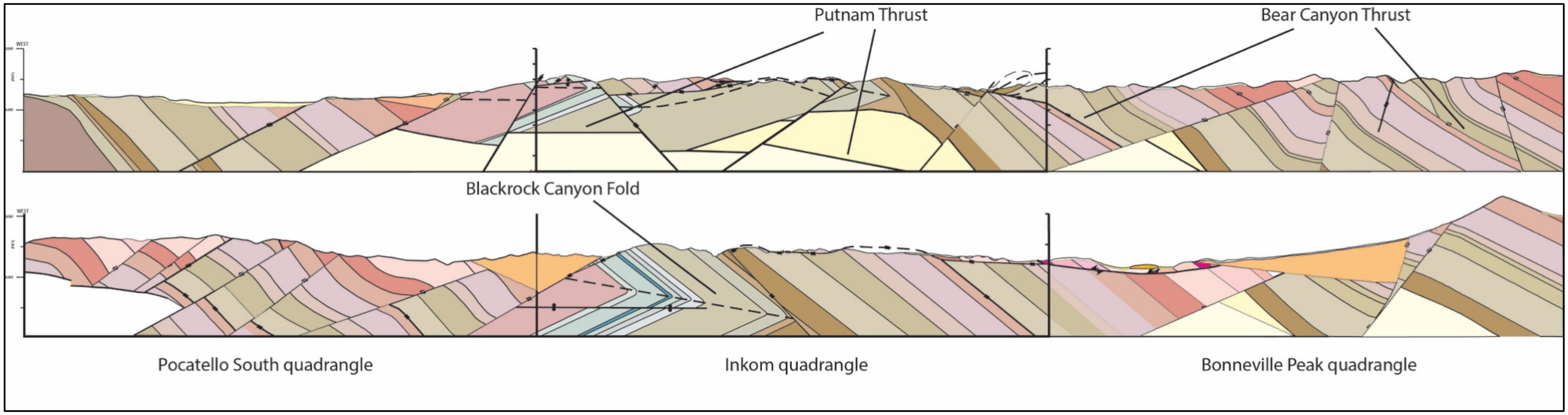

Figure 2.3 – Regional cross-sections depicting Bear Canyon thrust and hanging wall geometries of the Putnam thrust system. Modified from Rodgers and Othberg (1999), Rodgers et al. (2006), and Riesterer et al. (2000). Locations of cross sections shown in Fig. 2.5.

The Putnam Thrust Sheet

The study area is located within the hanging wall and near the leading edge of the Putnam thrust (Fig. 2.2; Kellogg, et al., 1989; Kellogg, 1992; Kellogg et al., 1999). Although no Mesozoic rocks are preserved in the Portneuf Range, contractional deformation inferred to result from the Sevier orogeny is pervasive. First described by Mansfield (1920) during initial geologic investigations of the Shoshone-Bannock Reservation, the Putnam thrust system was later recognized as an important Sevier-age structure (Trimble, 1982; Kellogg, 1992). Where it is exposed, the Putnam thrust placed upper Cambrian and Ordovician rocks over Mississippian and Pennsylvanian carbonates (Pogue, 1984; Kellogg, 1992; Kellogg et al., 1999). Trimble and Carr (1976) first proposed that the Putnam system was simply a northern continuation of the Paris thrust. However, stratigraphic displacement along the Putnam thrust decreases to the southeast before the thrust becomes concealed by Miocene and Quaternary rocks, whereas stratigraphic displacement along the Paris thrust decreases to the northwest as it approaches the inferred trace of the Putnam thrust (Rodgers and Janecke, 1992). Therefore, it is likely that the two thrust systems are equivalent, but a thrust transfer system exists between them, and the thrusts may not be connected directly at depth (Kellogg, 1992; Rodgers and Janecke, 1992; Steely et al., 2005).

Within the Putnam thrust sheet, several subsidiary thrust faults were interpreted to sole into the Putnam thrust; of these thrusts, the Putnam is the primary thrust structure and likely served as a major basal regional décollement (Kellogg, 1992; Rodgers and Long, 2012). The Putnam thrust sheet has been further subdivided into three smaller sub-sheets bounded by the Bear Canyon, Toponce, and Narrows thrusts (Kellogg, 1992; Kellogg et al., 1999). A smaller-displacement thrust, the Inman Pass thrust, is contained largely within the Cambrian Gibson Jack Formation (Riesterer et al., 2000), and likely contributes little to the overall shortening budget of the greater Putnam thrust system. The best exposed of all these structures is the Bear Canyon thrust, which is exposed along the western Portneuf Range front as far south as the Pebble Creek Ski Resort (Riesterer et al., 2000), and can be followed northward along-strike where it curves eastward toward the Toponce and Putnam thrusts (Fig. 2.4; Kellogg et al., 1989; Kellogg, 1990; Rodgers and Long, 2012). Along the western Portneuf Range, the Bear Canyon thrust displays a hanging wall flat-on-footwall flat thrust relationship, with the Proterozoic Caddy Canyon Quartzite in the hanging wall and the Cambrian-Neoproterozoic Camelback Mountain Quartzite in the footwall. In almost all exposures, the footwall rocks of the Bear Canyon thrust are stratigraphically upright (Riesterer et al., 2000). Along the western Portneuf Range front, the Bear Canyon thrust is east-dipping, likely due to eastward tilting during growth of the Cache-Pocatello culmination and tilting of fault blocks on down-to-the east normal faults in the region (Kellogg et al., 1999).

On the northeastern flank of the Portneuf Range, the Toponce thrust placed Neoproterozoic strata on overturned Ordovician carbonates and quartzites (Kellogg et al., 1989). This relationship is similar to the Bear Canyon thrust in some locations to the northwest and west in the Bonneville Peak and South Putnam Mountain quadrangles (Kellogg, 1990; Riesterer et al., 2000) where the same Neoproterozoic strata are placed on steeply dipping and overturned upper Cambrian and Ordovician rocks (Pogue, 1984; Kellogg et al., 1989; Kellogg, 1990). Based on these observations, Kellogg (1992) interpreted the Toponce thrust to be an eastward correlative of the Bear Canyon thrust. Thus, the name Bear Canyon-Toponce thrust is used for thrusts on the western and eastern flanks of the Portneuf Range that contain similar strata in their hanging walls. Due to these similarities, the two thrusts were inferred to bound the same thrust sheet, and merge with the Putnam thrust at depth (Kellogg, 1992). However, substantially different units are involved in each of the two thrust systems, and thus it remains unclear if these thrusts are the indeed the same, which was one subject of investigation in this thesis.

Despite recognition of the Putnam thrust as an important structure for over a century (Mansfield, 1920, Pogue, 1984; Kellogg, 1992; Kellogg et al., 1999), details regarding its internal geometry and its role in accommodating shortening within the greater Sevier fold-thrust belt continue to elude workers due to a lack of consensus. The two most recent studies that present cross sections for the northern Portneuf Range and Pocatello Range focus on different segments of the Putnam thrust sheet and are not reconcilable (Fig. 2.4).

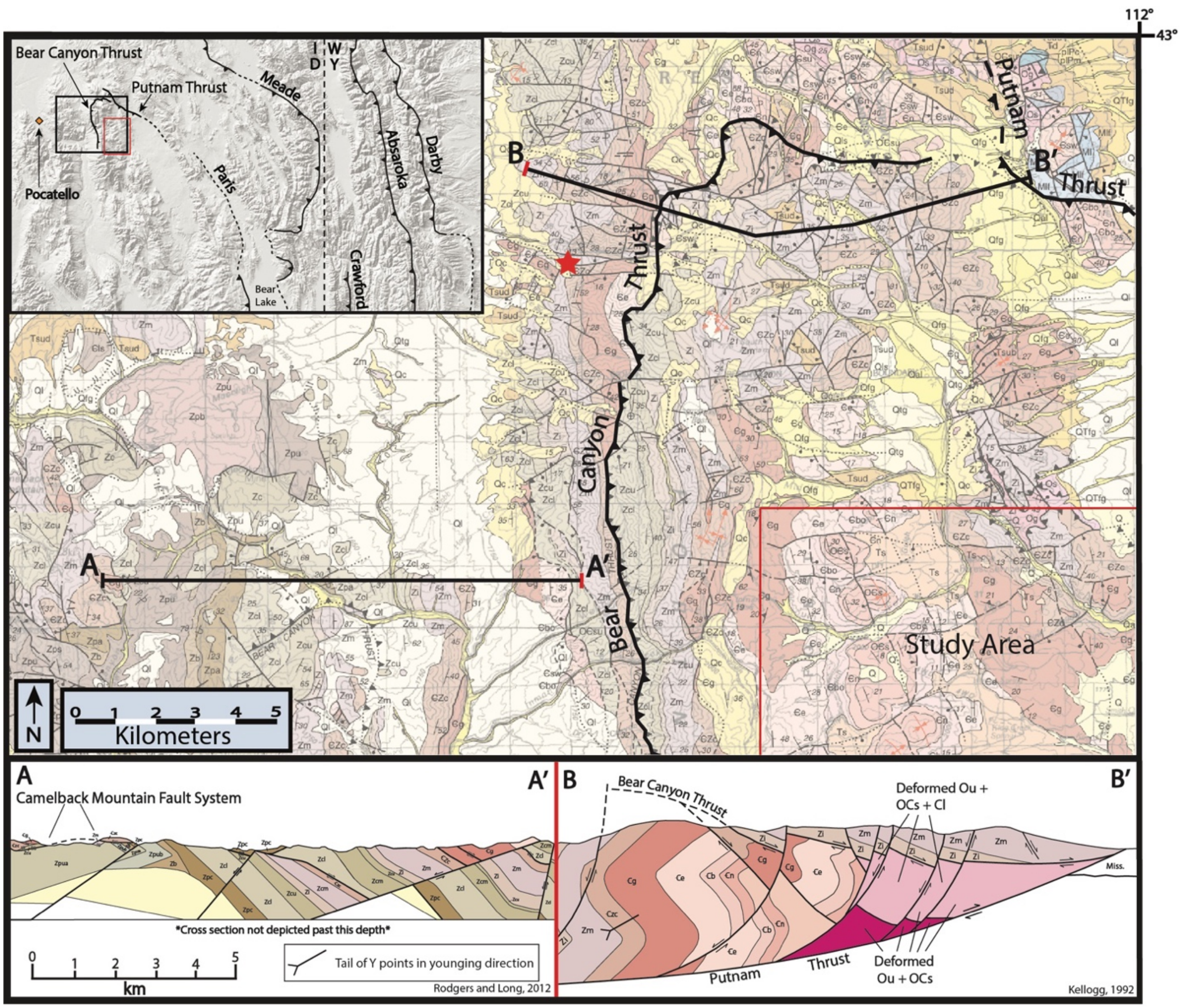

Figure 2.4 – Conflicting structural interpretations for the Putnam thrust sheet. Red star denotes overturned structures near Mill Creek. A-A’ modified from Rodgers and Long (2012), and B-B’ from Kellogg (1992).

For example, the model put forward by Kellogg (1992) focused on the eastern portion of the thrust sheet below the Bear Canyon-Toponce thrust, which was interpreted as a foreland dipping duplex with imbricates or small horses invoked to explain the overturned and recumbent folds (B-B', Fig. 2.4). This interpretation is based on mapping and observations in the South Putnam Mountain and Jeff Cabin Creek quadrangles (Kellogg et al., 1989; Kellogg, 1990), which characterize this subplate as having a high degree of internal deformation, with large panels of overturned strata in east-vergent folds, and overturned structures in the western part of this subplate near Mill Creek (Fig. 2.4) (Kellogg et al., 1999). This contrasts with the rocks above the Bear Canyon-Toponce thrust, which are upright and relatively internally undeformed. Rodgers and Long (2012) focused on the western portion of the thrust sheet to the south (A-A', Fig. 2.4) with an emphasis on explaining the regional-scale folding and overturned strata observed in the Pocatello Formation, in addition to the regional erosional patterns within the context of the Cache-Pocatello culmination. The key difference between these two cross sections is that the strata in the footwall of the Bear Canyon thrust to the south are upright and not overturned, yet along strike to the north, footwall strata are steeply dipping and overturned. (Kellogg, 1990; Riesterer et al., 2000; Rodgers and Long, 2012). When the two cross-sections are merged using a common stratigraphic horizon, they are geometrically and kinematically incompatible (Fig. 2.4), demonstrating the presence of unresolved/unidentified structural complexities for the Bear Canyon thrust along strike, (Fig. 2.4).

Despite these differences in observed structural style along strike, there is unity in that the models of Link et al. (1985), Kellogg (1992), Kellogg et al. (1999), and Rodgers and Long (2012) all necessitate a major frontal footwall ramp for the Putnam thrust somewhere west of its current location (Rodgers and Janecke, 1992; Rodgers and Long, 2012). This concealed ramp may be localized near a Proterozoic basement fault related to rifting and crustal thinning (Burgel et al., 1987). Major west-dipping normal faults that developed during Neoproterozoic rifting may have acted as major east-vergent thrust ramps during the Mesozoic (e.g., DeCelles, 2004; Yonkee and Weil, 2015, Gentry et al., 2018).

The Cache-Pocatello Culmination

Paleogeologic maps are valuable tools for visualizing simplified map-scale geologic structures, magnitudes of tectonic erosion, and thrust sheet geometries as they existed prior to the multiple phases of extension and deposition of Cenozoic rocks (e.g., Rodgers and Janecke, 1992; Carney et al., 2002; Steely et al., 2005; Long, 2012). Paleogeologic maps of southeastern Idaho (Rodgers and Janecke, 1992; Rodgers and Long, 2012) reveal a large exposure of Neoproterozoic and Cambrian rocks defining a series of large-wavelength folds beneath a regional pre-Miocene unconformity (Fig. 2.5). To the west of this Neoproterozoic and Cambrian strata, rocks decrease in age to Mississippian and Permian. Based on outcrop patterns of rocks below the Miocene rocks in the region, the Cache-Pocatello culmination was defined as a regional-scale antiformal structure in the hanging wall of the Paris-Putnam thrust sheets (Rodgers and Janecke, 1992; Carney et al., 2002; Steely et al., 2005).

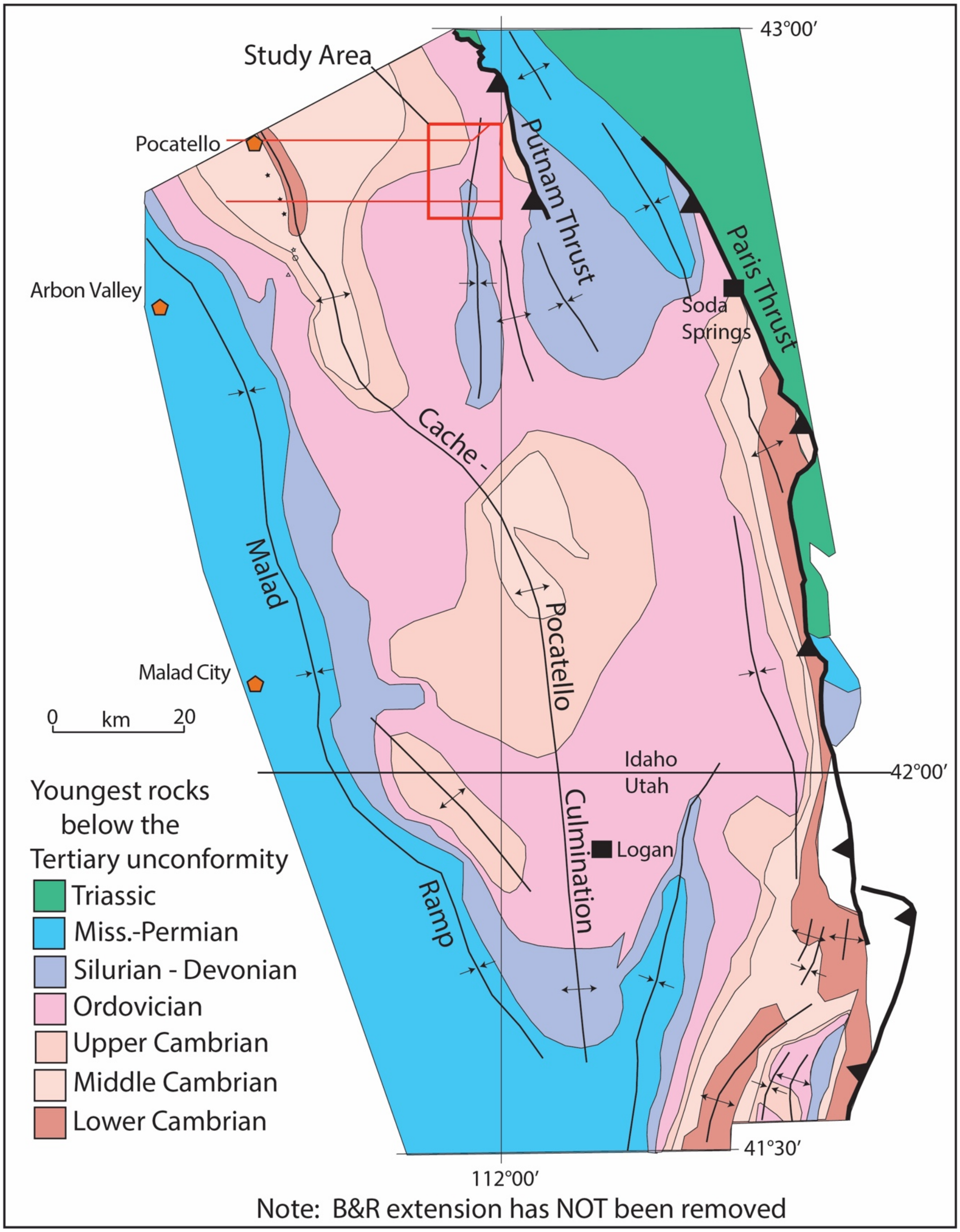

Figure 2.5 – Paleogeologic map showing exposed rocks beneath the Tertiary unconformity. This map pattern was used to interpret the presence of the Cache-Pocatello culmination, which is located west of the Paris-Putnam thrust system (modified from Steely et al., 2005). Study area outlined in red. Horizontal red lines indicate lines of existing cross sections in Figure 2.3 from maps of Rodgers and Othberg (1999), Rodgers et al. (2006), and Riesterer et al. (2000).

The Cache-Pocatello culmination is interpreted to have formed by eastward transport of the Paris-Putnam thrust sheets over a regional-scale footwall ramp-to-flat, which resulted in a regional-scale fault-bend fold antiform (Rodgers and Janecke, 1992; Steely et al., 2005; Rodgers and Long, 2012). Based on the high magnitude of structural relief, and its position relative to the trace of the Paris-Putnam thrust, the presence of this major structural culmination suggests that the basal décollement steps down to lower structural levels in this area and may have accommodated significant shortening. The location of this ramp is inferred to exist along a north-northwest axis between the towns of Malad and Arbon Valley, Idaho where west-dipping strata young westward from lower-Cambrian to flat-lying Pennsylvania-Permian (Rodgers and Janecke, 1992; Steely et al., 2005).

Involvement of Neoproterozoic passive margin strata in the Wasatch anticlinorium of north-central Utah is similar to the Cache-Pocatello culmination, where Neoproterozoic strata were detached from a concealed basement ramp (Steely et al., 2005; Rodgers and Long, 2012). The Wasatch anticlinorium is an antiformal structure built by duplexing of crystalline basement thrust slivers that were progressively removed from a major basement step (Fig. 2.6). In this manner, slip was transferred from basal Neoproterozoic strata upward into Cambrian shale to the east (Yonkee, 1992). The Cache-Pocatello culmination may represent the northern continuation of the Wasatch anticlinorium, a transitional zone between the eastern and western thrust systems defined in the Utah-Wyoming Sevier thrust belt (Yonkee, 1992).

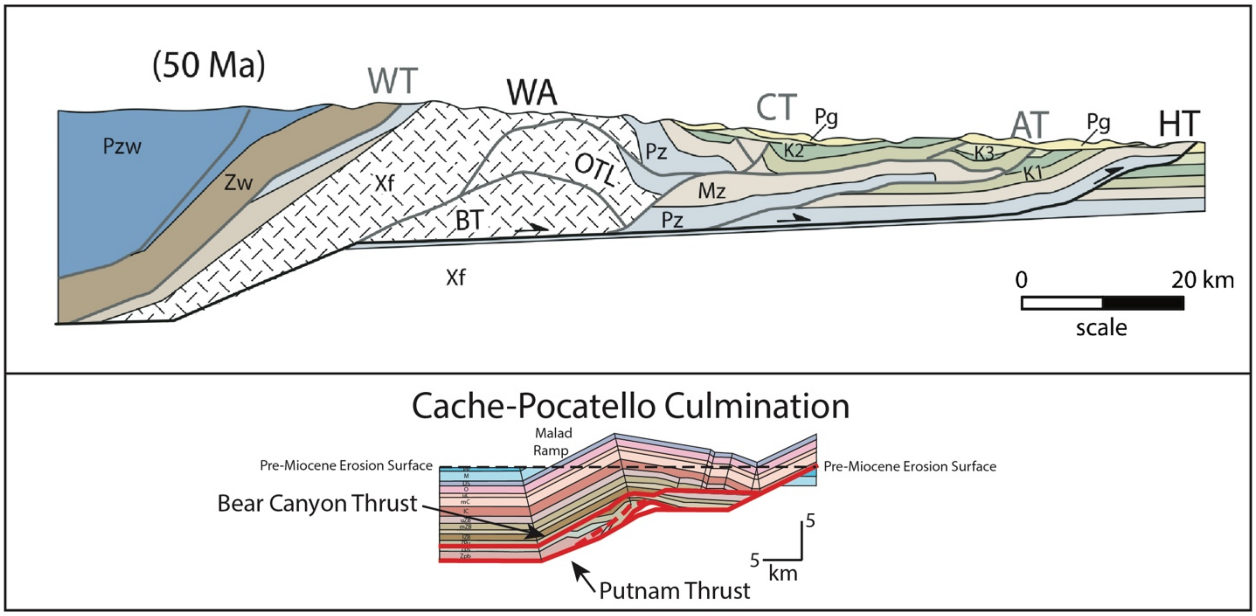

Figure 2.6 – Comparison of the Cache-Pocatello culmination (bottom) and the Wasatch anticlinorium (top). WA - Willard Thrust, WA - Wasatch Anticlinorium, CT - Crawford Thrust, AT - Absaroka Thrust, HT - Hogsback Thrust. Modified from Rodgers and Long (2012) and Yonkee and Weil (2015).

Unlike the Cache-Pocatello culmination, crystalline basement rocks and portions of the basal décollement are exposed at the surface within the hingezone of the Wasatch anticlinorium (Yonkee, 1992). This structure is significant because similar antiformal culminations in the North American Cordillera have been shown to focus early extensional collapse of the orogen (Yonkee, 1992; Carney, 2002; Constenius, et al., 2003; Carney and Janecke, 2005; Steely et al., 2005; Rodgers and Long, 2012; Long et al., 2015). Attempts at developing a working model for the evolution of Mesozoic contraction must contend with the effects of Cenozoic extension, block rotation, and subsequent obscuration of contractional structures.

Cenozoic History

Southeastern Idaho experienced two phases of Cenozoic extension. The first was interpreted to be related to orogenic collapse, with extension often localized by structural culminations (Coogan, 1992; Constenius, 1996; Carney and Janecke, 2005). The second phase was interpreted to be related to Basin and Range extension, a phenomenon related to evolving plate margins, and observed across most of western North America (Atwater, 1970; Dickinson, 2006; Faulds and Henry, 2008). Additionally, this latter phase of extension was enhanced (Rodgers et al., 2002) with increasing proximity to the Yellowstone-eastern Snake River Plain volcanic system (e.g., Camp et al., 2015).

Eocene-Oligocene Extensional Collapse of the Cordilleran Orogen

Following the termination of the Sevier-Laramide crustal shortening in early Paleogene time, western North American began to experience an early phase of extension, beginning with orogenic collapse of the Sevier belt and hinterland plateau (Coney and Harms, 1984; Constenius, 1996; Konstantinou et al., 2012; Vogl et al., 2012; Long et al., 2015). An erosional unconformity developed throughout southeastern Idaho and northeast Utah at this time (Rodgers and Janecke, 1992). This initial phase of Cordilleran extension was interpreted to result from the gravitational collapse of crust thickened during construction of the Cordilleran orogen, which was thermally weakened and preconditioned to spread laterally should the regional stress regime become perturbed (Constenius, 1996). In some cases, initiation of this type of deformation occurred after a brief hiatus between the termination of thrusting and the onset of extension, and saw the development of many metamorphic core-complexes, and regional magmatism linked to extension that accommodated high-magnitude horizontal extension focused in regions in the retroarc where the crust had been the most tectonically thickened. (Coney and Harms, 1984; Constenius, 1996; Vogl et al., 2012). The spatial-temporal pattern of onset for extension, metamorphic core-complex development, and magmatism decreases in age from north to south, beginning at 55-53 Ma in northern Idaho/southern British Columbia and migrating to southern Idaho by 32-25 Ma. (Konstantinou et al., 2012; Vogl et al., 2012). The Albion-Grouse Creek metamorphic core complex is located south-southwest of the Portneuf Range by approximately 140 km and records this initial arrival of magmatism and northwest-southeast extension in southern Idaho. Magmatism appears to have occurred prior to the onset of extension, beginning at 42 Ma, but generally overlapped with the beginning of extension, which occurred in two phases. The early minor phase occurred between 32-25 Ma and accompanied the diapiric rise of plutonic rocks, with the later phase occurring in the Miocene. In several areas within the thrust belt, extension appears to have been accommodated by normal faults that were previously active as thrusts and in some cases exploited thrust-related structures (Coogan, 1992; Constenius, 1996; Constenius et al., 2003). For example, the Bear Lake fault of southeastern Idaho is a reactivated normal fault which exploited a footwall ramp in the underlying Crawford thrust (Coogan, 1992). This early period of extensional collapse and the subsequent Basin and Range-style extensional episode are separate and distinct events, and are typically separated by a significant hiatus (Constenius, 1996; Konstantinou et al., 2012).

Basin and Range Extension

The development of the San Andreas fault along the western margin of North America beginning in Oligocene time had far-reaching effects on the geologic setting of the western U.S. Transition of the North American margin from Andean-type subduction to a right-lateral transform plate boundary fundamentally altered the stress regime, leading to a renewed episode of extension and magmatism in the Cordillera (Atwater, 1970; Dickinson, 2006; Faulds and Henry, 2008; McQuarrie and Oskin, 2010). With the inception of motion on the ancestral San

Andreas fault system, thrust faulting associated with the convergent plate margin that had dominated much of western North American since Late-Jurassic time began to transition to a dextral-transform boundary, leading to another phase of regionally distributed extension that migrated across in tectonically thickened crust and the hinterland of the Cordilleran fold-thrust belt (Dickinson, 2006; Konstantinou et al., 2012). In southeastern Idaho, Basin and Range extension appears to have been enhanced by Yellowstone hotspot volcanism and geomorphic development of the eastern Snake River Plain (Anders et al., 1989; Anders and Sleep, 1992; Pierce and Morgan, 2009; Camp et al., 2015).

In Idaho, Basin and Range-style crustal thinning appears to have begun at approximately 17-16 Ma (McQuarrie and Wernicke, 2005), following the onset of magmatism in northwestern Nevada and southeastern Oregon (Christian and Yeats, 1992; Stockli et al., 2003; McQuarrie and Wernicke, 2005). However, this is disputed by other workers who have suggested that extension was active prior to this, in the period 45-18 Ma (Coney, 1980; Livaccari, 1991; Camp et al., 2015). Compilations of fault activity broadly illustrates that Basin and Range extension has migrated northeastward through time along with northeast migration of the interpreted Yellowstone volcanic center (Fig. 2.8; Rodgers et al., 2002; Camilleri et al., 2017). Accordingly, acceleration of Basin and Range-related extension in the Albion-Raft River-Grouse Creek metamorphic core complex initiated a second phase of exhumation of metamorphic rocks at 13.5-10.5 Ma (Konstantinou et al., 2012). During this interval from ~13 to 8 Ma, older Miocene normal faults in the Albion-Raft River-Grouse Creek core-complex appear to have been cut and tilted significantly by younger fault sets (Konstantinou et al., 2012). Basin and Range-style extension is more spatially distributed than the high magnitude horizontal extension associated with the exhumation of crystalline metamorphic rock along low angle normal faults (Dickinson, 2006; Konstantinou et al., 2012). In southeastern Idaho, it is not clear whether extension has occurred in discrete pulses, or continuously, locally enhanced by the Yellowstone volcanic system. South of the eastern Snake River Plain (ESRP), several phases of extension have been identified which range in age from 16-10 Ma, 11-4 Ma, and 4 Ma to present (Rodgers et al., 2002; Steely et al., 2005; Long et al., 2006). Furthermore, it is unclear whether these phases are separated by periods of inactivity, or overlapped in time.

Proximal to the study area, there appear to be two overlapping phases of extension. Rodgers et al. (2002) identified an older, poorly understood phase which occurred between roughly 16-10 Ma, and a younger phase from 11-4 Ma (Fig. 2.8). This younger phase tracked closely with the location of the Yellowstone volcanic system (Rodgers and Long, 2012). The phase of extension that occurred between 16-10 Ma is broadly characterized by north-south striking, primarily west-dipping normal faults and resultant basins containing synextensional packages of fluvial, lacustrine, and lesser volcanic detritus (Rodgers et al., 2002). Sedimentation rates of 50-80 m/m.y. suggest slow rates of both subsidence and extension (Rodgers et al., 2002). Near the study area, there are two generation of normal faults that relate directly to this modified Basin and Range extension (Fig. 2.7). In the Pocatello Range, the undated Camelback Mountain fault is currently oriented subhorizontally, implying it was active during the older phase of extension in the area (Rodgers et al., 2006; Rodgers and Long, 2012). In contrast, the west-dipping Fort Hall Canyon and Portneuf Range Front faults are steeper and cut across the Camelback Mountain fault, indicating they are younger and have contributed to half-graben style topography of the area (Rodgers and Othberg, 1999; Rodgers et al., 2002; Rodgers et al., 2006; Rodgers and Long, 2012). Subhorizontal faults such as the Camelback Mountain fault are likely related to older deformation, and younger range-bounding faults likely date from the more recent phase of extension. In addition to the regional north to north-northeast system of Basin and Range normal faults, in southeastern Idaho, a series of east-west striking normal faults variably are cut by, and cut across the regional structural grain (Rodgers et al., 2002). East-west oriented normal faults are typically oblique to the margin of the ESRP and display a range of slip magnitudes from 90 to 1,500 meters (300 to 5,000 feet; Rodgers and Othberg, 1999).

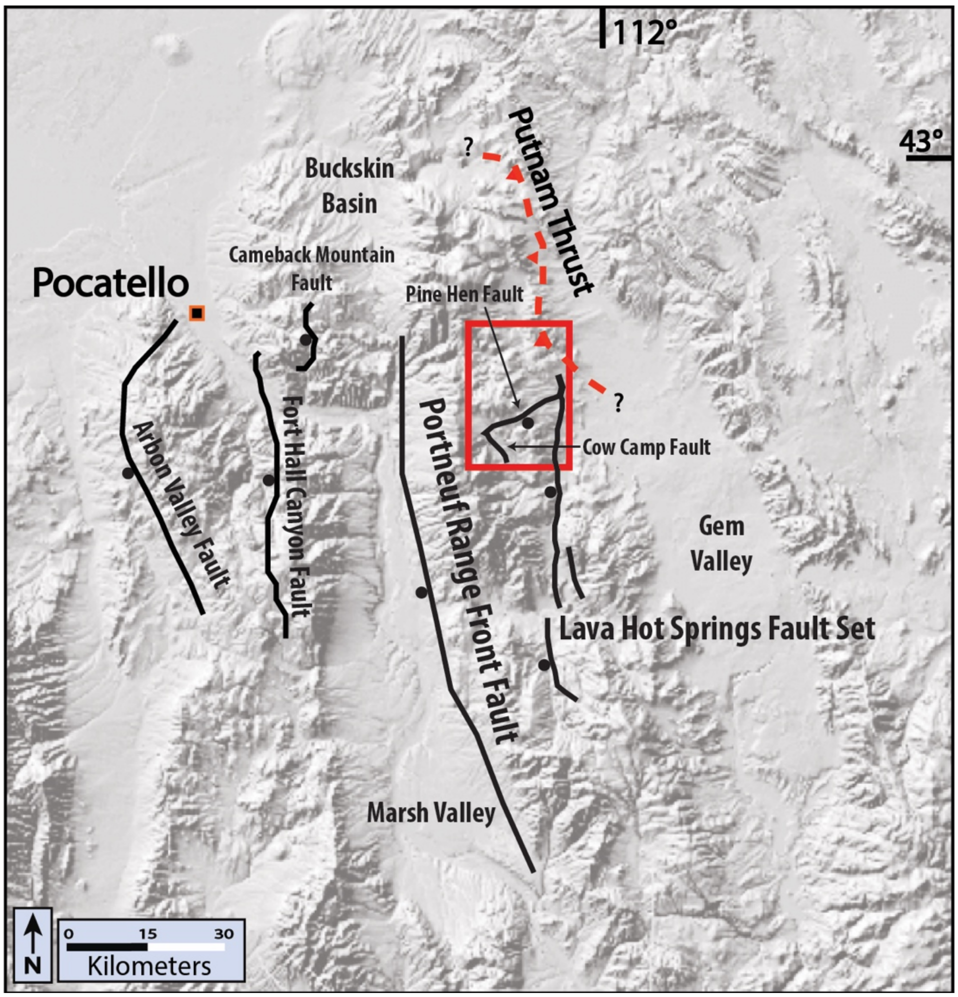

Figure 2.7 – Major normal faults of the Pocatello Area. Study area shown in red. Note the low-angle Camelback Mountain fault, which is cross-cut by the higher angle Fort Hall Canyon Fault.

The younger phase of extension (11-4 Ma) was also more intense, with sedimentation rates of 100-300 m/m.y. likely reflecting rapid horizontal extension rates of 4-6 km/m.y.

(Rodgers et al., 2002). This younger phase was also characterized by half-graben faulting, but in contrast to the first phase, it resulted in rapid basin tilting and deposition of thick clastic sediments including the upper Starlight Formation. Miocene basin fill in northern Utah and Idaho records tectonism in adjacent mountain ranges, and is variably referred to as either the Salt Lake or Starlight Formation depending on overall contribution of volcanic material (Trimble and Carr, 1976; Long et al., 2006). Generally, deposits that are predominantly clastic or carbonate fill are assigned to the Salt Lake Formation, whereas deposits found closer to the eastern Snake River Plain contain a significantly larger volume of volcanic and volcaniclastic material interpreted to have been derived from the Yellowstone volcanic system and are assigned to the Starlight Formation (Trimble and Carr, 1976). In southeastern Idaho, Rodgers et al. (2002) calculated 63 km of cumulative horizontal extension resulting from both episodes of crustal thinning.

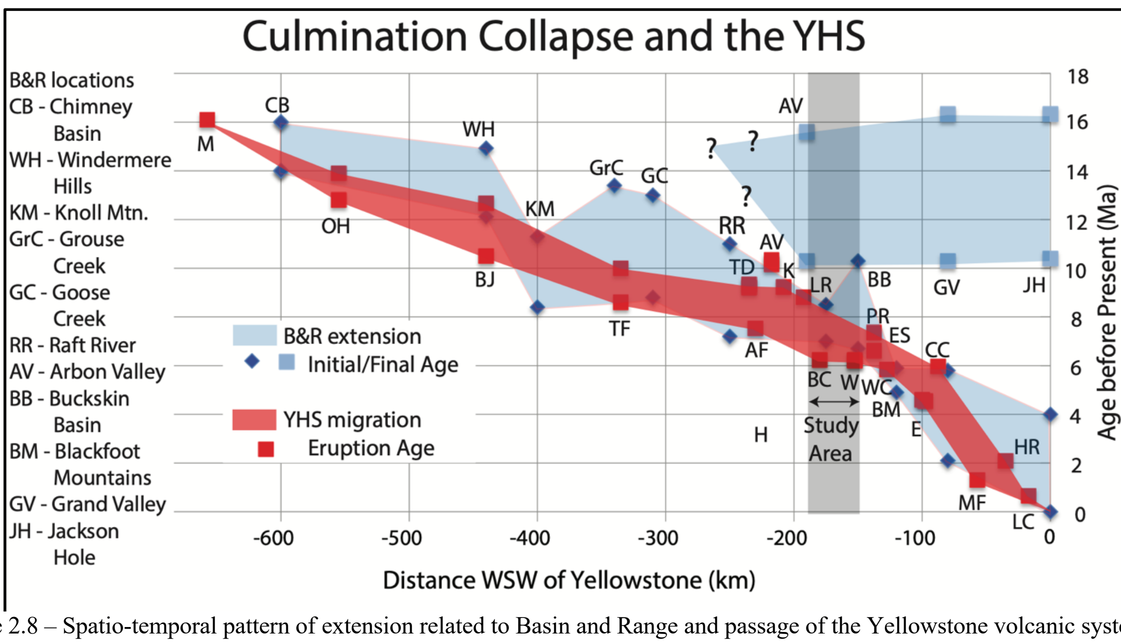

Figure 2.8 – Spatio-temporal pattern of extension related to Basin and Range and passage of the Yellowstone volcanic system (from Rodgers and Long, 2012). AF – Tuff of American Falls, BJ – Bruneau-Jarbidge volcanic center, BC – Tuff of Blue Creek, CC – Conant Creek Tuff, E – Tuff of Elkhorn Springs, ES – Tuff of Edie School, H – Tuff of Heise, HR – Huckleberry Ridge Tuff, K – Tuff of Kyle Canyon, LR – Tuff of Lost River Sinks, M – McDermitt Caldera, MF – Mesa Falls Tuff, OH – Owyhee-Humboldt volcanic center, PR – Tuff of Phillips Ridge, TD – Tuff of Timbered Dome, TF – Twin Falls Caldera, W – Walcott Tuff, WC – Tuff of Wolverine Creek.

The Yellowstone volcanic system

The Miocene initiation of the Yellowstone volcanic system was a significant event in North American geology and is responsible for much of the modern topography of southern Idaho (Pierce and Morgan, 1992; McQuarrie and Rodgers, 1998). A variety of hypotheses have been put forward to explain the abundant silicic volcanism associated with the Yellowstone volcanic center. These alternatives range from a mantle lithosphere source and reactivation of the western Idaho shear zone (WISZ) (Tikoff et al., 2008) to convective shear in the asthenosphere (Humphreys et al., 2000), upper-mantle upwellings related to subduction processes (Faccenna et al., 2010), and the effects of a mantle-derived hotspot (Pierce and Morgan, 1992; Nelson and Grand, 2018). However, most workers agree that it is the surface expression of a lower mantle-sourced plume head impinging on the lithosphere (Pierce and Morgan, 1992; Nelson and Grand, 2018). A tomographic study by Nelson and Grand (2018) revealed a narrow, slow velocity anomaly extending from the core-mantle boundary to the present-day location of Yellowstone National Park. This is supported by several key observations, including the presence of the ~100 km wide eastern Snake River Plain, and a northeast-younging, bimodal volcanic track (Pierce and Morgan, 1992). In addition to the time-transgressive volcanic track of the ESRP, the migration rate of ESRP volcanism and deformation relative to North America is approximately that of the North American plate velocity (Pierce and Morgan, 1992; Anders, 1994). An extension-adjusted rate of 2.30 cm/yr for the North American plate over the last 10.27 m.y. closely matches the extension-adjusted rate for migration of the ESRP deformation field at 2.38 ± 0.21 cm/yr (Anders et al., 2014).

The oldest rocks traditionally associated with the Yellowstone volcanic system belong to the 16.1 Ma McDermitt volcanic field of north-central Nevada and southeastern Oregon (Pierce and Morgan, 1992; Coble and Mahood, 2012). Volcanism associated with the hotspot was more regionally extensive between 16.1 and 10 Ma, and became more focused from 10 Ma to present (Pierce and Morgan, 1992; Shervais and Hanan, 2008; Camp and Wells, 2021). This has been attributed to the arrival of an extensive plume head that caused an early phase of widespread volcanism, followed by more spatially focused volcanic centers associated with the development of the modern eastern Snake River Plain (Pierce and Morgan, 1992). Volcanic material associated with the Yellowstone volcanic system is varied. The hotspot track generally consists of abundant basalts, but this mafic volcanism is thought to have post-dated emplacement of rhyolitic ignimbrites and calderas, which define the timing of the volcanic track (Pierce and Morgan, 1992). The (10-7 Ma) Picabo and (6.5-4.3 Ma) Heise volcanic fields were proximal to the study area, and were likely major sources of ash-fall deposits while they were active eruptive centers (Fig. 2.8).

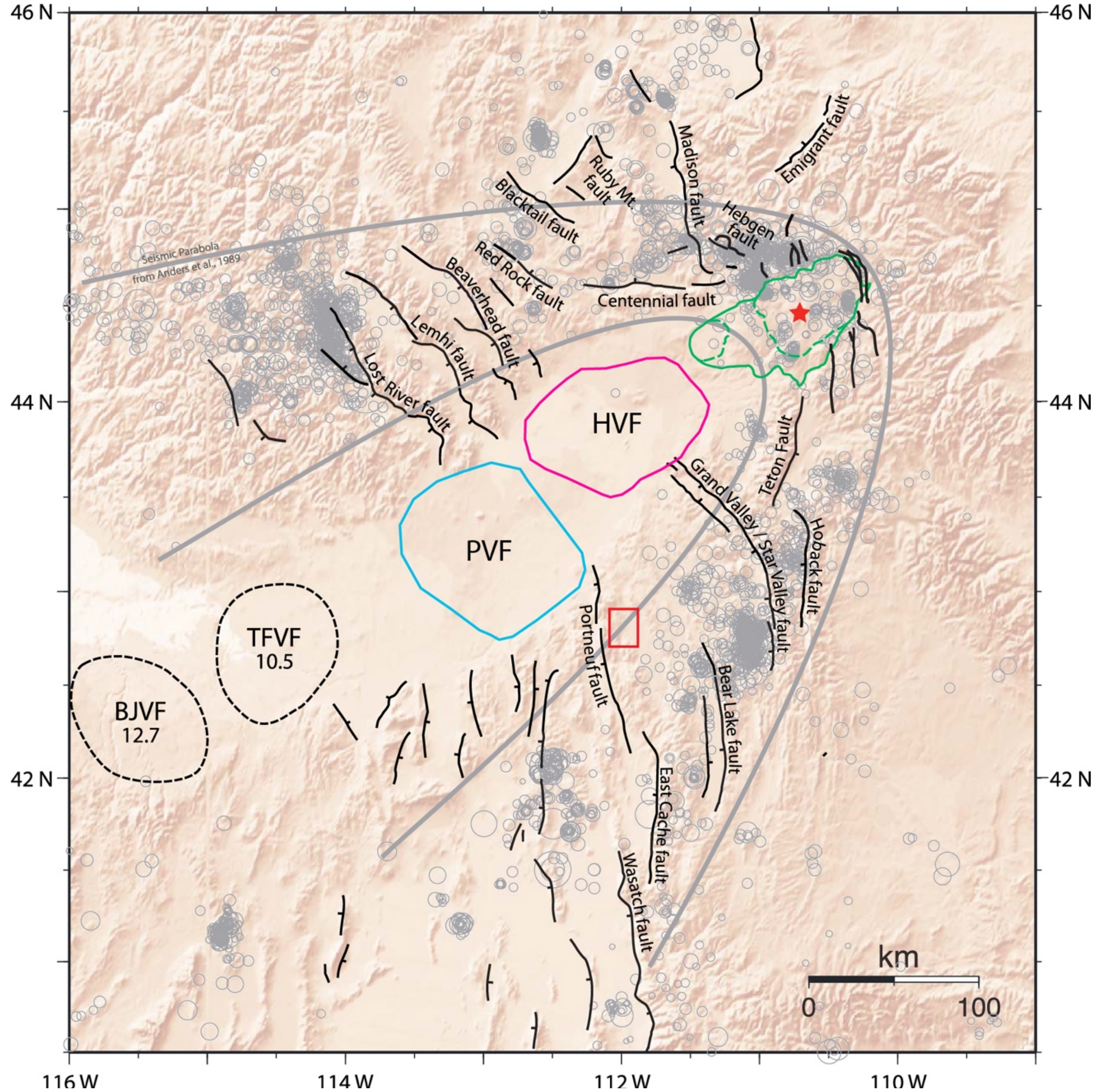

Figure 2.9 – Major eruptive centers and normal faults of the eastern Snake River Plain. Earthquake epicenters shown by translucent circles. Study location shown with red box. Present location of Yellowstone National Park shown by red star. BJVF (~12.5 Ma Bruneau-Jarbidge volcanic field), TFVF (Twin Falls volcanic field 12.5-7.5 Ma), PVF (10.2-7 Ma Picabo volcanic field), HVF (6.5-4.3 Ma Heise volcanic field). Modified from Anders et al. (2014).

Deformation associated with the Yellowstone volcanic system and development of the eastern Snake River Plain is evidenced by several prominent structural and geomorphic features within the region (e.g., Rodgers et al., 2002). Flexure and downwarping of the ESRP is attributed to mid-crustal loading of a thick (>10 km) mafic sill beneath the SRP (Sparlin et al., 1982;

Zentner, 1989; Anders and Sleep, 1992; McQuarrie and Rodgers, 1998; Rodgers et al., 2002). Small, low magnitude normal faults paralleling the ESRP to the north and south are interpreted to be the result of this flexure (Zentner, 1989; Rodgers et al., 2002; Schusler et al., 2020). This same crustal flexure caused fold axes in Paleozoic rocks flanking the northern SRP to systematically plunge into the plain (McQuarrie and Rodgers, 1998). A variety of geomorphic features also record dynamic paleotopography related to the Yellowstone highland and later subsidence of the ESRP. These include perched pediplains in the Bannock Range, barbed drainages along Bannock Creek indicating drainage reversals, and deep incision of the Portneuf River from 7 to 1 Ma (Pierce and Morgan, 1992; Rodgers et al., 2002; Thackray et al., 2011).

Quaternary History

The Quaternary geologic record of southeastern Idaho is highly varied. The Portneuf Range and surrounding ranges do not appear to have hosted alpine glaciers during either the Bull Lake or Pinedale glacial episodes (Licciardi and Pierce, 2018). The period post-dating the tenure of the Yellowstone volcanic system in southeastern Idaho saw an equilibration of the crust as the topographic highland migrated to the northeast (Rodgers et al., 2002; Thackray et al., 2011). The departure of the thermally-induced topographic highland resulted in systematic reorganization of drainage patterns, incision and down-cutting, and the development of the modern Snake River channel (Rodgers et al., 2002). Enigmatic volcanism continued in the region that does not seem to bear a simple relation to the Yellowstone caldera eruptions, particularly in the Gem Valley and nearby Blackfoot volcanic fields where voluminous basalt flows are chemically similar to the Yellowstone volcanic system, but appear to be localized by Cenozoic extension (McCurry et al., 2015). The basalt of Portneuf Valley, dated at 0.43 ± 0.07 Ma (unpublished whole rock $^{40}Ar/^{39}Ar$

date in Rodgers et al., 2006) occupies approximately 40 kilometers of the Portneuf River channel from its interpreted source near Gem Valley to its terminus in Pocatello. The configuration and extent of the Portneuf Valley basalt indicates that the river channel and drainage patterns have changed little since eruption of the basalt flow (Thackray et al., 2011). Neotectonic fault activity in southeastern Idaho has been interpreted to be a result of the continuing thermal effects associated with the Yellowstone volcanic system, which localized Basin and Range-style deformation. Quaternary faulting along the ESRP can be organized into arcuate zones of fault activity (Fig. 2.10; Anders et al., 1989). Fault activity closest to the ESRP is associated with waning activity on small faults, outboard of this area are faults which have been active within the past 15 ka, and the area beyond this is home to young escarpments that appear to be increasing in activity (Pierce and Morgan, 1992). The northern Portneuf Range is proximal to the ESRP and displays no history of active seismicity (Smith et al., 1985).

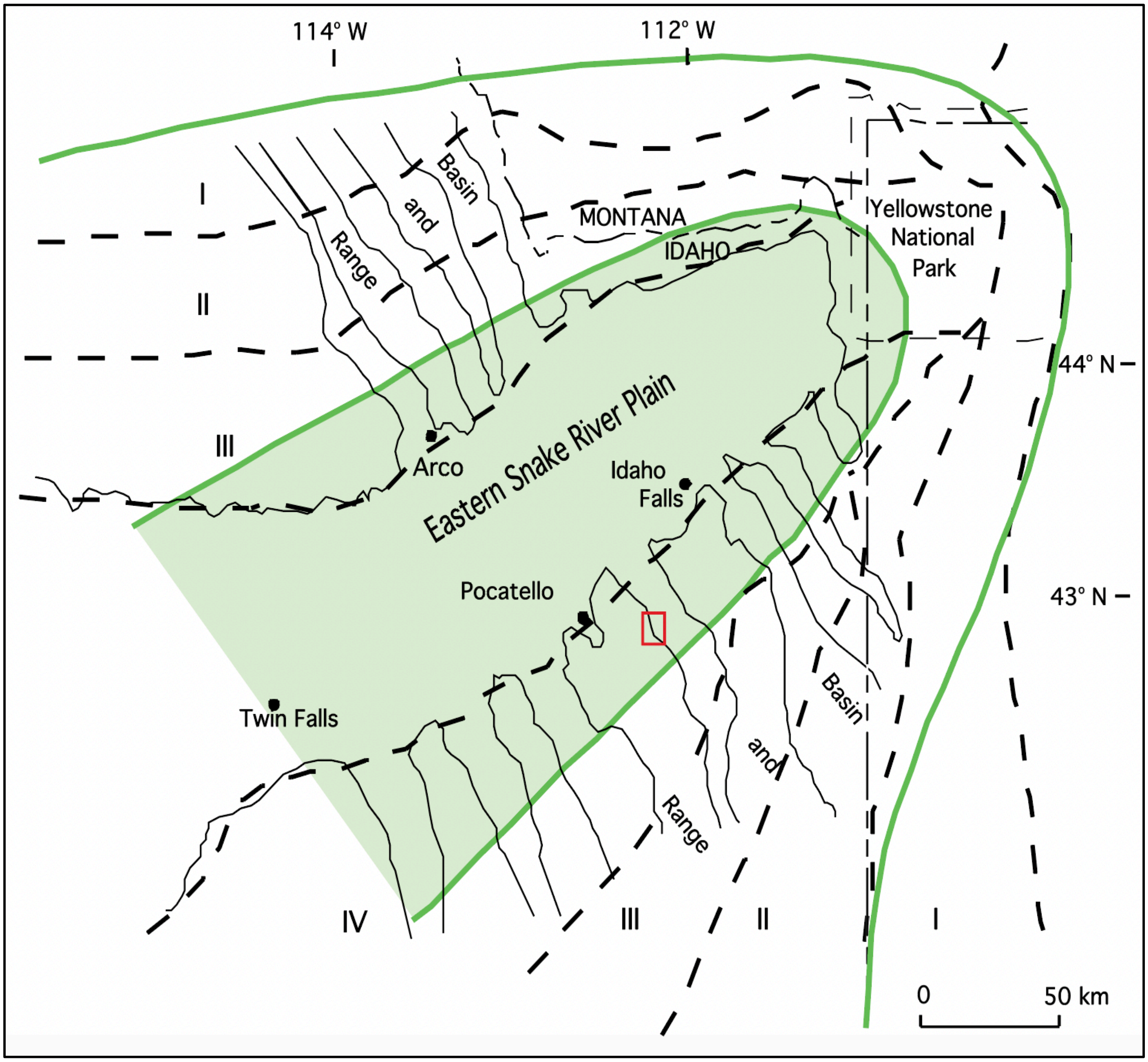

Figure 2.10 – Zones of seismic activity in southeastern Idaho, western Wyoming, and southwestern Montana. Red box is study area. Modified from Rodgers et al. (2002).

Thick deposits of loess are common adjacent to and paralleling the ESRP in south-central and southeastern Idaho. Loess is most abundant along the southern margin of the ESRP, and deposits thin and particle sizes decrease with distance from the ESRP (Lewis and Fosberg, 1982). In the vicinity of Pocatello and Gem Valley, deposits typically range from 1 to 8 meters to a maximum of 16 meters several km north of Pocatello (Lewis and Fosberg, 1982).

Previous Work

Several generations of geologists have mapped and worked in the Portneuf Range and surrounding areas, beginning with Mansfield (1920), who first identified the Putnam thrust. Additional mapping of the Putnam thrust was done by Carr and Trimble (1963), and Trimble (1976). During the 1970s, several students from Idaho State University mapped smaller areas of the Portneuf Range under the supervision of M.K. Corbett (Anderson, N.N., Nelson, L.B., Perkins, R.W., and Wieland, E.P.). Corbett (1978) compiled this existing mapping and conducted new mapping at a scale of 1:48,000 on the western flank of the Portneuf Range, where he identified and named the Toponce thrust for exposures above Toponce Creek, although overturned footwall rocks were not recognized at the time of mapping. He also mapped a thrust near Jeff Cabin Creek that he named the Jeff Cabin thrust. Following the efforts by Corbett and others in the 1970s, mapping in the Portneuf Range was focused largely on contractional structures to the north and northwest of the study area. Trimble, (1982), Pogue (1984) and Hladky (1986) conducted research in the vicinity of Putnam Mountain and Pogue (1984) proposed a model for the evolution of the greater Putnam thrust system and also identified the Bear Canyon thrust near South Putnam Mountain, where it placed primarily Neoproterozoic strata on Cambrian and Ordovician carbonates. Following the work of Corbett (1978), Pogue (1984) also mapped a thrust near Jeff Cabin Creek.

Link et al. (1985) proposed that eastward transport along the Putnam thrust initiated by detachment along an incompetent horizon, and ramped up-section through resistant lithologies, forming folds above the footwall ramp-flat transitions. As the Putnam décollement became inefficient by oversteepening or folding, new thrusts were interpreted to initiate in progressively higher stratigraphic positions. In this manner, major east-verging hanging wall folds were truncated by younger thrusts. Kellogg et al. (1989) and Kellogg (1990) mapped the Jeff Cabin Creek and South Putnam Mountain quadrangles, expanding work on the Sevier-aged structures exposed in those areas. Based on this mapping, Kellogg's (1992) revised model proposed that the upper plate of the Putnam thrust is a foreland-dipping duplex. Based on previous mapping and models, Kellogg (1992) also made the following modifications to prior work: (1) formal names were assigned to the different thrust-bound sheets that constitute the Putnam thrust sheet; (2) the geometry of each sheet was characterized and potential kinematic relationships with other sheets hypothesized; (3) folding was interpreted to be directly related to thrust faulting and major folds (wavelengths greater than 1 km) were interpreted to be likely expressions of concealed thrust ramps; (4) thrusts displacements were interpreted to be older up-section, as opposed to younger as in the model of Link et al. (1985); (5) the Bear Canyon and Toponce thrusts were interpreted to be the same fault; and (6) the Jeff Cabin thrust of Corbett (1978) was deemed unnecessary.

Some early workers in the region mapped many subhorizontal faults as thrust faults (e.g., Burgel et al., 1987). However, further work on large, low-angle faults demonstrates that they are likely late Cenozoic normal faults; this realization inspired reevaluation of many previously mapped thrust faults (Rodgers et al., 2006). In the nearby Pocatello Range, near Blackrock Canyon and Rapid Creek, large panels of what are now recognized as overturned strata were described variously as a west-vergent anticline (Anderson, 1928), west-vergent overturned folds (Ludlum, 1942), and thrust imbricates (Trimble, 1976). More recent work attributed these structures to fault-propagation folding over a major basement step (Rodgers and Long, 2012). Similar, but smaller, panels of overturned structures are present in the Portneuf Range in the vicinity of Mill Creek and Toponce Creek. Mapping of the Bonneville Peak quadrangle was completed in 2000 (Riesterer et al., 2000). Mapping to the south in the Lava Creek quadrangle by Crane et al. (2000) expanded the stratigraphy of the Salt Lake Formation, assigned ages to 11 ash beds, and hypothesized correlations with regional ashes of Perkins (1998). More recent contributions to understanding the anatomy of the Putnam thrust sheet were made with additional mapping of the Inkom quadrangle (Rodgers et al., 2006), which documented the overturned nature of the recumbent Blackrock Canyon fold, exposures of the Bear Canyon thrust, and recognition of the Camelback Mountain fault system. The most contemporary model for the Putnam thrust system was put forward by Rodgers and Long (2012), which united many regional observations into one model to explain the major features of the Putnam sheet.

CHAPTER 3: METHODS

Field Mapping

The primary mapping efforts within the study area were preceded by several days of reconnaissance investigations in the surrounding region to become familiarized with stratigraphy and contacts between units. Mapping within the field area was completed over the course of 66 days between late spring and fall of 2022. Field mapping was conducted at a scale of 1:24,000 on a 2013 USGS topographic base map of the Bear Camp Gulch 7.5-minute quadrangle. Unindexed aerial stereophotographs made for the USGS and United States Soil Conservation Service between 1938 and 1983 were used to supplement mapping of Quaternary surficial units. Structural and bedding attitudes were measured with a Brunton compass and the FieldMove Clino app installed on an Apple SE smartphone. Coordinates for each measurement's location were recorded from a Garmin InReach portable GPS unit.

Cartography

Hand-drawn map sheets were scanned and georeferenced in ArcMap 10.8. Linework was digitized over a georeferenced topographic base map of the Bear Camp Gulch quadrangle. All field map linework was digitized following the Federal Geographic Data Committee (FGDC) National Standard for the digital cartographic representation of geologic map features to ensure the use of correct line weights, symbols, and styles (https://www.fgdc.gov/). The database in ArcMap was structured using the Geologic Mapping Schema (GeMS) (https://pubs.er.usgs.gov/publication/tm11B10). Once essential cartographic elements were added in ArcMap 10.8, the map was brought into an Idaho Geological Survey technical report template for Adobe Illustrator where additional map elements such as a description of map units

(DoMU), correlation of map units (CoMU), appropriate cross sections and scales etc. were added in preparation for publication as an Idaho Geological Survey Technical Report.

Cross Sections

Cross-sections were constructed to highlight major structural features, important stratigraphic and fault relationships, reconstruct the pre-Cenozoic architecture, develop a viable model for the Putnam thrust system, and estimate magnitudes of shortening and extension in the Portneuf Range. Topographic profiles were constructed in Adobe Illustrator using the completed 1:24,000-scale geologic map of the Bear Camp Gulch quadrangle (Plate 1). Structural measurements for each cross-section line were compiled and apparent dips calculated using an apparent dip nomogram. Locations of faults, orientations, and contacts of bedding were projected to cross-section lines and used to interpret subsurface geometries and construct concealed structures. Based on the apparent dips of surface measurements, dip domains were defined for regions of the cross section that displayed similar ranges and orientations of attitudes. Axial surfaces of folds were modeled by bisecting the interlimb angle and treating folds generally as kink surfaces (Suppe, 1983). Because most normal fault surfaces were not exposed in the field, normal faults were interpreted to be steeply dipping on the basis of map patterns, and were drawn at angles of 60° from horizontal. However, due to a component of tilting accommodated by unknown normal faults, some previously steeply dipping faults may have been rotated into shallower orientations. Because the study area has been affected by both extension and contraction, contractional structures affected by extension must be reconstructed using cross sections, prior to estimating shortening magnitudes accommodated by thrust structures. Restoration of offset and untilting of fault blocks along extensional structures was performed following the methods of Gibbs (1983). Interpretation of the orientations and geometries of faults and folds in the subsurface was guided by models for fault-bend folds (Suppe, 1983) and fault-propagation folds (Mitra, 1990; Suppe and Medwedeff, 1990). Final cross-sections were drafted using Adobe Illustrator. Structural models were developed collaboratively with Matthew Ruggiero. Forward and inverse models created in Petroleum Experts' 2D MOVE modeling software by Matthew Ruggiero were then modified to test model viability for the study area.

Stratigraphic Separation Diagrams

Stratigraphic separation diagrams were constructed to chart the behavior of thrust faults and better understand the interplay between subsidiary thrust faults within the Putnam thrust sheet. Kellogg (1992) proposed a model for the Putnam thrust sheet in which the Toponce thrust is an eastward correlative of the Bear Canyon thrust. Tracking the behavior of these two thrusts with a separation diagram should help evaluate whether this this is a reasonable interpretation. Stratigraphic separation diagrams plot the exact geographic and stratigraphic locations where faults change stratigraphic position by cutting through stratigraphy, and are useful for analyzing the anatomy and behavior of a thrust system (Woodward, 1987; Wilkerson et al., 2002). Interpreting stratigraphic separation diagrams should be done in careful conjunction with field observations and as much regional geologic context as possible (Wilkerson et al., 2002). Using the Bonneville Peak (Riesterer, et al., 2000), South Putnam Mountain (Kellogg, 1990), and Jeff Cabin Creek (Kellogg, et al., 1989) 7.5-minute quadrangles, lengths of individual fault traces were measured, and stratigraphic position along their hanging-walls and footwalls were recorded and plotted on the separation diagrams. In this way, differentiating between concealed faults or faults that shared similar stratigraphic relationships was simplified, and determining the magnitude of stratigraphic separation for individual faults within the Putnam plate was more easily visualized.

Sampling Strategy and Preparation

A total of five samples (BCG-1, BCG-30, BCG-273, BCG-612, BCG-770) collected from the Miocene-Pliocene Starlight Formation were chosen for U-Pb zircon dating and trace element analysis by laser ablation-inductively coupled plasma-mass spectrometry (LA-ICP-MS), and subsequent Isotope-Dilution Thermal-Ionization Mass-Spectrometry (ID-TIMS) analysis. Outcrops that were interpreted to be primary airfall tuff ashes related to the passage/evolution of the Yellowstone volcanic system were targeted for sampling to bracket the timing and duration of crustal extension in this area, and identify the source of volcanic material. Samples were collected from mapped half-graben strata deposited during late-Cenozoic extension. Location coordinates, structural attitudes and lithological descriptions were recorded for each sample, prior to being secured in sample bags. Mineral separation procedures were conducted in the Idaho State University Mineral Separation Lab by undergraduate research assistant Kawner Sistrunk. These procedures entailed crushing by jaw crusher and disk mill, and then separation of zircon concentrate by Wilfley table, Frantz magnetic separator, and heavy liquid separation using methylene iodide.

Preparation for LA-ICP-MS analysis was conducted at the Boise State University Isotope Geology Laboratory by Yokel-Deliduka and Kawner Sistrunk, with supervision by Boise State University personnel from September 19th-23rd, 2022. This included handpicking of zircon grains from zircon concentrates, epoxy mounting and polishing, and cathodoluminescence imaging of zircon. Because calculation of a maximum depositional age (MDA) is predicated on determining the youngest zircon population within a given sample, inferred older grains were preferentially excluded from analyses. Highly rounded and darkened zircon grains were omitted in favor of euhedral, unweathered grains, potentially biasing samples toward having younger ages. Cathodoluminescence imaging of epoxy-mounted zircons was conducted on a Hitachi TM-4000 tabletop scanning electron microscope to better understand and visualize different grown domains and potential inclusions within zircon. Cathodoluminescence images were used to target ideal laser spot analyses on areas of original undisrupted zircon growth, and avoid inclusions and fractures. Results from the LA-ICP-MS analyses were used as a basis for selecting samples for later high-precision ID-TIMS analysis. To understand and constrain the timing of extension within the study area, high precision ages for the oldest and youngest tephras were determined using ID-TIMS on samples for which initial LA-ICP-MS geochronology determined to best represent these oldest and youngest tephra horizons in the field area.

U-Th-Pb Geochronology

Use of the U-Th-Pb (Uranium-Thorium-Lead) method in zircon, more commonly referred to as the U-Pb zircon method, has become widely popularized since its refinement during the latter half of the 20th century (Paterson, 1956; Tera and Wasserburg, 1975; Tucker et al., 1990). Depending on the focus of a particular study, the U-Pb zircon method may be applied to determine absolute age dates, or detrital zircon provenance studies, both of which commonly utilize LA-ICP-MS and ID-TIMS instrumental systems (Gehrels, 2012). The fundamental principles of U-Pb dating are based on the decay of a radioactive parent isotope (U) to a radiogenic daughter isotope (Pb). By measuring the abundances of radiogenic parent and daughter products, and applying a decay constant, an age can be calculated for a given material, assuming that it was a closed system. Trace amounts of radioactive uranium are incorporated into the crystal lattices of a range of minerals during formation. As a geochronometer, zircon holds many advantages over other minerals. It is ubiquitous in a variety of felsic igneous rocks, and it is stable at a wide range of temperatures, and as such can record metamorphic and igneous processes. It is incredibly resistant to mechanical and chemical weathering and therefore persists in the sedimentary record for extremely long periods of time. Importantly for geochronology, it incorporates detectable amounts of radioactive elements into its crystal structure and retains daughter products at high temperatures (Faure and Mensing, 2005).

A key advantage to the U-Pb system is that it involves three separate decay systems ($^{238}U \rightarrow {}^{206}Pb$, $^{235}U \rightarrow {}^{207}Pb$, and $^{206}Pb \rightarrow {}^{207}Pb$) with different half-lives, allowing for independent confirmation of measured ages (Gehrels, 2012). The two U-Pb decay systems are also linked by the constant ratio of $^{238}U/^{235}U$ (137.88) in most crustal rocks. The third geochronometer is provided by measuring the ratio of $^{206}Pb/^{207}Pb$. The non-radiogenic isotope of Pb (^{204}Pb) is used as a proxy for initial Pb present in the crystal, and is not a product of decay of ^{238}U. This "common" Pb is typically subtracted from the calculated and measured ratios. Because the amount of ^{235}U is much smaller relative to ^{238}U, the ratio of $^{207}Pb/^{235}U$ is commonly not measured directly as it would introduce significant uncertainty. Instead, it is calculated using the measured values of $^{206}Pb/^{238}U$ and $^{206}Pb/^{207}Pb$, and the known constant ratio of $^{238}U/^{235}U$ (Gehrels, 2012). These factors can be combined to efficiently visualize ages and uncertainties calculated with each decay scheme of the U-Pb system by plotting $^{206}Pb/^{238}U$ against $^{207}Pb/^{235}U$ as a function of age on a Pb/U concordia diagram (Wetherill, 1956). Calculated ages from the different decay systems that return the same age within error will plot along the concordia line, and are deemed "concordant". However, it is common for ages to be "discordant" and plot below the concordia line. Discordance is usually interpreted to be a result of Pb loss incurred by hydrothermal fluids, thermal instabilities, or inheritance of older material (Gehrels, 2012). Typically, discordance is expressed as a percentage of the ratio of $^{206}Pb/^{238}U$ and the $^{206}Pb/^{207}Pb$ ages. Ages for the two systems that completely agree with each other are 0% discordant, or 100% concordant. It is common in detrital zircon studies to filter data according to the degree of discordance, and reject analyses that exceed a filter criteria ranging from 5 to 30% (depending on the goals of the study). Because of the multiple decay schemes, discordant analyses that pass the filter criteria can still be utilized. Pb loss within the zircon will result in an apparent younger age, and ages will be pulled toward to the origin along the $^{206}Pb/^{207}Pb$ line. If an age or ages are discordant, a best-fit "upper-intercept" line through the analyses should intersect the concordia line at what can be interpreted to be the crystallization age, with the lower intercept representing the time of Pb loss. However, for young zircons that are undamaged and have relatively simple thermal histories, Pb loss is unlikely. For a study focused on young grains, (e.g., <100 Ma) it is inappropriate to apply this filter because it is difficult to measure $^{206}Pb/^{207}Pb$ for young grains (Puetz et al. 2021; Gehrels, 2012). Because of this issue, calculating discordance based on the ratio of $^{206}Pb/^{238}U$ and the $^{206}Pb/^{207}Pb$ ages becomes problematic due to the fact that discordance increases as ages decrease, and the concordia curve is close to linear near the origin. Therefore, the $^{206}Pb/^{207}Pb$ age for a discordant sample falling just right of this line will be projected to a much older age on the concordia line (Fig. 3.1). For this reason, applying the same discordance filter based on the difference between the $^{206}Pb/^{238}U$ and $^{206}Pb/^{207}Pb$ ages used for older grains to a population of young zircons is not practical. To contend with this, the Isotope Geology Laboratory at Boise State University instead uses a filter based on $^{206}Pb/^{238}U$ and $^{207}Pb/^{235}U$ ages, where discordance is calculated based on the distance that ages plot from concordia along the

$^{207}Pb/^{235}U$ axis (Fig. 3.1) (e.g., Gibson et al., 2021). The purpose of this is to remove the magnification of discordance for young zircon that would come with projecting age through analyses that plot just under concordia, and to account for error on the ^{207}Pb measurement. Because this method incorporates the large uncertainties inherent to measuring ^{207}Pb in young zircon, the filtering criteria is tightened to 5%, and includes error propagated on discordance (Gibson et al., 2021). While Pb loss with young zircons is generally not an issue, contamination by common Pb can have a catastrophic effect on zircons as their ages approach zero. Because quadrupole mass spectrometers have difficulty differentiating ^{204}Pb from ^{204}Hg, the Isotope Geology Laboratory at Boise State University does not measure ^{204}Pb directly, but instead takes advantage of the discordance calculation involving ^{207}Pb and ^{235}U as a means to account indirectly for common Pb contamination, as trace amounts of ^{204}Pb can greatly affect the signal for ^{207}Pb.

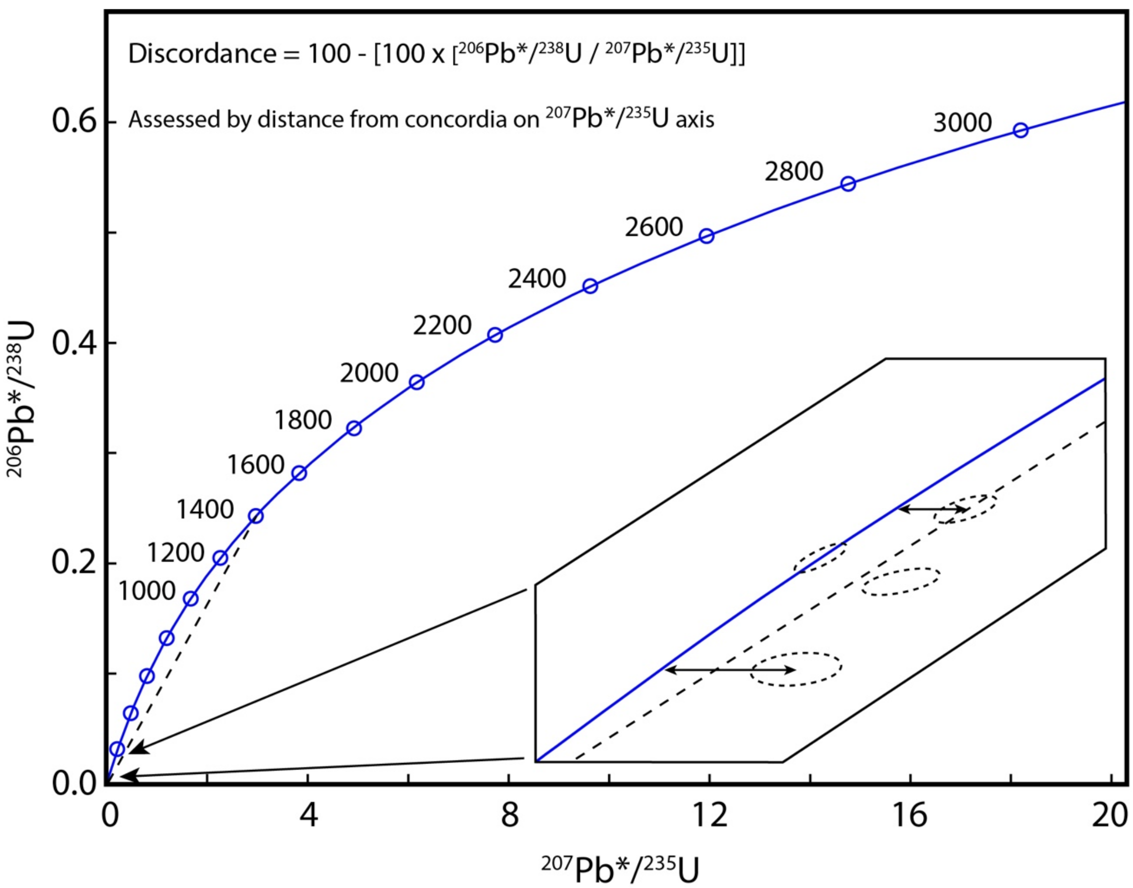

Figure 3.1 – Isotope Geology Laboratory discordance calculation for young zircons. Discordance is assessed by the distance an falls from the concordia curve on the 207Pb*/235U line. Discordance is tightened to 5% to incorporate large uncertainty of 207 Pb. Modified from Gehrels (2012).

LA-ICP-MS

Laser-Ablation Inductively-Coupled Plasma Mass-Spectrometry (LA-ICP-MS) yields rapid results, is cost-effective, ($4.25 per spot/grain analysis vs $225 per grain for ID-TIMS) and its precision is satisfactory for most detrital zircon studies involving a large population of zircon grains, and as a way to target individual zircon grains for more expensive single grain ID-TIMS analysis (Isakson, et al., 2022). LA-ICP-MS analysis of zircon crystals obtained from the five samples was conducted at the Boise State University Isotope Geology Laboratory between 19th-23rd of September 2022. A total of 229 grains were analyzed from samples BCG-1 (n=105), BCG-30 (n=14), BCG-273 (n=10), BCG-612 (n=75) and BCG-770 (n=25). Laser ablation analysis was accomplished with a ThermoFisher iCAP-RQ quadrupole ICP-MS used in conjunction with a Teledyne Analyte Excite+ 193 nm laser ablation system. Boise State University Isotope Geology Laboratory in-house protocol and standard materials were used for analytical work and data reduction when acquiring a suite of high field strength elements (HFSE) and rare earth elements (REE). Spot placement was guided by cathodoluminescence images, targeting primary growth domains, while avoiding major inclusions and fractures. 20 µm spots were ablated to a depth of ~10 µm deep over an analysis period of 45 seconds (15 s. gas blank, 30 s. ablation). Inert helium was used carry ablated material to the flow of plasma. Five standards (Plešovice, Zirconia, AUSZ2, 91500, Seiland) were included with analytes for quality control and validation.

ID-TIMS

ID-TIMS is the highest precision and accuracy deep-time geochronometer currently available for use, affording precision of 0.1 % or less (Bowering and Schmitz, 2006). Unlike LA-ICP-MS, ID-TIMS is a complex, expensive, and time-consuming process, involving careful preparation of samples in an extremely clean laboratory environment to prevent contamination by external Pb and U (Gehrels, 2012). After annealing, aliquots are completely dissolved and then diluted with tracer isotope “spikes” of U and Pb, from which the unknown amounts of U and Pb can be subtracted following ionization and measurement by mass-spectrometry. Following the initial round of dating via LA-ICP-MS, selected grains from samples BCG-612 and BCG-770 were prepared for subsequent ID-TIMS analysis conducted at the Boise State University Isotope Geology Laboratory during February and March of 2023. These samples were chosen for ID-TIMS based on the initial LA-ICP-MS analyses and calculation of probability density plots and weighted mean ages from the initial LA-ICP-MS analyses (see data analysis below). Furthermore, these samples were selected based on stratigraphic position, with BCG-612 interpreted to represent the upper most stratigraphic position in the Starlight Formation in the mapping area, and sample BCG-770 interpreted to represent the lowest exposed portion of the section. Individual zircon grains from these samples were picked from the mount based on internal zoning in cathodoluminescence images and the previous LA-ICP-MS analyses. A total of five grains were picked from sample BCG-612, and eight grains from sample BCG-770. Selected zircon grains were annealed in quartz beakers for 60 hours to repair radiation damage, then subjected to a modified chemical abrasion method (e.g., Mattinson, 2005). Grains were then spiked with a tracer solution, dissolved in several stages, U and Pb were purified by anion exchange chromatography, and were loaded onto a rhenium filament for mass spectrometry. Pb and U isotopes were measured using an IsotopX Isoprobe-T thermal ionization mass spectrometer. Dates and uncertainties were calculated following the methodology of Schmitz and Schoene (2007), U decay constants of Jaffey et al. (1971), and $^{238}U/^{235}U$ ratio of Hiess et al. (2012).

Data Analysis

Data reduction and filtering for all analyses was completed by personnel of the Boise State University Isotope Geology Laboratory, using an in-house Microsoft VBA spreadsheet for data normalization, concentration calibration, uncertainty propagation and age calculation. All ages are reported in 2σ absolute uncertainty. Propagation of all uncertainties was calculated by quadratic addition. Discordance was based on the measured difference between $^{207}Pb/^{235}U$ and $^{206}Pb/^{238}U$ dates, with those analyses with discordance outside of an uncertainty of 5% being rejected. Samples from the LA-ICP-MS analysis were chosen for ID-TIMS on the basis of weighted mean ages and probability density plots created at Idaho State University by Yokel-Deliduka using the Excel plug-in IsoplotR for weighted mean ages and the Arizona LaserChron MatLab tool AgeCalcML for probability density plots (github.com/kurtsundell/AgeCalcML). Of these samples, grains for ID-TIMS were selected based on the basis of cathodoluminescence imaging and the LA-ICP-MS spot analyses. The ID-TIMS weighted mean age for sample BCG-612 was calculated at the Boise State University Isotope Geology Laboratory. Because the amount of zircon recovered from several of the samples was limited, data from the LA-ICP-MS analysis that contained ages flagged by the Isotope Geology Laboratory as discordant were reassessed by Yokel-Deliduka using a looser filtering criterion in an effort to improve recovery of zircon. Because this study was focused on material associated with the Yellowstone volcanic system, and the fact that the majority of tephra ages from southeastern Idaho are younger than approximately 15 Ma, all iterations of new data filtering excluded analyses older than 15 Ma. The first round of new filtering used all Isotope Geology Laboratory ages with absolute uncertainty less than 20%, including those previously flagged as discordant.

CHAPTER 4: RESULTS

Mapping

New mapping at a scale of 1:24,000 of the 7.5-minute Bear Camp Gulch quadrangle (Plate 1) improves resolution of existing 1:48,000-scale (Corbett, 1978) and 1:100,000-scale mapping (Link and Stanford, 1999), and completes an east-west transect of 7.5-minute quadrangles (Rodgers and Othberg, 1999; Riesterer et al., 2000; Rodgers et al., 2006) that encompass the majority of the Putnam thrust sheet. Descriptions, appearances, and thicknesses of Paleozoic units within the study area were generally consistent with those of neighboring quadrangles (Kellogg et al., 1999; Kellogg, 1990; Riesterer et al., 2000), with one exception: The Cambrian Nounan Formation was anomalously thinner than was mapped and described in adjacent quadrangles, likely due to disagreement regarding the upper contact with the Cambrian Worm Creek Sandstone. The spatial extent of the Miocene Starlight Formation within the quadrangle was further delineated and described in greater detail than previous work, breaking out volcaniclastic sediments, tephra, and interbedded conglomerates from the Quaternary surficial deposits. Preliminary 1:48,000 mapping by Corbett (1978) assigned most of the non-Paleozoic strata in the study area to the Miocene Starlight Formation (Fig 4.1), which conflicts with observations made in this study. Much of what was previously mapped as Starlight Formation is now interpreted to instead be Quaternary in age, with the Starlight Formation being confined to the fault-bounded basin in the southeastern portion of the quadrangle (Fig. 4.2, Plate 1). Sampling of tephras within the Starlight Formation and collection of zircon U-Pb data in this fault bound basin was conducted to constrain the magnitude and timing of extension within the quadrangle, which ultimately refines the age of the Starlight Formation in the study area as latest Miocene (Messinian).

Overall, map-scale relationships define a broad north-south trending fold in the center part of the quadrangle hereafter referred to as the Bear Camp syncline (Fig. 4.2, Plate 1). To further develop the understanding of the Putnam thrust system, exposures of the Toponce thrust were revisited, which identified that strata in the footwall of this structure are overturned. Stratigraphic separation diagrams of the Bear Canyon-Toponce thrust were constructed for the entire Portneuf Range, that show complicated along-strike changes in décollement level that call into question earlier interpretations of the Bear Canyon-Toponce as a single thrust (e.g., Kellogg, 1992). Map position and relative ages of normal faults and episodes of extension were also refined. Cross-cutting relationships between normal fault sets reveal that most north-south striking faults were truncated by east-west striking normal faults (with some exceptions), suggesting that there are indeed two temporally spaced generations of extensional deformation within the study area (Fig. 4.2) (e.g. Rodgers et al., 2002). All of these results are discussed in detail in subsections below.

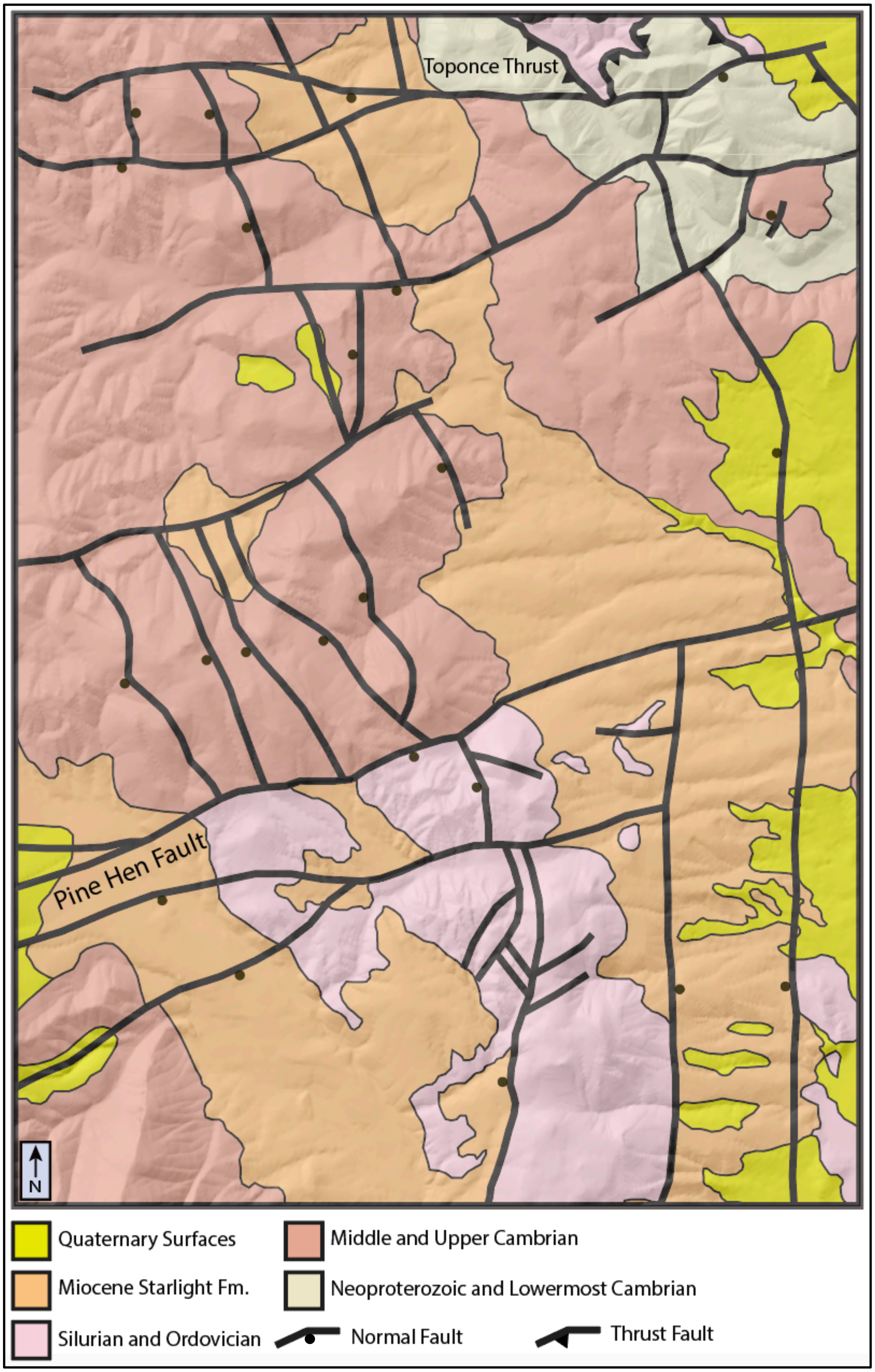

Figure 4.1 – Simplified geologic map of the Bear Camp Gulch quadrangle from previous mapping (Link and Stanford, 1999).

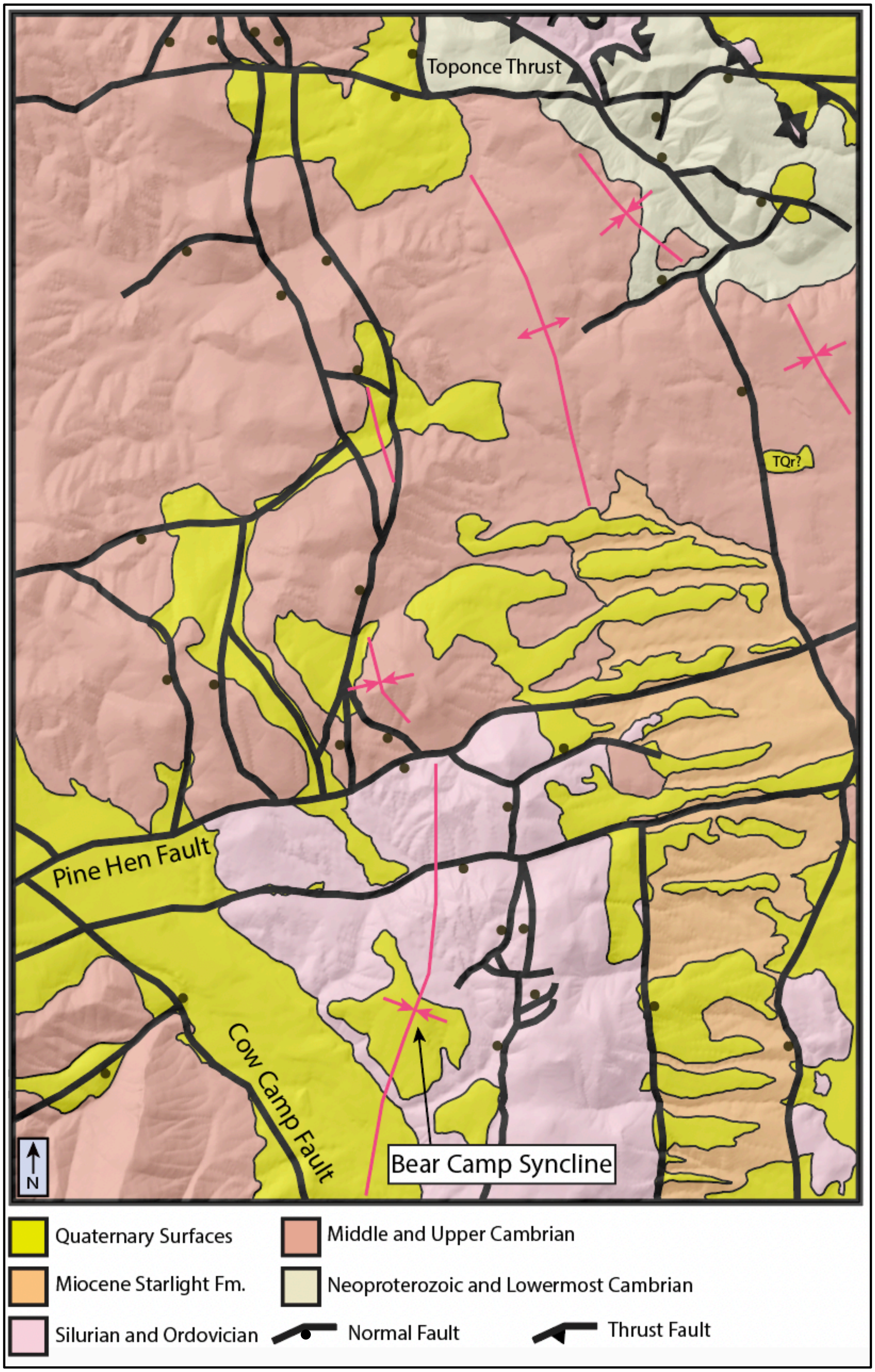

Figure 4.2 – Simplified geologic map of the Bear Camp Gulch quadrangle adapted from detailed 1:24,000-scale map in this study (full detailed map in Plate 1).

Unit Descriptions

Bedrock units found within the study area range from late Neoproterozoic to Miocene in age (Fig. 4.3), the majority of which are lower Cambrian to Silurian siliciclastic and carbonate rocks (Plate 1). Approximately 400 meters of tephra, tuffaceous sandstone, and conglomerate belonging to the Starlight Formation is exposed within a fault-bounded basin on the southeastern side of the map area (Fig. 4.2). A small outcrop of flow-banded rhyolite occurs near Smith Creek. The age is unknown, though it is likely similar in age to the Miocene basin fill or perhaps as young as the Basalt of Portneuf River. Quaternary surfaces onlap all older units, and range from stream channel alluvium to landslide and colluvial lag deposits.

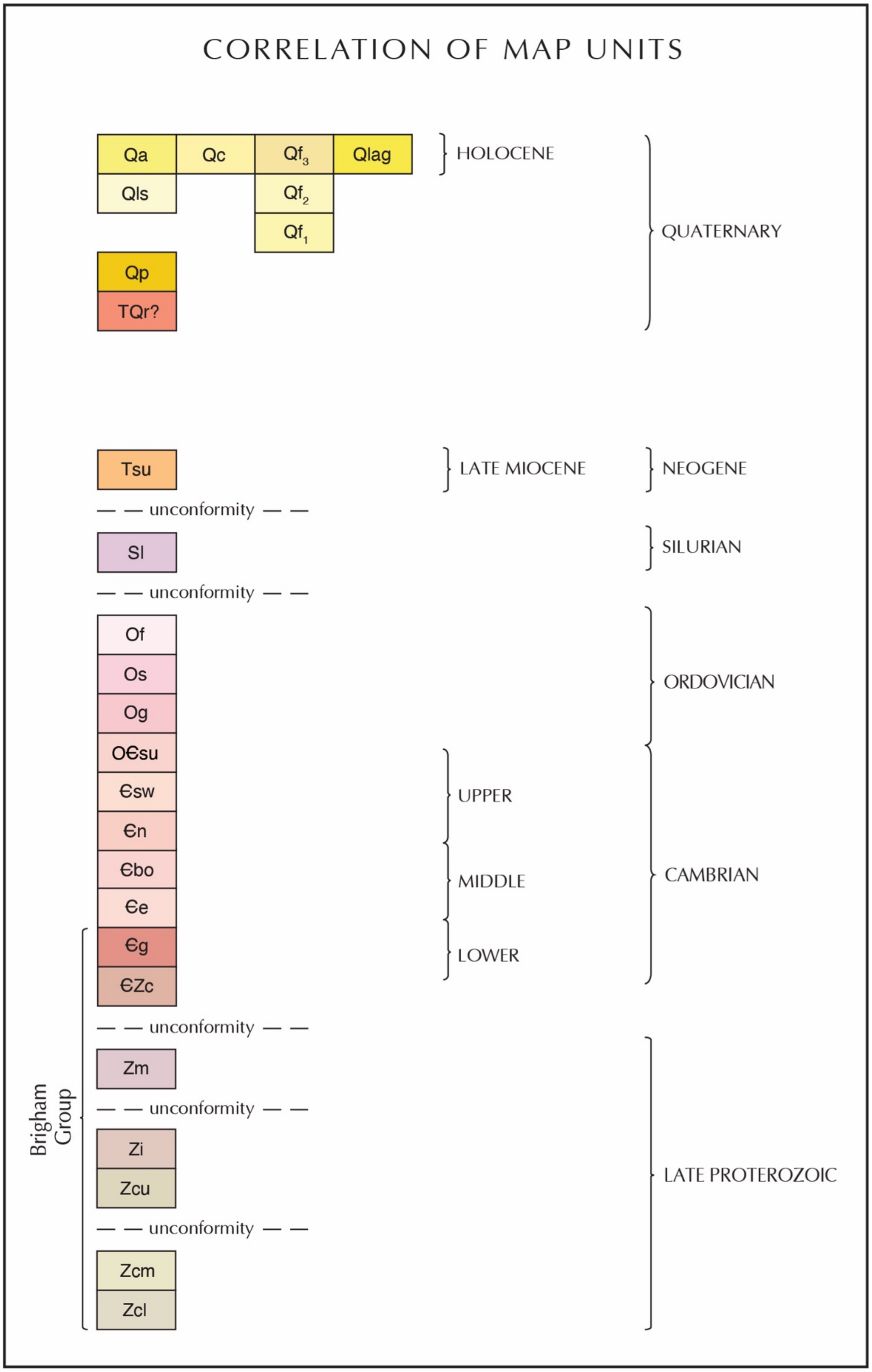

Figure 4.3 – Correlation diagram of stratigraphic units exposed within the Bear Camp Gulch quadrangle. Unit abbreviations correspond with the abbreviations within the unit description text.

Quaternary System

(Qa) Alluvium – Unconsolidated materials ranging in size from silt to boulders, found in active stream channels and valley bottoms.

(Qc) Colluvium and talus (Quaternary) – Poorly sorted material ranging from pebbles to boulders sourced from directly upslope or flanking mouths of valleys. Clasts consist of angular to subangular quartzites as large as 5 meters in diameter. Includes potential rock fall and talus slope materials.

(Qf) Alluvial Fan – Poorly consolidated material consisting of nearby bedrock detritus, eroded Cenozoic sediments, colluvium, and alluvium, ranging in size from clays and silt to as large as boulders. Upper part of unit may include a thin veneer of loess. Relative ages of fans determined from relative heights of fan surfaces. Numbers denote relative ages, e.g., Qf_1 oldest, Qf_3 youngest.

(Qls) Landslide Deposit – Poorly sorted, unconsolidated material consisting of alluvial fan, Miocene basin fill sediments, and terrace deposits. Deposits occur as hummocky, uneven surfaces and protruding quartzite boulders up to several meters in diameter. Mapped unit includes head scarp of landslide.

(Qp) Basalt of Portneuf River (Quaternary) – Massive, dark gray to black, aphanitic, vesicular basalt. Exposure is limited to the southeastern part of quadrangle, in an outcrop along the east bank of the Portneuf River. Occurs as a flat-topped flow mantled with unconsolidated alluvial sediments. Lower flow dated at 0.43 ± 0.07 Ma (whole rock, $^{40}Ar/^{39}Ar$) in the Inkom Quadrangle (unpublished date cited in Rodgers et al., 2006).

(Qlag) Colluvial Lag Deposit (Quaternary) – Poorly sorted, angular to subangular, unconsolidated material consisting almost entirely of cobbles and boulders interpreted to be from Swan Peak, Worm Creek, and Camelback Mountain formations. Source lithology is often not directly upslope. Typically covers broad flat surfaces and rounded hillocks. May represent weathered surface of oldest Quaternary alluvial fans.

Cenozoic System

(TQr?) Rhyolite (Miocene-Quaternary) – Massive, dark brown to reddish-gray, flow-banded rhyolite. Outcrops are poorly exposed, moderately welded and form small ledges accompanied by scattered black obsidian. Deposited unconformably on Gibson Jack Formation in a small area just north of Maggie's Road along Smith Creek and isolated from nearby outcrops of Starlight Formation. Age uncertain, but presumably latest Miocene to Quaternary.

Tsu – upper Starlight Formation (Miocene) – Conglomerate, tuffaceous sandstone, and air-fall tuff. Conglomerates are composed mostly of poorly sorted, carbonate-cemented, subangular quartzite clasts. Clasts range from granules to cobbles. Sandstones are moderately to poorly bedded and consist mostly of reworked pumice fragments, with minor chert and lithic fragments. Primary air-fall tuffs are white, well-bedded and ledge-forming. The Starlight Formation is poorly exposed in the mapping area but is inferred to occupy the normal fault-bounded basin in the eastern part of the quadrangle, where it is exposed in small patches in the straths beneath

Quaternary alluvial fans and terraces. The upper contact is not observed as it is interpreted to be truncated by a west dipping normal fault. Lower contact is an unconformity with underlying Gibson Jack Formation. The name Starlight Formation is preferred here because it denotes a closer proximity to, and a greater contribution from volcanic sources associated with the Yellowstone volcanic center, as well as following the naming convention of neighboring quadrangles (Kellogg et al., 1989; 1990; Riesterer et al., 2000). Thickens eastward to approximately 400 meters (1300 feet). U-Pb zircon ages of tuffaceous sandstones and ashfall tuffs interbedded within the Starlight Formation within the map area were dated using laser-ablation, inductively coupled plasma mass spectrometry (LA-ICPMS) and chemical abrasion, isotope-dilution, thermal-ionization mass spectrometry (CA-IDTIMS) at Boise State University. An epiclastic interval near the base of the formation (sample BCG-770) yielded a heterogenous range of $^{206}Pb/^{238}U$ zircon ages between 9.854 ± 0.078 to 6.421 ± 0.018 Ma, with an approximate maximum depositional age of 6.421 ± 0.018 Ma interpreted from the youngest CA-IDTIMS grain date. CA-IDTIMS dating of an air fall tuff interval near the top of the formation (BCG-612) yielded four concordant and equivalent grains with a weighted mean age of 6.032 ± 0.053 Ma.

Paleozoic System

(Sl) Laketown Dolomite (middle to upper Silurian) – The Laketown Dolostone consists of light gray to white, medium-to thick-bedded dolostone, and is often coarsely recrystallized to dolosparite. It is locally bioclastic, containing fragments of crinoids, brachiopods, and trilobites. The lower, unconformable contact with the Fish Haven Dolostone is difficult to locate and is placed at the first appearance of consistently light gray to white dolostone above the darker gray, fetid dolostone of the Fish Haven. The upper contact is not exposed in the field area, but approximately 122 meters is exposed. Outcrops are limited to the south-central part of the mapping area. Thickness approximately 245 meters (800 feet) in Lava Hot Springs quadrangle (Crane et al., 2000).

(Of) Fish Haven Dolomite (lower Silurian and Upper Ordovician) – Medium-to dark gray, mottled dolostone. Medium-to thick-bedded, bioclastic and coarsely recrystallized with distinct petroliferous odor. Outcrops normally appear as thick-bedded and dark gray. Discrete beds of fossil hash <20 cm thick occur locally and include abundant crinoids. Middle part of unit contains abundant black chert nodules. Upper contact with the Laketown Dolomite can be difficult to locate. Lower contact with Ordovician Swan Peak Quartzite is not exposed in the field area. Outcrops typically appear as moderately bedded, cliff-forming dolostone and talus-covered slopes. Thickness is approximately 250 meters (825 feet).

(Os) Swan Peak Quartzite (Middle Ordovician) – The Swan Peak Quartzite consists mostly of white to light gray, rarely light brown quartzite, and sandstone. Fresh surfaces are vitreous and white. The unit is characterized by being well-sorted, and fine-grained. Outcrops are cliff-forming and massively-bedded, appearing orange to brown to white. Planar bedding is typical of most of the unit, whereas crossbedding is rare and more common in the lower portion of the unit. As the lower contact with the Garden City Formation is approached, bedding becomes thinner and displays a higher degree of bioturbation. Trace burrows of *Skolithos* and *Cruziana/Planolites* occur locally. The middle portion of the unit exhibits a notable pitted/porous texture, possibly due to an original calcite cement (Oaks et al., 1977). The Swan Peak Quartzite may be mistaken for the Worm Creek Member of the St. Charles Formation or the Camelback Mountain Quartzite. However, its finer-grained, better-sorted, and less cross-bedded nature is adequate for differentiation. The lower member of Hladky (1986), containing sandy dolostone and coarse sandstone, was not observed in the field area. Thickness approximately 250 meters (825 feet).

(Og) Garden City Formation (Lower Ordovician) – The Garden City Formation consists of mottled light gray to gray, occasionally yellowish-tan, medium-to thick-bedded, fossiliferous limestone and minor dolostone. Silty laminations and intraformational conglomerate are common throughout the unit, mainly in the lower and middle portions. Ranges from dark micrite to gray coarsely crystalline sparite. Bedding parallel *Cruziana* and *Planolites* trace fossils are common. Bioclasts including crinoids occur locally. Outcrops are typically ledge-and cliff-forming and are light gray to tan. The upper portion of the unit contains centimeter-scale, bedded black chert, increasing in abundance up section as the lower contact with the Swan Peak Quartzite is approached. The Garden City Formation crops out in the southeastern corner of the quadrangle, and in the northeastern corner, north of Toponce Creek where it is overturned in the footwall of the Toponce thrust. The abundance of intraformational conglomerate and bedded black chert aids in distinguishing the Garden City Formation from other carbonates in the mapping area. Thickness approximately 396 meters (1300 feet).

St. Charles Formation (Lower Ordovician to upper Cambrian) – The Ordovician St. Charles formation consists of a lower clastic member with interbedded dolostone and an upper carbonate consisting of dolostone and limestone.

(O€su) Upper Member – The Upper Member of the St. Charles Formation consists of gray to light gray, coarse, medium-to thick-bedded dolostone and minor medium-grained limestone. Base is mapped at the abrupt transition from fine-grained arkosic arenite of the Worm Creek Member to limestone. Exposures are limited, but the best are found in the southeastern part of the quadrangle. Thickness approximately 115 meters (375 feet).

(€sw) Worm Creek Member – The Worm Creek Member consists of arkosic sandstone, quartzite, and interbedded dolostone. Dolostone interbeds are ledge-forming, gray to light gray to white, coarsely to medium crystalline. The upper Worm Creek is dominated by ledge and cliff forming, highly resistant arkosic sandstone and quartzite. Outcrops appear tan to pink and have a unique, black-speckled appearance from black lichen inhabiting feldspar weathering pits (Pogue, 1984). Crossbedding and herringbone crossbedding is common throughout. Fresh surfaces commonly exhibit orange limonite weathering spots from the alteration of feldspars. Asymmetric ripples are observed locally. Lower sandstones are slope and talus forming, brown to tan, abundantly cross-bedded and rarely calcite-cemented. They are medium-to coarse-grained and well-sorted. Detrital zircon spectra from the Worm Creek contain a ubiquitous 497 Ma peak whose age and εHf values overlap with that of the Deep Creek and Beaverhead plutons intruded into the Lemhi arch of east-central Idaho (Link et al., 2017). These alkalic plutons are inferred to be a major source of siliciclastic sediment for the Worm Creek Quartzite. The base was mapped at the first appearance of sandstone above the thinly bedded, tan carbonate of the upper Nounan Formation. Although normal faulting has increased the apparent thickness of the Worm Creek significantly in the mapping area, in nearby quadrangles the typical thickness ranges from 152 to 396 meters (500 to 1300 feet) (Riesterer, et al., 2000; Kellogg et al., 1989). Apparent thickness in the Bear Camp Gulch quadrangle is approximately 350 meters (1150 feet).

(Ꞓn) Nounan Formation (middle and upper Cambrian) – The Nounan Formation consists of massive to thin-bedded, limestone, sandy limestone and dolostone. Lower limestones are massive, cliff-forming, medium-to dark gray, locally fossiliferous, micrite and recrystallized sparite. Silty partings increase in abundance and thickness moving upsection as siliciclastic input increases. Limestone becomes thinly bedded and ledge forming in the middle to upper sections and as silty intervals increase from millimeter-scale to centimeter. Upper limestones are light to dark brown, display abundant *Cruziana* and *Planolites*, and are well-bedded. The Nounan Formation in the quadrangle appears to be thinner than reported elsewhere (e.g., Pogue, 1984; Hladky, 1986; Link et al., 1987). This may result from disagreement about where the upper contact with the Worm Creek Member of the St. Charles Formation is placed, and whether the first appearance of clastic input is included in the Nounan Formation (Trimble and Carr, 1976), or instead marks the beginning of the Worm Creek Member. The lower contact is placed at the first massive limestones above greenish-brown shale of the Bloomington Formation. The upper contact is placed at the first appearance of cross-bedded sandstone above silty carbonate, as suggested by Link (written communication, 2022). Thickness approximately 115 meters (375 feet).

(Ꞓbo) Bloomington Formation (middle Cambrian) – The Bloomington Formation consists of roughly equal parts limestone and fine-grained siliciclastic rocks, including sandstone, argillite, and shale. Limestone is ledge-forming, medium-to thick-bedded, light gray to gray, micrite and rare recrystallized sparite, with ubiquitous silty partings and laminations. Clastic beds are slope forming, often obscured by vegetation, and consist of green to brown shale and fine sandstone, with occasional green limestone nodules and marcasite nodules (0.5 – 2 cm). Ooids (1-3 mm) and oncolites (.5-2 cm) occur in discrete beds in the limestone. Intraformational conglomerate is common. The lower contact is placed at the first appearance of green shale above the silty, massive beds of the Elkhead Limestone. In areas of poor exposure, the presence of green limestone nodules within the shales were important for identifying the Bloomington Formation. Relative to units above and below, the Bloomington is less competent and accommodates more deformation and small-scale folding. Thickness approximately 275 meters (900 feet).

(Ꞓe) Elkhead Limestone (middle Cambrian) – The Elkhead Limestone consists mostly of cliff-forming, massive-to thick-bedded limestone, silty limestone, and minor shale. Limestone is typically moderate-to well-bedded, gray to medium gray micrite, locally recrystallized to coarse sparite. Tan, silty laminae are common, as well as characteristic red silts. Dolomitization occurs locally and typically appears as massive, gray to yellow gray and tan, poorly bedded dolostone. Fossils occur throughout the unit, and typically appear as intervals of fossil-hash and disarticulated brachiopods, crinoids and trilobites which are often altered to calcite. Oncolites (0.5-8 cm) are present throughout, sometimes very closely spaced and appear in discrete beds up to 30 cm thick. Ooids (1-4 mm) are common throughout the Elkhead, often weathering brown to reddish. Crossbedding and mudcracks also occur but are rare. The upper contact with the Bloomington Formation is placed at the first appearance of greenish shale above thick beds of carbonate of the Elkhead. The lower contact is placed at the first massive, gray limestone above brown shale of the Gibson Jack Formation. The Elkhead Limestone is likely correlative with the Blacksmith Limestone and Bancroft Limestone (Oriel and Armstrong, 1971; Oriel and Platt, 1980). Thickness approximately 366 meters (1200 feet).

Lower Cambrian and Neoproterozoic System

Brigham Group

The Brigham Group was originally named by Walcott (1908) for exposures near Brigham, Utah. In southeastern Idaho, Anderson, (1928) identified the Brigham Quartzite, and described it as follows:

> "…massive, more or less vitreous quartzite or quartzitic sandstone, generally of purplish or reddish tinge, together with conglomeratic layers, and some beds of hard, sandy, and more or less micaceous shale."

Early workers did not separate the Brigham Quartzite into separate formations but treated all Late Proterozoic and early Cambrian quartzose sandstones and siltstones as a single formation. Crittenden et al. (1971) and Trimble (1976) were the first to refine the definition and separated the Brigham Group into six constituent formations, from stratigraphically lower to highest these include: the Papoose Creek Formation, Caddy Canyon Quartzite, Inkom Formation, Mutual Formation, Camelback Mountain Quartzite, and the Gibson Jack Formation. Link et al. (1987) further refined the Brigham Group and formally defined the various formations. The Brigham Group contains four, disconformity-bound, stratigraphic sequences, each representing a major transgressive or regressive sequence (Link et al., 1987). This synthesis of the stratigraphy and regional persistence of lithofacies indicates the Brigham Group was deposited in a post-rift setting, prior to the transition to carbonate deposition along the Cordilleran passive margin.

(Ꞓg) Gibson Jack Formation (lower Cambrian) – The Gibson Jack Formation is the uppermost formation of the Brigham Group, and consists of olive-green to brown shale, brown to gray argillite, sandstone, and minor limestone. Shale is very strongly cleaved, such that bedding is often indiscernible. Moderately resistant sandstone occurs as protruding ledges and discontinuous outcrops. Rare limestone occurs as ledges of dark gray to gray micrite. Shale is highly fissile and ranges from dark gray to light brown and exhibits planar and wispy laminations. Sandstone is fine to medium-grained and varies from arkose to litharenite and locally displays wavy oxide staining and rare crossbedding. All lithologies of the Gibson Jack are abundantly micaceous. A trilobite hash (*Naraoia*?) is found below the contact with the Elkhead Limestone just north of the south fork of Toponce Creek. In general, outcrops are rare and typically appear as small, non-vegetated areas consisting of broken talus and pencil shale. The upper contact with the Elkhead is marked by an abrupt transition from shale and fine sandstone to massive gray limestone. The lower contact is placed at the last appearance of light tan to white quartzite of the Camelback Mountain below argillite of the overlying Gibson Jack. The informal members A, B, and C, of Trimble and Carr (1976) were not recognized in the field area. Thickness approximately 610 meters (2000 feet), though faulting, folding, and poor exposure has likely resulted in greater apparent thickness, especially in northwestern corner near Inman thrust.

(ЄZc) Camelback Mountain Quartzite (lower Cambrian and Neoproterozoic) – The Camelback Mountain Quartzite consists of light tan to white, poorly sorted, coarse to medium-grained quartzite. Occasional pebbles and granules of quartz and chert occur in the lower sections, but in general the unit becomes finer up section. Outcrops weather brown to black and are massive and cliff-forming. Boulder covered slopes are typical of areas underlain by the Camelback Mountain Quartzite. Fresh surfaces commonly display prominent Liesegang banding and red and yellow oxide staining near faults and areas of alteration. Bedding ranges from approximately sub-meter scale to massive, with rare cross bedding and graded beds. The Camelback Mountain Quartzite becomes intensely brecciated and fractured near fault and fracture zones and differentiating it from the other quartzites in the field area can be difficult, but careful consideration of the overall grain size, clast composition, and outcrop characteristics such as oxide staining, and sedimentary structures should aid in identification. To the north at Rock Creek, the contact with the Mutual Formation is a sequence boundary where the Camelback Mountain Quartzite is incised into the upper Mutual Formation (Link et al., 1987). In the quadrangle the lower contact is placed at the last appearance of pebble conglomerate containing clasts of white vein quartz and red chert. Thickness approximately 396 meters (1300 feet).

(Zm) Mutual Formation (upper Neoproterozoic) – The Mutual Formation ranges from conglomerate to quartzite, with minor shale. Overall, the unit is very poorly sorted, coarse sand to granule sandstone and conglomerate. It is very resistant, but outcrops usually appear as low ledges and boulder covered slopes. In the quadrangle, the Mutual Formation is predominantly coarse sandstone to conglomerate. Outcrops weather purple and maroon to pink and tan and exhibit abundant trough and crossbedding. Most exposures contain poorly sorted intervals of coarse sand and granules to cobbles with clasts of rounded to subangular white quartz, red chert, and argillite. The unit is locally feldspathic and contains crystals of subangular feldspar as large as 1 centimeter. The Mutual Formation contains abundant Grenville-aged detrital zircon grains, indicating a distal, mid-continent source supplying mature siliciclastic sediment to a broad basin, likely resulting from an early episode of rifting. The upper Mutual contains Archean zircon grains, a reflection of increasing local sediment input (Yonkee et al., 2014). The upper contact is gradational over several meters and the lower contact is not observed in the field area. Thickness approximately 473 meters (1550 feet).

(Zi) Inkom Formation (upper Neoproterozoic) – The Inkom Formation is the oldest unit exposed in the field area and is confined to a small outcrop along the northern quadrangle boundary where a section is exposed in the hanging wall of the Toponce thrust. Outcrops of the Inkom Formation are slope-forming and appear mainly as small exposures and talus covered slopes. The Inkom is strongly cleaved, laminated, dark brown to green weathering siltstone and argillite. Fresh surfaces are greenish brown to tan. Inferred submarine channels filled with conglomerate and siltstone rip-up clasts have been observed within the Inkom Formation nearby (Link et al., 1987) but were not observed in the quadrangle. Thickness approximately 198 meters (650 feet).

Structural Framework

Thrust Faults

The only thrust structure exposed in the Bear Camp Gulch quadrangle is located in the northeastern corner of the study area above Toponce Creek (Fig. 4.2, Plate 1). Map patterns of the thrust indicate that this structure is currently oriented horizontal to sub-horizontal, with the footwall strata revealed in an erosional window (Figs. 4.2 and 4.4). In the Bear Camp Gulch quadrangle, this thrust placed the Neoproterozoic Mutual and Inkom formations primarily on the Ordovician Swan Peak Quartzite and Garden City Limestone. Units within the footwall and hanging wall in this area are highly brecciated, though details can still be worked out. In the hanging wall of the thrust, the Mutual and Inkom formations are upright and dip shallowly to the east and west (7-30°), defining a series of gentle folds. In the footwall of the thrust, Ordovician strata dip moderately to steeply the west (23-58°). However, in a small exposure of the Swan Peak Quartzite just to the north of Toponce Canyon Road, cuspate back-fill in vertical burrows (*Skolithos*) are observed to be upside down (Fig. 4.4). This provides confirmation that the footwall rocks are indeed overturned to the west. Beyond the map boundary just to the north in the Jeff Cabin Creek quadrangle, this same thrust placed the Neoproterozoic Inkom Formation through the Cambrian-Neoproterozoic Camelback Mountain Quartzite on the same Ordovician strata (Kellogg et al., 1989). This is the Toponce thrust of Corbett (1978) and Kellogg et al. (1989), which was interpreted in the neighboring Jeff Cabin Creek quadrangle to be the same as the Bear Canyon thrust (Kellogg et al., 1989; Kellogg, 1992).

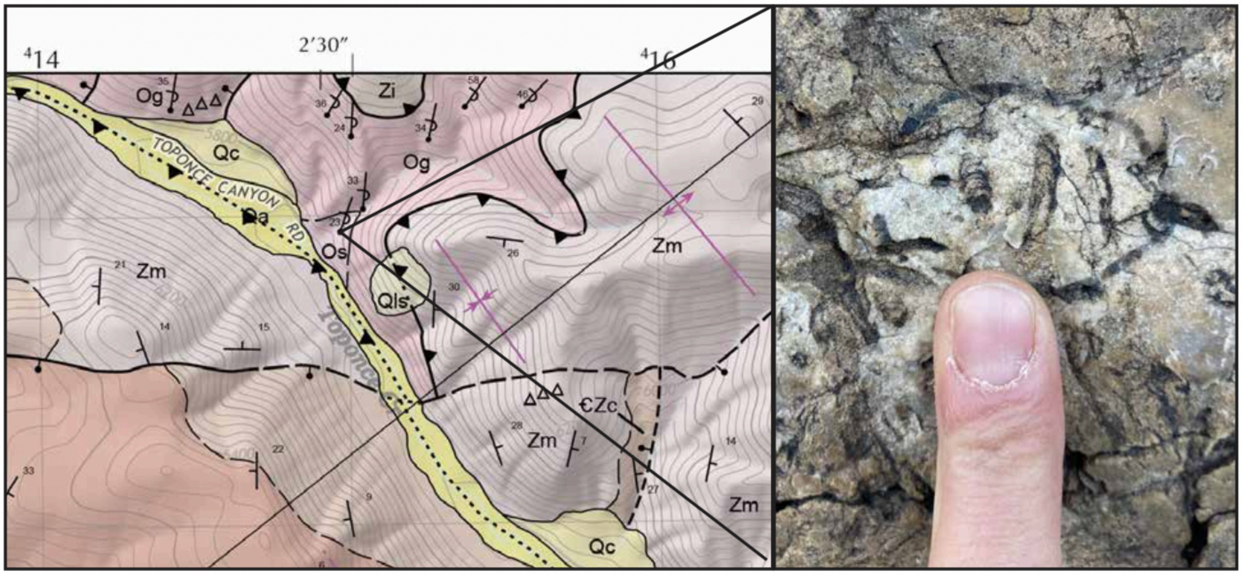

Figure 4.4 – An erosional window into the footwall of the Toponce thrust along Toponce Canyon Road (left). Overturned *Skolithos* in an outcrop of Ordovician Swan Peak Quartzite in the footwall of Toponce thrust (Right).

Stratigraphic Separation Diagrams

Stratigraphic separation diagrams were constructed for the Bear Canyon, Toponce and Putnam thrusts primarily to evaluate the interpretation that the Bear Canyon and Toponce thrusts are the same structure by highlighting the stratigraphic positions of each fault's hanging wall and footwall (Kellogg, 1992; Kellogg et al., 1999). Stratigraphic separation diagrams track the footwall and hanging wall behavior for a given fault as it interacts with stratigraphy. These diagrams help elucidate where different thrust structures are located and how they connect in the subsurface in the drafted cross-sections. Diagrams were constructed using new mapping of the Bear Camp Gulch Quadrangle (this study) and existing quadrangles (Kellogg et al., 1989; Kellogg, 1990; Riesterer et al., 2000) that capture the entirety of the thrust system throughout the Portneuf Range.

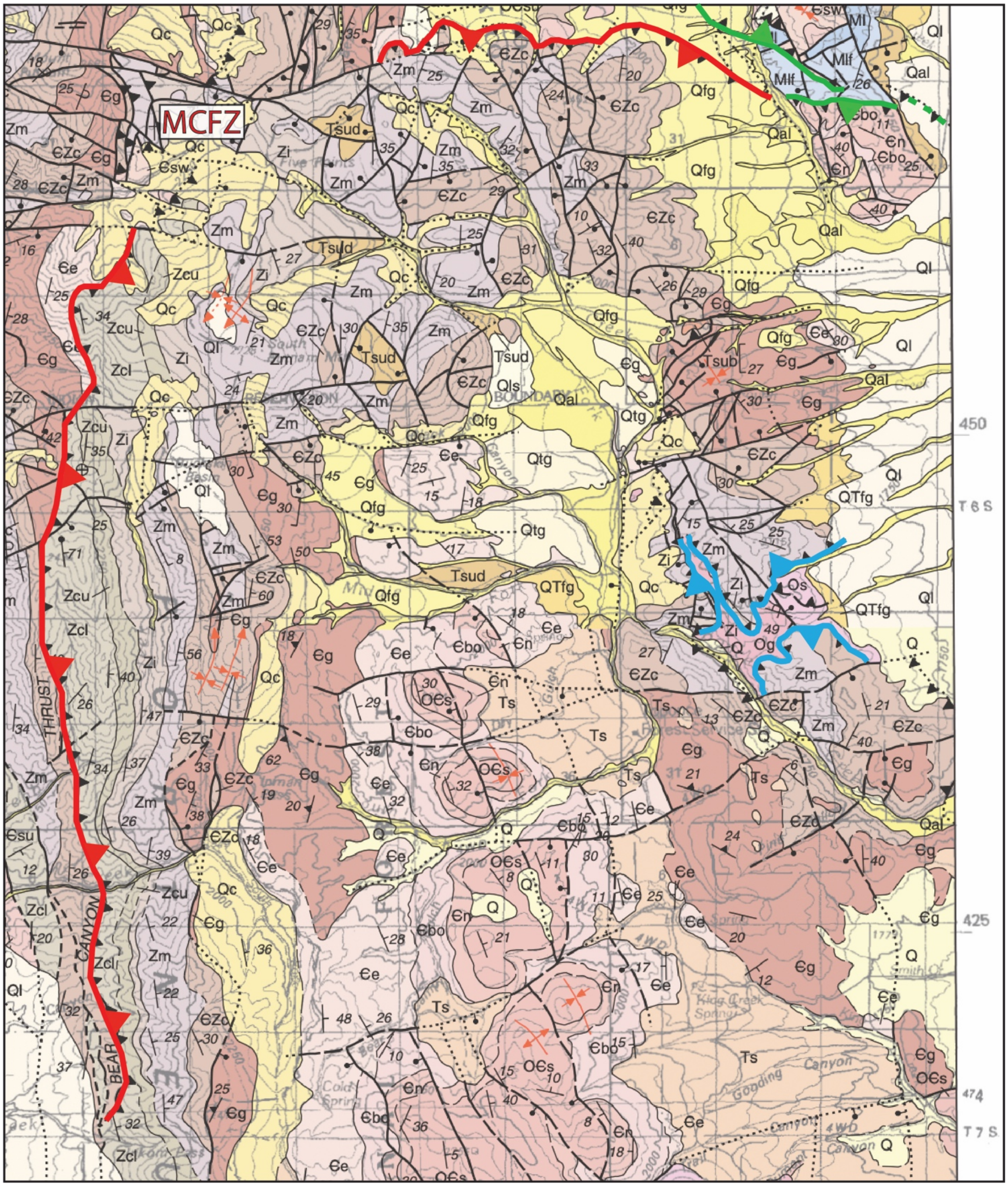

Figure 4.5 – Map of northern Porteneuf Range showing Bear Canyon (red), Toponce (blue), and Putnam (green) thrusts and Mill Creek fault zone (MCFZ). Modified from Link and Stanford (1999).

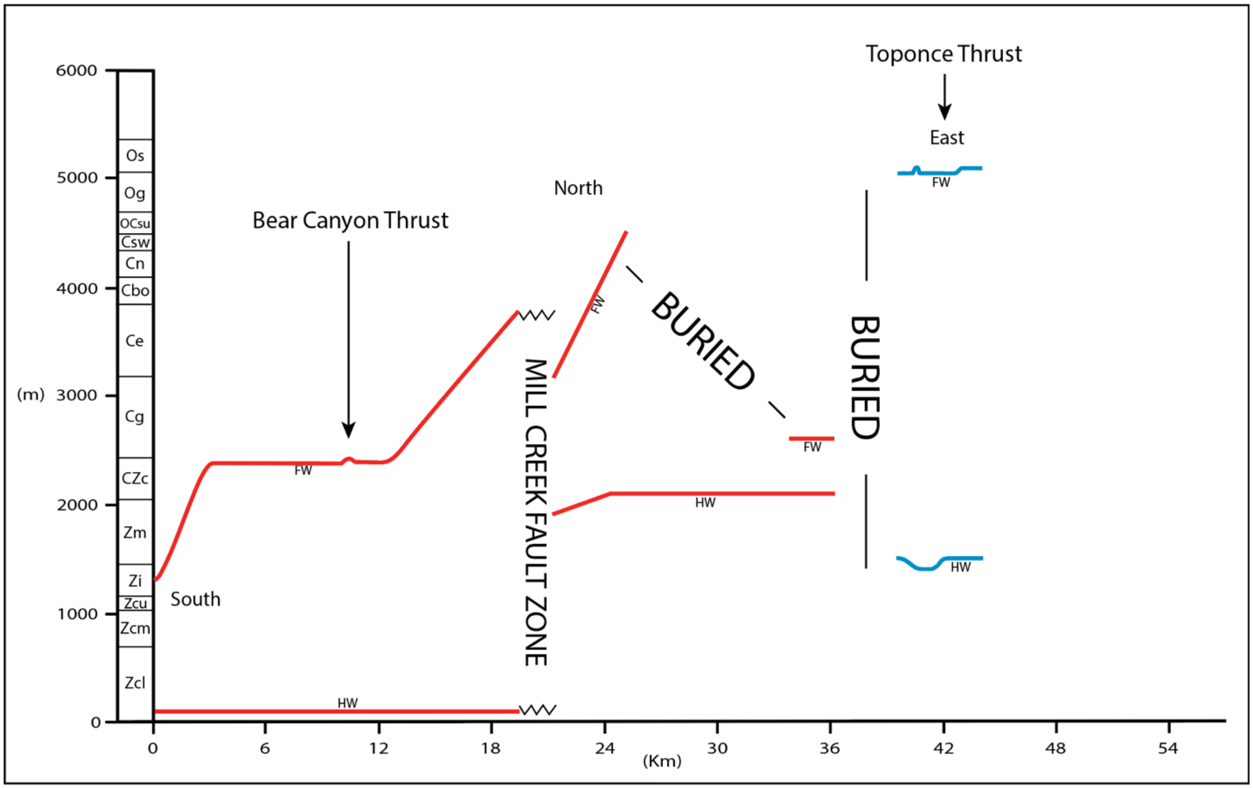

Figure 4.6 – Stratigraphic separation diagram for Bear Canyon (red) and Toponce (blue) thrusts, showing their footwall (FW) and hanging wall (HW) behavior in the northern Portneuf Range. Map above shows locations of faults and stratigraphy.

Results from the separation diagram show 45 km of along-strike changes in the footwall and hanging wall stratigraphic positions of strata in the Bear Canyon (red) and Toponce thrusts (blue) (Fig. 4.6). Beginning in the south along the western Portneuf Range front (Fig. 4.5), the hanging wall of the Bear Canyon thrust remains within the same stratigraphic horizon near the base of the lower Camelback Mountain Formation. In contrast, the stratigraphic position in the footwall cuts up from the Mutual Formation to a flat at the base of the Gibson Jack Formation, and then cuts up again to the Bloomington Formation. However, the pattern of the separation diagram is disrupted by an east-west striking fault zone near Mill Creek (Kellogg, 1990) (Fig. 4.6). North of this fault zone, the Bear Canyon thrust's hanging wall and footwall appear in different stratigraphic positions: The footwall position of the thrust is observed lower in the section, where it continues cutting upward toward the north from the base of the Cambrian Elkhead Limestone to the base of the Ordovician Upper St. Charles Formation over a short distance along-strike before becoming concealed beneath Quaternary sediments. Farther north and east beyond the Quaternary cover, the footwall position of the thrust is observed again changing positions to a lower stratigraphic horizon near the base of the Cambrian Gibson Jack Formation. In contrast, north of the Mill Creek fault zone, the hanging wall position of the Bear Canyon thrust has also changed to a higher stratigraphic position, remaining within a flat at the base of the Camelback Mountain Quartzite.

Where the Toponce thrust is mapped, its exposures are limited, but the pattern on the separation diagram is simple compared to that of the Bear Canyon fault: The footwall and hanging wall of the thrust are consistent in their stratigraphic positions, and do not cut up-section. However, they are in different units than the Bear Canyon to the north and west. The footwall position is located within the uppermost Garden City Limestone and lowermost Swan Peak Quartzite, whereas the hanging wall position is located within the uppermost Inkom Formation and lowermost Mutual Formation.

Folds and Stereonets

The geologic mapping defines a roughly NNW-SSE trending syncline consisting of a thick panel of Neoproterozoic and Cambrian through Silurian carbonate and clastic sedimentary rocks that bisects the Bear Camp Gulch quadrangle (Fig. 4.2, Plate 1). Similarly trending smaller wavelength folds are superimposed upon this feature, mainly in the northeastern part of the quadrangle within the Cambrian Gibson Jack Formation, which crops out extensively and appears more expansive than its true stratigraphic thickness as a result of several broad folds.

This regionally extensive syncline resides within the hanging-wall of the Toponce thrust, and is given the informal name the Bear Camp syncline. Several north-south and east-west striking normal faults have partially dismantled this syncline, yet it is still apparent from map patterns and lower-hemisphere stereonet diagrams (Fig. 4.7).

Poles to planes of bedding attitudes for all Paleozoic units were plotted on equal-area stereonet diagrams to highlight structural orientations, and contoured to show density of measurements using the program Stereonet (Richard W. Allmendinger © 2020-2022). The average dip for the west limb of the fold is 27°E, and 14°W for the eastern limb. This orientation produces an interlimb angle of 69.5°, dipping steeply to the west, indicating the fold is asymmetrical. A pi-plot using a cylindrical best fit to the poles to bedding define fold-axes plunging 3° toward 162°. However, the original orientation of the Mesozoic fold was likely altered by Cenozoic normal faulting. Attitudes of bedding measured within the Starlight Formation (Fig. 4.8) are east-dipping, with the exception of a single measurement which displayed a westward dip. Dip magnitudes ranged from 12°E to 27°E, with beds in the lower part of the Starlight Formation displaying greater dip magnitudes. However, the majority of steeper measurements cluster around 20°E, with only one measurement of 27°E. Restoring 20° of eastward tilt to the Bear Camp syncline results in an asymmetric fold with an eastern limb that originally dipped 34°W and a western limb with a pre-tilt dip of 7°E, and an axial surface dipping steeply to the east (Fig. 4.7).

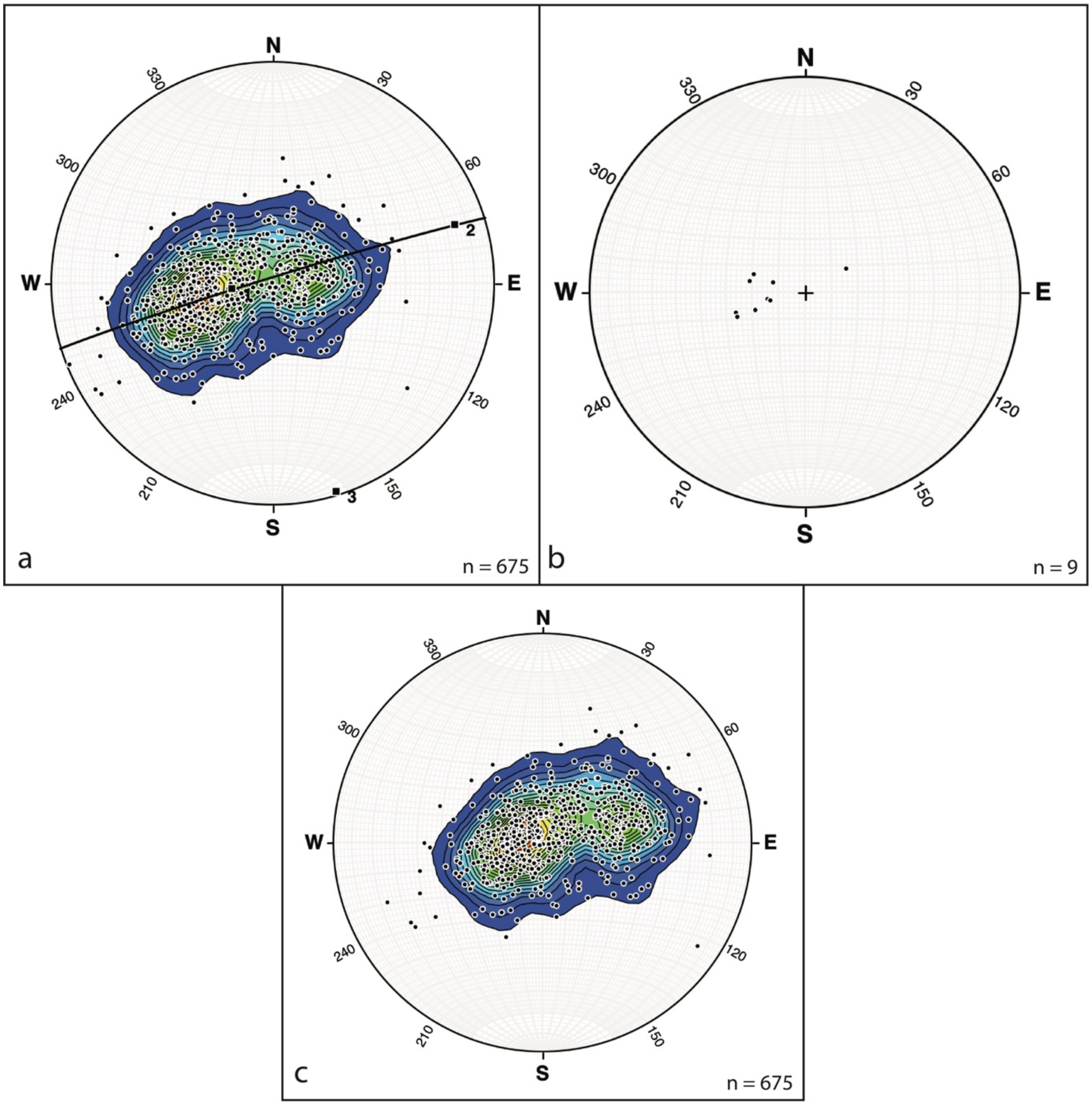

Figure 4.7 – Stereograms showing: a) poles to planes of all Paleozoic bedding attitudes measured in Bear Camp syncline. A cylindrical best fit applied to the poles shows the fold axis trends 163 SSE and plunges 3 degrees. b) Poles to planes of bedding measured in the Starlight Formation showing eastward dip. c) bedding attitudes in Bear Camp syncline corrected for 20° of eastward tilt.

Normal Faults

An array of mutually perpendicular normal faults is exposed within the quadrangle, striking mostly north-south and east-west. In general, north-south striking faults, such as the fault bounding the Miocene basin, are consistent with fault orientations related to regional Basin and

Range-related structures. East-west striking faults are typically found in mountain ranges proximal to the ESRP (Allmendinger, 1982; Rodgers and Othberg, 1999; Rodgers et al., 2002). The Pine Hen fault was recognized by Corbett (1978), but is informally named in this study. It is a major map-scale feature that roughly divides the quadrangle into two age domains, with units as old as Neoproterozoic to its north, and primarily Ordovician and Silurian strata to its south. Based on its map pattern, it is steeply south-dipping and placed the Late-Ordovician Fish Haven Dolostone against Upper-Cambrian Worm Creek Quartzite (Fig. 4.2, Plate 1). This fault cross-cut the Bear Camp syncline at approximately right angles and truncated some of the north-south striking normal faults as well, with a minimum offset of approximately 3000 feet. The Cow Camp fault in the southwestern corner of the quadrangle was named for exposures near the Pebble Cow Camp and Big Springs Campground where the Ordovician Swan Peak Quartzite was juxtaposed against the Cambrian Elkhead Formation (Fig. 4.2, Plate 1). The fault is northwest-southeast striking, parallel to the broad alluvial valley occupied by Pebble Creek, and is dipping to the east. The footwall of this fault consists of an east-dipping homocline of Cambrian Gibson Jack Formation, Elkhead Limestone, and the Bloomington Formation. The strike of the fault is acute to bedding and the hanging wall consists of poorly exposed outcrops of the Swan Peak Quartzite.

Another important normal fault bounds the eastern side of a small basin in the southeastern portion of the map area (Fig. 4.2, Plate 1). The fault is generally north-south striking, and west-dipping, placing east-dipping Miocene Starlight Formation (Ts) in its hanging wall against similarly east-dipping Cambrian St. Charles Formation in the footwall. In the footwall of the fault, the Paleozoic strata form a prominent bedrock topographic high along the very eastern margin of the map area. In contrast, the topography in the hanging wall is subdued, and the Starlight Formation is covered and variably beveled by Quaternary fans and terraces. Outcrops of Starlight Formation are sparse and poorly exposed (Fig. 4.8), typically found in the straths between active drainages and elevated terraces of Qf1 and Qlag (Fig 4.2).

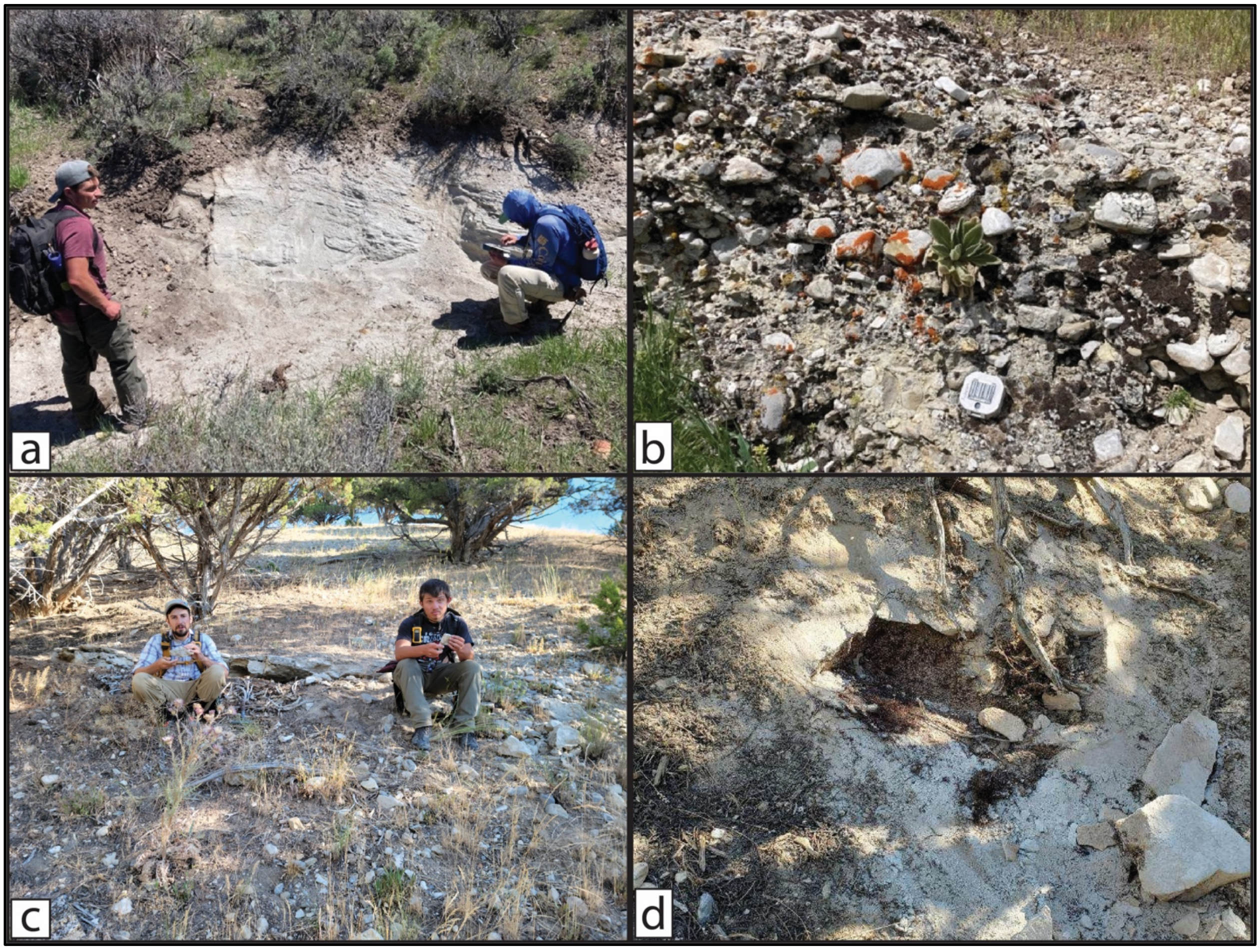

Figure 4.8 – Outcrops of Starlight Formation a) Tuffaceous beds in TS where sample BCG-1 was collected. b) Conglomeratic interval with locally derived clasts of quartzite, sandstone, and carbonate. c) Sampling location of BCG-612. d) Structureless ash-fall deposits.

All but a single outcrop of the Starlight Formation is east-dipping, with dip magnitudes increasing from 12° in the east to 27° in the western part of the basin (Fig. 4.8, Plate 1). The western side of the basin is bounded by a low-offset, east-dipping antithetic normal fault.

Cross-Sections

Three cross-sections were drawn to highlight major features of the study area (Plate 1). The northern cross-section (C-C’) (Fig. 4.9) was drawn to highlight the thrust relationships within the study area and better visualize how the Inman Pass, Bear Canyon, and Toponce thrusts relate to one another. Dip angles for normal faults were determined by solving 3-point problems in areas where appropriate data points could be located. In areas with insufficient data points, dip angles were assumed to be 60°. Based on the new mapping and separation diagrams in this study, and the geometric requirements of the cross-sections, it can be shown that the study area resides within the hanging wall of the Bear Canyon and/or the Toponce thrust. In the northern cross section of the adjacent Bonneville Peak quadrangle to the west, the Inman Pass thrust is contained within the Gibson Jack Formation, where it thickened the unit substantially (Riesterer et al., 2000). Based on folds in the Camelback Mountain Quartzite near Inman Pass, the interpretation of Riesterer et al. (2000) that the Inman Pass thrust accommodated minimal slip, and the apparent return to regional thickness in the eastern limb of the Bear Camp syncline, the Inman Pass thrust is interpreted to terminate in a fault propagation fold in the subsurface of cross-section C-C’. The Bear Canyon thrust is not visible in this cross-section, though it is inferred to be at depth based on the neighboring mapping and cross-sections of Riesterer et al. (2000) where it placed the Caddy Canyon Quartzite on the Camelback Mountain Quartzite in a flat-on-flat relationship.

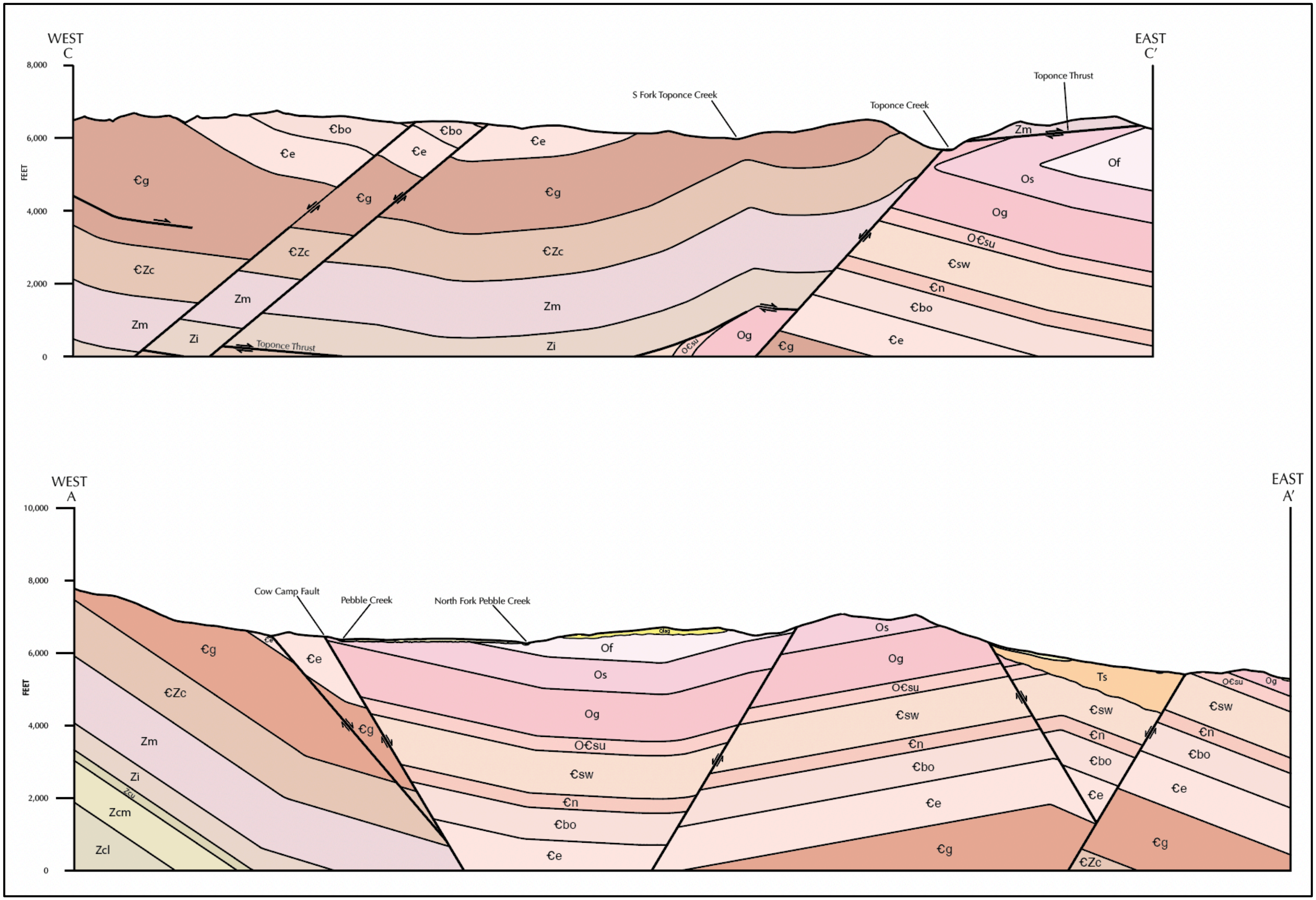

Figure 4.9 – Cross sections for the southern transect (below)(A-A') and northern transect (above)(C-C').

Farther to the east, the Toponce thrust is visible, where it placed the Neoproterozoic Inkom and Mutual formations on overturned Ordovician units. Stratigraphically upright units within the footwall of the Toponce thrust are assumed to be west-dipping based on the orientation of the Bear Canyon thrust in this area, from which the Toponce likely formed as an out-of-sequence imbricate. The Putnam thrust is beneath the Bear Canyon and Toponce faults, and crops out approximately 8 km north of the Toponce thrust (Kellogg et al., 1989).

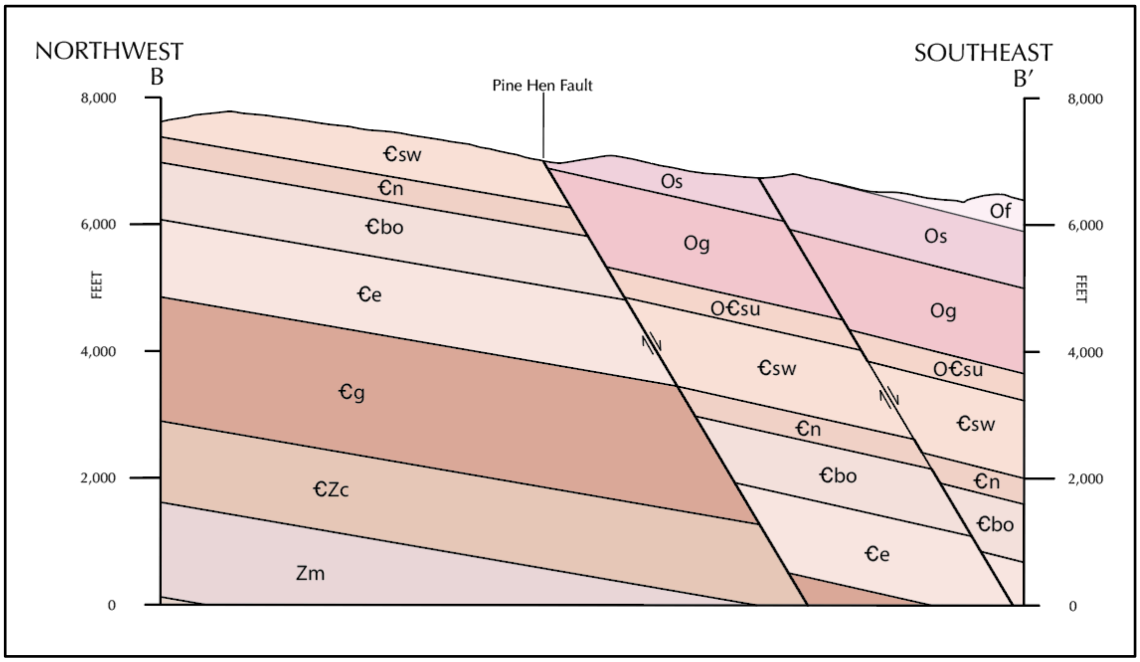

Figure 4.10 – Cross section B-B' illustrating offset along the Pine Hen fault.

The central cross-section (B-B')(Fig. 4.10) is oriented north-south to capture the architecture of east-west striking normal faults and highlights approximately 900 meters (3,000 feet) of offset along the south-dipping Pine Hen fault. Apparent dips of strata in this cross-section illustrate a gentle southeasterly tilt of bedding, and the faults are dipping acute to the bedding though at a steeper orientation. The A-A' (Fig. 4.11). cross section follows an east-west line in the southern part of the map area, and depicts the geometry of the Bear Camp syncline that defines the map area, as well as the Cenozoic basin on the southeastern portion of the map. Significant offset on the northeast-dipping Cow Camp fault on the order of approximately 1,770 meters (5,800 feet) is also visible. In its present configuration, the Bear Camp syncline is a gentle fold, with a slightly more steeply dipping western limb (~27°) and a gently dipping eastern limb (14°). On the eastern side of cross-section A-A', the Starlight Formation thickens to the east in a small basin bound on both sides by normal faults (Fig. 4.11). All exposures of the Starlight Formation, except for a single outcrop, are east-dipping. Based on these observations, the west-dipping fault likely accommodated a greater magnitude of slip, with a lesser magnitude of offset accommodated by the east-dipping fault. Based on outcrop patterns of Paleozoic rocks straddling this basin, the Starlight Formation may be as thick as 400 meters (1,300 feet) but could be less. Also revealed in the subsurface of cross section A-A' is an anticline similar in scale to the Bear Camp syncline, however the axis of the fold is concealed by outcrops of Starlight Formation. In general, the northern and southern cross-sections are kinematically compatible with those of the adjacent Bonneville Peak quadrangle to the west (Riesterer et al., 2000).

Geochronology

LA-ICP-MS

The first phase of geochronologic analysis involved Laser-Ablation Inductively-Coupled Plasma Mass-Spectrometry (LA-ICP-MS) dating of zircon. We analyzed 228 zircon grains, from five samples of the Miocene Starlight Formation. Of these, 117 were deemed concordant analyses (Appendix A,B). In addition to U-Pb ratio dates, this analysis collected a suite of high field strength elements, rare earth elements, and elemental titanium concentrations. A complete data table for all measured isotopic ratios, as well as trace-element data for each analysis is found in appendices A,B,C. Cathodoluminescence imaging of zircon grains was used to locate spot analyses (Appendix G). The primary purpose of LA-ICP-MS dating was to identify the oldest and youngest beds exposed in the basin and proceed with high-precision ID-TIMS dating for these samples to better bracket the onset and duration of extension within the study area. Four of the five samples (BCG-1, BCG-612, BCG-30, BCG-770) contained predominantly late Miocene age zircons. However, age spectra for one of these samples, BCG-273, was dominated by late Cambrian-aged grains, likely recycled from the Cambrian Worm Creek Quartzite Member of the St. Charles Formation (Link et al., 2017). For this reason, this sample was deemed inappropriate for calculating a maximum deposition age (MDA) of the Starlight Formation and was omitted from further analysis. Filtered and reduced data from the Boise State University Isotope Geology Laboratory was used in conjunction with AgeCalcML to generate weighted-mean ages for each sample. Because this study is focused on maximum depositional ages and material related to the Neogene history of the Yellowstone volcanic system, ages older than 15 Ma were omitted from weighted-mean age calculations. Probability density plots were also generated from this data using AgeCalcML (github.com/kurtsundell/AgeCalcML). Weighted mean ages and probability density plots for samples BCG-1, BCG-612, BCG-30, and BCG-770, are shown in Figure 4.11 and are as follows: (a) BCG-612 = 5.94 ± 0.1 Ma, (b) BCG-1 = 6.12 ± 0.09 Ma, (c) BCG-30 = 6.82 ± 0.43 Ma, (d) BCG-770 = 7.51 ± 0.22 Ma. Probability density plots for samples BCG-612 (n=33) and BCG-1 (n=43) are robust, and agree well with their calculated weighted mean ages (Fig. 4.11a,b). Samples BCG-30 (n=5) and BCG-770 (n=9) are less straightforward (Fig. 4.11c,d). In general, these two samples yielded fewer zircon grains, and those recovered spanned a greater age range. The probability density plot and weighted mean age plots for BCG-30 indicate two populations of zircon, however considering this sample contained only five grains, this is not a robust interpretation.

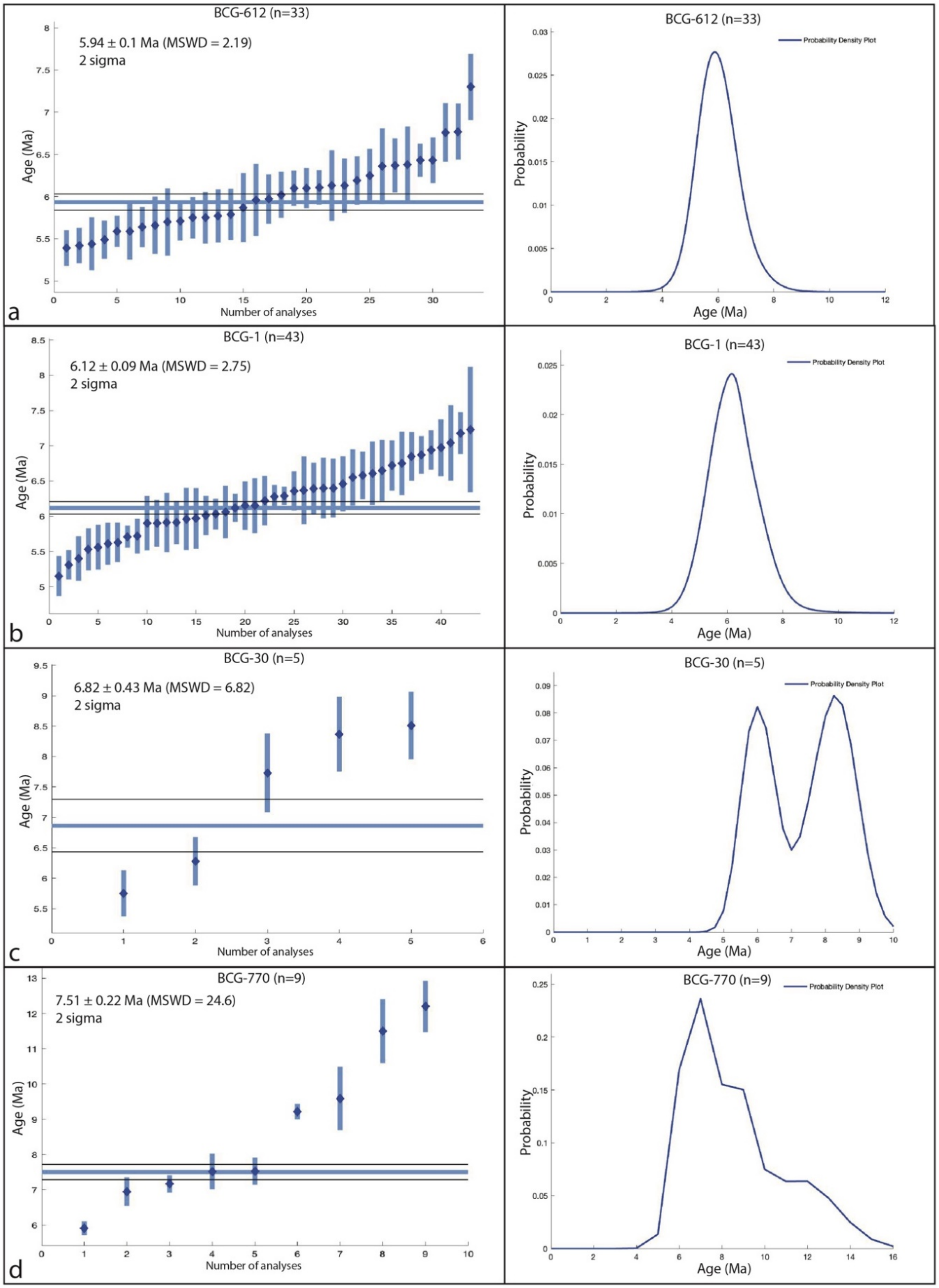

Figure 4.11 – Weighted mean ages and probability density plots for a) sample BCG-612, b) sample BCG-1, c) sample BCG-30, and d) sample BCG-770.

The probability density plots and weighted mean age plot for BCG-770 are also suggestive of a more complex age population (Fig. 4.11d). Several grains define an older zircon population, which is visible on the probability density plots as a small shoulder. Exclusion of the older population of grains from BCG-770 yields a weighted mean age of 7.24 ± 0.34 Ma (n=4) and more symmetric probability density plots that is consistent with a single population (Fig. 4.12)

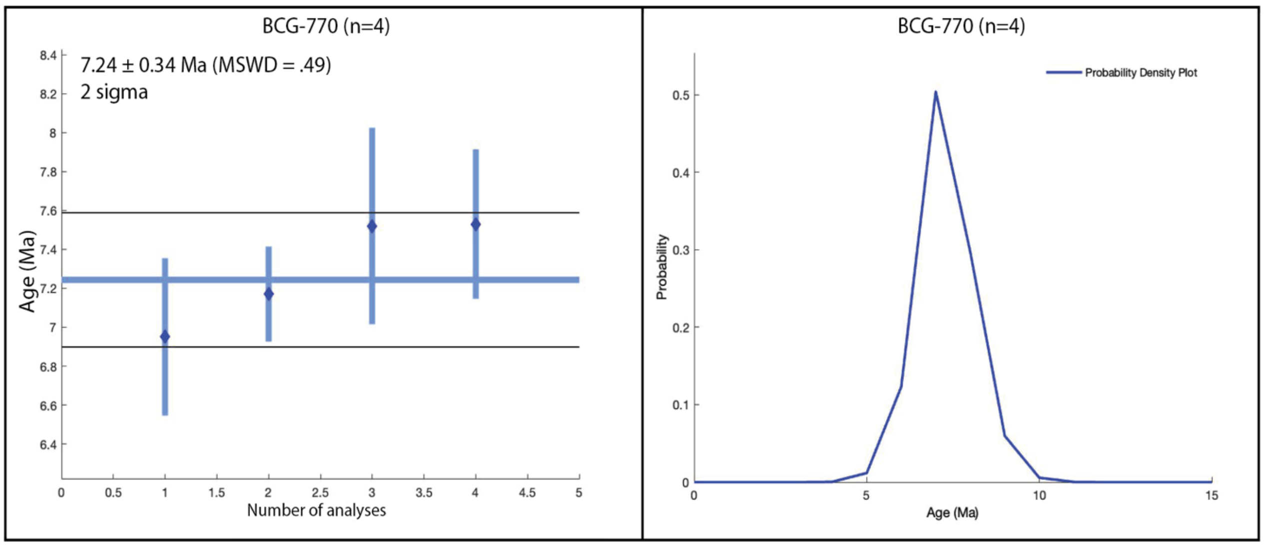

Figure 4.12 – Weighted mean age and PDP for BCG-770 with ages trimmed to the younger isolate age population seen in figure 4.11.

These samples were placed in geologic context from noting their stratigraphic position in the field, considering the measured bedding attitude where the sample was collected, and by plotting them on the eastern portion of cross-section A-A' (Fig. 4.13). From these data, a maximum depositional age probability density plot for a particular bed within the Starlight Formation can be determined. The LA-ICPMS data make it clear that late Miocene volcanic centers associated with the Yellowstone volcanic system and development of the eastern Snake River Plain were an important sediment source for this basin, although Cambrian-aged zircons derived from plutonic rocks of central Idaho were also transported as sediment during this time, as evidenced by the presence of well-documented Cambrian-aged zircons in sample (BCG-273).

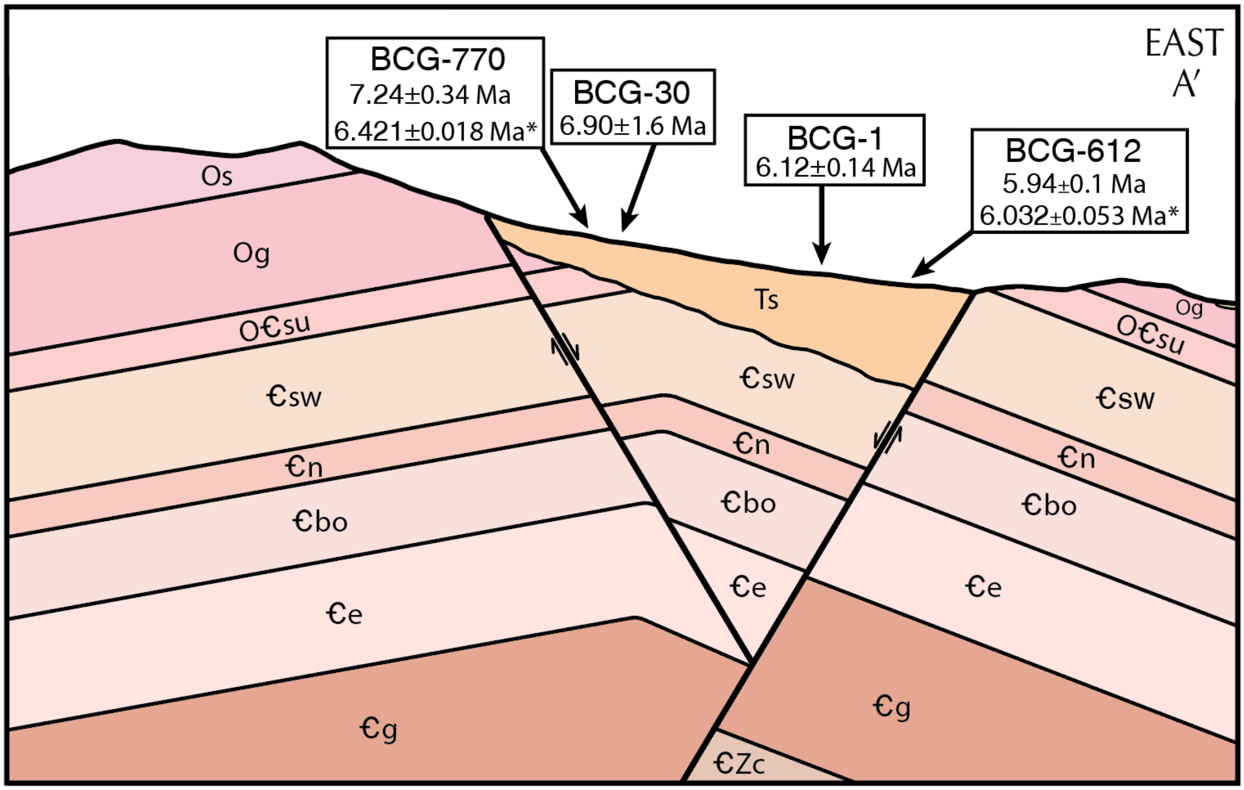

Figure 4.13 – Cenozoic basin in the eastern part of the map area, with locations of sampled beds and LA-ICP-MS ages. Asterisk denotes ID-TIMS age.

The majority of sampled outcrops, though small and discontinuous, displayed consistent eastward-dipping bedding orientations that dip shallowly to the east. The most steeply dipping bed sampled, BCG-770 (27° E), is the farthest from the eastern basin-bounding fault, and also yielded the oldest weighted-mean age from the LA-ICP-MS data. Sample BCG-612 (12° E), was closest to the eastern graben-bounding fault, had the shallowest dip, and yielded the youngest weighted mean age. Based on this context, samples BCG-770 was interpreted to best represent the lower (7.24 ± 0.34 Ma, 27° E) part of the section, and BCG-612 was interpreted to represent the upper parts of the section (5.94 ± 0.1 Ma, 12° E). Accordingly, these two samples were chosen for ID-TIMS to further refine the age of the Starlight Formation in this area and constrain the onset and duration of extension in the study area.

ID-TIMS

Seven grains from BCG-612, and eight grains from BCG-770 were chosen for ID-TIMS on the basis of cathodoluminescence imaging and the oldest and youngest weighted mean ages calculated from LA-ICP-MS spot analyses. Seven grains were analyzed from sample BCG-612, two of which were too enriched in common Pb for ages to be interpreted, and another grain displayed characteristics which indicated isotopic inheritance.

The remaining four grains comprised a pyroclastic zircon population and yielded equivalent dates with a weighted mean $^{206}Pb/^{238}U$ date of 6.032 ± 0.053 Ma (MSWD = 0.88, n=4) which represents the eruption and primary deposition age (Fig. 4.14).

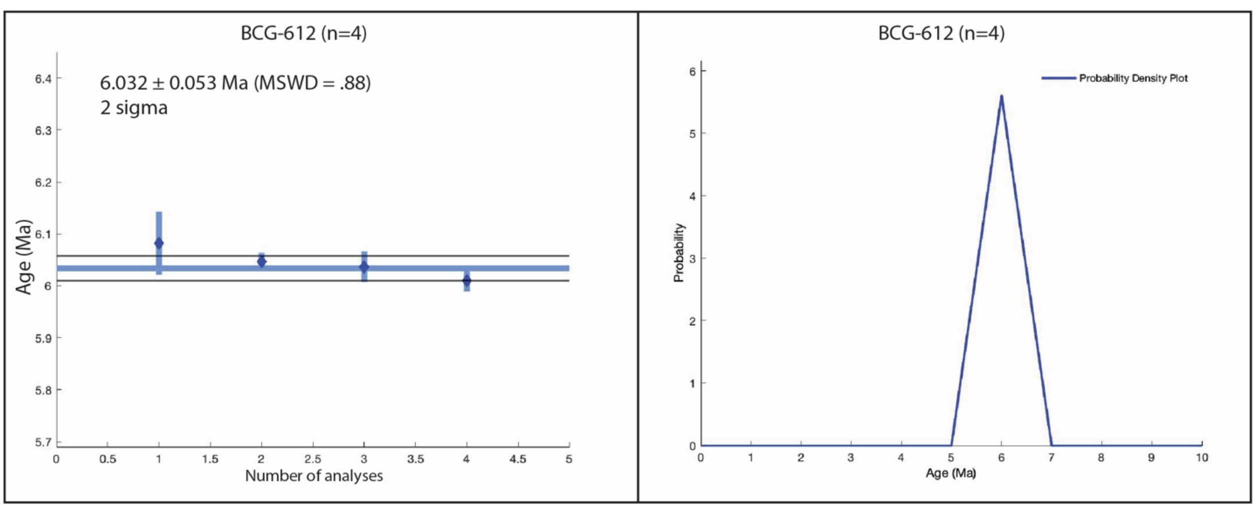

Figure 4.14 – Weighted mean age (left) and probability distribution plot (right) for ID-TIMS analysis of BCG-612.

Sample BCG-770 (Fig. 4.16) yielded more complex data, and likely reflects an epiclastic of zircon rather than a simple primary ash bed. The eight analyzed grains displayed a wider range of $^{206}Pb/^{238}U$ dates from 9.854 ± 0.078 to 6.421 ± 0.018 Ma. The majority of dates fell between 7.916 ± 0.144 and 7.537 ± 0.188 Ma, with the youngest date being represented by a single grain. This youngest age can be interpreted to be the maximum depositional age (MDA) of the bed this sample originated from. However, this sample represents input from several eruptive events. Based on these results, the lowest dated stratigraphic horizon is 6.421 ± 0.0421 Ma, and the uppermost is 6.032 ± 0.053 Ma. Therefore, the Starlight Formation in the study area is latest Miocene in age (Messinian), and belongs to the upper Starlight Formation.

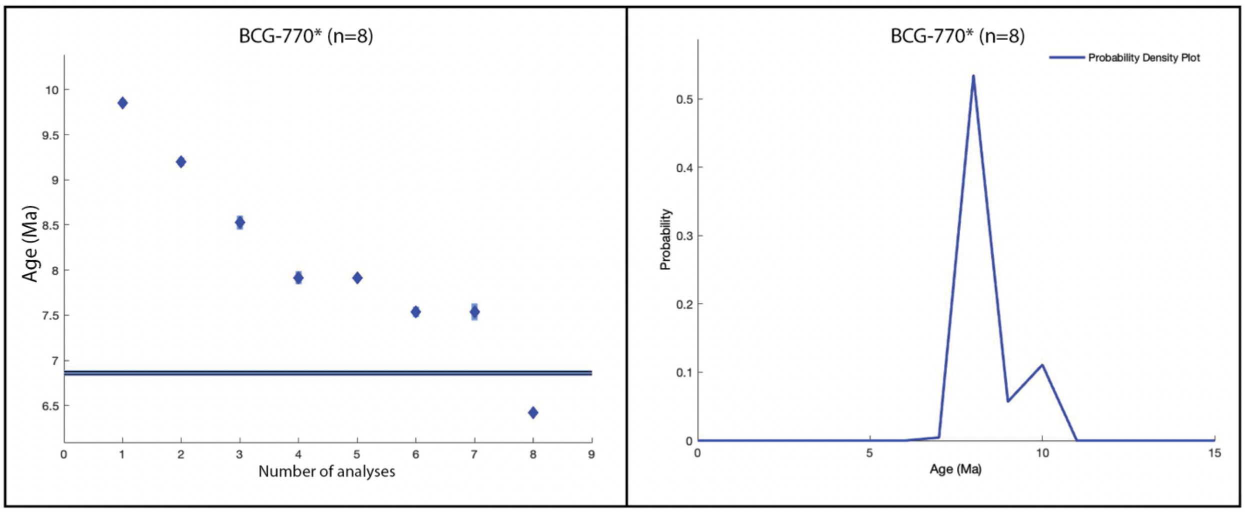

Figure 4.15 – Weighted mean age (left) and probability density plot (right) for ID-TIMS analysis of BCG-770

CHAPTER 5: DISCUSSION

New mapping at a scale of 1:24,00 of the Bear Camp Gulch Quadrangle is a significant improvement on the existing mapping for the eastern flank of the Portneuf Range. The large syncline that defines the study area, the Bear Camp syncline, is a south-southeast trending, and south-plunging fold within the hanging wall of the Toponce thrust. The majority of units exposed in the study area are lower and middle Cambrian in age, with a significant portion of the map area represented by the lower Cambrian Gibson Jack Formation, which is folded along the eastern limb of the syncline, increasing its exposure area (Fig. 5.1). The Neoproterozoic Inkom and Mutual formations of the Brigham Group are exposed only within the northeastern corner of the study area, where they constitute the hanging wall of the Toponce thrust. Ordovician and Silurian units are confined to the southern mapping area, south of the Pine Hen fault.

Preliminary mapping by Corbett (1978), and other previous workers (Link and Stanford, 1999) had mapped large parts of the study area as the Starlight Formation (Fig. 4.1).

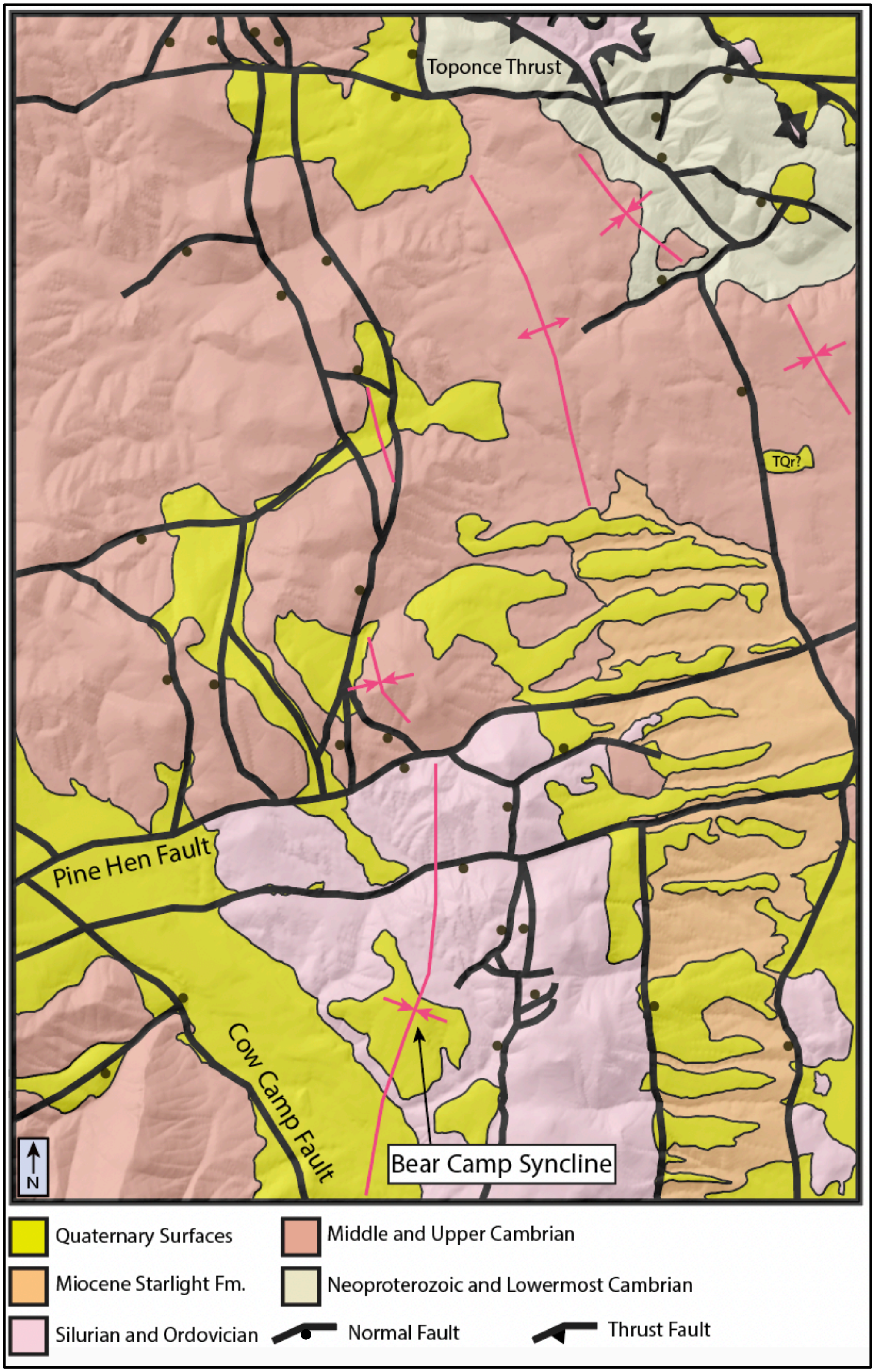

Figure 5.11 – Simplified Map of Bear Camp Gulch quadrangle showing major faults, the Bear Camp syncline, and the revised extent of the Miocene upper Starlight Formation.

However, many of these surfaces previously mapped as the Starlight Formation did not fit the description for lithologies representative of the Starlight Formation, which commonly includes conglomerates, breccias, sandstones, lacustrine carbonates, rhyolite lavas, tuffs, and basalts (Rodgers and Othberg, 1999; Kellogg, et al., 1989; Crane et al., 2000; Konstantinou et al., 2012). In the study area, many of these areas consisted primarily of unconsolidated colluvium and landslide deposits, and had a geomorphic character more consistent with being a Quaternary surface. A conspicuous boulder lag deposit (Qlag) consisting of predominantly quartzite with lesser carbonate was observed in several places within the study area. Clasts ranged in size from cobbles to boulders, with some boulders reaching several meters in diameter. Most alluvial fans were mantled by this material, as well as areas of low topographic relief. These were interpreted to be the eroded remnants of alluvial fans and older Quaternary surfaces. The understanding of the relative age relationships between normal faults within the study area was also improved by this new mapping. Cross-cutting relationships between north-south and east-west striking faults, and truncation of north-south striking faults by east-west faults was highlighted by this study, demonstrating a multiphase extensional history for the Bear Camp Gulch quadrangle.

Cenozoic Deformation

Normal Faulting and Influence of the Yellowstone Hotspot

The study area contains both north-south striking and east-west striking normal faults. Offset along these faults ranges from several hundred feet to several thousand feet, the majority of which have low-magnitudes of offset, and were mapped based on the apparent repetition of stratigraphy. However, several normal faults display greater amounts of offset.

The most significant normal fault in the study area is the northeast-dipping Cow Camp fault (Fig. 5.1), which was identified on the basis of missing stratigraphic section, requiring the presence of a fault. The pre-existing map (Corbett 1978) interpreted a thrust fault (the Portneuf thrust) to exist west of this problem area, at what is currently mapped as the stratigraphic contact between the Elkhead Limestone and overlying Bloomington Formation (Plate 1). The Pocatello 30 x 60-minute quadrangle of Link and Stanford (1999) shows no thrust structure in this area, shows the contact between the Elkhead Limestone and Bloomington Formation as stratigraphic, and also reveals the aforementioned missing stratigraphy. Placement of the Portneuf fault here fails to remedy the previously mentioned space problem. No observed stratigraphic relationships were made in this area that necessitated this thrust fault, and considering the placement of this fault at what is a lithologic contact, as well as the paucity of thrust faults in this area, it is unlikely that the Portneuf thrust exists. Exposures of the fault near the southern boundary of the Bear Camp Gulch quadrangle are poor as the area is densely forested. Near the Big Springs campground, the Cow Camp fault is inferred to strike to the northwest and merge with an east-dipping normal fault in the adjacent Bonneville Peak quadrangle (Riesterer et al., 2000).

In addition to the north-south striking structures attributed to typical the Basin and Range faulting and extension direction, east-west striking normal faults and associated deformation are also evident within the study area. Northeast-striking normal fault systems have been documented elsewhere in southeastern Idaho, typically along the margins of the ESRP, and are hypothesized to be related to the passage of the Yellowstone volcanic system (Zentner, 1989; Rodgers et al., 2002). However, this system of east to east-northeast striking faults does not parallel the ESRP, and appear to be unrelated to the extension direction commonly associated with the Yellowstone volcanic system. East to east-northeast striking faults within the study area and surrounding region are generally south-dipping, and in some cases accommodated up to a thousand meters of offset (Fig. B-B’ cross section). For example, the Pine Hen fault accommodated approximately 1 km of offset, and truncated several north-south striking normal faults in the center of the study area. However, this is in slight contrast with similarly striking faults more proximal to the ESRP, whose displacement is small compared to the north-south striking faults bounding major mountain ranges (Zentner, 1989; Schusler et al., 2016). Faults proximal to the ESRP also generally tend to dip toward the plain, and are interpreted to be the result of flexure within the upper crust related to passage of the Yellowstone volcanic system and subsequent, density-driven subsidence and flexure of the ESRP (McQuarrie and Rodgers, 1998; Rodgers et al., 2002). Other workers (Pogue, 1984; Hladky, 1986; Kellogg, 1990; Kellogg et al., 1999) interpreted some east-west striking normal faults to be Mesozoic tear faults reactivated as normal faults. However, lateral offset associated with east-west striking faults was not observed in the study area, and faults that cross-cut oppositely dipping limbs of the Bear Camp syncline show they are dip-slip and not strike-slip faults.

Assigning relative ages to these perpendicular sets of normal faults within the field area is difficult due to complex cross-cutting relationships and poor outcrops. However, an observed regional trend (Allmendinger, 1982; Pogue, 1984; Hladky, 1986; Rodgers et al., 2006) suggests that north-south striking faults are older, and resulted from Basin and Range style deformation, whereas the east-west striking faults are of a younger phase. This is supported by observations from the field area where many north-south striking faults are offset by east northeast-west southwest striking faults, although there are examples of northeast-southwest faults being offset by north-south faults. This relationship between north-south and east-west striking normal faults may allude to a period of overlap between ongoing Basin and Range style extension, and a modification to the local stress field which resulted in north-south directed extension. This modification of the regional stress resulted in a relative decrease in the magnitude of the horizontal, north-south principal stress, resulting in north-south horizontal extension.

In addition to normal faulting, deformation attributed to the passage of the Yellowstone volcanic system is expressed in additional ways throughout southeastern Idaho. To the north of the ESRP, McQuarrie and Rodgers (1998) documented the downwarping of Mesozoic fold axes into the ESRP. To the south and north of the ESRP, Miocene volcanic rocks are tilted toward the ESRP (e.g., Anders et al., 1989; Rodgers et al., 2002). The plunges of fold axes and volcanic rocks are attributed to flexure induced by mid-crustal injection of a mafic sill related to the Yellowstone volcanic system (McQuarrie and Rodgers, 1998). However, within the Bear Camp Gulch quadrangle, the Bear Camp syncline plunges slightly to the south. This suggests that downwarping that occurred as a result of mid-crustal loading did not affect rocks this far (~40 km) from the ESRP, consistent with the observation of a narrow zone of downwarping present 10-20 km from the margins of the ESRP (McQuarrie and Rodgers, 1998).

Significance of U-Pb Zircon Geochronologic Ages

Because all radioisotopic systems are thermochronometers and may be open to diffusion at high enough temperatures (Reiners et al., 2005), it is important to consider whether the radioisotopic age results are recording a crystallization age or some other thermal process. For this study, ages of volcanic ash samples were determined by means of U-Pb in zircon rather than $^{40}Ar/^{39}Ar$ analysis of the potassic feldspar sanidine, which has been used extensively for Yellowstone volcanic material due to an abundance of feldspar within erupted material (Armstrong et al., 1975; Kellogg and Marvin, 1988; Anders et al., 2014; Rivera et al., 2016). The

$^{40}Ar/^{39}Ar$ dating method is based on the decay of ^{40}K to ^{40}Ar. This method utilizes the ratio of radiogenic ^{40}Ar to ^{39}Ar, which is produced by irradiation of ^{39}K, allowing for measuring of the parent and daughter in the gas phase via incremental heating of the sample to release argon (McDougall and Harrison, 1999). Because the closure temperature for sanidine is lower than that of zircon, the accumulation of radiogenic argon in sanidine is traditionally assumed to begin with rapid cooling resulting from eruption of that material (Schmitz and Kuiper, 2013). Ages derived from $^{40}Ar/^{39}Ar$ analysis of sanidine are assumed to represent the time of eruption and emplacement more accurately, as opposed to U-Pb in zircon which may record an older crystallization age while the crystal was still in the magma reservoir, prior to eruption. Recently, the increasing use of high precision CA-ID-TIMS geochronology has prompted a reevaluation of this assumption, and suggests that assembly and eruption of silicic magma reservoirs in the Yellowstone caldera system takes place over a period of hundreds to thousands of years (Wotzlaw et al., 2014). Rivera et al. (2016) showed that $^{40}Ar/^{39}Ar$ ages of the Mesa Falls Tuff overlap with, and are indistinguishable from ID-TIMS U-Pb zircon ages for the same sample. Though zircon of the Mesa Falls Tuff crystal cargo may have indeed existed prior to eruption, nucleation and growth likely only occurred within 10 kyr of eruption (Rivera et al., 2016). Thus, for this study the ID-TIMS U-Pb zircon ages from ash beds are assumed to reflect the primary eruption and deposition age, and not an older subsurface cooling event within the magma chamber prior to eruption.

Timing and Magnitude of Extension within the Portneuf Range

Sedimentation in active extensional regimes and the resultant sedimentary facies are powerful tools for quantifying extension magnitude within a given basin (McMechan and Price, 1980; Constenius, 1996; Constenius and Layer, 2003). Because extensional deformation in southeastern Idaho occurred contemporaneously with volcanism related to the Yellowstone volcanic system, tephra and volcaniclastic sediments can be excellent targets for geochronologic dating that when paired with their measured structural attitudes can provide constraints on timing and magnitude of extension within a basin (Fig. 5.2) (Constenius, 1996).

Approximately 400 meters (1,300 feet) of Miocene upper Starlight Formation occupies the normal fault-bounded basin (Fig. 5.1) in the southeastern quarter of the quadrangle. This basin trends north-south and is bounded on its east and west flanks by normal faults. The moderately east-dipping, Cambro-Ordovician St. Charles Formation and Ordovician Garden City Formation define the eastern side of the basin, with more gently west-dipping Ordovician Garden City Formation and Swan Peak Quartzite defining the western side. Considering that eastward dips observed in the Starlight Formation increase to the west, away from the eastern fault bounding the basin, the basin is interpreted to have a half-graben geometry, despite the small normal fault to the west. In this scenario, the Starlight Formation was deposited syntectonically as growth strata in the active extensional basin. Pairing of the zircon U-Pb results, primarily the maximum depositional ages determined from ID-TIMS ages, with context from measured structural attitudes for these key horizons, allows for the temporal reconstruction of extension during the observed interval of time (Fig. 5.2). Ages of the lower and uppermost horizons of the upper Starlight Formation (BCG-770 and BCG-612) indicate that extension was active in the study area during late Miocene time, during which approximately 15° of down-to-the-east tilting occurred during the period between 6.421 ± 0.018 and 6.032 ± 0.053 Ma.

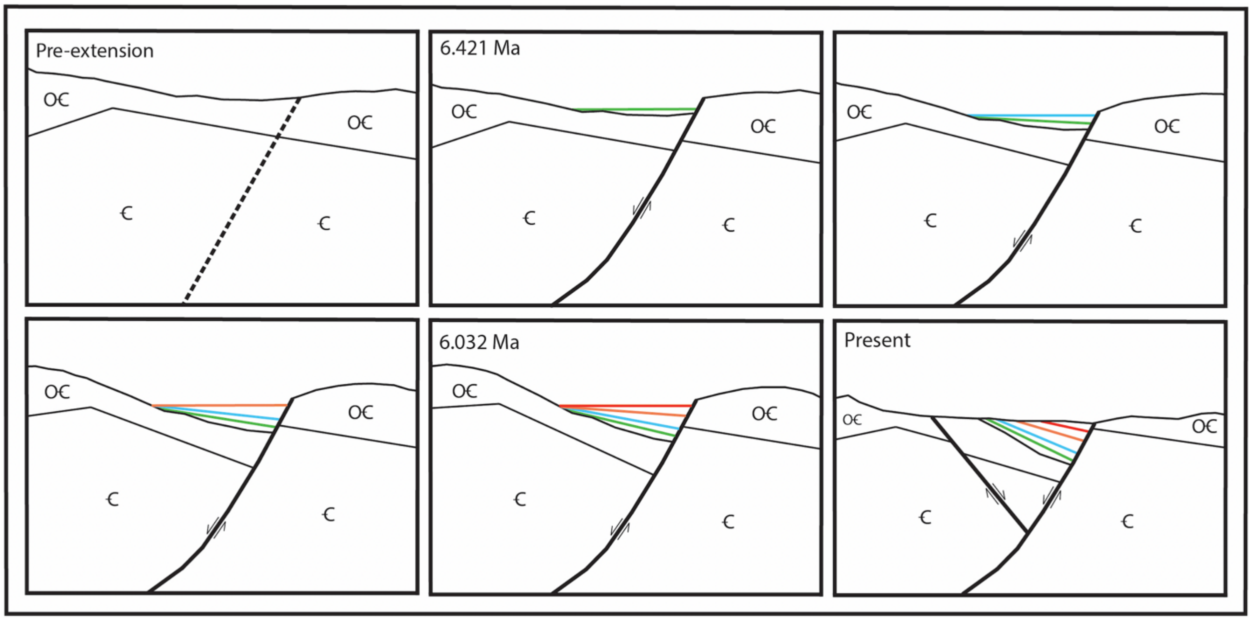

Figure 5.2 – Schematic cross sectional diagrams illustrating evolution of the Miocene basin and syntectonic deposition of the upper Starlight Formation (colored lines) in the Bear Camp Gulch quadrangle.

The fault bounding this Miocene basin is likely a splay or continuation of a north-south striking, west-dipping normal fault system defining the western boundary of the Fish Creek Range (Fig. 5.3). This fault system appears to extend to the south where it joins the Lava Hot Springs fault set ~20 km to the south (Fig. 5.3) (Crane et al., 2000). In the Lava Hot Springs quadrangle, major normal faults are west-dipping and contain middle Paleozoic carbonate strata in their hanging walls. Dates of ashes sampled here range from 9.3 to 7.0 Ma and may represent the period of extension associated with faulting in the Portneuf Valley (Rodgers et al., 2002). The Portneuf Range is bounded on the west by two generations of normal faults. The older fault dips approximately 30° to the west, and was truncated by a younger fault in the south where it bounds a basin containing upper Starlight Formation (Riesterer et al., 2000). Offset along the Portneuf Range front fault increases from 3.3 km in the north to 6.5 km in the south (Riesterer, et al., 2000). The timing of slip on the younger Portneuf Range frontal fault is not well understood, but is likely late Miocene (Tortonian) in age based on the ages of upper Starlight Formation basin fill (Riesterer, et al., 2000). The older, more shallowly dipping Portneuf Range fault may be related to an earlier period of slip (Rodgers et al., 2002), and may be similar in age to the shallowly west-dipping Fort Hall Canyon fault near Pocatello which was active from 8.2 to approximately 7.4 Ma (Rodgers and Othberg, 1999).

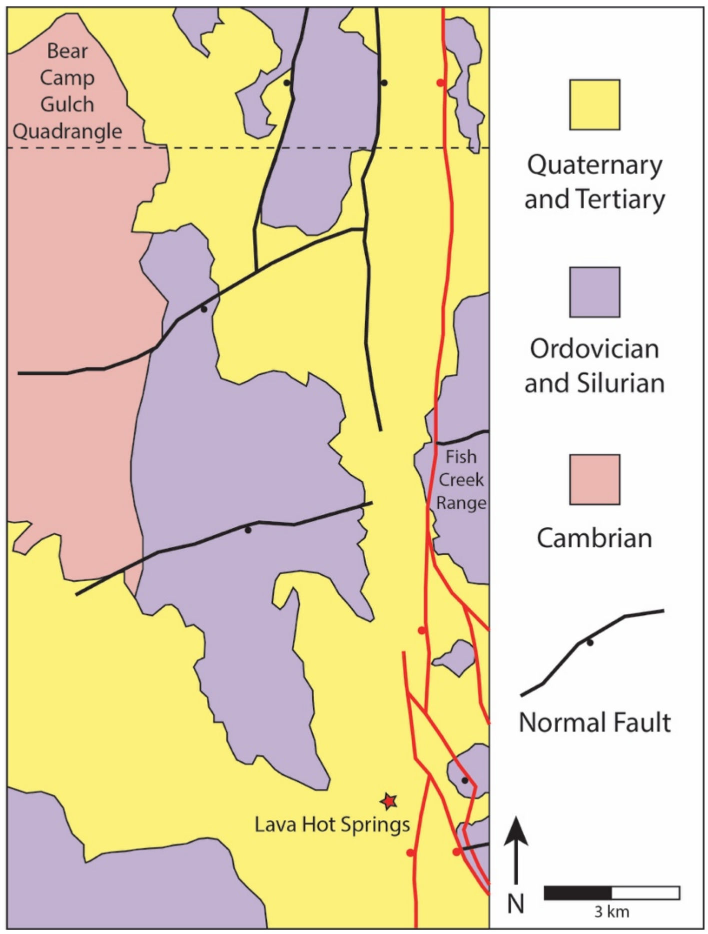

Figure 5.3 – Normal faults (red) of the regional basin continuing northward from Lava Hot Springs.

Based on the relative ages of the upper Starlight Formation in the Lava Hot Springs quadrangle to the south, extension and basin formation there appears to have initiated prior to extension in the study area. High topography and a lack of accommodation space as a result of its proximity to the ESRP may also contribute to the preservation of volcanic material in the study area. Additionally, the Starlight Formation in the Lava Hot Springs quadrangle reach thicknesses of up to 1200 meters, compared to 400 meters in the study area (Crane et al., 2000). Considering the greater thickness of basin fill, and presence of older ashes in the Lava quadrangle, the formation of accommodation space and preservation of basin fill may have migrated northward from Lava Hot Springs and into the study area. Decreasing thickness of basin fill to the north may allude to a fault-scaling relationship in this area where offset along this normal fault and accompanying accommodation space diminished to the north (Dawers et al., 1993; Peacock, 2002). The range of zircon ages from the stratigraphically lowest sample, BCG-770, may be evidence of an older period of extension. Zircon grains from this sample range in age from 9.8 to 7.5 Ma (n=7), with a single young grain defining the age of the bed. This sample is heterogenous and represents mixed detrital input, in contrast with the stratigraphically highest sample, BCG-612, which represents a single eruptive event. The presence of these older grains in BCG-770 suggests reworking of older erupted material, and that the catchment area for streams at this time included several different tephras.

The high precision afforded by ID-TIMS allows for the potential correlation of these zircon ages with those of well-documented tuffs associated with major eruptive centers of the ESRP. Anders et al. (2014) conducted new $^{40}Ar/^{39}Ar$ age dating of rocks from drill core and silicic ignimbrites, tephras, and related volcanic rocks along the ESRP and correlated them with the Miocene Heise and Picabo volcanic fields of the eastern ESRP. Based on these new, high precision ages, both the Picabo (10-7 Ma) and Heise (6.5-4.3 Ma) volcanic fields were supplying material to the study area. Sample BCG-612 (weighted mean $^{206}Pb/^{238}U$ date of 6.032 ± 0.053 Ma) may correlate with the Tuff of Wolverine Creek of the Heise volcanic field. Sample BCG-770 displays a more complex zircon population, and contains grains that range in age from 9.8 to

6.4 Ma (appendix B,D), demonstrating a joint Picabo and Heise source, and a significant degree of reworking of volcanic material.

Regional Context of Extension within the Portneuf Range

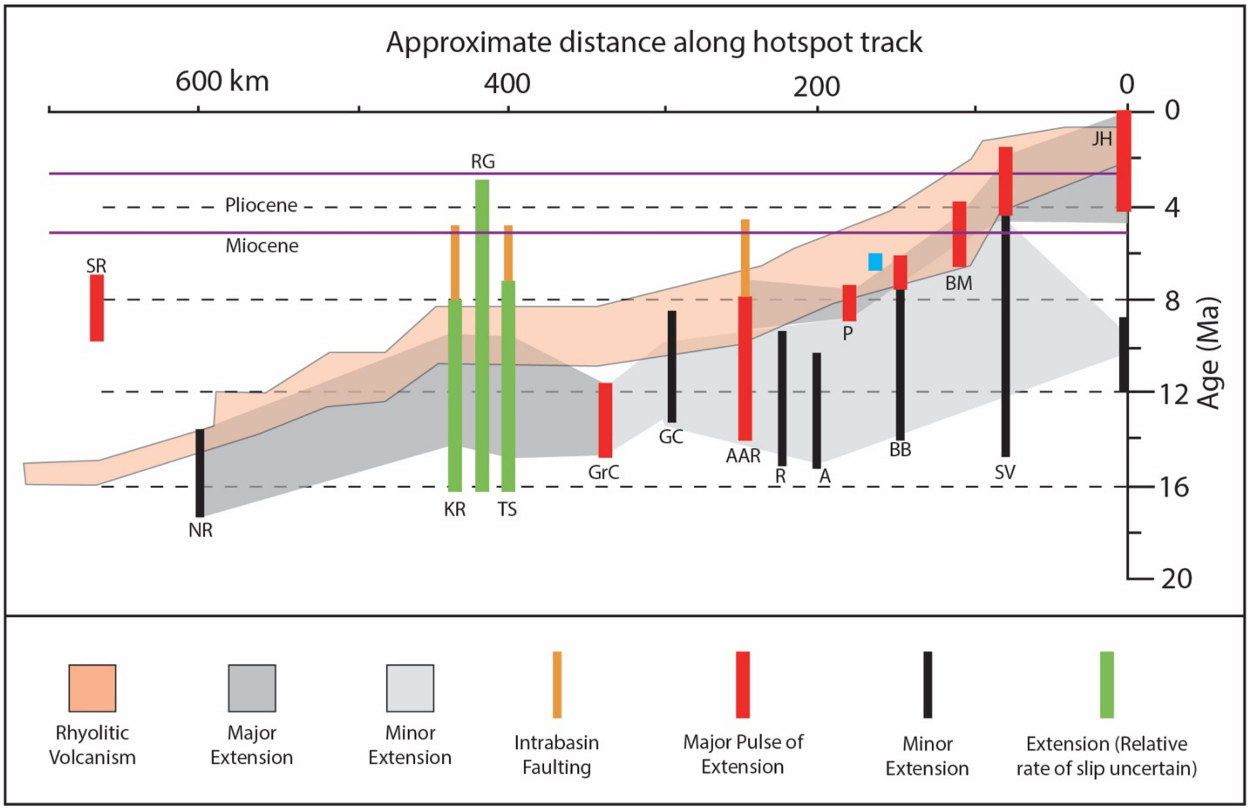

Figure 5.4 – Diagram illustrating timing and location of extension and rhyolitic volcanism along Snake River Plain. Phase of extension identified in study area in blue. Modified from Rodgers et al. (2002) and Camilleri et al. (2017). AAR – Albion-Raft River, A – Arbon Valley, BB – Buckskin Basin, BM – Blackfoot Mountains, GC – Goose Creek, GrC – Grouse Creek Valley, JH – Jackson Hole, KR – Knoll-Ruby, NR – Nevada Rift, P – Portneuf Valley, R – Rockland Valley, RG – Rogerson Graben, SR – Santa Rosa Range, SV – Swan Valley, TS – Thousand Springs.

Between approximately 11-4 Ma, a major pulse of time-transgressive extension occurred along the southern ESRP, focused at any one time near the approximate locus of silicic volcanism (Rodgers et al., 2002). Based on measured sections of basin fill in Raft River Valley, Rockland Valley, Arbon Valley, Portneuf Valley and Buckskin Basin, Rodgers et al. (2002) estimated sedimentation rates of 100-300 m/m.y. for this region, interpreted to reflect rapid extension. The ages of tephras sampled from the upper Starlight Formation indicate that the observed period of extension in the study area overlapped in time with this 11-4 Ma period of rapid extension associated with the passage of the Yellowstone volcanic system and the development of the ESRP (Fig. 5.3) (Rodgers et al., 2002; Camilleri et al., 2017). More specifically, this period of extension appears to overlap with a pulse of rapid extension that occurred near Buckskin Basin and the Blackfoot Mountains between ~7.5 and 4 Ma (Rodgers et al., 2002; Camilleri et al., 2017). This was preceded by a similar period of rapid extension in Portneuf Valley between ~9 and 7.5 Ma (Rodgers et al., 2002). Thus, the observed episode of extension may represent a period of transition where the locus of extension was beginning to shift to the northeast.

Because the thickness of the upper Starlight Formation in the study area is poorly constrained, sedimentation rates cannot be provided. However, the observed tilting of the dated beds show that a minimum 15° of tilting occurred between 6.421 and 6.032 Ma within Miocene sedimentary rocks within the field area, a period of ~389 ka. Based on the observed eastward dip of the lowest dated bed, it is likely that up to 27° of tilting occurred in at least the eastern part of the study area, though it is unclear how much of this tilt can be attributed to faults within the study area. Regionally, tilting of Miocene sedimentary rocks ranges from 20° to 45° (Kellogg et al., 1999; Rodgers and Othberg, 1999). Steeper tilt magnitudes may be attributed to an older episode of extension (10-16 Ma) that rotated older normal faults to subhorizontal orientations (Fig. 5.4)(Rodgers et al., 2002; Rodgers and Othberg, 2006; Camilleri et al., 2017).

Two pulses of extension and rotation of fault blocks occurred within southeastern Idaho, south of the ESRP. An older, poorly constrained period of extension was likely the result of ongoing Basin and Range deformation, which was subsequently modified and accelerated by the encroaching Yellowstone volcanic system (Allmendinger, 1982; Pogue, 1984; Crane et al., 2000; Rodgers et al., 2002; Long et al., 2006). This resulted in an accelerated pulse of extension and block rotation during upper Miocene time, evidenced by the syntectonic deposition and tilting of the upper Starlight Formation within the study area (Kellogg et al., 1989; Kellogg, 1990; 1992; Rodgers et al., 2002).

Miocene Fault Block Rotation

Mesozoic structures related to the Sevier orogeny have been complexly dismembered by Cenozoic normal faults (Coney, 1984; Constenius, 1996; Dickinson, 2006; Vogl, 2012; Yonkee and Weil, 2015). Approximately 15-20 km west of the study area, large, east-verging folds were interpreted by some prior workers to have been rotated into subhorizontal orientations (Burgel et al., 1987; Kellogg, 1992; Rodgers et al., 2006) and structural culminations experienced localized extension (Rodgers and Long, 2012). Attempts at developing a working model for the evolution of Mesozoic contraction must contend with the effects of Cenozoic extension, block rotation, and subsequent obscuration of contractional structures. Therefore, a necessary first step in reconstructing Mesozoic deformation is to successfully retro-deform slip along major faults and restore fault blocks to their original, pre-extension orientations. At present, many Sevier-aged structures in the area display an eastward tilt, which has been interpreted to be largely a result of Neogene tilting (Kellogg, et al., 1999); however some of this observed tilt may be attributed to their original orientations prior to Cenozoic extension. For instance, the Bear Canyon thrust may have been rotated by approximately 30° by the Portneuf Range front fault into an east-dipping orientation, assuming it was originally horizontal. Alternatively, the Bear Canyon thrust may have had a pre-extension eastward dip.

Because the original Mesozoic configurations for these structures are unclear, and can vary depending on the preferred model for their development, it was decided to rotate the entire field area by assuming that normal faults systematically tilted blocks by domino-style normal faulting (Proffett, 1977). An important consideration when restoring slip on normal faults is their assumed subsurface geometry. Fault blocks that are bounded by faults interpreted to become listric at depth cannot be treated as simple fault blocks and untilted as a homogenous dip-panel. If a fault block is interpreted to be bound by a listric fault, then the degree of observed tilting is not equal at all structural levels. If slip along major normal faults is restored, faults such as the Bear Canyon and Inman Pass thrusts become subhorizontal (Rodgers and Long, 2012). As a simplified assumption, in the study area, I interpret that Mesozoic structures, fault blocks, and even normal faults have likely been rotated a minimum of 20° to the east, as shown by the range of orientations within the upper Starlight Formation. Untilting pre-Cenozoic rocks by this magnitude resulted in rotation the Bear Camp syncline into its current orientation, tilted older normal faults and Sevier-aged structures, and created the aforementioned Miocene basin. Restoring 20° of eastward rotation to the Bear Camp syncline produces an asymmetrical fold, with an axial surface dipping steeply to the east. Considering that the study area is in the hanging wall of the Toponce thrust, this restored geometry for the Bear Camp syncline may reflect a concealed footwall ramp. Restoring slip on cross sections A-A' and C-C' (Fig. 5.5) allows for the calculation of an approximate extension magnitude. Slip along normal faults in the southern cross section (A-A') accommodated 13% extension, whereas normal faulting in the northern cross section (C-C') accommodated 25% extension.

Mesozoic Deformation

Bear Canyon-Toponce Thrust

The two major thrusts exposed within the Portneuf Range are the Bear Canyon and Toponce thrusts. The Bear Canyon thrust, while not directly exposed within the study area, is inferred to exist at depth (Fig. 5.7). However, the Toponce thrust is exposed at the surface within the northeastern corner of the study area. The model of Kellogg (1992) for the Putnam thrust

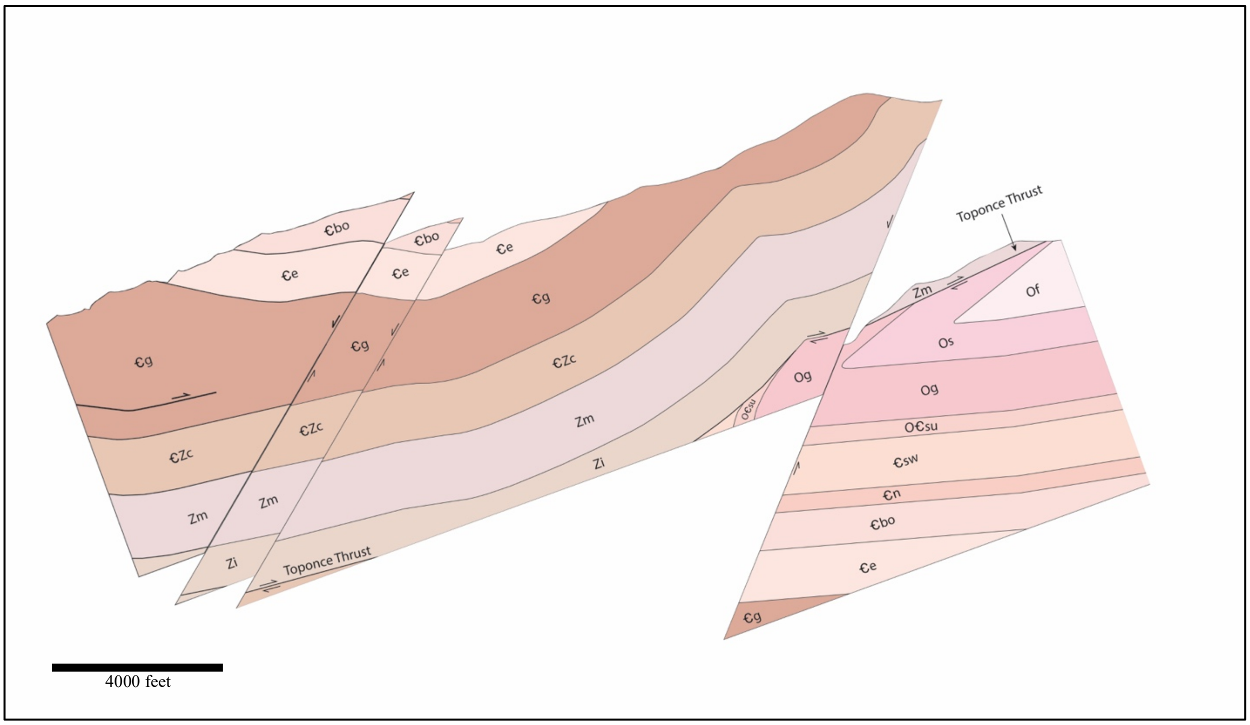

Figure 5.5 - Cross section C-C' showing restored slip on normal faults and removal of 20° of down-to-the east tilting.

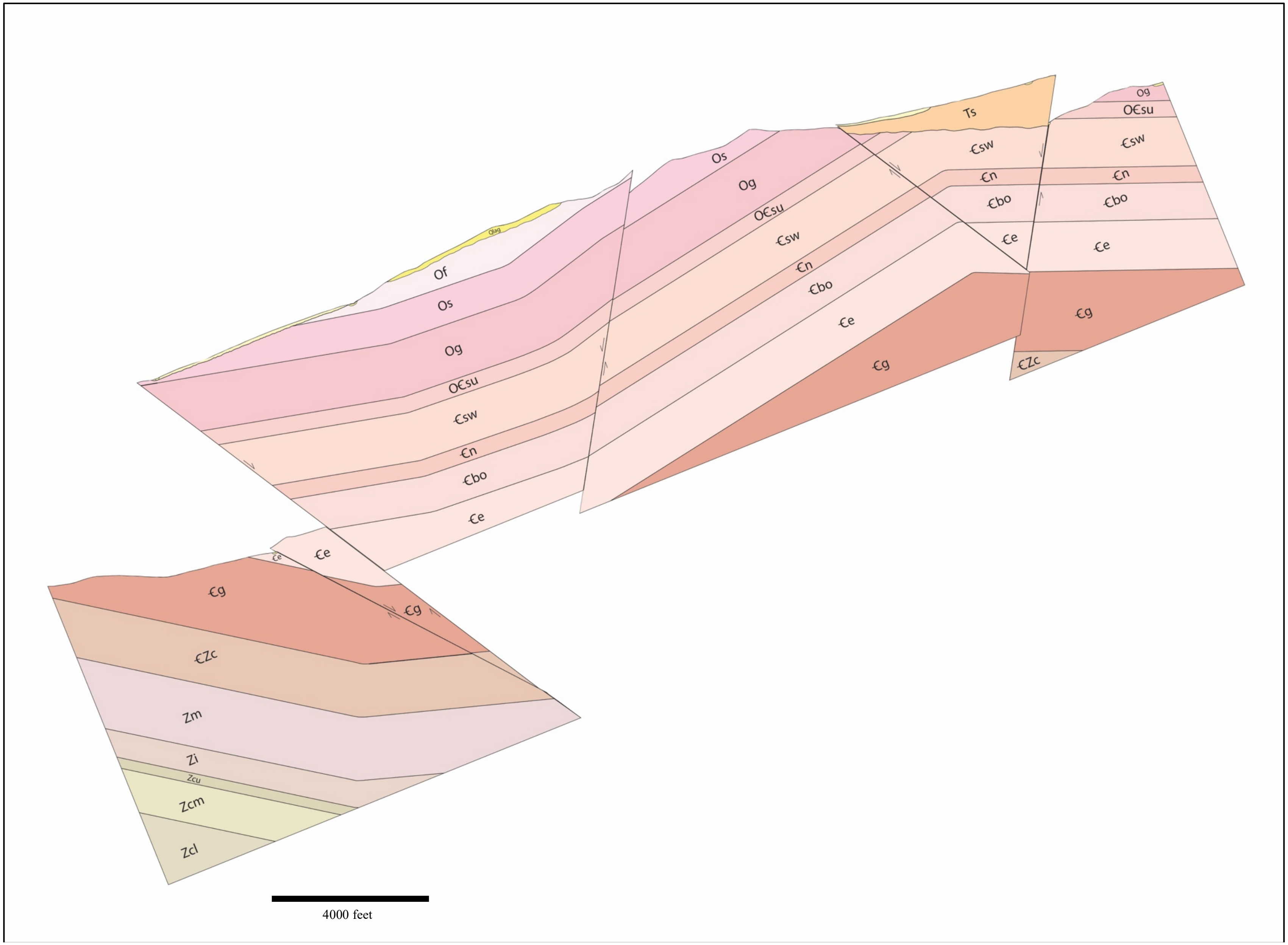

Figure 5.6 - Cross section A-A' showing restored slip on normal faults and removal of 20° of down-to-the east tilting.

system considered these two faults to be equivalent structures, where the Toponce is an eastern expression of the Bear Canyon thrust (Kellogg et al., 1999).This interpretation is based on similar stratigraphy found in their hanging walls and footwalls in neighboring quadrangles to the north and northwest (Kellogg et al., 1989; Kellogg, 1990). However, stratigraphic separation diagrams (Fig. 4.5, 4.6) for these thrusts call this interpretation into question. Though the two thrusts do indeed share similar hanging wall and footwall stratigraphy, the behavior for the Bear Canyon and Toponce thrusts as deduced from the separation diagrams is problematic (Fig. 4.6).

On the western flank of the Portneuf Range, the Bear Canyon thrust carried Neoproterozoic strata it its hanging wall, whereas the footwall ramped through Neoproterozoic and middle Cambrian strata until both the footwall and hanging wall become obscured in the Mill Creek fault zone. East of the Mill Creek Fault Zone, the footwall and hanging wall of the Bear Canyon thrust change stratigraphic positions, and the footwall appears lower in the section (Fig. 4.5, 4.6). Southeast of here, the Toponce thrust is observed putting Neoproterozoic strata on overturned Ordovician footwall rocks (Fig. 4.5,4.6).

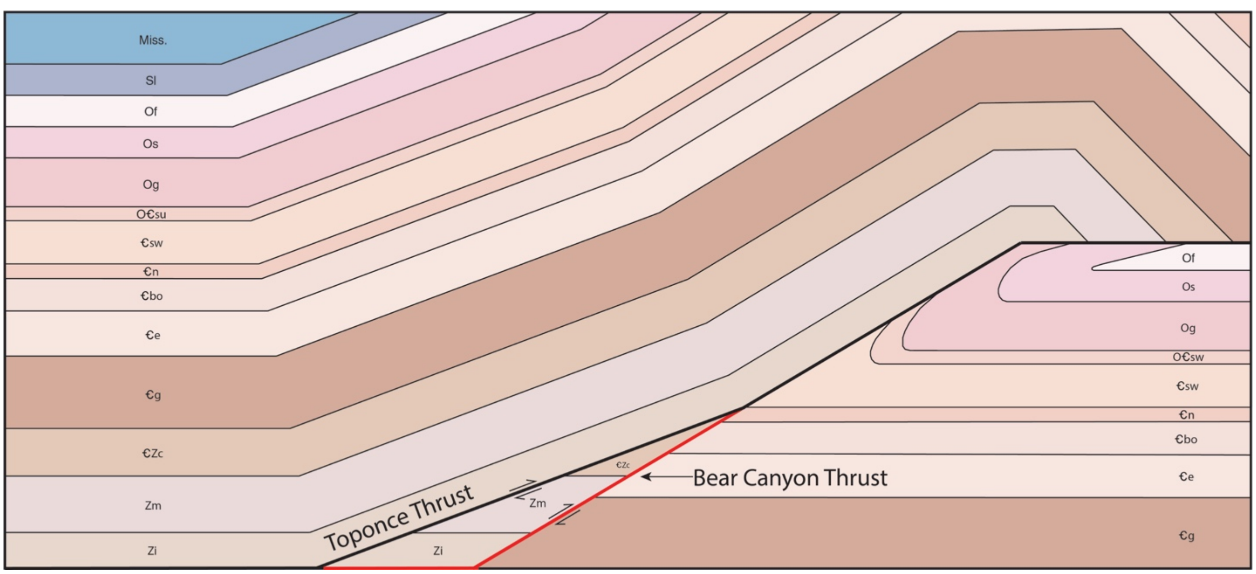

Figure 5.7 – Simplified view of the Toponce thrust (black) showing overturned footwall syncline, and older Bear Canyon thrust (red).

These inconsistencies between the stratigraphic positions of the Bear Canyon and Toponce thrusts are problematic for models that treat them as the same fault, as it would either require segments of the Bear Canyon-Toponce thrust to cut down-section in the direction of transport, or cut out-of-sequence as a breakthrough thrust in folded strata. This interpretation would also require a significant amount of lateral ramping to explain the sudden jumps in stratigraphic levels for both the hanging wall and footwall within the mapped extent of the Bear Canyon thrust, and particularly the zone where it has been hypothesized to merge with the Toponce thrust. Though lateral ramps are interpreted to exist in the area, (e.g., the Narrows thrust), this amount of lateral ramping within a relatively small area is unlikely. In contrast with the Bear Canyon thrust, the stratigraphic separation diagram for the Toponce thrust is much simpler and contrasts with the Bear Canyon thrust. For these reasons, we favor the interpretation that the Bear Canyon and Toponce thrusts each exhibit different behavior, and should not be considered the same fault. As such, an alternate hypothesis for the Bear Canyon and Toponce thrusts must be considered.

In this model, the Bear Canyon and Toponce thrusts are separate faults, with the Toponce forming as an out-of-sequence imbricate of the Bear Canyon thrust (Fig. 5.5, 5.7). In this scenario, conditions for further slip along the Bear Canyon thrust became unfavorable, and the Toponce thrust initiated within the hanging wall of the Bear Canyon thrust. Exposures of the Toponce thrust in the northeastern corner of the study area (Plate 1) include the overturned and west-dipping, Ordovician Garden City Formation and Swan Peak Quartzite. Hanging wall units include the gently folded Neoproterozoic Inkom and Mutual Formations, and the Cambrian-Neoproterozoic Camelback Mountain Quartzite. Within the hanging wall, the Inkom Formation is observed only in a small outcrop near the northern map boundary, and in most places the

Toponce thrust placed the Mutual Formation directly on the Garden City Limestone. Overturned footwall units here were interpreted by Kellogg (1992) as being part of a foreland-dipping duplex, bound by the Bear Canyon-Toponce roof thrust above and by the Putnam thrust below. In the new model, the overturned units in the footwall are interpreted to be a footwall syncline, likely formed by breakthrough of a fault propagation fold in the early stages of thrusting (e.g., Mitra, 1990).

This modified model also accounts for the minor Inman Pass thrust. The Inman Pass thrust is named for exposures near Inman Pass, where it placed the uppermost Camelback Mountain Quartzite on the Cambrian Gibson Jack Formation, and thickened the Gibson Jack Formation significantly. The Inman Pass thrust is also inferred to occur west of this exposure, where it is concealed beneath Quaternary material, and presumably responsible for the increased thickness of the Gibson Jack Formation in that area (Riesterer et al., 2000). The Inman Pass thrust is a hanging wall structure of the Bear Canyon thrust, and as such, it is also east-dipping. Within the study area, east of Inman Pass, the Gibson Jack Formation is the westernmost unit mapped. Based on mapped contacts of the Gibson Jack Formation in the study area, and those in the Bonneville Peak quadrangle, the Gibson Jack appears to have been significantly thickened in this part of the study area (Fig. 4.9). East of these exposures, where the Gibson Jack reappears in the eastern limb of the Bear Camp syncline, it appears to have returned to its normal stratigraphic thickness (Fig. 4.9, cross-section C-C’). Either an additional ramp for the Inman Pass thrust, or fault propagation/detachment folding is required to account for the observed thickness. Based on these observations, the Inman Pass thrust is inferred to terminate near the northwestern corner of the study area, where slip along the fault diminishes and shortening was accommodated by localized folding and thickening of the unit. This interpretation is supported by abundant folds to the north of Inman Pass (Riesterer et al., 2000).

Revised Kinematic Model for the Putnam Thrust System

The incomplete understanding of the Putnam thrust stems in part from ambiguous relationships between thrust faults within the thrust plate, such as the Bear Canyon and Toponce thrusts, and how they operate within the context of the greater Putnam system. A revised model for the Putnam system can improve understanding of the kinematics within the foreland-hinterland transition. Improving our understanding of the geometry of thrusts in the Putnam sheet can ultimately lead to a refined estimate for shortening accommodated by the Putnam system. Expanding on our new mapping, existing mapping, and the existing models of Kellogg et al. (1999) and Rodgers and Long (2012), we propose a modified model for the development of the Putnam thrust system. Based on revised interpretations of the interplay between the Toponce and Bear Canyon thrusts, as well as existing mapping to the west, north, and northwest (Kellogg et al., 1989; Kellogg, 1990; Riesterer et al., 2000; Rodgers et al., 2006; Rodgers and Long, 2012), strong argument can be made for a dominantly in-sequence model with a minor caveat. In this scenario, major thrusts root into a master décollement, and get younger with depth as they propagate eastward. In the vicinity of Blackrock Canyon, the Bear Canyon thrust is structurally above the recumbent Blackrock Canyon fold, and is east-dipping, suggesting that movement on the Putnam thrust folded the Bear Canyon thrust during creation of the Blackrock Canyon fold (Rodgers et al., 2006; Rodgers and Long, 2012). This scenario would also explain a degree of eastward dip of the Bear Canyon thrust that existed prior to extensional tilting.

Considering that the Bear Canyon thrust likely merged with the Putnam thrust at depth, and the Toponce thrust crops out between these two faults, the Toponce thrust then is likely a separate fault within the hanging wall of the Bear Canyon thrust. In our revised model, a hanging wall ramp of the Bear Canyon thrust, consisting of the Inkom Formation, Mutual Formation, and Camelback Mountain Quartzite is in contact with a footwall ramp consisting of the Cambrian Gibson Jack Formation through Swan Peak Quartzite. This juxtaposition of hanging wall and footwall ramps is interpreted to have become inefficient for the Bear Canyon thrust and prevented further slip (Fig. 5.8b), and the Toponce thrust initiated by stepping back and propagating upward through the Inkom, Mutual and Camelback Mountain Quartzite, putting these units on overturned Ordovician strata (Fig. 5.7, 5.9c). The Toponce thrust then formed an out-of-sequence, trailing imbricate where it branched from the Bear Canyon at depth near the western edge of the study area, and rejoined the original footwall flat of the Bear Canyon thrust (Fig. 5.9c). This interpretation of the behavior for the Toponce and Bear Canyon thrusts satisfies stratigraphic relationships for the Toponce thrust in the study area, and the Bear Canyon thrust to the west and northwest (Kellogg, 1990; Riesterer et al., 2000).

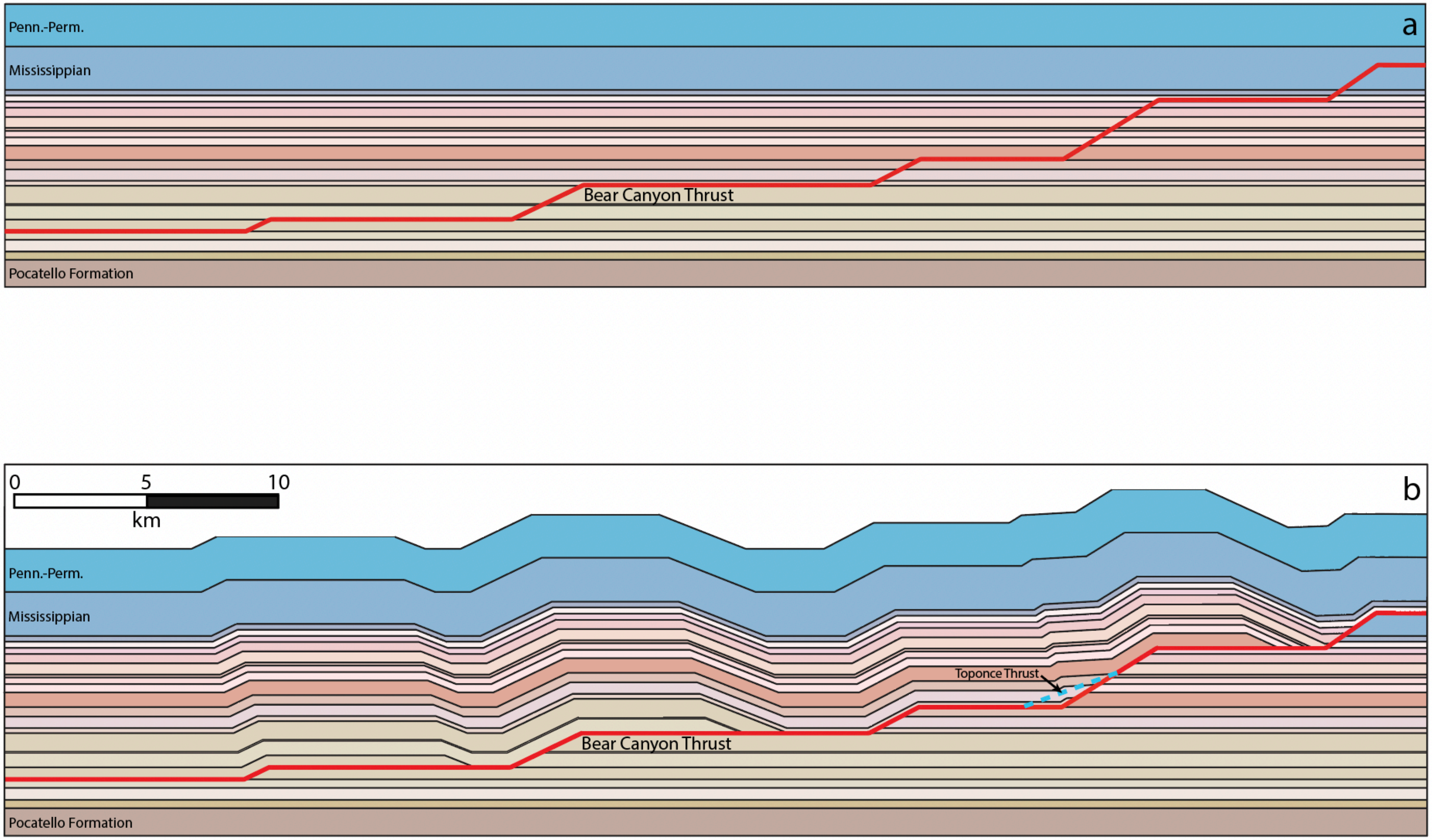

Figure 5.8 - Models for the development of the Putnam thrust system. a.) Undeformed stratigraphy with unslipped Bear Canyon thrust (dashed). b.) Slip on the Bear Canyon thrust, and unslipped Toponce thrust (dashed, blue). Line of section is approximately west-east. Models were initially developed by Matthew Ruggiero and modified for study area. No vertical exaggeration.

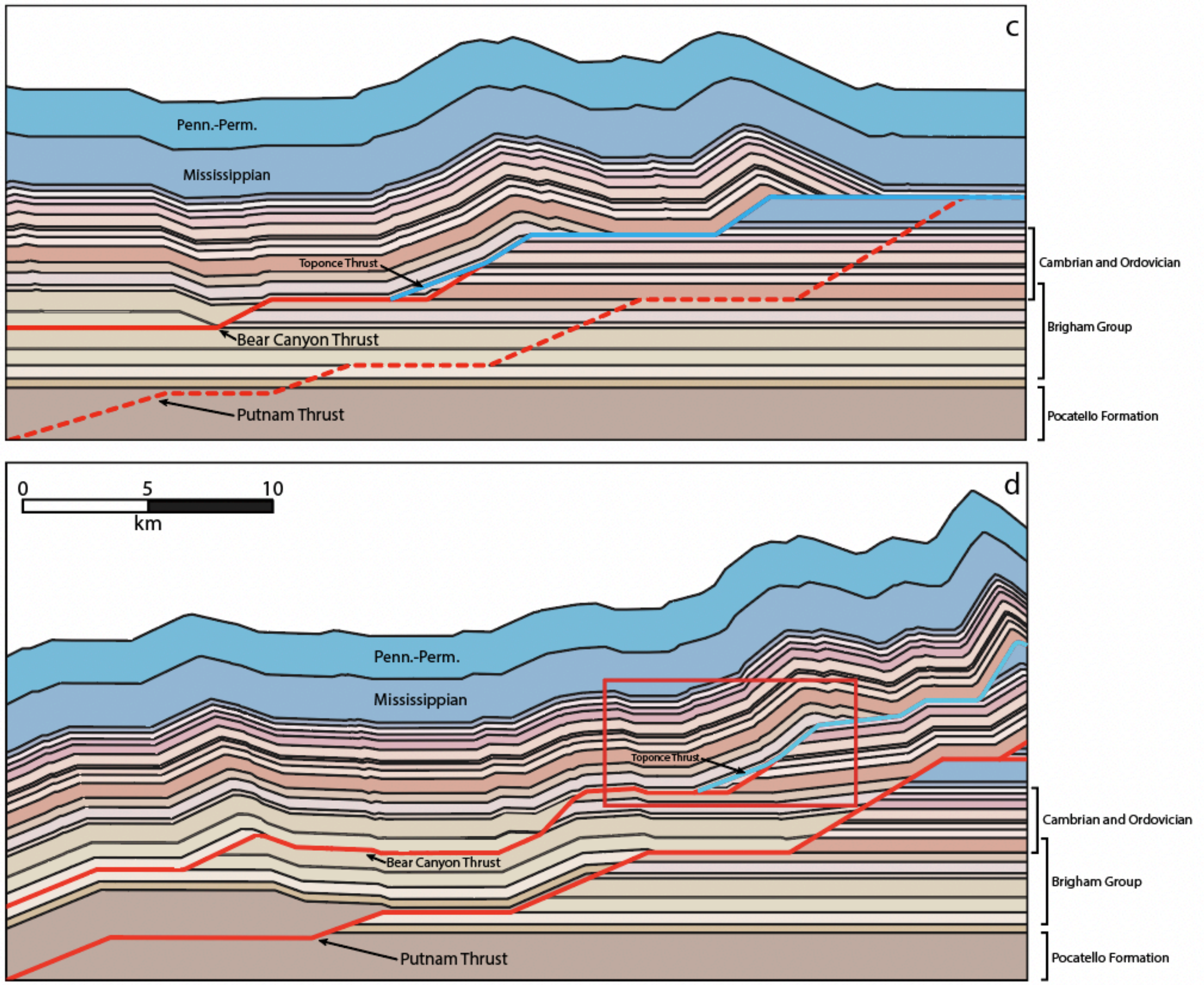

Figure 5.9 – Models for the development of the Putnam thrust system. c.) Slip on Toponce and Bear Canyon thrusts, and formation of the Bear Camp syncline as a hanging-wall syncline. d.) Slip on Bear Canyon, Toponce, and Putnam thrusts, accentuating the hanging wall syncline that forms the Bear Camp syncline (red box). Creation of the Blackrock Canyon fold by the Putnam thrust would have resulted in greater structural relief but has been omitted for simplicity. Line of section is approximately west-east. Models were initially developed by Matthew Ruggiero and modified for study area. No vertical exaggeration.

Minor ramps and flats within this area may exist in the subsurface, but they are not required by surface or other geometric constraints. In the northern cross section for the Bonneville Peak quadrangle, (Riesterer et al., 2000) the Bear Canyon thrust is depicted carrying the middle and upper Caddy Canyon Quartzite in its hanging wall. Because these units do not reappear in the Toponce thrust, or farther east, it is inferred that these units terminate in hanging wall ramps, and only the Inkom Formation is carried farther east in the hanging wall of the Bear Canyon and Toponce thrusts. Upper Cambrian through Ordovician footwall strata here have now been subjected to thrusting on both the Bear Canyon and Toponce thrusts (Fig. 5.9c) and have likely become highly deformed in the process. This repeated deformation may explain the presence of several normal faults in the area, which may exploit older fault surfaces, or axial-planar cleavage associated with folding. This interpretation was favored by the model of Kellogg (1992) where several normal faults are interpreted to root into the Toponce thrust. Kellogg (1992) credited this localized extension with zones of intense brecciation in this area, particularly of Brigham Group quartzites. This brecciation was also observed in this study, proximal to the Toponce thrust and to the east in the overturned Swan Peak Quartzite. Overturned strata in the footwall of the Toponce thrust are likely related to thrusting, forming via fault-propagation folding (Suppe and Medwedeff, 1984; Mitra, 1990). Conflicting along strike differences in orientations of footwall strata for the Bear Canyon thrust (Fig. 2.4) may also be attributed to fault-propagation folding and with varying thrust breakthrough. In the vicinity of Mill Creek, Neoproterozoic and Cambrian footwall strata in the footwall are overturned to the west, whereas to the south, near Inman Pass, identical footwall strata are upright and east-dipping. This seemingly conflicting relationship could be the result of fault-propagation folding in which the thrust ramped up through the axial surface of a fold in the Mill Creek area, and could place upright strata in the hanging wall on an overturned limb of a footwall syncline (Fig. 5.10). Whereas to the south in the Inman Pass area, the thrust broke through further east of the fault propagation fold, placing upright strata on upright strata (Fig. 5.10). This interpretation would reconcile the contrasting thrust models for the Bear Canyon thrust (Kellogg, 1992; Kellogg et al., 1999; Rodgers and Long, 2012), while still honoring the observations of previous detailed work (Kellogg, 1990; Riesterer et al., 2000). Visible in cross section C-C’ (Fig. 4.9) are the overturned footwall units of the Toponce, the termination of the Inman Pass thrust, and the northern portion of the Bear Canyon syncline. These structures are disrupted by several west-dipping normal faults. Three-point problems solved for these normal faults show they are approximately 40° west-dipping, suggesting that they may have experienced some rotation since their formation.

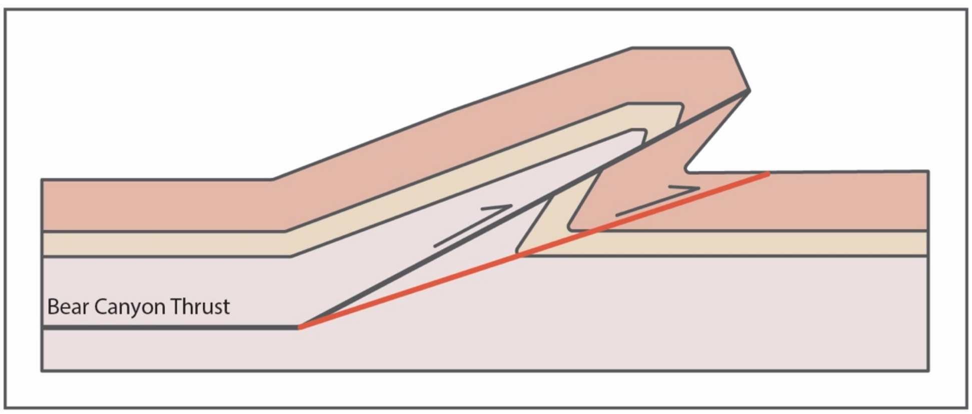

Figure 5.10 – Schematic diagram illustrating geometry of the Bear Canyon thrust on western flank of the Portneuf Range. Northwest of the study area near Mill Creek, footwall strata of the Bear Canyon thrust are overturned to the west, possibly a result of the thrust breaking through near the axial surface of a fault-propagation fold (black). To the south near Inman Pass, the thrust broke through east of a footwall syncline and overturned strata (red), and footwall strata are upright.

In an in-sequence model, development of the Putnam sheet would have continued with slip on the Bear Canyon and Toponce thrusts eventually generating enough structural relief to promote the initiation of slip along the Putnam thrust in lower stratigraphic levels, putting middle Cambrian rocks on Mississippian rocks north of the study area (Fig. 5.9d)(Kellogg et al., 1989). The Bear Camp syncline likely formed as a fault-bend fold on the Bear Canyon and Toponce thrusts, and was accentuated by folding attributed to the Putnam thrust. The Toponce thrust also appears to have been folded, likely as a result of movement on the Putnam thrust (Kellogg et al., 1999). Assuming the Putnam system evolved largely in-sequence, then slip along the Putnam thrust would have folded overlying strata and thrust structures, likely contributing to complexities observed at the surface, such as tilting of the Bear Canyon thrust and regional folding. Rodgers and Janecke (1998) pointed out that folds in this area with wavelengths greater than 1 km were likely expressions of concealed ramps, with short-wavelength folds being related to internal deformation of thrust sheets.

Within the broader scope of this model, the Putnam thrust sheet formed a large duplex structure, with the Bear Canyon thrust sheet structurally above the Putnam sheet. The Bear Canyon thrust was partially reactivated by the Toponce thrust, and with activation of the Putnam thrust, these surfaces link up at depth, becoming the hanging wall rocks of the Putnam sheet. The models for the Putnam system shown above strongly resemble cross sections for the Idaho-Wyoming salient (Yonkee and Weil, 2015) which are partially constrained by subsurface seismic and borehole data. These cross sections interpret much of the western and central portions of the Idaho-Wyoming salient to be composed of large duplexes, imbricate fans, and fault-propagation folding.

CHAPTER 6: CONCLUSIONS

Extensive overprinting of Sevier-age thrust structures by Neogene extension has been well-documented in southeastern Idaho, and is responsible for obscuring many important contractional structures near the hinterland-foreland transitional zone of the Sevier fold-thrust belt. Understanding this history of extension is critical to reconstructions of thrust systems which seek to provide an estimate of shortening for a given thrust system, and a viable kinematic model for the Putnam thrust system has so far eluded workers due to a lack of available subsurface data, complex extensional overprinting, and poor exposures. New detailed mapping and zircon U-Pb ages from Miocene volcanic basin fill provided by this study have identified key structural elements related to extension and contraction, and refined the timing, geometry, and magnitude of extension within this region. By reconstructing normal faulting in the study area, and considering the regional patterns of thrust faults, a new kinematic model for the Putnam thrust sheet is now possible. Major conclusions from this study include:

1: An episode of extension occurred in the northern Portneuf Range between 6.421 and 6.032 Ma, constraining the age of the Starlight Formation in this area to upper Miocene (Messinian). This agrees with previous work (Rodgers et al., 2002) that documented a major period of extension in this area and immediately to the northeast, which occurred between approximately 6-7 Ma.

2: Based on orientations of the upper Starlight Formation, extension within the study area is interpreted here to have resulted in approximately 20° of eastward tilting, and has dismantled the Toponce thrust and the Bear Camp syncline.

3: The Yellowstone volcanic system was an active source of volcanic and volcaniclastic material during extensional deformation in the study area. The Picabo (10-7 Ma) and Heise (6.5 – 4.3 Ma) volcanic fields were likely supplying much of the volcanic material deposited in the Miocene Starlight Formation within the study area.

4: The mapped extent of the Starlight Formation has been significantly reduced to a small basin in the southeastern corner of the study area, which may be a northern continuation of a regional basin. This is in contrast to the preliminary mapping for this area, which assigned many Quaternary surfaces to the Starlight Formation.

5: Many north-south striking normal faults were truncated by east-west striking normal faults, consistent with observations in neighboring quadrangles (Rodgers and Othberg, 1999; Riesterer et al., 2000). The tectonic and regional context of these east-west striking faults is unclear, but required a reduction in the north-south magnitude of stress.

6: As shown by stratigraphic separation diagrams, the Bear Canyon and Toponce thrusts are likely two distinct faults. The amount of lateral ramping required for these to be equivalent surfaces is unlikely within their close proximities, and would also require thrusts to cut down-section in the direction of transport.

7: The Putnam thrust sheet likely evolved as a dominantly in-sequence system, with thrusts propagating eastward and younging with depth. A minor caveat involves the development of the Toponce thrust, which evolved as an out-of-sequence imbricate within the hanging wall of the Bear Canyon thrust. The Bear Camp syncline, which defines the study area, was formed as a hanging wall syncline of the Bear Canyon and Toponce thrusts, and was later accentuated by slip on the Putnam thrust.

8. The axis of the Bear Camp syncline trends south-southeast, and plunges to the south by 3°. This is in contrast with many structures that plunge toward the ESRP as a result of downwarping due to emplacement of a mafic sill beneath the ESRP. This suggests that the study area is far enough from the ESRP and was not affected by this flexure.

This work thus documents that extension and block rotation were occurring within the Portneuf Range and surrounding region for a minimum of 4 Myr. The observed duration of extension likely represents a continuum of extension which was occurring in the region, and may reflect a period of transition when the locus of extension was migrating to the northeast (Rodgers et al., 2002). This extension heavily modified Sevier-age thrust structures in the region, necessitating restoration of extensional structures in order to understand the geometry and kinematics of Mesozoic thrusting.

The Putnam system remains an important transitional area between major thrusts to the east, and hinterland structures to the west, and furthering our understanding of the internal structure of the Putnam sheet is vital to understanding the evolution of the western Sevier belt. Major thrust structures within the Portneuf Range, to the north and south of the study area, likely represent important elements of the Putnam system. The along-strike intricacies of the Bear Canyon thrust on the western flank of the Portneuf Range allude to unrecognized structures and a more complicated development for the Bear Canyon thrust. Conducting new mapping in the vicinity of

Inman Pass and Mill Creek may provide for a revised interpretation of closely spaced overturned and upright structures, and ultimately lead to a better model for the Putnam system and the Idaho-Wyoming salient of the Sevier fold-thrust belt.

The effects of Cenozoic deformation, like Mesozoic deformation, are not completely understood. Important questions regarding the various generations of normal faults within the region remain unresolved. In particular, what is the spatial and temporal relationship between east-west striking normal faults, Basin and Range-style normal faults, and normal faults associated with Yellowstone volcanic center deformation? East-west striking normal faults are distinct from Basin and Range faults and seem to reflect a disruption of the local stress field as they accommodate north-south directed extension. Passage of the Yellowstone volcanic center and development of the ESRP may have perturbed the regional stress field such that north-south directed extension was favorable instead of east-west and northwest-southeast directed extension.

References

Almendinger, R.W., 1982, Sequence of late Cenozoic deformation in the Blackfoot Mountains, southeastern Idaho, *in* Bonnichsen, B., and Breckenridge, R.M., eds., Cenozoic Geology of Idaho: Idaho Bureau of Mines and Geology Bulletin 26, p. 505-516.

Anders, M. H., Geissman, J.W., Piety, L.A., and Sullivan, J.T., 1989, Parabolic distribution of circumeastern Snake River Plain seismicity and latest Quaternary faulting: Migratory pattern and association with the Yellowstone hotspot: Journal of Geophysical Research, v. 94, p. 1589–1621, doi:10.1029/JB094iB02p01589.

Anders, M.H., and Sleep, N.H., 1992, Magmatism and extension: The thermal and mechanical effects of the Yellowstone hotspot: Journal of Geophysical Research-Solid Earth, v. 97, p. 15379–15393, doi:10.1029/92JB01376.

Anders, M.H., 1994, Constraints on North American plate velocity from the Yellowstone hotspot deformation field: Nature, v. 369, p. 53–55, doi:10.1038/369053a0.

Anders, M.H., Rodgers, D.W., Hemming, S.R., Satlzman, J., DiVenere, V.J., Hagstrum, J.T., Embree, Embree G.F., and Walter, R.C., 2014, A fixed sublithospheric source for the late Neogene track of the Yellowstone hotspot: Implications of the Heise and Picabo volcanic fields, Journal of Geophysical Research: Solid Earth, v. 119, p. 2871-2906, doi:10.1002/2013JB010483.

Anderson, A.L., 1928, Portland cement materials near Pocatello, Idaho, Idaho Bureau of Mines and Geology Pamphlet, no. 28.

Armstrong, F.C., and Oriel, S.S., 1965, Tectonic development of Idaho-Wyoming thrust belt: Assoc. Petroleum Geologists Bull, v. 49, p. 1847–1866, doi:10.1306/A663386E-16C0-11D7-8645000102C1865D.

Armstrong, R.L., 1968, Sevier Orogenic Belt in Nevada and Utah, GSA Bulletin, v. 79, no. 4, p. 429-458, doi:10.1130/0016-7606(1968)79[429:SOBINA]2.0.CO;2.

Armstrong, R.L., 1974, Magmatism, orogenic timing, and orogenic diachronism in the Cordillera from Mexico to Canada: Nature, v. 247, p. 348–351, doi:10.1038/247348a0.

Armstrong, R. L., Leeman, W.P., and Malde, H.F., 1975, K-Ar dating, Quaternary and Neogene volcanic rocks of the Snake River Plain, Idaho: American Journal of Science, v. 275(3), p. 225–251, doi:10.2475/ajs.275.3.225

Armstrong, R.L., Taubeneck, W.H., and Hales, P.O., 1977, Rb-Sr and K-Ar geochronology of Mesozoic granitic rocks and their Sr isotopic composition, Oregon, Washington, and Idaho, GSA Bulletin, v. 88, p.397-411, doi:10.1130/0016-7606(1977)88<397:RAKGOM>2.0.CO;2.

Atwater, T., 1970, Implications of Plate Tectonics for the Cenozoic Tectonic Evolution of Western North America: GSA Bulletin, v. 81, no. 12, p. 3513–3536, doi:10.1130/0016-7606(1970)81[3513:IOPTFT]2.0.CO;2.

Beranek, L.P., Link, P.K., and Fanning C.M., Detrital zircon record of mid-Paleozoic convergent margin activity in the northern U.S. Rocky Mountains: Implications for the Antler orogeny and early evolution of the North American Cordillera: Lithosphere, v. 8, no. 5, p. 533-550, doi:10.1130/L557.1.

Bond, G.C., Christie-Blick, N., Kominz, M.A., and Devlin, W.J., 1985, An early Cambrian rift to post-rift transition in the Cordillera of western North America: Nature, v. 315, p. 742-745, doi:10.1038/315742a0.

Bowering, S.A., and Schmitz, M.D., 2003, High-Precision U-Pb Zircon Geochronology and the Stratigraphic Record: Reviews in Mineralogy and Geochemistry, v. 53, no. 1, p. 305-326, doi:10.2113/0530305.

Brennan, D.T., Pearson, D.M., Link, P.K., and Milton, J., 2023, Neoproterozoic to early Paleozoic tectono-stratigraphic framework for central Idaho: Windermere Supergroup in the northern sector of the U.S. Cordillera, *in* Whitmeyer, S.J., Williams, M.L., Kellett, D.A., and Tikoff, B., eds., Laurentia: Turning Points in the Evolution of a Continent: GSA Memoir 220, p. 457–486, doi:10.1130/2022.1220(23).

Burchfiel, B.C., and Davis, G.A., 1972, Structural Framework and Evolution of the Southern part of the Cordilleran Orogen, Western United States: American Journal of Science, v. 272, no. 2, p. 97-118, doi:10.2475/ajs.272.2.97.

Burchfiel, B.C., and Davis, G.A., 1975, Nature and Controls of Cordilleran Orogenesis, Western United States: Extensions of an Earlier Synthesis: American Journal of Science, v. 275, p. 363-396.

Burchfiel, B.C., Cowan, D.S., and Davis, G.A., 1992, Tectonic overview of the Cordilleran orogen in the western United States, *in* Burchfiel, B.C., Lipman, P.W., and Zoback, M.L., eds., the Cordilleran Orogen: Conterminous U.S.: Boulder, Colorado, Geological Society of America, The Geology of North America, v. G-3. P. 407-479, doi:10.1130/DNAG-GNA-G3.407.

Burgel, W.D., Rodgers, D.W., and Link, P.K., 1987, Mesozoic and Cenozoic structures of the Pocatello region, southeastern Idaho: Wyoming Geological Association Guidebook, The Thrust Belt Revisited; 38th Annual Field Conference Guidebook, p. 91–100.

Camilleri, P., Deibert, J., and Perkins, M., 2017, Middle Miocene to Holocene tectonics, basin evolution, and paleogeography along the southern margin of the Snake River Plain in the Knoll Mountain-Ruby-East Humboldt Range region, northeastern Nevada and south-central Idaho: Geosphere, v. 13, no. 6, p. 1901-1948, doi:10.1130/GES01318.1.

Camp V.E., Pierce, K.L., and Morgan, L.A., 2015, Yellowstone plume trigger for Basin and Range extension, and coeval emplacement of the Nevada–Columbia Basin magmatic belt: Geosphere, v. 11, no. 2, p. 203-225, doi:10.1130/GES01051.1.

Camp, V.E., and Wells, R.E., 2021, The Case for a Long-Lived and Robust Yellowstone Hotspot: GSA Today, v. 31, no. 1, p. 4-10, doi:10.1130/GSATG477A.1.

Carney, S.M., 2002, Evolution of a Miocene–Pliocene low-angle normal-fault system in the southern Bannock Range, southeast Idaho [M.S. thesis]: Logan, Utah State University, 177 p.

Carney, S.M., and Janecke, S.U., 2005, Excision and the original low dip of the Miocene-Pliocene Bannock detachment system, SE Idaho: Northern cousin of the Sevier Desert detachment?, GSA Bulletin, v. 117(3-4), p. 334–353, doi:10.1130/B25428.1.

Carr, W.J., and Trimble, D.E., 1963, Geology of the American Falls quadrangle, Idaho: U.S. Geological Survey Bulletin 1121-G, 44 p.

Cashman, P.H., and Sturmer, D.M., 2023, The Antler orogeny reconsidered and implications for late Paleozoic tectonics of western Laurentia: Geology, v. XX, no. XX, doi:10.1130/G50977.1

Christiansen, R.L., Yeats, R.S., Graham, S.A., Niem, W.A., Niem, A.R., and Snavely, P.D., Jr., 1992, Post-Laramide geology of the U.S. Cordillera region, *in* Burchfiel, B.C., Lipman, P.W., and Zoback, M.L., eds., The Cordilleran Orogen: conterminous U.S.: Boulder, Colorado, Geological Society of America, The Geology of North America, v. G-3, p. 261-406, doi:10.1130/DNAG-GNA-G3.261.

Coble, M.A., and Mahood, G.A., 2012, Initial impingement of the Yellowstone plume located by widespread silicic volcanism contemporaneous with Columbia River flood basalts: Geology, v. 40, no. 7, p. 655-658, doi:10.1130/G32692.1.

Coney, P.J., 1976, Plate tectonics and the Laramide orogeny, *in* Woodward, L.A., and Northrop, S.A., eds., Tectonics and mineral resources of southwestern North America: New Mexico Geological Society Special Publication 6, p. 5-10.

Coney, P.J., and Reynolds, S.J., 1977, Cordilleran Benioff zones: Nature, v. 270, p. 403-406.

Coney, P.J., Jones, D.L., and Monger, J.W.H., 1980, Cordilleran suspect terranes: Nature, v. 288, p. 329-333, doi:10.1038/288329a0.

Coney, P.J., and Harms, T.A., 1984, Cordilleran metamorphic core complexes: Cenozoic extensional relics of Mesozoic compression: Geology, v. 12, no. 9, p. 550-554, doi: 10.1130/0091-7613(1984)12<550:CMCCCE>2.0.CO;2.

Coney, P.J., and Evenchick, C.A., 1994, Consolidation of the American Cordilleras: Journal of South American Earth Sciences, v. 7, p. 241-262, doi:10.1016/0895-9811(94)90011-6.

Constenius, K.N., 1996, Late Paleogene extensional collapse of the Cordilleran foreland fold and thrust belt: GSA Bulletin, v. 108, no. 1, p. 20-39, doi:10.1130/0016-7606(1996)108<0020:LPECOT>2.3.CO;2.

Constenius, K., Esser, R.P., and Layer, P.W., 2003, Extensional collapse of the Charleston-Nebo salient and its relationship to space-time variations in Cordilleran orogenic belt tectonism and continental stratigraphy, *in* Raynolds, R.G., Flores, R.M., eds., Cenozoic Systems of the Rocky Mountain Region, Rocky Mountain SEPM, Denver, CO, p. 303-353.

Coogan, J.C., 1992, Structural evolution of piggyback basins in the Wyoming-Idaho-Utah thrust belt, *in* Link, P.K., Kuntz, M.A., and Platt, L.B., eds., Regional Geology of Eastern Idaho and Western Wyoming: GSA Memoir, v. 179, p. 55–80, doi:10.1130/MEM179.

Corbett, M.K., 1978, Geologic map of the northern Portneuf Range: U.S. Geological Survey Open-File Report 78-1018, scale 1:48,000.

Crane, T. C., 2000, Geologic mapping and gravity survey of the Lava Hot Springs, Idaho, 7.5 min. quadrangle: Evidence for a late Miocene supradetachment basin in Southeast Idaho [M.S. thesis]: Pocatello, Idaho State University, 147 p.

Crane, T.J., Link, P.K., and Oriel, S.S., 2000, Geologic Map of the Lava Hot Springs Quadrangle, Bannock County, Idaho: Idaho Geological Survey Technical Report 01-3, scale 1:24,000, 1 sheet.

Crittenden, M.E., Jr., F.E Schaeffer, D.E. Trimble, and L.A. Woodward, 1971, Nomenclature and correlation of some upper Precambrian and basal Cambrian sequences in western Utah and southeastern Idaho: GSA Bulletin, v. 82, no.3, p. 581-602, doi:10.1130/0016-7606(1971)82[581:NACOSU]2.0.CO;2.

Dahlstrom, C.D.A., 1970, Structural geology in the eastern margin of the Canadian Rocky Mountains: Bulletin of Canadian Petroleum Geology, v. 18, no. 3, p.332-406, doi:10.35767/gscpgbull.18.3.332.

Dawers, N.H., Anders, M.H., and Scholz, C.H., 1993, Growth of normal faults: Displacement-length scaling: Geology, v. 21, no. 12, p. 1107-1110, doi: https://doi.org/10.1130/0091-7613(1993)021<1107:GONFDL>2.3.CO;2.

DeCelles, P.G., and Mitra, G., 1995, History of the Sevier orogenic wedge in terms of critical taper models, northeast Utah and southwest Wyoming: GSA Bulletin, v. 107, no. 4, p. 454-462, doi:10.1130/0016-7606(1995)107<0454:HOTSOW>2.3.CO;2.

DeCelles, P.G., 2004, Late Jurassic to Eocene evolution of the Cordilleran thrust belt and foreland basin system, Western U.S.A.: American Journal of Science, v. 304, no. 4, p. 105–168, doi:10.2475/ajs.304.2.105.

DeCelles, P.G., and Coogan, J.C., 2006, Regional structure and kinematic history of the Sevier fold-and-thrust belt, central Utah: GSA Bulletin, v. 118, no. 7/8, p. 841-864, doi:10.1130/B25759.1.

Dehler, C.M., Fanning, M.C., Link, P.K., Kingsbury, E.M., and Rybczynski, D., 2010, Maximum depositional age and provenance of the Uinta Mountain Group and Big Cottonwood Formation, northern Utah: Paleogeography of rifting western Laurentia: GSA Bulletin, v. 122, no. 9-10, p. 1686-1699, doi:10.1130/B30094.1.

Dewey, J.F., and Bird, J.M., 1970, Mountain Belts and the New Global Tectonics: Journal of Geophysical Research, v. 75, no. 14, p. 2625-2647, doi:10.1029/JB075i014p02625.

Dickinson, W.R., and Snyder, W.S., 1978, Plate tectonics of the Laramide orogeny, *in* Matthews, V.W. Ed., Laramide Folding Associated with Block Faulting in the Western United States: GSA Memoir 151, p. 355-366, doi:10.1130/MEM151-p355.

Dickinson, W.R., 2004, Evolution of the North American Cordillera: Annual Review of Earth and Planetary Sciences, v. 32, p. 13-45, doi:10.1146/annurev.earth.32.101802.120257.

Dickinson, W.R., 2006, Geotectonic evolution of the Great Basin: Geosphere, v. 2, no. 7, p. 353-368, doi:10.1130/GES00054.

Erslev, E.A., 1993, Thrusts, back-thrusts, and detachment of Rocky Mountain foreland arches, Geological Society of America, *in* Schmidt, C. J., Chase, R. B,, and Erslev, E. A., eds., Laramide Basement Deformation in the Rocky Mountain Foreland of the Western United States: Boulder, v. 280, doi:10.1130/SPE280-p339.

Faccenna, C., Becker, T.W., Lallemand, S., Lagabrielle, Y., Funiciella, F., and Piromallo, C., 2010, Subduction-triggered magmatic pules: A new class of plumes?: Earth and Planetary Science Letters, v. 299(1-2), p. 54-68, doi:10.1016/j.epsl.2010.08.012.

Faulds, J.E., and Henry, C.D., 2008, Tectonic influences on temporal and spatial evolution of the Walker Lane: An incipient transform fault along the evolving Pacific-North American plate boundary, *in* Spencer, J.E., and Titley, S.R., eds., Ores and orogenesis: Circum Pacific tectonics, geologic evolution, and ore deposits: Arizona Geological Society Digest 22, p. 437-470.

Faure, G., and Mensing, T.M., 2005, The U-Pb, Th-Pb, and Pb-Pb Methods, in ISOTOPES Principles and Applications (third edition): John Wiley and Sons, Hoboken, p. 214-255.

Gehrels, G., 2012, Detrital zircon U-Pb geochronology: current methods and new opportunities: *in* Busby, C. and Azor, A., eds., Tectonics of Sedimentary Basins: Recent Advances (first edition), John Wiley and Sons, Ltd, p. 47-62, doi:10.1002/9781444347166.ch2.

Gentry, A., Yonkee, W.A., Wells, M.L., Balgord, E.A., 2018, Resolving the history of early fault slip and foreland basin evolution along the Wyoming salient of the Sevier fold-and-thrust belt: Integrating detrital zircon geochronology, provenance modeling, and subsidence analysis, *in* Ingersoll, R.V., Lawton, T.F., and Graham, S.A., eds., Tectonics, Sedimentary Basins, and Provenance: A Celebration of William R. Dickinson's Career: GSA Special paper 540, p. 509–545, doi:10.1130/SPE540.

Geslin, J.K., 1998, Distal ancestral Rocky Mountains tectonism: Evolution of the Pennsylvanian–Permian Oquirrh–Wood River basin, southern Idaho: GSA Bulletin, v. 110, p. 644–663, doi:10.1130 /0016-7606 (1998)110 <0644:DARMTE>2.3.CO;2.

Gibbs, A.D., 1983, Balanced cross-section construction from seismic sections in areas of extensional tectonics: Journal of Structural Geology, v. 5, no. 2, p. 153-160, doi:10.1016/0191-8141(83)90040-8.

Hamilton, W., 1969, Mesozoic California and the underflow of Pacific mantle, GSA Bulletin, v. 80, no. 12, p. 2409-2430, doi:10.1130/0016-7606(1969)80[2409:MCATUO]2.0.CO;2.

Harris, A.G., Wardlaw, B.R., Rust, C.C., and Merrill, G.K., 1980, Maps for assessing thermal maturity (conodont color alteration index maps) in Ordovician through Triassic rocks in Nevada and Utah and adjacent parts of Idaho and California: U.S. Geological Survey Miscellaneous Investigations Series, Map I-1249, scale 1:2,500,000.

Hiess, J., Condon, D.J., McLean, N., and Noble, S.R., 2012, 238U/235U Systematics in Terrestrial Uranium-Bearing Minerals: Science, v. 335, no. 6076, p. 1610-1614, doi:10.1126/science.1215507.

Hladky, F.R., 1986, Geology of an area north of the narrows of Ross Fork Canyon, northernmost Portneuf Range, Fort Hall Indian Reservation, Bannock and Bingham Counties, Idaho: Pocatello, Idaho, Idaho State University: [M.S. thesis], 110 p., 2 plates.

Housen, B.A., and Beck, M.E. Jr., 1994, Testing terrane transport: An inclusive approach to the Baja B.C. controversy: Geology, v. 27, no. 12, p. 1143-1146, doi:10.1130/0091-7613(1999)027<1143:TTTAIA>2.3.CO;2.

Humphreys, E.D., Dueker, K.G., Schutt, D.L., and Smith, R.B., 2000, Beneath Yellowstone: Evaluating plume and nonplume models using teleseismic images of the upper mantle: GSA Today, v. 10, no. 12, p. 1-6.

Irving, E., Wynne, P.J., Thorkelson, D.J., and Schiarizza, P., 1996, Large (1000 to 4000 km) northward movements of tectonic domains in the northern Cordillera, 83 to 45 Ma: Journal of Geophysical Research–Solid Earth, v. 101, p. 17901–17916, doi:10.1029/96JB01181.

Isakson, V.H., Schmitz, M.D., Dehler, C.M., Macdonald, F.A., and Yonkee, W.A, 2022, A robust age model for the Cryogenian Pocatello Formation of southeastern Idaho (northwestern USA) from tandem in situ and isotope dilution U-Pb dating of volcanic tuffs and epiclastic detrital zircons: Geosphere, v. 18, no. 2, p. 825-849, doi:10.1130/GES02437.1.

Jaffey, A.H., Flynn, K.F., Glendenin, L.E., Bentley, W.C., and Essling, A.M., 1971, Precision measurement of half-lives and specific activities of ^{235}U and ^{238}U: Physical Review, v. 4, no. 5, p. 1889-1906, doi:10.1103/PhysRevC.4.1889.

Jones, D.L., Silberling, N.J., and Hillhouse, J., 1977, Wrangellia – A displaced terrane in northwestern North America: Canadian Journal of Earth Sciences, v. 14, no. 11, doi:10.1139/e77-222.

Kellogg, K.S., Marvin, R. F., 1988, New potassium-argon ages, geochemistry, and tectonic setting of upper Cenozoic volcanic rocks near Blackfoot, Idaho, United States Geological Survey, no. 1806, doi:10.3133/b1806.

Kellogg, K.S., Oriel, S.S., Amerman, R.E., Link, P.K., and Hladky, F.R., 1989, Geologic map of the Jeff Cabin Creek quadrangle, Bannock and Caribou counties, Idaho, United States Geological Survey, GQ-1669, scale 1:24,000.

Kellogg, K.S., 1990, Geologic map of the south Putnam Mountain quadrangle, Bannock and Caribou counties, Idaho, United States Geological Survey, GQ-1665, scale 1:24,000.

Kellogg, K.S., 1992, Cretaceous thrusting and Neogene block rotation in the northern Portneuf Range region, southeastern Idaho, *in* Link, P.K., Kuntz, M., and Platt, L.B., eds., Geology of southeastern Idaho: GSA Memoir, v. 179, p. 95–113, doi:10.1130/MEM179-p95.

Kellogg, K.S., Rodgers D.W., Hladky F.R., Kiessling M.A., and Riesterer J.W., 1999, The Putnam Thrust Plate, Idaho – Dismemberment and Tilting by Tertiary Normal Faults, *in* Hughes, S.S., and Thackray, G.D., eds., Guidebook to the Geology of Eastern Idaho: Pocatello, Idaho Museum of Natural History, p. 97-114.

Konstantinou, A., Strickland, A., Miller, E.L., and Wooden, J.P., 2012, Multistage Cenozoic extension of the Albion-Raft River-Grouse Creek metamorphic core complex: Geochronologic and stratigraphic constraints: Geosphere, v. 8, no. 6, p. 1429-1466, doi:10.1130/GES00778.1.

Lewis G.C., and Fosberg, M.A., 1982, Distribution and Character of Loess and Loess Soils in Southeastern Idaho, *in* Bonnichsen, B., and Breckenridge, R.M., eds., Cenozoic Geology of Idaho: Idaho Bureau of Mines and Geology Bulletin 26, p. 705-716.

Licciardi, J.M., and Pierce, K.L., 2018, History and dynamics of the Greater Yellowstone Glacial System during the last two glaciations: Quaternary Science Reviews, v. 200, doi:10.1016/j.quascirev.2018.08.027.

Link, P.K., Jansen, S.T., Halimdihardja, P., Lande, A., Zahn, P., 1987, Stratigraphy of the Brigham Group (Late Proterozoic-Cambrian), Bannock, Portneuf, and Bear River Ranges, southeastern Idaho, *in* Miller, W.R., ed., The thrust belt revisited: Wyoming Geological Association, 38th Field Conference, Guidebook, p. 133-148.

Link, P.K., Warren, I., Preacher, J., and Skipp, B., 1996, Stratigraphic analysis and interpretation of the Mississippian Copper Basin Group, McGowan Creek Formation, and White Knob Limestone, south-central Idaho, in M. W, Longman and M. D. Sonnenfeld, eds., Paleozoic Systems of the Rocky Mountain Region: Society for Sedimentary Geology Special Publication, p. 117–144.

Link, P.K., and Stanford, L.R., 1999, Geologic map compilation of the Pocatello 30 x 60-minute quadrangle, Idaho: Idaho Geological Survey Technical Report 99-2, scale 1:100,000.

Link, P.K., Todt, M.K., Pearson, D.M., and Thomas, R.C., 2017, 500-490 Ma detrital zircons in Upper Cambrian Worm Creek and correlative sandstones, Idaho, Montana, and Wyoming: Magmatism and tectonism within the passive margin: Lithosphere, v. 9, no. 6, p. 910-926, doi:10.1130/L671.1.

Lipman, P. W., Prostka, H. J., and Christiansen, R. L., 1971, Evolving subduction zones in the western United States, as interpreted from igneous rocks: Science, v. 174, no. 4011, p. 821-825, doi:10.1126/science.174.4011.8.

Livaccari, R.F., Burke, K., and Şengör, A.M.C., 1981, Was the Laramide orogeny related to subduction of an oceanic plateau?: Nature, v. 289, p. 276-278, doi:10.1038/289276a0.

Livaccari, R.F., 1991, Role of crustal thickening and extensional collapse in the tectonic evolution of the Sevier-Laramide orogeny, western United States: Geology, v. 19, no. 11, p. 1104-1107, doi:10.1130/0091-7613(1991)019<1104:ROCTAE>2.3.CO;2.

Long, S.P., 2004, Geology of the Henderson Creek Quadrangle, Oneida County, Idaho: Multiple Phases of Tertiary Extension and Deposition, [M.S. thesis]: Idaho State University, 158 p.

Long, S.P., Link, P.K., Janecke, S.U., Perkins, M.E., and Fanning, C.M., 2006, Multiple phases of Tertiary extension and synextensional deposition of the Miocene-Pliocene Salt Lake Formation in an evolving supradetachment basin, Malad Range, southeast Idaho, U.S.A.: Rocky Mountain Geology, v. 41, no. 1, p. 1-27, doi:10.2113/gsrocky.41.1.1.

Long, S.P., 2012, Magnitudes and spatial patterns of erosional exhumation in the Sevier hinterland, eastern Nevada and western Utah, USA: Insights from a Paleogene paleogeologic map: Geosphere, v. 8, no. 4, p. 881-901, doi:10.1130/GES00783.

Long, S.P., Thomson, S.N., Reiners, P.W., and Di Fiori, R.V., 2015, Synorogenic extension localized by upper-crustal thickening: An example from the Late Cretaceous Nevadaplano: Geology, v. 43, no. 4, p. 351-354, doi:10.1130/G36431.1.

Mansfield, G.R., 1920, Geography, geology, and mineral resources of the Fort Hall Indian Reservation, Idaho: U.S. Geological Survey Bulletin, v. 713, p. 152, doi:10.3133/b713.

Mattinson, J.M., 2005, Zircon U/Pb chemical abrasion (CA-TIMS) method; combined annealing and multi-step partial dissolution analysis for im- proved precision and accuracy of zircon ages: Chemical Geology, v. 220, p. 47-66, doi:10.1016/j.chemgeo.2005.03.011.

McClelland, W.C., Tikoff, B., and Manduca, C.A., 2000, Two-phase evolution of accretionary margins: examples from the North American Cordillera: Tectonophysics, v. 326, p. 37-55, doi:10.1016/S0040-1951(00)00145-1.

McDougall, I., Harrison, T.M., 1999, Geochronology and thermochronology by the $^{40}Ar/^{39}Ar$ method: New York, Oxford University Press, p. 269.

McKee, E. D., 1951, Sedimentary basins of Arizona and adjoining areas: GSA Bulletin, v. 62, no. 5, p. 481-506, doi:10.1130/0016-7606(1951)62[481:SBOAAA]2.0.CO;2.

McMechan, R.D. and Price, R.A., 1980, Reappraisal of a reported unconformity in the Paleogene (Oligocene) Kishenehn Formation: Implications for Cenozoic tectonics in the Flathead Valley graben, southeastern British Columbia: Bulletin of Canadian Petroleum Geology, v. 28, no. 1, p. 37-45, doi:10.35767/gscpgbull.28.1.037.

McQuarrie, N., and Rodgers, D.W., 1998, Subsidence of a volcanic basin by flexure and lower crustal flow: The eastern Snake River Plain, Idaho: Tectonics, v. 17, no. 2, p. 203-220, doi:10.1029/97TC03762.

McQuarrie, N., and Wernicke, B.P., 2005, An animated tectonic reconstruction of southwestern North America since 36 Ma: Geosphere, v. 1, no. 3, p. 147-172, doi:10.1130/GES00016.1.

McQuarrie, N., and Oskin, M., 2010, Palinspastic restoration of NAVDat and implications for the origin of magmatism in southwestern North America: Journal of Geophysical research, v. 115, doi:10.1029/2009JB006435.

Miller, E.L., Miller, M.M., Stevens, C.H., Wright, J.E., and. Madrid, R., 1992, Late Paleozoic paleogeographic and tectonic evolution of the western U.S. Cordillera, *in* Burchfield, B.C., Lipman, P.W., and Zoback, M.L., eds. The Cordilleran Orogen: Conterminous U.S.: Boulder Colorado, Geological Society of America, The Geological Society of America, v. G-3, p. 57-106, doi:10.1130/DNAG-GNA-G3.57.

Mitra, S., 1990, Fault-propagation folds: Geometry, kinematic evolution, and hydrocarbon traps: 474 American Association of Petroleum Geologists Bulletin, v. 74, no.6, p. 921–945, doi:10.1306/0C9B23CB-1710-11D7-8645000102C1865D.

Monger, J.W.H., Price, R.A., and Tempelman-Kluit, D.J., 1982, Tectonic accretion and the origin of the two major metamorphic and plutonic welts in the Canadian Cordillera: Geology, v. 10, no. 2, p. 70-75, doi:10.1130/0091-7613(1982)10<70:TAATOO>2.0.CO;2.

Nelson, P.L., and Grand, S.P., 2018, Lower-mantle plume beneath the Yellowstone hotspot revealed by core waves: Nature Geoscience, v. 11, p. 280-284, doi:10.1038/s41561-018-0075-y.

Oaks, R.J.,Jr., James, W.C., Francis. G.G., and Schulingkamp, W.J., II, 1977, Summary of middle Ordovician stratigraphy and tectonics, northern Utah, southern and central, Idaho, *in* Heisey, E.L., Lawson, D.E., Norwood, E.R., Wach, P.H., and Hale, L.A., eds., Rocky Mountain Thrust Belt Geology and Resources: Wyoming Geological Association, 29th Annual Field Conference, Guidebook, p. 101-118.

Oriel, S.S., and Armstrong, F.C., 1971, Uppermost Precambrian and lowest Cambrian rocks in Southeastern Idaho: U.S. Geological Survey Open-File Report 394, 57 p., doi:10.3133/pp394.

Oriel, S.S., and Platt, L.B., 1980, Geologic map of the Preston 1°x 2° quadrangle, southeastern Idaho and western Wyoming: U.S. Geological Survey, I-1127, scale: 1:250,000.

Pană, D.I., and van der Pluijm, B., 2015, Orogenic pulses in the Alberta Rocky Mountains: Radiometric dating of major faults and comparison with the regional tectono-stratigraphic record: GSA Bulletin, v. 127, no. 3/4, p. 480-502, doi:10.1130/B31069.1.

Paull, R.A., Wolbrink, M.A., Volkmann, R.G., and Grover, R.L., 1972, Stratigraphy of Copper Basin Group, Pioneer Mountains, South-Central Idaho: The American Association of Petroleum Geologists Bulletin, v. 56, no. 8, p. 1370-1401, doi:10.1306/819A40EC-16C5-11D7-8645000102C1865D.

Peacock, D.C.P., 2002, Propagation, interaction and linkage in normal fault systems: Earth Science Reviews, v. 58, p. 121-142, doi:10.1016/S0012-8252(01)00085-X.

Pierce, K.L., and Morgan, L.A., 1992, The track of the Yellowstone hot spot: Volcanism, faulting, and uplift, *in* Link, P.K., Kuntz, M.A., and Platt, L.B., Regional Geology of Eastern Idaho and Western Wyoming: GSA Memoir 179, doi:10.3133/ofr90415.

Pierce, K.L., and Morgan, L.A., 2009, Is the track of the Yellowstone hotspot driven by a deep mantle plume? — Review of volcanism, faulting, and uplift in light of new data: Journal of Volcanology and Geothermal Research, vol. 188, doi:10.1016/j.jvolgeores.2009.07.009.

Pogue, K.R., 1984, The geology of the Mt. Putnam area, northern Portneuf range, Bannock and Caribou counties, Idaho [M.S. thesis]: Idaho State University p. 111.

Proffett, J.M., 1977, Cenozoic geology of the Yerington district, Nevada, and implications for the nature and origin of Basin and Range faulting: GSA Bulletin, v. 88, p. 247–266, doi:10.1130/0016-7606(1977)88<247:CGOTYD>2.0.CO;2.

Puetz, S.J., Spencer, C.J., and Ganade, C.E., 2021, Analyses from a validated global U-Pb detrital zircon database: Enhanced methods for filtering discordant U-Pb zircon analyses and optimizing crystallization age estimates: Earth Science Reviews, v. 220, doi:10.1016/j.earscirev.2021.103745.

Reiners, P.W., Ehlers, T.A., and Zeitler, P.K., 2005, Past Present, and Future of Thermochronology: Reviews in Mineralogy and Geochemistry, v. 58, doi:10.2138/rmg.2005.58.1.

Riesterer, J.W., Link, P.K., and Rodgers, D.W., 2000, Geologic map of the Bonneville Peak quadrangle, Bannock and Caribou counties, Idaho: Idaho Geological Survey, technical report 00-3, scale 1:24,000.

Rivera, T.A., Schmitz, M.D., Jicha, B.R., and Crowley, J.L., 2016, Zircon Petrochronology and $^{40}Ar/^{39}Ar$ Sanidine Dates for the Mesa falls Tuff: Crystal-scale Records of Magmatic Evolution and the Short Lifespan of a Large Yellowstone Magma Chamber: Journal of Petrology, v. 57, no. 9, p. 1677-1704, doi:10.1093/petrology/egw053.

Rodgers, D.W., and Janecke, S.U., 1992, Tertiary paleogeographic maps of the western Idaho-Wyoming-Montana thrust belt, *in* Link, P.K., Kuntz, M., and Platt, L.B., eds., Regional Geology of Eastern Idaho and Western Wyoming: GSA Memoir 179, p. 83–94, doi:10.1130/MEM179-P83.

Rodgers, D.W., and Othberg, K.L., 1999, Geologic map of the Pocatello South quadrangle, Bannock and Power counties, Idaho: Idaho Geological Survey, GQ-1665, scale 1:24,000.

Rodgers, D.W., Ore, H.T., Bobo, R.T., McQuarrie, N., and Zentner, N., 2002, Extension and subsidence of the Eastern Snake River Plain, Idaho, *in* Bonnichsen, B., White, C.M., McCurry, M., eds., Tectonic and Magmatic Evolution of the Snake River Plain Volcanic Province: Idaho Geological Survey Bulletin 30, p. 121-155.

Rodgers, D.W., Long, S.P., McQuarrie N., Burgel, W.D., and Hersley, C.F., 2006, Geologic map of the Inkom quadrangle, Bannock county, Idaho: Idaho Geological Survey, technical report 06-2, scale 1:24,000, 2 sheets.

Rodgers, D.W., and Long, S.P., 2012, Creation and collapse of the northern Cache-Pocatello culmination, southeastern Idaho: Eos Trans., American Geophysical Union 92 (56), Fall Meet. Suppl., Abstract T11B-2313.

Royse, Frank, Jr., Warner, M.A., and Reese, D.L., 1975, Thrust belt structural geometry and related stratigraphic problems, Wyoming-Idaho-northern Utah, *in* Bolyard, D.W., ed., Deep drilling frontiers of the central Rocky Mountains: Denver, Colorado, Rocky Mountain Association of Geologists Symposium, p. 41–54.

Saleeby, J., 2003, Segmentation of the Laramide Slab – evidence from the southern Sierra Nevada region: GSA Bulletin, v. 115, no. 6, p. 655-668, doi:10.1130/0016-7606(2003)115<0655:SOTLSF>2.0.CO;2.

Schmitz, M.D., and Schoene, B., 2007, Derivation of isotope ratios, errors, and error calculations for U-Pb geochronology using ^{205}Pb-^{235}U-(^{233}U)-spiked isotope dilution thermal ionization mass spectrometric data: Geochemistry, Geophysics, Geosystems, v. 8, no. 8, doi:10.1029/2006GC001492.

Schmitz, M.D., and Kuiper, K.F., 2013, High-Precision Geochronology: Elements, v. 9, no. 1, p. 25-30, doi:10.2113/gselements.9.1.25.

Schusler, K.L., McCurry, M., Anders, M.H., Pearson, D.M., and Bartholomay, R.C., 2020, Regionally continuous Miocene rhyolites beneath the eastern Snake River Plain reveal localized flexure at its western margin: Idaho National Laboratory and vicinity, The Mountain Geologist, v. 57, no. 3, p. 241-270, doi:10.31582/rmag.mg.57.3.241.

Schwartz, J.J., Johnson, K., Mueller, P., Valey, J., Strickland, A., and Wooden, J.L., 2014, Time scales and processes of Cordilleran batholith construction and high-Sr/Y magmatic pulses: Evidence from the Bald Mountain Batholith, northeastern Oregon: Geosphere, v. 10, no. 6, p. 1456-1481, doi:10.1130/GES01033.1.

Shervais, J.W., and Hanan B.B., 2008, Lithosphere topography, tilted plumes, and the track of the Snake River-Yellowstone hot spot: Tectonics, v. 27, doi:10.1029/2007TC002181.

Skipp, B., Sando, W.J., and Hall, W.E., 1979, The Mississippian and Pennsylvanian (Carboniferous) Systems in the United States – Idaho: U.S. Geological Survey Professional Paper, doi:10.3133/pp1110AL.

Sloss, L.L., 1963, Sequences in the Cratonic Interior of North America: GSA Bulletin, v. 74, no. 2, p. 93-114, doi:10.1130/0016-7606(1963)74[93:SITCIO]2.0.CO;2.

Smith, R.B., Richins, W.D., and Doser, D.I., 1985, The 1983 Borah Peak earthquake: Regional seismicity, kinematics of faultings, and tectonic mechanism, *in* Stein, R.S., and Bucknam, R.C., eds., Proceedings of Workshop XXVIII on the Borah Peak, Idaho, Earthquake: U.S. Geological Survey Open-File Report 85-290, v. A, p. 236-263.

Smith, L.H., Kaufman, A.J., Knoll, A.H., and Link, P.K., 1994, Chemostratigraphy of predominantly siliciclastic Neoproterozoic successions: a case study of the Pocatello Formation and lower Brigham Group, Idaho, USA: Geological Magazine, v. 131, no. 3, p. 301–314, doi:10.1017/s0016756800011079.

Sparlin, M.A., Braile, L.W., and Smith, R.B., 1982, Crustal structure of the eastern Snake River Plain determined from ray trace modeling of seismic refraction data: Journal of Geophysical Research, v. 87, no. B4, p. 2619-2633, doi:10.1029/JB087iB04p02619.

Speed, R.C., and Sleep, N.H., 1982, Antler orogeny and foreland basin: A model: GSA Bulletin, v. 93, no. 9, p.815-828, doi:10.1130/0016-7606(1982)93<815:AOAFBA>2.0.CO;2.

Steely, A.N., Janecke, S.U., Long, S.P., Carney, S.M., Oaks Jr., R.Q., Langenheim, V.E., and Link, P.K., 2005, Evolution of a late Cenozoic supradetachment basin above a flat-on-flat detachment with a folded lateral ramp, SE Idaho, *in* Pederson, J., and Dehler, C.M., eds., Interior Western United States: GSA Field Guide 6, p. 169–198, doi:10.1130/2005.fld006(08).

Stewart, J.H., 1972, Initial deposits in the Cordilleran geosyncline--evidence of late Precambrian 850 m.y., continental separation: GSA Bulletin, v. 83, no. 5, p. 1345-1360, doi:10.1130/0016-7606(1972)83[1345:IDITCG]2.0.CO;2.

Stewart, J.H., and Poole, F.G., 1974, Lower Paleozoic and uppermost Precambrian Cordilleran miogeocline, Great Basin, western United States, *in* Dickinson, W.R., ed., Tectonics and Sedimentation, v. 22, doi:10.2110/pec.74.22.0028.

Stockli, D.F., Dumitru, T.A., Mcwilliams, M., and Farley K.A., 2003, Cenozoic tectonic evolution of the White Mountains, California and Nevada: GSA Bulletin, v. 115, no. 7, p. 788-816, doi:10.1130/0016-7606(2003)115<0788:CTEOTW>2.0.CO;2.

Suppe, J., 1983, Geometry and kinematics of fault-bend folding: American Journal of Science, v. 283, p. 684–721, doi:10.2475/ajs.283.7.684.

Suppe, J., and Medwedeff, D.A., 1984, Fault-propagation folding: Geological Society of America Abstracts with Programs, v. 16, p. 670.

Suppe, J., and Medwedeff, D.A., 1990, Geometry and kinematics of fault-propagation folding: Eclogae 490 Geologicae Helvetiae, v. 454, p. 409–454, doi:10.5169/seals-166595.

Tera, F., and Wasserburg, G.J., 1975, Precise Isotopoc Analysis of Lead in Picomole and Subpicomole Quantities: Analytical Chemistry, v. 47, no. 13, p. 2214-2220, doi:10.1021/ac60363a036.

Thackray, G.D., Rodgers, D.W., and Drabick, A., 2011, Neogene drainage development of Marsh and Portneuf valleys, eastern Idaho, *in* Lee, J., and Evans, J.P., eds., Geologic Field Trips to the Basin and Range, Rocky Mountains, Snake River Plain, and Terranes of the U.S. Cordillera: GSA Field Guide 21, p. 89-101, doi:10.1130/2011.0021(04).

Tikoff, B., Benford, B., and Giorgis, S., 2008, Lithospheric Control on the Initiation of the Yellowstone Hotspot: Chronic Reactivation of Lithospheric Scars: International Geology Review, v. 50, no. 3, p. 305-324, doi:10.2747/0020-6814.50.3.305.

Trimble, D.E., 1976, Geology of the Michaud and Pocatello quadrangles, Bannock and Power counties, Idaho: United States Geological Survey Bulletin 1400, 88 p., doi:10.3133/b1400.

Trimble, D.E., 1982, Geologic map of the Yandel Springs quadrangle, Bannock and Bingham Counties, Idaho: United States Geological Survey Geologic Quadrangle Map, GQ-1553, scale 1:48:000.

Trimble, D.E., and W.J. Carr, 1976, Geology of the Rockland and Arbon quadrangles, Power County, Idaho: United States Geological Survey Bulletin 1399, 115 p., doi:10.3133/b1399.

Tucker, R.D., Krogh, T.E., Ross, R.J., and Williams, S.H., 1990, Time-scale calibration by high-precision U-Pb zircon dating of interstratified volcanic ashes in the Ordovician and Lower Silurian stratotypes of Britain: Earth and Planetary Science Letters, v. 100, p. 51-58, doi:10.1016/0012-821X(90)90175-W.

Walcott, C.D., 1908, Cambrian geology and paleontology, I; No. 1, Nomenclature of some Cambrian Cordilleran formations: Smithsonian Miscellaneous Collections, v. 53, no. 1804.

Wells, M.L., 2016, A major mid-Cretaceous shortening event in the southern Sevier orogenic belt: Continental record of global plate reorganization?: Geological Society of America Abstracts with Programs, v. 48, no. 7, p. 143-11, doi:10.1130/abs/2016AM-287809.

Wetherill, G.W., 1956, Discordant Uranium-Lead Ages, I: EOS Transactions, American Geophysical Union, v. 37, no. 3, p. 320-326, doi:10.1029/TR037i003p00320.

Wilkerson, M.S., Apotria, T., and Farid, T., 2002, Interpreting the geologic map expression of contractional fault-related fold terminations: lateral/oblique ramps versus displacement gradients: Journal of Structural Geology, v. 24, p. 593-607, doi:10.1016/S0191-8141(01)00111-0.

Wilson, E., Preacher, J.M., and Link, P.K., 1994, New constraints on the nature of the Early Mississippian sedimentary basin in Idaho, *in* Embry, A.F., et al., eds., Pangaea: Global environments and resources: Canadian Society of Petroleum Geologists Memoir 17, p. 155–174.

Wiltschko, D.V., and Dorr, J.A. Jr., 1983, Timing of Deformation in Overthrust Belt and Foreland of Idaho, Wyoming, and Utah: American Association of Petroleum Geologists Bulletin, v. 67, no. 8, p. 1304-1322, doi:10.1306/03B5B740-16D1-11D7-8645000102C1865D.

Woodward, N.B., 1987, Stratigraphic Separation Diagrams and Thrust Belt Structural Analysis: Wyoming Geological Association Guidebook, The Thrust Belt Revisited; 38th Annual Field Conference Guidebook, p. 69-77.

Wotzlaw, J.F., Binderman, I.N., Watts, K.E., Schmitt, A.K., Caricchi, L., and Schaltegger, U., 2014, Linking rapid magma reservoir assembly and eruption trigger mechanisms at evolved Yellowstone-type supervolcanoes: Geology, v. 42, no. 9, p. 807-810, doi:10.1130/G35979.1.

Yonkee, A.W., 1992, Basement-cover relations, Sevier orogenic belt, northern Utah: GSA Bulletin, v. 104, no.3, p. 280-302.

Yonkee, A.W., and Weil, A.B., 2015, Tectonic evolution of the Sevier and Laramide belts within the North American Cordilleran orogenic system: Earth-Science Reviews 150, v. 150, p. 531–593, doi:10.1016/j.earscirev.2015.08.001.

Yonkee, A.W., Dehler, C.D., Link, P.K., Balgord, E.A., Keeley, J.A., Hayes, D.S., Wells, M.L., Fanning, C.M., and Johnston S.M., 2014, Tectono-stratigraphic framework of Neoproterozoic to Cambrian strata, west-central U.S.: Protracted rifting, glaciation, and evolution of the North American Cordilleran margin: Earth-Science Reviews, v. 136, p. 59–95, doi:10.1016/j.earscirev.2014.05.004.

Yonkee, A.W., Eleogram, B., Wells, M.L., Stockli, D.F., Kelley, S., Barber, D.E., 2019, Fault Slip and Exhumation History of the Willard Thrust Sheet, Sevier Fold-Thrust Belt, Utah: Relations to Wedge Propagation, Hinterland Uplift, and Foreland Basin Sedimentation: Tectonics, v. 38, no. 8, doi:10.1029/2018TC005444.

Zentner, N.C., 1989, Neogene normal faults related to the structural origin of the eastern Snake River Plain, Idaho [M.S. thesis]: Idaho State University, 47 p.

Appendix A: LA-ICP-MS U-Pb Composition and Isotopic Ratios

Table S2. U-Pb isotope ratios and trace element concentrations by LA-ICPMS: sample data

				Composition								Corrected isotope ratios						
	U	Th	Pb		206Pb	206Pb		208Pb	±2s	207Pb	±2s	206Pb	±2s	error	238U	±2s	207Pb	±2s
Analysis	ppm	ppm	ppm	Th/U	cps	204Pb	±1s	232Th	(%)	235U	(%)	238U	(%)	corr.	206Pb	(%)	206Pb	(%)
BCG-1	**42.802426**	**112.012557**																
BCG-1_S_111	~~120~~	~~48.7~~	~~0.199~~	~~0.407~~	~~157~~	~~14~~	~~2~~	~~0.00185~~	~~51.5771965~~	~~0.0338~~	~~54.3~~	~~0.00068~~	~~25.9~~	~~0.47696222~~	~~1480.38~~	~~25.9~~	~~0.36275~~	~~47.8~~
BCG-1_S_107	244	151	0.263	0.619	368	848	44	0.00039	39.468066	0.0068	44.2	0.00080	11.1	0.24969878	1251.13	11.1	0.06131	42.8
BCG-1_L_5	~~199~~	~~112~~	~~0.218~~	~~0.564~~	~~297~~	~~7~~	~~0~~	~~0.00041~~	~~42.3943233~~	~~0.0096~~	~~45.3~~	~~0.00080~~	~~12.4~~	~~0.27290926~~	~~1248.86~~	~~12.4~~	~~0.08718~~	~~43.6~~
BCG-1_S_127	262	150	0.285	0.573	394	569	20	0.00041	31.9382259	0.0063	34.8	0.00082	7.9	0.22557623	1213.49	7.9	0.05520	33.9
BCG-1_L_12	264	205	0.320	0.776	411	8	0	0.00045	40.8015057	0.0043	71.6	0.00084	11.7	0.16314012	1193.70	11.7	0.03730	70.6
BCG-1_L_6	~~283~~	~~171~~	~~0.361~~	~~0.605~~	~~440~~	~~18~~	~~1~~	~~0.00060~~	~~33.0669458~~	~~0.0100~~	~~27.9~~	~~0.00085~~	~~7.2~~	~~0.25711377~~	~~1176.41~~	~~7.2~~	~~0.08559~~	~~27.0~~
BCG-1_L_4	~~195~~	~~107~~	~~0.236~~	~~0.550~~	~~281~~	~~11~~	~~1~~	~~0.00050~~	~~48.2910095~~	~~0.0127~~	~~48.0~~	~~0.00085~~	~~14.2~~	~~0.29556775~~	~~1173.78~~	~~14.2~~	~~0.10777~~	~~45.8~~
BCG-1_S_133	273	162	0.321	0.594	402	55	3	0.00050	26.9230751	0.0058	53.4	0.00086	10.7	0.20074359	1165.45	10.7	0.04903	52.3
BCG-1_S_110	299	183	0.325	0.614	458	72	4	0.00031	38.151516	0.0063	36.0	0.00086	11.5	0.31832147	1158.77	11.5	0.05314	34.1
BCG-1_S_149	~~270~~	~~167~~	~~0.309~~	~~0.616~~	~~401~~	~~28~~	~~2~~	~~0.00034~~	~~28.3228053~~	~~0.0114~~	~~32.0~~	~~0.00087~~	~~10.2~~	~~0.31772677~~	~~1151.26~~	~~10.2~~	~~0.09510~~	~~30.3~~
BCG-1_S_134	350	236	0.414	0.674	561	39	2	0.00042	39.1078693	0.0067	31.5	0.00087	10.6	0.33642783	1149.41	10.6	0.05563	29.6
BCG-1_S_129	~~295~~	~~159~~	~~0.350~~	~~0.539~~	~~442~~	~~16~~	~~1~~	~~0.00050~~	~~30.8255189~~	~~0.0088~~	~~28.0~~	~~0.00087~~	~~13.0~~	~~0.46256451~~	~~1148.05~~	~~13.0~~	~~0.07299~~	~~24.8~~
BCG-1_S_125	285	163	0.327	0.571	417	417	23	0.00048	37.1442302	0.0025	64.2	0.00087	9.9	0.15381274	1143.70	9.9	0.02093	63.5
BCG-1_L_17	~~296~~	~~160~~	~~0.366~~	~~0.540~~	~~448~~	~~11~~	~~1~~	~~0.00054~~	~~33.1211423~~	~~0.0102~~	~~33.7~~	~~0.00088~~	~~12.1~~	~~0.35955258~~	~~1136.87~~	~~12.1~~	~~0.08429~~	~~31.5~~
BCG-1_S_101	562	379	0.630	0.673	903	23	1	0.00029	35.0897893	0.0069	23.4	0.00089	5.5	0.23232762	1129.32	5.5	0.05637	22.7
BCG-1_M_62	228	107	0.276	0.472	398	28	1	0.00061	31.8487194	0.0063	42.2	0.00089	8.6	0.20453563	1126.54	8.6	0.05154	41.3
BCG-1_L_11	~~253~~	~~116~~	~~0.322~~	~~0.459~~	~~392~~	~~16~~	~~1~~	~~0.00062~~	~~36.969218~~	~~0.0148~~	~~26.0~~	~~0.00089~~	~~14.3~~	~~0.54910469~~	~~1122.23~~	~~14.3~~	~~0.12044~~	~~21.7~~
BCG-1_L_3	~~234~~	~~118~~	~~0.272~~	~~0.503~~	~~378~~	~~378~~	~~32~~	~~0.00039~~	~~32.1790584~~	~~0.0103~~	~~42.7~~	~~0.00090~~	~~16.1~~	~~0.37635022~~	~~1110.83~~	~~16.1~~	~~0.08312~~	~~39.6~~
BCG-1_L_13	~~226~~	~~118~~	~~0.272~~	~~0.521~~	~~349~~	~~17~~	~~1~~	~~0.00049~~	~~38.6588641~~	~~0.0080~~	~~25.7~~	~~0.00090~~	~~8.9~~	~~0.34446046~~	~~1108.32~~	~~8.9~~	~~0.06411~~	~~24.1~~
BCG-1_L_8	~~251~~	~~132~~	~~0.310~~	~~0.525~~	~~406~~	~~29~~	~~2~~	~~0.00046~~	~~28.7451418~~	~~0.0136~~	~~35.1~~	~~0.00091~~	~~14.5~~	~~0.41406248~~	~~1101.54~~	~~14.5~~	~~0.10835~~	~~31.9~~
BCG-1_L_2	~~164~~	~~73.6~~	~~0.218~~	~~0.450~~	~~276~~	~~10~~	~~1~~	~~0.00073~~	~~73.1756292~~	~~0.0136~~	~~61.5~~	~~0.00091~~	~~14.9~~	~~0.24156881~~	~~1093.58~~	~~14.9~~	~~0.10796~~	~~59.7~~
BCG-1_S_140	311	181	0.352	0.584	479	479	30	0.00031	42.6871785	0.0080	39.0	0.00092	13.1	0.33476995	1092.45	13.1	0.06317	36.8
BCG-1_S_105	~~459~~	~~294~~	~~0.567~~	~~0.639~~	~~771~~	~~565~~	~~26~~	~~0.00038~~	~~24.969942~~	~~0.0120~~	~~18.1~~	~~0.00092~~	~~9.7~~	~~0.5354284~~	~~1092.44~~	~~9.7~~	~~0.09507~~	~~15.2~~
BCG-1_L_9	231	123	0.317	0.534	395	87	6	0.00082	32.1553617	0.0038	42.5	0.00092	11.3	0.26507999	1092.29	11.3	0.02982	40.9
BCG-1_M_49	270	136	0.316	0.505	438	107	6	0.00039	33.1651037	0.0087	41.9	0.00092	14.2	0.33907113	1090.29	14.2	0.06896	39.4
BCG-1_S_116	287	207	0.359	0.723	451	451	26	0.00041	24.1502054	0.0079	62.0	0.00092	10.4	0.16771954	1090.09	10.4	0.06278	61.1
BCG-1_M_57	~~163~~	~~106~~	~~0.239~~	~~0.652~~	~~284~~	~~31~~	~~2~~	~~0.00074~~	~~41.9146611~~	~~0.0111~~	~~58.7~~	~~0.00092~~	~~14.5~~	~~0.24681269~~	~~1088.67~~	~~14.5~~	~~0.08763~~	~~56.9~~
BCG-1_S_132	~~364~~	~~201~~	~~0.435~~	~~0.553~~	~~570~~	~~179~~	~~11~~	~~0.00041~~	~~31.5956255~~	~~0.0097~~	~~32.7~~	~~0.00092~~	~~11.6~~	~~0.35389338~~	~~1087.68~~	~~11.6~~	~~0.07618~~	~~30.6~~
BCG-1_M_41	~~145~~	~~73.4~~	~~0.235~~	~~0.506~~	~~239~~	~~10~~	~~1~~	~~0.00097~~	~~40.247561~~	~~0.0302~~	~~30.9~~	~~0.00092~~	~~11.8~~	~~0.38114438~~	~~1085.65~~	~~11.8~~	~~0.23766~~	~~28.6~~
BCG-1_S_102	~~239~~	~~135~~	~~0.294~~	~~0.566~~	~~395~~	~~15~~	~~1~~	~~0.00038~~	~~39.1848425~~	~~0.0143~~	~~33.0~~	~~0.00092~~	~~8.4~~	~~0.25241755~~	~~1084.47~~	~~8.4~~	~~0.11223~~	~~32.0~~
BCG-1_S_146	317	258	0.391	0.816	475	13	1	0.00033	39.0418176	0.0083	31.0	0.00092	14.9	0.47933763	1081.47	14.9	0.06497	27.2
BCG-1_S_124	200	123	0.265	0.614	302	6	0	0.00061	29.2895051	0.0062	56.3	0.00093	14.5	0.25661824	1079.99	14.5	0.04880	54.4
BCG-1_L_15	~~203~~	~~106~~	~~0.279~~	~~0.523~~	~~338~~	~~34~~	~~2~~	~~0.00071~~	~~36.0227046~~	~~0.0109~~	~~25.0~~	~~0.00093~~	~~12.4~~	~~0.49441656~~	~~1075.19~~	~~12.4~~	~~0.08514~~	~~21.7~~
BCG-1_M_43	~~214~~	~~136~~	~~0.288~~	~~0.637~~	~~363~~	~~8~~	~~1~~	~~0.00048~~	~~30.7243541~~	~~0.0157~~	~~38.1~~	~~0.00093~~	~~12.0~~	~~0.3136621~~	~~1073.80~~	~~12.0~~	~~0.12213~~	~~36.2~~
BCG-1_M_52	227	167	0.300	0.737	385	26	1	0.00051	42.7978396	0.0037	59.0	0.00093	9.2	0.15602414	1071.87	9.2	0.02854	58.3
BCG-1_L_16	306	176	0.387	0.577	502	33	2	0.00051	36.9220818	0.0059	36.6	0.00094	7.3	0.19721539	1067.96	7.3	0.04600	35.9
BCG-1_S_123	~~331~~	~~172~~	~~0.393~~	~~0.519~~	~~500~~	~~27~~	~~2~~	~~0.00040~~	~~40.5128565~~	~~0.0086~~	~~28.5~~	~~0.00094~~	~~12.0~~	~~0.41950669~~	~~1067.80~~	~~12.0~~	~~0.06634~~	~~25.9~~
BCG-1_S_112	189	140	0.289	0.739	318	16	1	0.00079	46.8610487	0.0022	69.1	0.00094	12.3	0.17810506	1063.05	12.3	0.01660	68.0
BCG-1_M_55	~~206~~	~~95.8~~	~~0.258~~	~~0.466~~	~~333~~	~~333~~	~~19~~	~~0.00053~~	~~41.8753307~~	~~0.0106~~	~~35.5~~	~~0.00094~~	~~10.8~~	~~0.30426521~~	~~1059.22~~	~~10.8~~	~~0.08147~~	~~33.8~~
BCG-1_S_114	~~261~~	~~129~~	~~0.312~~	~~0.494~~	~~440~~	~~17~~	~~1~~	~~0.00038~~	~~45.1900705~~	~~0.0104~~	~~41.9~~	~~0.00094~~	~~14.1~~	~~0.33530581~~	~~1058.97~~	~~14.1~~	~~0.07977~~	~~39.4~~
BCG-1_S_113	~~246~~	~~149~~	~~0.379~~	~~0.604~~	~~411~~	~~41~~	~~2~~	~~0.00084~~	~~35.9200737~~	~~0.0127~~	~~25.8~~	~~0.00095~~	~~9.9~~	~~0.38272267~~	~~1052.42~~	~~9.9~~	~~0.09690~~	~~23.9~~
BCG-1_S_126	368	306	0.452	0.831	637	32	1	0.00031	25.7267584	0.0052	36.0	0.00095	6.5	0.18106728	1052.14	6.5	0.03947	35.4
BCG-1_S_108	270	138	0.309	0.513	459	16	1	0.00035	38.5002074	0.0030	81.4	0.00095	11.2	0.1372256	1048.36	11.2	0.02250	80.7
BCG-1_S_139	203	126	0.249	0.618	343	30	2	0.00041	32.1767664	0.0048	84.0	0.00096	12.7	0.15117009	1047.01	12.7	0.03662	83.0
BCG-1_M_36	~~614~~	~~373~~	~~0.716~~	~~0.608~~	~~1141~~	~~1141~~	~~88~~	~~0.00026~~	~~25.7933143~~	~~0.0085~~	~~21.6~~	~~0.00096~~	~~6.4~~	~~0.2951071~~	~~1046.17~~	~~6.4~~	~~0.06445~~	~~20.6~~
BCG-1_S_100	236	126	0.284	0.532	397	397	25	0.00045	42.2349667	0.0005	70.4	0.00097	11.3	0.16041189	1035.12	11.3	0.00399	69.5
BCG-1_M_66	~~169~~	~~90.8~~	~~0.207~~	~~0.538~~	~~291~~	~~9~~	~~1~~	~~0.00026~~	~~48.647635~~	~~0.0176~~	~~44.4~~	~~0.00097~~	~~20.6~~	~~0.46391065~~	~~1034.38~~	~~20.6~~	~~0.13226~~	~~39.3~~
BCG-1_S_99	~~326~~	~~225~~	~~0.439~~	~~0.690~~	~~554~~	~~554~~	~~27~~	~~0.00043~~	~~32.2519057~~	~~0.0126~~	~~35.6~~	~~0.00097~~	~~7.9~~	~~0.22261368~~	~~1031.99~~	~~7.9~~	~~0.09416~~	~~34.7~~
BCG-1_S_103	~~211~~	~~142~~	~~0.310~~	~~0.671~~	~~358~~	~~88~~	~~6~~	~~0.00064~~	~~45.5047756~~	~~0.0097~~	~~45.5~~	~~0.00097~~	~~13.1~~	~~0.28860297~~	~~1026.78~~	~~13.1~~	~~0.07253~~	~~43.5~~
BCG-1_S_138	2378	1586	2.86	0.667	3978	3978	109	0.00030	13.0489377	0.0069	14.3	0.00097	5.2	0.36398474	1026.08	5.2	0.05139	13.3
BCG-1_S_136	~~231~~	~~127~~	~~0.321~~	~~0.547~~	~~403~~	~~68~~	~~3~~	~~0.00053~~	~~33.9966449~~	~~0.0202~~	~~31.0~~	~~0.00098~~	~~8.0~~	~~0.25889434~~	~~1024.89~~	~~8.0~~	~~0.15046~~	~~29.9~~

Appendix A: LA-ICP-MS U-Pb Composition and Isotopic Ratios

Table S2. U-Pb isotope ratios and trace element concentrations by LA-ICPMS: sample data

				Composition				Corrected isotope ratios										
	U	Th	Pb		206Pb	206Pb		208Pb	±2s	207Pb	±2s	206Pb	±2s	error	238U	±2s	207Pb	±2s
Analysis	ppm	ppm	ppm	Th/U	cps	204Pb	±1s	232Th	(%)	235U	(%)	238U	(%)	corr.	206Pb	(%)	206Pb	(%)
BCG-1_S_109	300	164	0.353	0.548	533	130	4	0.00032	49.4984861	0.0047	41.9	0.00098	4.1	0.09720985	1023.75	4.1	0.03512	41.7
BCG-1_S_147	~~203~~	~~102~~	~~0.300~~	~~0.500~~	~~305~~	~~305~~	~~18~~	~~0.00086~~	~~34.0882298~~	~~0.0126~~	~~38.9~~	~~0.00098~~	~~10.2~~	~~0.26294125~~	~~1023.31~~	~~10.2~~	~~0.09388~~	~~37.5~~
BCG-1_M_65	~~288~~	~~158~~	~~0.380~~	~~0.547~~	~~506~~	~~18~~	~~1~~	~~0.00045~~	~~29.9791529~~	~~0.0143~~	~~35.9~~	~~0.00098~~	~~12.0~~	~~0.33288042~~	~~1020.94~~	~~12.0~~	~~0.10590~~	~~33.9~~
BCG-1_M_60	~~133~~	~~54.4~~	~~0.197~~	~~0.410~~	~~228~~	~~63~~	~~6~~	~~0.00093~~	~~27.98957~~	~~0.0187~~	~~35.8~~	~~0.00098~~	~~22.9~~	~~0.63994965~~	~~1018.31~~	~~22.9~~	~~0.13775~~	~~27.5~~
BCG-1_M_51	~~279~~	~~169~~	~~0.364~~	~~0.605~~	~~486~~	~~77~~	~~4~~	~~0.00043~~	~~30.0407391~~	~~0.0094~~	~~40.9~~	~~0.00098~~	~~11.7~~	~~0.28668808~~	~~1017.84~~	~~11.7~~	~~0.06950~~	~~39.2~~
BCG-1_S_135	~~267~~	~~141~~	~~0.337~~	~~0.527~~	~~461~~	~~34~~	~~2~~	~~0.00043~~	~~39.7688458~~	~~0.0097~~	~~40.1~~	~~0.00099~~	~~8.3~~	~~0.20718823~~	~~1014.77~~	~~8.3~~	~~0.07161~~	~~39.3~~
BCG-1_M_44	266	155	0.345	0.583	498	18	1	0.00048	28.678441	0.0058	32.2	0.00099	8.7	0.26992606	1012.94	8.7	0.04296	31.0
BCG-1_M_58	169	104	0.240	0.616	329	30	2	0.00062	29.9425591	0.0076	50.8	0.00099	15.1	0.29716241	1011.03	15.1	0.05576	48.5
BCG-1_M_39	321	230	0.427	0.717	565	1302	63	0.00042	32.475218	0.0066	44.7	0.00099	11.5	0.25673658	1007.60	11.5	0.04809	43.2
BCG-1_L_19	261	136	0.360	0.523	440	29	2	0.00072	35.3880844	0.0029	49.7	0.00099	13.4	0.26978206	1007.37	13.4	0.02138	47.8
BCG-1_L_18	271	146	0.366	0.540	451	331	22	0.00061	35.998572	0.0056	53.8	0.00099	13.1	0.24333427	1007.29	13.1	0.04110	52.2
BCG-1_M_54	~~193~~	~~109~~	~~0.276~~	~~0.564~~	~~353~~	~~60~~	~~5~~	~~0.00055~~	~~38.6121676~~	~~0.0185~~	~~30.8~~	~~0.00099~~	~~15.6~~	~~0.50440332~~	~~1005.83~~	~~15.6~~	~~0.13517~~	~~26.6~~
BCG-1_L_7	~~206~~	~~119~~	~~0.336~~	~~0.576~~	~~396~~	~~11~~	~~1~~	~~0.00082~~	~~28.1528815~~	~~0.0231~~	~~22.9~~	~~0.00100~~	~~13.8~~	~~0.60253325~~	~~1002.43~~	~~13.8~~	~~0.16806~~	~~18.3~~
BCG-1_M_34	228	128	0.273	0.560	443	42	2	0.00033	23.7356472	0.0031	60.6	0.00100	12.1	0.19998265	997.07	12.1	0.02256	59.4
BCG-1_M_53	~~195~~	~~102~~	~~0.282~~	~~0.520~~	~~358~~	~~79~~	~~6~~	~~0.00073~~	~~37.6487181~~	~~0.0095~~	~~30.5~~	~~0.00100~~	~~12.6~~	~~0.4136058~~	~~996.45~~	~~12.6~~	~~0.06857~~	~~27.7~~
BCG-1_S_122	~~175~~	~~82.7~~	~~0.260~~	~~0.472~~	~~281~~	~~28~~	~~3~~	~~0.00083~~	~~32.8983094~~	~~0.0143~~	~~39.8~~	~~0.00101~~	~~22.6~~	~~0.56711308~~	~~987.69~~	~~22.6~~	~~0.10237~~	~~32.8~~
BCG-1_S_117	~~99.2~~	~~54.5~~	~~0.247~~	~~0.549~~	~~173~~	~~13~~	~~1~~	~~0.00188~~	~~37.5372581~~	~~0.0645~~	~~32.4~~	~~0.00102~~	~~20.1~~	~~0.62038592~~	~~983.87~~	~~20.1~~	~~0.46011~~	~~25.4~~
BCG-1_M_61	238	143	0.342	0.600	450	43	3	0.00062	40.3915969	0.0081	45.5	0.00102	12.2	0.26713704	983.57	12.2	0.05799	43.9
BCG-1_M_46	~~291~~	~~158~~	~~0.380~~	~~0.543~~	~~518~~	~~14~~	~~1~~	~~0.00039~~	~~23.3922853~~	~~0.0112~~	~~40.9~~	~~0.00102~~	~~8.4~~	~~0.204954~~	~~980.33~~	~~8.4~~	~~0.07983~~	~~40.0~~
BCG-1_S_141	262	136	0.302	0.522	429	429	27	0.00024	28.4895032	0.0043	51.0	0.00102	10.2	0.20044383	979.66	10.2	0.03030	50.0
BCG-1_M_38	~~258~~	~~163~~	~~0.391~~	~~0.633~~	~~481~~	~~14~~	~~1~~	~~0.00058~~	~~33.8866669~~	~~0.0186~~	~~31.6~~	~~0.00102~~	~~10.0~~	~~0.31676723~~	~~977.61~~	~~10.0~~	~~0.13178~~	~~30.0~~
BCG-1_S_130	~~237~~	~~172~~	~~0.360~~	~~0.727~~	~~415~~	~~17~~	~~1~~	~~0.00058~~	~~23.7043569~~	~~0.0135~~	~~33.5~~	~~0.00102~~	~~6.5~~	~~0.19414431~~	~~976.52~~	~~6.5~~	~~0.09537~~	~~32.9~~
BCG-1_M_47	~~279~~	~~163~~	~~0.358~~	~~0.585~~	~~515~~	~~24~~	~~1~~	~~0.00034~~	~~36.307357~~	~~0.0094~~	~~30.2~~	~~0.00103~~	~~9.6~~	~~0.31549273~~	~~974.76~~	~~9.6~~	~~0.06633~~	~~28.7~~
BCG-1_M_42	~~266~~	~~155~~	~~0.339~~	~~0.584~~	~~488~~	~~34~~	~~3~~	~~0.00029~~	~~25.1122813~~	~~0.0120~~	~~28.7~~	~~0.00103~~	~~13.6~~	~~0.47247666~~	~~974.46~~	~~13.6~~	~~0.08459~~	~~25.3~~
BCG-1_S_143	266	139	0.329	0.524	424	424	28	0.00041	43.7887896	0.0027	47.2	0.00103	13.6	0.28855351	974.28	13.6	0.01935	45.2
BCG-1_S_119	~~272~~	~~194~~	~~0.360~~	~~0.712~~	~~432~~	~~54~~	~~3~~	~~0.00032~~	~~39.8387303~~	~~0.0123~~	~~27.9~~	~~0.00103~~	~~10.0~~	~~0.35869514~~	~~973.59~~	~~10.0~~	~~0.08691~~	~~26.1~~
BCG-1_L_20	~~107~~	~~56.9~~	~~0.196~~	~~0.532~~	~~202~~	~~45~~	~~5~~	~~0.00119~~	~~48.217145~~	~~0.0257~~	~~39.6~~	~~0.00103~~	~~20.2~~	~~0.50955267~~	~~973.05~~	~~20.2~~	~~0.18143~~	~~34.1~~
BCG-1_S_131	228	135	0.330	0.591	433	48	3	0.00065	35.7443283	0.0073	52.7	0.00103	13.1	0.24753461	968.31	13.1	0.05155	51.1
BCG-1_S_144	241	164	0.325	0.682	426	426	20	0.00038	27.057846	0.0097	37.2	0.00104	10.6	0.28587275	959.45	10.6	0.06725	35.6
BCG-1_M_37	214	126	0.338	0.587	400	21	2	0.00085	32.0387258	0.0059	41.4	0.00105	13.4	0.32245752	953.82	13.4	0.04092	39.1
BCG-1_M_40	~~205~~	~~115~~	~~0.281~~	~~0.562~~	~~394~~	~~394~~	~~25~~	~~0.00042~~	~~25.4084679~~	~~0.0127~~	~~37.7~~	~~0.00106~~	~~12.6~~	~~0.3344715~~	~~947.32~~	~~12.6~~	~~0.08739~~	~~35.5~~
BCG-1_L_10	~~194~~	~~156~~	~~0.292~~	~~0.802~~	~~366~~	~~16~~	~~1~~	~~0.00047~~	~~59.8572599~~	~~0.0109~~	~~39.0~~	~~0.00106~~	~~10.9~~	~~0.27971775~~	~~946.89~~	~~10.9~~	~~0.07479~~	~~37.5~~
BCG-1_M_59	~~215~~	~~130~~	~~0.293~~	~~0.603~~	~~423~~	~~13~~	~~1~~	~~0.00040~~	~~35.1302049~~	~~0.0104~~	~~16.4~~	~~0.00106~~	~~10.8~~	~~0.65949899~~	~~944.11~~	~~10.8~~	~~0.07104~~	~~12.3~~
BCG-1_S_106	374	244	0.488	0.652	692	169	8	0.00037	30.0182376	0.0019	57.7	0.00106	10.1	0.17489614	940.68	10.1	0.01265	56.8
BCG-1_S_121	254	176	0.330	0.694	429	8	0	0.00034	26.3207804	0.0030	44.1	0.00107	7.8	0.17714558	937.96	7.8	0.02051	43.4
BCG-1_S_137	325	218	0.422	0.671	591	55	2	0.00033	27.8564041	0.0036	37.1	0.00108	8.0	0.21638713	928.40	8.0	0.02430	36.2
BCG-1_M_64	231	143	0.340	0.619	449	449	22	0.00053	33.1726732	0.0101	43.9	0.00108	11.6	0.26360124	924.35	11.6	0.06790	42.3
BCG-1_M_56	~~278~~	~~189~~	~~0.431~~	~~0.679~~	~~531~~	~~53~~	~~2~~	~~0.00053~~	~~20.241055~~	~~0.0149~~	~~19.2~~	~~0.00109~~	~~6.7~~	~~0.34697105~~	~~916.22~~	~~6.7~~	~~0.09884~~	~~18.0~~
BCG-1_M_48	168	93.5	0.268	0.555	325	325	23	0.00083	33.7721497	0.0069	54.9	0.00109	15.2	0.2762928	914.95	15.2	0.04552	52.8
BCG-1_M_45	~~293~~	~~168~~	~~0.487~~	~~0.573~~	~~562~~	~~36~~	~~2~~	~~0.00074~~	~~28.8373139~~	~~0.0207~~	~~18.4~~	~~0.00110~~	~~11.2~~	~~0.61023992~~	~~908.55~~	~~11.2~~	~~0.13643~~	~~14.6~~
BCG-1_S_120	444	231	0.606	0.519	755	3169	195	0.00040	32.6544796	0.0086	22.9	0.00111	8.3	0.36298563	897.09	8.3	0.05583	21.3
BCG-1_S_145	~~275~~	~~169~~	~~0.502~~	~~0.615~~	~~521~~	~~115~~	~~6~~	~~0.00093~~	~~32.3062701~~	~~0.0214~~	~~29.1~~	~~0.00112~~	~~9.7~~	~~0.33406952~~	~~892.54~~	~~9.7~~	~~0.13825~~	~~27.4~~
BCG-1_L_1	54.3	34.1	0.135	0.628	132	132	15	0.00209	28.8618762	0.0085	114.2	0.00112	24.6	0.21509079	890.78	24.6	0.05504	111.6
BCG-1_L_14	~~126~~	~~74.3~~	~~0.296~~	~~0.591~~	~~247~~	~~29~~	~~3~~	~~0.00154~~	~~25.8002437~~	~~0.0436~~	~~31.9~~	~~0.00114~~	~~16.1~~	~~0.50327418~~	~~875.59~~	~~16.1~~	~~0.27675~~	~~27.5~~
BCG-1_M_50	~~113~~	~~41.2~~	~~0.221~~	~~0.366~~	~~236~~	~~8~~	~~0~~	~~0.00183~~	~~34.6388856~~	~~0.0207~~	~~58.9~~	~~0.00116~~	~~12.3~~	~~0.20853381~~	~~864.66~~	~~12.3~~	~~0.12977~~	~~57.6~~
BCG-1_M_63	~~193~~	~~103~~	~~0.636~~	~~0.533~~	~~443~~	~~1020~~	~~62~~	~~0.00322~~	~~59.2601789~~	~~0.0594~~	~~36.1~~	~~0.00116~~	~~22.7~~	~~0.62935046~~	~~861.94~~	~~22.7~~	~~0.37104~~	~~28.1~~
BCG-1_S_118	~~198~~	~~106~~	~~0.333~~	~~0.537~~	~~414~~	~~87~~	~~5~~	~~0.00060~~	~~37.6434382~~	~~0.0196~~	~~38.0~~	~~0.00125~~	~~11.3~~	~~0.29690342~~	~~798.75~~	~~11.3~~	~~0.11343~~	~~36.3~~
BCG-1_S_115	~~190~~	~~114~~	~~0.547~~	~~0.601~~	~~494~~	~~430~~	~~23~~	~~0.00154~~	~~25.0942435~~	~~0.0633~~	~~23.5~~	~~0.00153~~	~~13.3~~	~~0.56563464~~	~~651.90~~	~~13.3~~	~~0.29926~~	~~19.4~~
BCG-1_S_142	~~125~~	~~50.0~~	~~0.478~~	~~0.399~~	~~313~~	~~15~~	~~1~~	~~0.00462~~	~~37.197873~~	~~0.0653~~	~~36.4~~	~~0.00154~~	~~17.8~~	~~0.49027074~~	~~650.61~~	~~17.8~~	~~0.30816~~	~~31.7~~
BCG-1_S_104	~~155~~	~~64.2~~	~~0.568~~	~~0.414~~	~~435~~	~~80~~	~~6~~	~~0.00371~~	~~35.0448541~~	~~0.0698~~	~~29.3~~	~~0.00165~~	~~15.2~~	~~0.51760925~~	~~607.47~~	~~15.2~~	~~0.30758~~	~~25.0~~
BCG-1_S_128	~~254~~	~~172~~	~~0.933~~	~~0.675~~	~~621~~	~~64~~	~~3~~	~~0.00220~~	~~23.6613373~~	~~0.0783~~	~~26.9~~	~~0.00166~~	~~13.1~~	~~0.48764167~~	~~603.04~~	~~13.1~~	~~0.34249~~	~~23.5~~
BCG-1_S_148	~~116~~	~~76.8~~	~~0.669~~	~~0.664~~	~~414~~	~~414~~	~~52~~	~~0.00378~~	~~25.2587176~~	~~0.1412~~	~~40.0~~	~~0.00232~~	~~26.8~~	~~0.67094885~~	~~430.33~~	~~26.8~~	~~0.44066~~	~~29.7~~
BCG-1_M_33	~~109~~	~~55.9~~	~~1.16~~	~~0.512~~	~~624~~	~~16~~	~~2~~	~~0.01022~~	~~40.0387632~~	~~0.2783~~	~~39.5~~	~~0.00338~~	~~37.3~~	~~0.94210338~~	~~296.05~~	~~37.3~~	~~0.59760~~	~~13.2~~

Appendix A: LA-ICP-MS U-Pb Composition and Isotopic Ratios

Table S2. U-Pb isotope ratios and trace element concentrations by LA-ICPMS: sample data

				Composition								Corrected isotope ratios						
Analysis	U ppm	Th ppm	Pb ppm	Th/U	206Pb cps	206Pb/204Pb	±1s	208Pb/232Th	±2s (%)	207Pb/235U	±2s (%)	206Pb/238U	±2s (%)	error corr.	238U/206Pb	±2s (%)	207Pb/206Pb	±2s (%)
BCG-1_M_35	~~249~~	~~278~~	~~4.03~~	~~1.11~~	~~2055~~	~~17~~	~~1~~	~~0.00776~~	~~24.3267734~~	~~0.4408~~	~~27.2~~	~~0.00440~~	~~26.8~~	~~0.98338873~~	~~227.18~~	~~26.8~~	~~0.72629~~	~~4.9~~
BCG-273	**42.754171**	**112.021274**																
BCG-273_L_23	254	138	0.317	0.545	415	83	5	0.00049	29.1767909	0.0068	50.7	0.00094	11.8	0.23158384	1060.55	11.8	0.05204	49.3
BCG-273_M_71	406	242	0.608	0.596	801	65	2	0.00048	26.088779	0.0076	44.9	0.00117	6.6	0.1453471	855.32	6.6	0.04697	44.5
BCG-273_M_72	~~101~~	~~61.5~~	~~0.236~~	~~0.609~~	~~268~~	~~14~~	~~1~~	~~0.00106~~	~~35.0736958~~	~~0.0242~~	~~48.3~~	~~0.00153~~	~~11.5~~	~~0.23701003~~	~~652.60~~	~~11.5~~	~~0.11475~~	~~46.9~~
BCG-273_S_161	387	410	41.3	1.06	50933	4071	38	0.02475	2.95316922	0.5831	3.2	0.07645	1.7	0.49843823	13.08	1.7	0.05532	2.7
BCG-273_S_163	80.7	46.5	7.84	0.577	10896	1199	13	0.02549	8.56438951	0.6260	6.3	0.07930	3.1	0.47764917	12.61	3.1	0.05726	5.5
BCG-273_S_159	39.9	35.1	4.21	0.880	5260	1538	47	0.02617	13.2665849	0.6599	7.1	0.07942	4.0	0.55133714	12.59	4.0	0.06026	5.9
BCG-273_S_158	112	78.2	11.1	0.700	14365	14365	121	0.02375	5.20838923	0.5890	5.9	0.07955	3.6	0.6108011	12.57	3.6	0.05370	4.6
BCG-273_S_162	64.1	39.7	6.26	0.620	8648	257	5	0.02386	6.26468748	0.5962	7.5	0.08005	3.2	0.41687525	12.49	3.2	0.05402	6.8
BCG-273_S_164	78.8	47.9	7.90	0.608	11342	1216	55	0.02444	3.81850907	0.6162	11.6	0.08241	3.3	0.2795078	12.13	3.3	0.05423	11.1
BCG-273_S_160	~~2431~~	~~893~~	~~443~~	~~0.367~~	~~585052~~	~~2841~~	~~41~~	~~0.03307~~	~~13.0656724~~	~~2.5351~~	~~17.2~~	~~0.11694~~	~~16.9~~	~~0.98235528~~	~~8.55~~	~~16.9~~	~~0.15723~~	~~3.2~~
BCG-30	**42.751736**	**112.021480**																
BCG-30_S_154	202	152	0.277	0.755	285	28	3	0.00058	34.3261344	0.0084	72.3	0.00089	13.2	0.1829357	1121.07	13.2	0.06825	71.1
BCG-30_S_153	193	139	0.256	0.722	305	14	1	0.00045	39.3751817	0.0068	42.0	0.00097	12.7	0.30156645	1025.67	12.7	0.05085	40.0
BCG-30_S_151	~~218~~	~~132~~	~~0.324~~	~~0.605~~	~~388~~	~~14~~	~~1~~	~~0.00060~~	~~17.7718238~~	~~0.0115~~	~~22.8~~	~~0.00106~~	~~10.4~~	~~0.45462493~~	~~944.07~~	~~10.4~~	~~0.07847~~	~~20.3~~
BCG-30_L_21	~~133~~	~~76.3~~	~~0.207~~	~~0.575~~	~~306~~	~~25~~	~~2~~	~~0.00049~~	~~26.4587276~~	~~0.0154~~	~~46.5~~	~~0.00118~~	~~12.2~~	~~0.26264843~~	~~846.01~~	~~12.2~~	~~0.09464~~	~~44.8~~
BCG-30_L_22	~~76.9~~	~~46.4~~	~~0.174~~	~~0.604~~	~~151~~	~~11~~	~~1~~	~~0.00144~~	~~31.9178317~~	~~0.0305~~	~~60.7~~	~~0.00119~~	~~20.9~~	~~0.34470505~~	~~838.84~~	~~20.9~~	~~0.18541~~	~~56.9~~
BCG-30_M_70	101	56.2	0.196	0.556	228	170	15	0.00122	40.5436842	0.0110	48.6	0.00120	16.9	0.34742894	833.57	16.9	0.06630	45.6
BCG-30_M_69	~~82.2~~	~~57.3~~	~~0.187~~	~~0.698~~	~~172~~	~~42~~	~~5~~	~~0.00114~~	~~36.0637104~~	~~0.0327~~	~~38.7~~	~~0.00126~~	~~20.7~~	~~0.53550637~~	~~792.19~~	~~20.7~~	~~0.18774~~	~~32.7~~
BCG-30_M_67	153	102	0.262	0.670	360	360	30	0.00055	48.6722247	0.0084	46.6	0.00130	14.7	0.31600502	769.73	14.7	0.04674	44.2
BCG-30_M_68	69.8	33.3	0.162	0.477	170	34	3	0.00193	62.6527636	0.0124	57.2	0.00132	13.0	0.2269925	757.37	13.0	0.06823	55.7
BCG-30_S_152	~~242~~	~~128~~	~~0.463~~	~~0.528~~	~~531~~	~~51~~	~~3~~	~~0.00092~~	~~25.7485466~~	~~0.0131~~	~~37.4~~	~~0.00136~~	~~10.3~~	~~0.27397695~~	~~735.03~~	~~10.3~~	~~0.06982~~	~~36.0~~
BCG-30_S_150	~~98.5~~	~~58.8~~	~~0.239~~	~~0.597~~	~~229~~	~~24~~	~~2~~	~~0.00130~~	~~31.9652222~~	~~0.0234~~	~~48.2~~	~~0.00151~~	~~13.4~~	~~0.27730351~~	~~661.89~~	~~13.4~~	~~0.11254~~	~~46.4~~
BCG-30_S_157	49.4	37.3	4.74	0.755	6233	1440	31	0.02319	10.4786055	0.5338	10.7	0.07609	3.5	0.3197362	13.14	3.5	0.05088	10.1
BCG-30_S_155	122	134	13.4	1.10	16295	797	42	0.02463	3.60099045	0.5960	7.8	0.07941	3.7	0.46973315	12.59	3.7	0.05443	6.9
BCG-30_S_156	77.4	49.6	7.66	0.641	10279	419	15	0.02479	6.65451362	0.6141	8.8	0.07995	3.4	0.37899035	12.51	3.4	0.05570	8.2
BCG-612	**42.765764**	**112.013782**																
BCG-612_S_178	~~577~~	~~404~~	~~0.626~~	~~0.701~~	~~376~~	~~18~~	~~1~~	~~0.00036~~	~~35.9167821~~	~~0.0095~~	~~34.0~~	~~0.00078~~	~~12.5~~	~~0.36810295~~	~~1282.19~~	~~12.5~~	~~0.08817~~	~~31.7~~
BCG-612_L_27	~~436~~	~~263~~	~~0.576~~	~~0.602~~	~~265~~	~~18~~	~~1~~	~~0.00071~~	~~34.6764128~~	~~0.0154~~	~~33.7~~	~~0.00079~~	~~14.9~~	~~0.4435243~~	~~1267.24~~	~~14.9~~	~~0.14157~~	~~30.2~~
BCG-612_S_170	~~388~~	~~265~~	~~0.528~~	~~0.682~~	~~253~~	~~10~~	~~1~~	~~0.00072~~	~~28.0838063~~	~~0.0115~~	~~69.6~~	~~0.00081~~	~~13.1~~	~~0.18794611~~	~~1240.19~~	~~13.1~~	~~0.10308~~	~~68.3~~
BCG-612_S_176	917	865	1.01	0.942	610	610	24	0.00026	22.2623672	0.0049	28.7	0.00084	7.9	0.27369603	1195.77	7.9	0.04239	27.6
BCG-612_S_185	649	438	0.710	0.674	436	137	7	0.00032	37.1567151	0.0077	53.2	0.00084	7.8	0.14621009	1188.71	7.8	0.06620	52.6
BCG-612_S_169	503	407	0.613	0.809	314	314	21	0.00047	44.7630762	0.0009	49.7	0.00084	11.6	0.23227188	1184.35	11.6	0.00742	48.3
BCG-612_L_32	~~375~~	~~216~~	~~0.496~~	~~0.577~~	~~257~~	~~566~~	~~44~~	~~0.00063~~	~~40.6330792~~	~~0.0157~~	~~43.9~~	~~0.00085~~	~~11.8~~	~~0.26775003~~	~~1173.29~~	~~11.8~~	~~0.13341~~	~~42.3~~
BCG-612_S_172	637	439	0.713	0.689	406	7	0	0.00035	23.0553239	0.0061	43.8	0.00085	8.2	0.1879173	1173.06	8.2	0.05186	43.0
BCG-612_S_197	~~646~~	~~451~~	~~0.788~~	~~0.698~~	~~427~~	~~427~~	~~29~~	~~0.00045~~	~~17.5414514~~	~~0.0087~~	~~30.0~~	~~0.00086~~	~~13.3~~	~~0.44167004~~	~~1159.15~~	~~13.3~~	~~0.07322~~	~~26.9~~
BCG-612_M_77	~~398~~	~~328~~	~~0.621~~	~~0.824~~	~~247~~	~~24~~	~~2~~	~~0.00072~~	~~43.2091657~~	~~0.0153~~	~~57.3~~	~~0.00086~~	~~18.1~~	~~0.31602774~~	~~1158.92~~	~~18.1~~	~~0.12876~~	~~54.4~~
BCG-612_S_207	~~506~~	~~324~~	~~0.618~~	~~0.640~~	~~341~~	~~341~~	~~21~~	~~0.00048~~	~~37.94348~~	~~0.0092~~	~~43.5~~	~~0.00086~~	~~11.8~~	~~0.2716304~~	~~1157.35~~	~~11.8~~	~~0.07743~~	~~41.8~~
BCG-612_M_84	792	515	0.950	0.650	529	90	4	0.00044	28.268743	0.0073	29.2	0.00087	6.6	0.22633243	1153.46	6.6	0.06145	28.4
BCG-612_S_194	542	298	0.615	0.549	361	13	1	0.00044	30.1884168	0.0058	50.5	0.00087	12.1	0.2384226	1151.88	12.1	0.04864	49.0
BCG-612_M_90	~~827~~	~~588~~	~~0.943~~	~~0.711~~	~~499~~	~~58~~	~~3~~	~~0.00026~~	~~34.2191623~~	~~0.0130~~	~~31.1~~	~~0.00087~~	~~9.0~~	~~0.28966777~~	~~1150.87~~	~~9.0~~	~~0.10811~~	~~29.8~~
BCG-612_S_174	~~379~~	~~256~~	~~0.515~~	~~0.676~~	~~250~~	~~29~~	~~3~~	~~0.00062~~	~~35.6616321~~	~~0.0122~~	~~39.6~~	~~0.00087~~	~~13.6~~	~~0.34218964~~	~~1150.55~~	~~13.6~~	~~0.10200~~	~~37.2~~
BCG-612_S_184	591	426	0.697	0.720	415	415	21	0.00042	49.0438225	0.0030	78.4	0.00088	8.5	0.10779224	1142.11	8.5	0.02478	78.0
BCG-612_S_205	423	314	0.556	0.742	291	21	1	0.00056	32.5338798	0.0050	70.4	0.00088	12.0	0.17068248	1139.01	12.0	0.04160	69.4
BCG-612_S_182	658	494	0.791	0.752	447	447	28	0.00040	25.7729546	0.0049	48.6	0.00088	14.0	0.2875884	1131.27	14.0	0.04030	46.5
BCG-612_S_192	1063	767	1.18	0.721	705	103	4	0.00027	23.765801	0.0076	27.5	0.00089	8.0	0.29181685	1129.10	8.0	0.06184	26.3
BCG-612_M_86	461	343	0.547	0.744	319	88	4	0.00039	44.4927578	0.0025	74.5	0.00089	8.6	0.11505241	1121.22	8.6	0.02025	74.0
BCG-612_L_26	729	453	0.879	0.620	515	515	24	0.00045	28.9881651	0.0061	44.1	0.00089	10.6	0.23962337	1120.31	10.6	0.04987	42.8
BCG-612_M_79	569	348	0.661	0.611	362	362	20	0.00037	34.4784152	0.0065	35.4	0.00090	10.9	0.30841914	1115.96	10.9	0.05257	33.7
BCG-612_S_195	1138	1048	1.42	0.921	756	79	4	0.00036	25.9252066	0.0054	40.1	0.00090	10.5	0.26144183	1112.39	10.5	0.04378	38.7
BCG-612_M_78	~~525~~	~~425~~	~~0.721~~	~~0.809~~	~~351~~	~~43~~	~~2~~	~~0.00049~~	~~35.8630959~~	~~0.0112~~	~~38.2~~	~~0.00091~~	~~11.9~~	~~0.31127969~~	~~1098.41~~	~~11.9~~	~~0.08959~~	~~36.3~~
BCG-612_S_171	534	403	0.710	0.754	366	24	2	0.00054	18.5390035	0.0039	82.0	0.00091	14.0	0.17024042	1097.07	14.0	0.03076	80.8

Appendix A: LA-ICP-MS U-Pb Composition and Isotopic Ratios

Table S2. U-Pb isotope ratios and trace element concentrations by LA-ICPMS: sample data

				Composition								Corrected isotope ratios						
	U	Th	Pb		206Pb	206Pb		208Pb	±2s	207Pb	±2s	206Pb	±2s	error	238U	±2s	207Pb	±2s
Analysis	ppm	ppm	ppm	Th/U	cps	204Pb	±1s	232Th	(%)	235U	(%)	238U	(%)	corr.	206Pb	(%)	206Pb	(%)
BCG-612_M_89	~~734~~	~~404~~	~~1.02~~	~~0.550~~	~~441~~	~~49~~	~~2~~	~~0.00070~~	~~38.2541161~~	~~0.0125~~	~~30.2~~	~~0.00092~~	~~9.9~~	~~0.32687156~~	~~1088.38~~	~~9.9~~	~~0.09897~~	~~28.5~~
BCG-612_S_175	~~484~~	~~343~~	~~0.583~~	~~0.709~~	~~349~~	~~349~~	~~27~~	~~0.00030~~	~~46.8350793~~	~~0.0128~~	~~33.1~~	~~0.00092~~	~~12.2~~	~~0.36903512~~	~~1085.72~~	~~12.2~~	~~0.10088~~	~~30.8~~
BCG-612_S_209	452	350	0.594	0.775	322	322	24	0.00051	31.5177057	0.0014	63.2	0.00093	14.4	0.22729706	1080.60	14.4	0.01107	61.6
BCG-612_S_188	626	525	0.758	0.838	428	14	1	0.00032	35.6356324	0.0049	49.8	0.00093	9.8	0.19698977	1079.10	9.8	0.03801	48.8
BCG-612_S_199	~~976~~	~~658~~	~~1.29~~	~~0.675~~	~~698~~	~~698~~	~~27~~	~~0.00049~~	~~25.5704099~~	~~0.0113~~	~~36.8~~	~~0.00093~~	~~8.4~~	~~0.22865133~~	~~1074.58~~	~~8.4~~	~~0.08820~~	~~35.8~~
BCG-612_S_202	~~559~~	~~382~~	~~0.923~~	~~0.682~~	~~420~~	~~23~~	~~1~~	~~0.00081~~	~~31.7568101~~	~~0.0261~~	~~23.9~~	~~0.00093~~	~~11.4~~	~~0.47462378~~	~~1073.83~~	~~11.4~~	~~0.20351~~	~~21.0~~
BCG-612_S_198	951	925	1.24	0.972	657	12	0	0.00036	27.7926511	0.0052	36.5	0.00093	9.1	0.24910605	1070.75	9.1	0.04020	35.4
BCG-612_L_25	~~652~~	~~463~~	~~0.849~~	~~0.710~~	~~468~~	~~94~~	~~7~~	~~0.00042~~	~~37.4051503~~	~~0.0101~~	~~35.3~~	~~0.00094~~	~~15.4~~	~~0.43720832~~	~~1060.83~~	~~15.4~~	~~0.07786~~	~~31.7~~
BCG-612_L_28	~~559~~	~~324~~	~~0.726~~	~~0.579~~	~~419~~	~~419~~	~~21~~	~~0.00050~~	~~43.3882615~~	~~0.0104~~	~~22.5~~	~~0.00095~~	~~10.3~~	~~0.45481802~~	~~1057.63~~	~~10.3~~	~~0.08004~~	~~20.0~~
BCG-612_S_206	1473	868	1.69	0.589	1094	1094	34	0.00031	21.0306585	0.0055	29.0	0.00095	6.9	0.23608516	1056.75	6.9	0.04216	28.1
BCG-612_S_180	839	844	1.08	1.01	643	707	32	0.00031	20.7151313	0.0056	49.0	0.00095	7.9	0.1600418	1056.63	7.9	0.04281	48.4
BCG-612_L_29	642	360	0.835	0.561	494	11	0	0.00056	29.3405182	0.0071	31.3	0.00095	6.7	0.21396724	1055.33	6.7	0.05424	30.6
BCG-612_M_75	393	266	0.547	0.677	272	14	1	0.00061	29.4549356	0.0055	52.8	0.00095	13.7	0.2592351	1051.67	13.7	0.04191	51.0
BCG-612_S_200	703	440	0.877	0.625	508	27	1	0.00040	24.7528081	0.0091	61.4	0.00095	10.5	0.17102803	1050.94	10.5	0.06911	60.5
BCG-612_M_80	~~717~~	~~480~~	~~0.940~~	~~0.668~~	~~467~~	~~32~~	~~2~~	~~0.00043~~	~~39.6569073~~	~~0.0104~~	~~36.7~~	~~0.00096~~	~~15.5~~	~~0.42331843~~	~~1041.93~~	~~15.5~~	~~0.07884~~	~~33.2~~
BCG-612_M_92	1153	497	1.38	0.431	790	440	18	0.00045	24.1000586	0.0073	30.4	0.00096	9.2	0.30380276	1041.67	9.2	0.05549	28.9
BCG-612_S_168	~~333~~	~~193~~	~~0.417~~	~~0.582~~	~~241~~	~~21~~	~~1~~	~~0.00031~~	~~93.1285789~~	~~0.0178~~	~~41.5~~	~~0.00096~~	~~10.3~~	~~0.24773621~~	~~1038.55~~	~~10.3~~	~~0.13429~~	~~40.2~~
BCG-612_S_173	~~2259~~	~~1867~~	~~3.04~~	~~0.827~~	~~1640~~	~~180~~	~~12~~	~~0.00041~~	~~16.9454139~~	~~0.0084~~	~~20.9~~	~~0.00097~~	~~6.5~~	~~0.3098521~~	~~1035.92~~	~~6.5~~	~~0.06292~~	~~19.9~~
BCG-612_M_73	453	269	0.619	0.595	324	6	0	0.00060	36.492522	0.0071	56.9	0.00097	10.2	0.17826322	1031.53	10.2	0.05308	55.9
BCG-612_S_177	~~398~~	~~275~~	~~0.526~~	~~0.691~~	~~304~~	~~9~~	~~1~~	~~0.00038~~	~~43.0492267~~	~~0.0150~~	~~39.0~~	~~0.00097~~	~~9.5~~	~~0.24382163~~	~~1031.42~~	~~9.5~~	~~0.11243~~	~~37.9~~
BCG-612_M_81	~~475~~	~~321~~	~~0.787~~	~~0.676~~	~~340~~	~~9~~	~~1~~	~~0.00085~~	~~30.2099261~~	~~0.0147~~	~~53.1~~	~~0.00098~~	~~11.9~~	~~0.22353566~~	~~1016.21~~	~~11.9~~	~~0.10849~~	~~51.7~~
BCG-612_M_82	494	410	0.649	0.830	318	64	3	0.00034	44.3828608	0.0078	35.8	0.00099	14.1	0.39331026	1012.32	14.1	0.05701	32.9
BCG-612_S_187	650	369	0.793	0.568	498	35	2	0.00034	29.6352128	0.0082	39.3	0.00099	10.1	0.25690283	1011.95	10.1	0.06035	38.0
BCG-612_L_31	540	376	0.678	0.697	412	14	1	0.00035	49.2628115	0.0042	55.6	0.00099	14.2	0.25548217	1010.04	14.2	0.03043	53.8
BCG-612_M_76	812	448	0.987	0.552	596	14	0	0.00036	38.3363084	0.0044	58.2	0.00100	6.1	0.10429712	1002.60	6.1	0.03209	57.9
BCG-612_S_186	910	803	1.18	0.882	669	37	2	0.00031	25.0659631	0.0066	18.8	0.00100	8.4	0.44728519	1001.49	8.4	0.04787	16.8
BCG-612_M_85	~~1254~~	~~799~~	~~1.59~~	~~0.637~~	~~918~~	~~45~~	~~2~~	~~0.00032~~	~~23.5275787~~	~~0.0098~~	~~21.1~~	~~0.00100~~	~~9.3~~	~~0.44177073~~	~~999.39~~	~~9.3~~	~~0.07086~~	~~18.9~~
BCG-612_L_30	~~545~~	~~246~~	~~0.707~~	~~0.451~~	~~411~~	~~11~~	~~1~~	~~0.00046~~	~~40.8941985~~	~~0.0132~~	~~35.1~~	~~0.00100~~	~~8.7~~	~~0.24622389~~	~~995.05~~	~~8.7~~	~~0.09540~~	~~34.1~~
BCG-612_S_179	~~1006~~	~~654~~	~~1.38~~	~~0.650~~	~~773~~	~~773~~	~~32~~	~~0.00046~~	~~26.9348344~~	~~0.0117~~	~~18.1~~	~~0.00101~~	~~7.0~~	~~0.38231737~~	~~993.31~~	~~7.0~~	~~0.08429~~	~~16.8~~
BCG-612_S_167	~~2252~~	~~2050~~	~~3.63~~	~~0.910~~	~~1552~~	~~79~~	~~4~~	~~0.00057~~	~~12.2708587~~	~~0.0151~~	~~18.5~~	~~0.00101~~	~~6.4~~	~~0.34476023~~	~~989.15~~	~~6.4~~	~~0.10836~~	~~17.4~~
BCG-612_M_91	~~518~~	~~444~~	~~0.839~~	~~0.857~~	~~371~~	~~68~~	~~3~~	~~0.00056~~	~~36.6590892~~	~~0.0182~~	~~26.2~~	~~0.00102~~	~~8.6~~	~~0.32672049~~	~~984.03~~	~~8.6~~	~~0.13002~~	~~24.7~~
BCG-612_S_193	~~420~~	~~322~~	~~0.782~~	~~0.767~~	~~340~~	~~340~~	~~37~~	~~0.00097~~	~~33.5015754~~	~~0.0155~~	~~59.3~~	~~0.00102~~	~~19.8~~	~~0.33342119~~	~~975.74~~	~~19.8~~	~~0.10959~~	~~55.9~~
BCG-612_M_83	~~328~~	~~231~~	~~0.529~~	~~0.704~~	~~238~~	~~268~~	~~26~~	~~0.00072~~	~~48.6863722~~	~~0.0124~~	~~57.7~~	~~0.00103~~	~~16.5~~	~~0.28667025~~	~~971.77~~	~~16.5~~	~~0.08736~~	~~55.3~~
BCG-612_L_24	~~440~~	~~313~~	~~0.704~~	~~0.711~~	~~373~~	~~373~~	~~24~~	~~0.00063~~	~~24.3958956~~	~~0.0178~~	~~34.9~~	~~0.00103~~	~~11.0~~	~~0.31364434~~	~~968.13~~	~~11.0~~	~~0.12467~~	~~33.1~~
BCG-612_S_165	~~598~~	~~330~~	~~0.740~~	~~0.551~~	~~452~~	~~13~~	~~1~~	~~0.00022~~	~~30.9286825~~	~~0.0138~~	~~31.5~~	~~0.00104~~	~~12.4~~	~~0.39221684~~	~~965.07~~	~~12.4~~	~~0.09659~~	~~29.0~~
BCG-612_M_87	~~156~~	~~85.6~~	~~0.352~~	~~0.548~~	~~111~~	~~24~~	~~3~~	~~0.00178~~	~~30.8734277~~	~~0.0334~~	~~40.3~~	~~0.00105~~	~~26.4~~	~~0.65497911~~	~~955.89~~	~~26.4~~	~~0.23136~~	~~30.5~~
BCG-612_S_208	463	160	0.610	0.346	386	17	2	0.00080	34.5824906	0.0022	104.4	0.00105	10.3	0.09872708	953.56	10.3	0.01517	103.8
BCG-612_S_166	656	411	0.952	0.627	519	17	2	0.00057	27.2980513	0.0090	38.7	0.00105	9.8	0.25395661	951.24	9.8	0.06227	37.5
BCG-612_S_190	~~689~~	~~422~~	~~1.16~~	~~0.612~~	~~545~~	~~32~~	~~1~~	~~0.00075~~	~~17.0914789~~	~~0.0195~~	~~22.7~~	~~0.00111~~	~~6.1~~	~~0.26607354~~	~~897.91~~	~~6.1~~	~~0.12722~~	~~21.8~~
BCG-612_M_74	~~414~~	~~217~~	~~1.04~~	~~0.524~~	~~356~~	~~27~~	~~2~~	~~0.00246~~	~~56.9047797~~	~~0.0179~~	~~55.8~~	~~0.00111~~	~~23.2~~	~~0.414566~~	~~897.74~~	~~23.2~~	~~0.11636~~	~~50.8~~
BCG-612_M_88	~~330~~	~~239~~	~~0.576~~	~~0.722~~	~~249~~	~~13~~	~~1~~	~~0.00059~~	~~28.5439466~~	~~0.0275~~	~~28.2~~	~~0.00113~~	~~12.0~~	~~0.42440476~~	~~885.63~~	~~12.0~~	~~0.17682~~	~~25.5~~
BCG-612_S_181	516	430	0.747	0.833	428	44	3	0.00034	34.7040723	0.0073	58.5	0.00113	10.7	0.18324348	882.81	10.7	0.04646	57.5
BCG-612_S_191	~~1292~~	~~830~~	~~2.36~~	~~0.642~~	~~1035~~	~~1035~~	~~44~~	~~0.00082~~	~~18.4382904~~	~~0.0266~~	~~18.7~~	~~0.00113~~	~~9.0~~	~~0.47984876~~	~~882.61~~	~~9.0~~	~~0.17006~~	~~16.4~~
BCG-612_S_183	~~627~~	~~480~~	~~1.47~~	~~0.766~~	~~566~~	~~30~~	~~2~~	~~0.00131~~	~~37.0768718~~	~~0.0299~~	~~33.6~~	~~0.00114~~	~~12.8~~	~~0.38009524~~	~~873.71~~	~~12.8~~	~~0.18917~~	~~31.1~~
BCG-612_S_196	~~455~~	~~310~~	~~0.920~~	~~0.681~~	~~392~~	~~7~~	~~1~~	~~0.00099~~	~~41.6802898~~	~~0.0291~~	~~42.8~~	~~0.00117~~	~~23.4~~	~~0.54623481~~	~~857.31~~	~~23.4~~	~~0.18099~~	~~35.9~~
BCG-612_S_203	~~629~~	~~536~~	~~1.57~~	~~0.852~~	~~647~~	~~27~~	~~4~~	~~0.00120~~	~~31.7317992~~	~~0.0454~~	~~34.9~~	~~0.00117~~	~~20.5~~	~~0.58731287~~	~~856.85~~	~~20.5~~	~~0.28226~~	~~28.2~~
BCG-612_S_201	~~586~~	~~411~~	~~2.55~~	~~0.701~~	~~690~~	~~28~~	~~1~~	~~0.00293~~	~~10.4285963~~	~~0.0978~~	~~15.0~~	~~0.00164~~	~~9.5~~	~~0.63341584~~	~~607.97~~	~~9.5~~	~~0.43122~~	~~11.6~~
BCG-612_S_189	~~10724~~	~~7859~~	~~113~~	~~0.733~~	~~17227~~	~~30~~	~~2~~	~~0.01150~~	~~52.3375865~~	~~0.0573~~	~~39.2~~	~~0.00171~~	~~21.9~~	~~0.55731802~~	~~583.97~~	~~21.9~~	~~0.24270~~	~~32.6~~
BCG-612_S_204	~~298~~	~~168~~	~~1.54~~	~~0.562~~	~~446~~	~~103~~	~~13~~	~~0.00506~~	~~52.1536862~~	~~0.0637~~	~~50.9~~	~~0.00189~~	~~35.4~~	~~0.69508815~~	~~527.76~~	~~35.4~~	~~0.24382~~	~~36.6~~
BCG-612_S_210	~~296~~	~~360~~	~~3.93~~	~~1.22~~	~~1009~~	~~1009~~	~~93~~	~~0.00532~~	~~25.5511989~~	~~0.3535~~	~~22.2~~	~~0.00439~~	~~18.0~~	~~0.81137487~~	~~227.79~~	~~18.0~~	~~0.58396~~	~~12.9~~
BCG-770	**42.751940**	**112.022740**																
BCG-770_S_215	894	580	0.980	0.649	1425	1425	44	0.00023	20.4371441	0.0070	18.8	0.00092	6.6	0.34953396	1090.08	6.6	0.05563	17.6
BCG-770_S_219	~~105~~	~~54.7~~	~~0.169~~	~~0.522~~	~~219~~	~~25~~	~~2~~	0.00105	32.2821469	0.0143	61.0	0.00098	17.9	0.29298466	1019.94	17.9	0.10572	58.3

Appendix A: LA-ICP-MS U-Pb Composition and Isotopic Ratios

Table S2. U-Pb isotope ratios and trace element concentrations by LA-ICPMS: sample data

				Composition								Corrected isotope ratios						
	U	Th	Pb		206Pb	206Pb		208Pb	±2s	207Pb	±2s	206Pb	±2s	error	238U	±2s	207Pb	±2s
Analysis	ppm	ppm	ppm	Th/U	cps	204Pb	±1s	232Th	(%)	235U	(%)	238U	(%)	corr.	206Pb	(%)	206Pb	(%)
BCG-770_M_96	372	268	0.477	0.720	641	705	38	0.00022	25.715276	0.0072	34.5	0.00108	11.6	0.33712479	926.38	11.6	0.04852	32.4
BCG-770_M_93	358	348	0.572	0.974	682	1501	58	0.00046	23.1907296	0.0069	27.2	0.00111	6.8	0.24884272	898.61	6.8	0.04505	26.4
BCG-770_S_220	~~317~~	~~192~~	~~0.507~~	~~0.605~~	~~605~~	~~30~~	~~1~~	0.00058	25.0384039	0.0162	25.2	0.00116	10.2	0.4047905	863.22	10.2	0.10157	23.0
BCG-770_M_97	~~347~~	~~210~~	~~0.520~~	~~0.607~~	~~654~~	~~63~~	~~3~~	0.00044	31.7174935	0.0115	29.4	0.00116	10.6	0.36024604	862.02	10.6	0.07208	27.4
BCG-770_S_217	158	71.4	0.229	0.452	313	313	23	0.00053	31.2856631	0.0094	50.8	0.00117	13.4	0.26335342	857.21	13.4	0.05852	49.0
BCG-770_S_218	224	179	0.365	0.800	438	24	2	0.00052	24.4725866	0.0101	32.1	0.00117	10.2	0.31797597	855.65	10.2	0.06284	30.4
BCG-770_S_222	781	372	1.32	0.477	1852	2038	55	0.00047	29.4121639	0.0091	27.5	0.00143	4.8	0.17419394	698.50	4.8	0.04587	27.1
BCG-770_S_226	75.2	49.9	0.176	0.663	192	34	3	0.00130	40.8347346	0.0026	74.7	0.00149	18.8	0.25125375	671.44	18.8	0.01269	72.3
BCG-770_M_94	~~189~~	~~143~~	~~0.426~~	~~0.756~~	~~462~~	~~78~~	~~4~~	0.00074	37.8093844	0.0207	37.0	0.00156	13.2	0.3556251	642.85	13.2	0.09669	34.6
BCG-770_S_223	~~153~~	~~112~~	~~0.449~~	~~0.728~~	~~468~~	~~32~~	~~4~~	0.00129	35.9254571	0.0427	32.1	0.00172	18.7	0.58183564	579.73	18.7	0.17967	26.1
BCG-770_S_229	81.4	51.5		0.633	235	235	19	0.00091	39.5856725	#DIV/0!	#DIV/0!	0.00178	15.8	#DIV/0!	562.04	15.8	#DIV/0!	#DIV/0!
BCG-770_S_211	158	123	0.390	0.782	514	514	36	0.00069	32.205996	0.0107	49.0	0.00190	12.0	0.24427417	527.45	12.0	0.04085	47.5
BCG-770_S_225	~~207~~	~~124~~	~~0.905~~	~~0.598~~	~~929~~	~~37~~	~~2~~	0.00238	48.2356975	0.0465	42.2	0.00267	12.4	0.29430289	374.47	12.4	0.12631	40.4
BCG-770_S_228	~~89.3~~	~~102~~	~~0.638~~	~~1.14~~	~~706~~	~~706~~	~~40~~	0.00124	21.9810843	0.0604	23.5	0.00540	9.2	0.3893515	185.34	9.2	0.08117	21.6
BCG-770_S_214	47.0	55.7	5.00	1.19	6328	131	2	0.02267	5.904126	0.6455	5.9	0.07624	3.1	0.52126115	13.12	3.1	0.06140	5.0
BCG-770_M_95	501	611	56.7	1.22	65041	3328	48	0.02542	2.31385908	0.6161	4.0	0.07737	3.0	0.74015324	12.92	3.0	0.05775	2.6
BCG-770_S_224	196	157	19.5	0.798	28216	796	14	0.02148	4.69822311	0.6078	5.3	0.07892	2.8	0.52562485	12.67	2.8	0.05585	4.5
BCG-770_S_216	481	238	46.1	0.495	70507	77556	3184	0.02370	3.65254167	0.6388	3.8	0.07896	2.5	0.6367421	12.66	2.5	0.05868	2.9
BCG-770_M_98	333	377	37.7	1.13	45770	100683	1171	0.02571	2.49303547	0.6036	4.0	0.07992	2.8	0.70082544	12.51	2.8	0.05478	2.8
BCG-770_S_212	214	110	21.0	0.512	30642	30642	462	0.02461	5.26421343	0.6228	5.0	0.08163	2.8	0.54885713	12.25	2.8	0.05533	4.2
BCG-770_S_221	159	38.2	41.5	0.241	61885	7166	226	0.04319	9.32275438	2.9430	6.7	0.22897	6.1	0.90964282	4.37	6.1	0.09322	2.7
BCG-770_S_213	122	124	41.1	1.01	52404	5764	112	0.06729	3.03862366	2.9672	4.3	0.24622	3.0	0.68730264	4.06	3.0	0.08740	3.1
BCG-770_S_227	244	65.8	82.7	0.270	128159	6877	223	0.06171	7.37143504	4.0203	3.4	0.28383	2.4	0.69129468	3.52	2.4	0.10273	2.4

Appendix B: LA-ICP-MS U-Pb Dates

Table S2. U-Pb isotope ratios and trace element concentrations by LA-ICP-MS: sample data

							Dates (Ma)								
	208Pb	±2s	±2s-sys	207Pb	±2s	±2s-sys	207Pb	±2s	±2s-sys	**206Pb**	±2s	±2s-sys	disc.	±2s	
Analysis	232Th	(Ma)	(Ma)	206Pb	(Ma)	(Ma)	235U	(Ma)	(Ma)	**238U**	(Ma)	(Ma)	(%)	(%)	Experiment
BCG-1	**42.802426**	**112.012557**													
BCG-1_S_111	~~37.4~~	~~19.3~~	~~19.3~~	~~**3761**~~	~~**725**~~	~~**725**~~	~~33.7~~	~~18.0~~	~~18.0~~	~~4.35~~	~~1.13~~	~~1.13~~	~~87.1~~	~~7.7~~	~~Zircon_22Sep22_YD_ISU_1~~
BCG-1_S_107	7.87	3.11	3.12	650	920	920	6.84	3.02	3.02	**5.15**	**0.570**	**0.573**	24.7	34.2	Zircon_22Sep22_YD_ISU_1
BCG-1_L_5	~~8.36~~	~~3.54~~	~~3.55~~	~~**1365**~~	~~**839**~~	~~**839**~~	~~9.73~~	~~4.38~~	~~4.39~~	~~5.16~~	~~0.638~~	~~0.641~~	~~47.0~~	~~24.8~~	~~Zircon_22Sep22_YD_ISU_1~~
BCG-1_S_127	8.33	2.66	2.67	420	756	756	6.35	2.20	2.20	**5.31**	**0.417**	**0.422**	16.4	29.7	Zircon_22Sep22_YD_ISU_2
BCG-1_L_12	9.19	3.75	3.76	-535	1893	1893	4.37	3.12	3.12	**5.40**	**0.631**	**0.634**	-23.7	89.5	Zircon_22Sep22_YD_ISU_1
BCG-1_L_6	~~12.1~~	~~3.99~~	~~4.01~~	~~**1329**~~	~~**522**~~	~~**522**~~	~~10.1~~	~~2.82~~	~~2.82~~	~~5.48~~	~~0.395~~	~~0.400~~	~~46.0~~	~~15.5~~	~~Zircon_22Sep22_YD_ISU_1~~
BCG-1_L_4	~~10.1~~	~~4.86~~	~~4.87~~	~~**1762**~~	~~**838**~~	~~**838**~~	~~12.8~~	~~6.09~~	~~6.09~~	~~5.49~~	~~0.779~~	~~0.781~~	~~57.0~~	~~21.4~~	~~Zircon_22Sep22_YD_ISU_1~~
BCG-1_S_133	10.0	2.70	2.71	149	1227	1227	5.87	3.13	3.13	**5.53**	**0.593**	**0.597**	5.9	51.2	Zircon_22Sep22_YD_ISU_2
BCG-1_S_110	6.20	2.37	2.38	335	772	772	6.40	2.29	2.30	**5.56**	**0.637**	**0.640**	13.1	32.7	Zircon_22Sep22_YD_ISU_1
BCG-1_S_149	~~6.85~~	~~1.94~~	~~1.95~~	~~**1530**~~	~~**572**~~	~~**572**~~	~~11.5~~	~~3.66~~	~~3.66~~	~~5.60~~	~~0.570~~	~~0.574~~	~~51.3~~	~~16.3~~	~~Zircon_22Sep22_YD_ISU_2~~
BCG-1_S_134	8.44	3.30	3.31	438	660	660	6.75	2.12	2.12	**5.61**	**0.594**	**0.598**	17.0	27.5	Zircon_22Sep22_YD_ISU_2
BCG-1_S_129	~~10.1~~	~~3.13~~	~~3.14~~	~~**1014**~~	~~**504**~~	~~**504**~~	~~8.86~~	~~2.47~~	~~2.48~~	~~5.61~~	~~0.728~~	~~0.731~~	~~36.7~~	~~19.5~~	~~Zircon_22Sep22_YD_ISU_2~~
BCG-1_S_125	9.73	3.61	3.62	-2441	2654	2654	2.56	1.64	1.64	**5.63**	**0.557**	**0.561**	-120.2	142.9	Zircon_22Sep22_YD_ISU_2
BCG-1_L_17	~~10.9~~	~~3.62~~	~~3.64~~	~~**1299**~~	~~**612**~~	~~**612**~~	~~10.3~~	~~3.47~~	~~3.47~~	~~5.67~~	~~0.688~~	~~0.691~~	~~45.1~~	~~19.6~~	~~Zircon_22Sep22_YD_ISU_1~~
BCG-1_S_101	5.85	2.05	2.06	467	503	503	6.96	1.62	1.62	**5.71**	**0.312**	**0.318**	18.1	19.6	Zircon_22Sep22_YD_ISU_1
BCG-1_M_62	12.3	3.92	3.94	265	947	948	6.39	2.69	2.69	**5.72**	**0.495**	**0.499**	10.4	38.5	Zircon_22Sep22_YD_ISU_1
BCG-1_L_11	~~12.6~~	~~4.64~~	~~4.66~~	~~**1963**~~	~~**387**~~	~~**387**~~	~~14.9~~	~~3.84~~	~~3.85~~	~~5.74~~	~~0.819~~	~~0.822~~	~~61.5~~	~~11.3~~	~~Zircon_22Sep22_YD_ISU_1~~
BCG-1_L_3	~~7.91~~	~~2.55~~	~~2.56~~	~~**1272**~~	~~**772**~~	~~**773**~~	~~10.4~~	~~4.43~~	~~4.43~~	~~5.80~~	~~0.933~~	~~0.936~~	~~44.3~~	~~25.3~~	~~Zircon_22Sep22_YD_ISU_1~~
BCG-1_L_13	~~9.81~~	~~3.79~~	~~3.81~~	~~**745**~~	~~**509**~~	~~**510**~~	~~8.07~~	~~2.06~~	~~2.07~~	~~5.81~~	~~0.515~~	~~0.520~~	~~27.9~~	~~19.5~~	~~Zircon_22Sep22_YD_ISU_1~~
BCG-1_L_8	~~9.22~~	~~2.65~~	~~2.67~~	~~**1772**~~	~~**583**~~	~~**583**~~	~~13.7~~	~~4.76~~	~~4.77~~	~~5.85~~	~~0.850~~	~~0.852~~	~~57.2~~	~~16.1~~	~~Zircon_22Sep22_YD_ISU_1~~
BCG-1_L_2	~~14.8~~	~~10.8~~	~~10.8~~	~~**1765**~~	~~**1090**~~	~~**1090**~~	~~13.7~~	~~8.38~~	~~8.39~~	~~5.89~~	~~0.875~~	~~0.878~~	~~57.1~~	~~27.0~~	~~Zircon_22Sep22_YD_ISU_1~~
BCG-1_S_140	6.22	2.65	2.66	714	781	781	8.06	3.13	3.14	**5.90**	**0.771**	**0.774**	26.9	30.0	Zircon_22Sep22_YD_ISU_2
BCG-1_S_105	~~7.63~~	~~1.91~~	~~1.92~~	~~**1530**~~	~~**287**~~	~~**287**~~	~~12.1~~	~~2.17~~	~~2.18~~	~~5.90~~	~~0.571~~	~~0.575~~	~~51.3~~	~~9.9~~	~~Zircon_22Sep22_YD_ISU_1~~
BCG-1_L_9	16.5	5.30	5.33	-1177	1263	1263	3.82	1.62	1.62	**5.90**	**0.665**	**0.668**	-54.6	67.8	Zircon_22Sep22_YD_ISU_1
BCG-1_M_49	7.87	2.61	2.62	898	813	814	8.82	3.68	3.68	**5.91**	**0.840**	**0.843**	33.0	29.6	Zircon_22Sep22_YD_ISU_1
BCG-1_S_116	8.31	2.01	2.02	701	1302	1302	8.03	4.96	4.96	**5.91**	**0.615**	**0.619**	26.4	46.1	Zircon_22Sep22_YD_ISU_2
BCG-1_M_57	~~14.9~~	~~6.23~~	~~6.26~~	~~**1374**~~	~~**1094**~~	~~**1094**~~	~~11.2~~	~~6.54~~	~~6.54~~	~~5.92~~	~~0.858~~	~~0.860~~	~~47.2~~	~~31.8~~	~~Zircon_22Sep22_YD_ISU_1~~
BCG-1_S_132	~~8.27~~	~~2.61~~	~~2.62~~	~~**1100**~~	~~**612**~~	~~**612**~~	~~9.76~~	~~3.18~~	~~3.18~~	~~5.92~~	~~0.686~~	~~0.689~~	~~39.3~~	~~21.0~~	~~Zircon_22Sep22_YD_ISU_2~~
BCG-1_M_41	~~19.7~~	~~7.92~~	~~7.95~~	~~**3104**~~	~~**455**~~	~~**456**~~	~~30.2~~	~~9.20~~	~~9.21~~	~~5.94~~	~~0.700~~	~~0.703~~	~~80.3~~	~~6.4~~	~~Zircon_22Sep22_YD_ISU_1~~
BCG-1_S_102	~~7.65~~	~~3.00~~	~~3.01~~	~~**1836**~~	~~**579**~~	~~**579**~~	~~14.4~~	~~4.72~~	~~4.72~~	~~5.94~~	~~0.497~~	~~0.501~~	~~58.7~~	~~14.0~~	~~Zircon_22Sep22_YD_ISU_1~~
BCG-1_S_146	6.71	2.62	2.63	773	572	572	8.38	2.58	2.59	**5.96**	**0.885**	**0.888**	28.9	24.4	Zircon_22Sep22_YD_ISU_2
BCG-1_S_124	12.3	3.59	3.61	138	1278	1278	6.31	3.54	3.54	**5.97**	**0.862**	**0.865**	5.4	54.8	Zircon_22Sep22_YD_ISU_2
BCG-1_L_15	~~14.4~~	~~5.20~~	~~5.23~~	~~**1319**~~	~~**421**~~	~~**421**~~	~~11.0~~	~~2.74~~	~~2.75~~	~~5.99~~	~~0.742~~	~~0.745~~	~~45.6~~	~~15.1~~	~~Zircon_22Sep22_YD_ISU_1~~
BCG-1_M_43	~~9.79~~	~~3.01~~	~~3.03~~	~~**1988**~~	~~**644**~~	~~**644**~~	~~15.8~~	~~5.98~~	~~5.98~~	~~6.00~~	~~0.719~~	~~0.722~~	~~62.0~~	~~15.1~~	~~Zircon_22Sep22_YD_ISU_1~~
BCG-1_M_52	10.2	4.39	4.40	-1315	1856	1856	3.72	2.19	2.19	**6.01**	**0.555**	**0.559**	-61.5	96.3	Zircon_22Sep22_YD_ISU_1
BCG-1_L_16	10.4	3.82	3.84	-2	866	866	6.01	2.20	2.20	**6.03**	**0.437**	**0.443**	-0.3	37.4	Zircon_22Sep22_YD_ISU_1
BCG-1_S_123	~~8.13~~	~~3.30~~	~~3.30~~	~~**817**~~	~~**540**~~	~~**540**~~	~~8.66~~	~~2.46~~	~~2.46~~	~~6.03~~	~~0.721~~	~~0.725~~	~~30.3~~	~~21.4~~	~~Zircon_22Sep22_YD_ISU_2~~
BCG-1_S_112	15.9	7.45	7.47	-3554	3770	3770	2.18	1.51	1.51	**6.06**	**0.746**	**0.749**	-177.6	194.5	Zircon_22Sep22_YD_ISU_1
BCG-1_M_55	~~10.6~~	~~4.45~~	~~4.46~~	~~**1233**~~	~~**664**~~	~~**664**~~	~~10.7~~	~~3.78~~	~~3.79~~	~~6.08~~	~~0.658~~	~~0.662~~	~~43.2~~	~~21.0~~	~~Zircon_22Sep22_YD_ISU_1~~
BCG-1_S_114	~~7.66~~	~~3.46~~	~~3.47~~	~~**1191**~~	~~**778**~~	~~**779**~~	~~10.5~~	~~4.37~~	~~4.37~~	~~6.08~~	~~0.855~~	~~0.857~~	~~42.0~~	~~25.5~~	~~Zircon_22Sep22_YD_ISU_1~~
BCG-1_S_113	~~17.0~~	~~6.11~~	~~6.14~~	~~**1565**~~	~~**447**~~	~~**447**~~	~~12.8~~	~~3.29~~	~~3.29~~	~~6.12~~	~~0.606~~	~~0.610~~	~~52.2~~	~~13.2~~	~~Zircon_22Sep22_YD_ISU_1~~
BCG-1_S_126	6.31	1.62	1.63	-386	920	921	5.24	1.88	1.88	**6.12**	**0.400**	**0.407**	-16.9	42.7	Zircon_22Sep22_YD_ISU_2

Appendix B: LA-ICP-MS U-Pb Dates

Table S2. U-Pb isotope ratios and trace element concentrations by LA-ICP-MS: sample data

	Dates (Ma)														
Analysis	208Pb/232Th	±2s (Ma)	±2s-sys (Ma)	207Pb/206Pb	±2s (Ma)	±2s-sys (Ma)	207Pb/235U	±2s (Ma)	±2s-sys (Ma)	**206Pb/238U**	±2s (Ma)	±2s-sys (Ma)	disc. (%)	±2s (%)	Experiment
BCG-1_S_108	6.99	2.69	2.70	-2149	3137	3137	3.00	2.44	2.44	**6.15**	**0.688**	**0.691**	-104.8	168.2	Zircon_22Sep22_YD_ISU_1
BCG-1_S_139	8.36	2.69	2.70	-584	2249	2249	4.89	4.09	4.09	**6.15**	**0.782**	**0.785**	-26.0	106.7	Zircon_22Sep22_YD_ISU_2
BCG-1_M_36	~~5.29~~	~~1.37~~	~~1.38~~	~~**757**~~	~~**435**~~	~~**435**~~	~~8.59~~	~~1.85~~	~~1.85~~	~~6.16~~	~~0.394~~	~~0.400~~	~~28.3~~	~~16.1~~	~~Zircon_22Sep22_YD_ISU_1~~
BCG-1_S_100	9.15	3.86	3.88				0.540	0.380	0.380	**6.22**	**0.704**	**0.707**		822.2	Zircon_22Sep22_YD_ISU_1
BCG-1_M_66	~~5.35~~	~~2.60~~	~~2.61~~	~~**2128**~~	~~**688**~~	~~**688**~~	~~17.7~~	~~7.81~~	~~7.81~~	~~6.23~~	~~1.28~~	~~1.28~~	~~64.9~~	~~17.1~~	~~Zircon_22Sep22_YD_ISU_1~~
BCG-1_S_99	~~8.77~~	~~2.83~~	~~2.84~~	~~**1511**~~	~~**655**~~	~~**655**~~	~~12.7~~	~~4.49~~	~~4.49~~	~~6.24~~	~~0.496~~	~~0.501~~	~~50.8~~	~~17.8~~	~~Zircon_22Sep22_YD_ISU_1~~
BCG-1_S_103	~~13.0~~	~~5.92~~	~~5.94~~	~~**1001**~~	~~**884**~~	~~**884**~~	~~9.84~~	~~4.45~~	~~4.45~~	~~6.28~~	~~0.824~~	~~0.827~~	~~36.2~~	~~30.0~~	~~Zircon_22Sep22_YD_ISU_1~~
BCG-1_S_138	5.97	0.779	0.796	259	307	307	6.99	0.998	1.00	**6.28**	**0.329**	**0.337**	10.1	13.7	Zircon_22Sep22_YD_ISU_2
BCG-1_S_136	~~10.6~~	~~3.61~~	~~3.62~~	~~**2351**~~	~~**511**~~	~~**511**~~	~~20.3~~	~~6.24~~	~~6.24~~	~~6.29~~	~~0.505~~	~~0.510~~	~~69.1~~	~~9.8~~	~~Zircon_22Sep22_YD_ISU_2~~
BCG-1_S_109	6.51	3.22	3.23	-699	1157	1157	4.79	2.00	2.00	**6.29**	**0.259**	**0.269**	-31.4	55.2	Zircon_22Sep22_YD_ISU_1
BCG-1_S_147	~~17.4~~	~~5.91~~	~~5.93~~	~~**1506**~~	~~**708**~~	~~**709**~~	~~12.8~~	~~4.93~~	~~4.93~~	~~6.30~~	~~0.644~~	~~0.648~~	~~50.7~~	~~19.7~~	~~Zircon_22Sep22_YD_ISU_2~~
BCG-1_M_65	~~9.18~~	~~2.75~~	~~2.77~~	~~**1730**~~	~~**621**~~	~~**621**~~	~~14.4~~	~~5.14~~	~~5.14~~	~~6.31~~	~~0.755~~	~~0.758~~	~~56.2~~	~~16.5~~	~~Zircon_22Sep22_YD_ISU_1~~
BCG-1_M_60	~~18.7~~	~~5.24~~	~~5.28~~	~~**2199**~~	~~**478**~~	~~**478**~~	~~18.8~~	~~6.66~~	~~6.67~~	~~6.33~~	~~1.45~~	~~1.45~~	~~66.3~~	~~14.2~~	~~Zircon_22Sep22_YD_ISU_1~~
BCG-1_M_51	~~8.74~~	~~2.63~~	~~2.64~~	~~**914**~~	~~**807**~~	~~**807**~~	~~9.52~~	~~3.87~~	~~3.88~~	~~6.33~~	~~0.743~~	~~0.747~~	~~33.5~~	~~28.2~~	~~Zircon_22Sep22_YD_ISU_1~~
BCG-1_S_135	~~8.79~~	~~3.49~~	~~3.50~~	~~**975**~~	~~**801**~~	~~**801**~~	~~9.83~~	~~3.93~~	~~3.93~~	~~6.35~~	~~0.529~~	~~0.534~~	~~35.4~~	~~26.4~~	~~Zircon_22Sep22_YD_ISU_2~~
BCG-1_M_44	9.66	2.77	2.79	-170	773	773	5.92	1.90	1.90	**6.36**	**0.555**	**0.559**	-7.4	35.8	Zircon_22Sep22_YD_ISU_1
BCG-1_M_58	12.6	3.76	3.79	443	1078	1078	7.69	3.89	3.89	**6.37**	**0.962**	**0.964**	17.2	43.7	Zircon_22Sep22_YD_ISU_1
BCG-1_M_39	8.44	2.74	2.76	104	1021	1022	6.66	2.97	2.97	**6.39**	**0.735**	**0.738**	4.0	44.2	Zircon_22Sep22_YD_ISU_1
BCG-1_L_19	14.6	5.17	5.19	-2354	1958	1958	2.97	1.47	1.47	**6.40**	**0.858**	**0.861**	-115.6	110.8	Zircon_22Sep22_YD_ISU_1
BCG-1_L_18	12.3	4.41	4.43	-281	1328	1328	5.70	3.06	3.06	**6.40**	**0.838**	**0.841**	-12.3	62.0	Zircon_22Sep22_YD_ISU_1
BCG-1_M_54	~~11.1~~	~~4.30~~	~~4.32~~	~~**2166**~~	~~**464**~~	~~**464**~~	~~18.6~~	~~5.70~~	~~5.70~~	~~6.41~~	~~0.997~~	~~1.000~~	~~65.6~~	~~11.8~~	~~Zircon_22Sep22_YD_ISU_1~~
BCG-1_L_7	~~16.7~~	~~4.69~~	~~4.72~~	~~**2538**~~	~~**306**~~	~~**306**~~	~~23.2~~	~~5.25~~	~~5.26~~	~~6.43~~	~~0.887~~	~~0.890~~	~~72.3~~	~~7.3~~	~~Zircon_22Sep22_YD_ISU_1~~
BCG-1_M_34	6.57	1.56	1.58	-2139	2304	2304	3.16	1.91	1.92	**6.46**	**0.784**	**0.788**	-104.3	126.1	Zircon_22Sep22_YD_ISU_1
BCG-1_M_53	~~14.8~~	~~5.59~~	~~5.61~~	~~**886**~~	~~**573**~~	~~**573**~~	~~9.59~~	~~2.91~~	~~2.91~~	~~6.47~~	~~0.815~~	~~0.818~~	~~32.6~~	~~22.1~~	~~Zircon_22Sep22_YD_ISU_1~~
BCG-1_S_122	~~16.8~~	~~5.52~~	~~5.55~~	~~**1667**~~	~~**606**~~	~~**606**~~	~~14.4~~	~~5.69~~	~~5.70~~	~~6.52~~	~~1.47~~	~~1.47~~	~~54.7~~	~~20.6~~	~~Zircon_22Sep22_YD_ISU_2~~
BCG-1_S_117	~~38.1~~	~~14.3~~	~~14.3~~	~~**4118**~~	~~**377**~~	~~**377**~~	~~63.4~~	~~19.9~~	~~19.9~~	~~6.55~~	~~1.31~~	~~1.32~~	~~89.7~~	~~3.8~~	~~Zircon_22Sep22_YD_ISU_2~~
BCG-1_M_61	12.6	5.08	5.10	529	961	961	8.22	3.73	3.73	**6.55**	**0.797**	**0.801**	20.3	37.4	Zircon_22Sep22_YD_ISU_1
BCG-1_M_46	~~7.97~~	~~1.86~~	~~1.89~~	~~**1193**~~	~~**790**~~	~~**790**~~	~~11.3~~	~~4.61~~	~~4.62~~	~~6.57~~	~~0.552~~	~~0.557~~	~~42.0~~	~~24.1~~	~~Zircon_22Sep22_YD_ISU_1~~
BCG-1_S_141	4.85	1.38	1.39	-1128	1525	1525	4.32	2.20	2.20	**6.58**	**0.673**	**0.677**	-52.2	79.0	Zircon_22Sep22_YD_ISU_2
BCG-1_M_38	~~11.8~~	~~3.99~~	~~4.01~~	~~**2122**~~	~~**525**~~	~~**525**~~	~~18.7~~	~~5.86~~	~~5.86~~	~~6.59~~	~~0.661~~	~~0.665~~	~~64.8~~	~~11.6~~	~~Zircon_22Sep22_YD_ISU_1~~
BCG-1_S_130	~~11.7~~	~~2.78~~	~~2.80~~	~~**1535**~~	~~**619**~~	~~**619**~~	~~13.6~~	~~4.52~~	~~4.53~~	~~6.60~~	~~0.430~~	~~0.437~~	~~51.4~~	~~16.5~~	~~Zircon_22Sep22_YD_ISU_2~~
BCG-1_M_47	~~6.93~~	~~2.52~~	~~2.53~~	~~**817**~~	~~**600**~~	~~**600**~~	~~9.48~~	~~2.85~~	~~2.86~~	~~6.61~~	~~0.632~~	~~0.636~~	~~30.3~~	~~22.0~~	~~Zircon_22Sep22_YD_ISU_1~~
BCG-1_M_42	~~5.89~~	~~1.48~~	~~1.49~~	~~**1306**~~	~~**491**~~	~~**491**~~	~~12.1~~	~~3.45~~	~~3.45~~	~~6.61~~	~~0.897~~	~~0.900~~	~~45.3~~	~~17.3~~	~~Zircon_22Sep22_YD_ISU_1~~
BCG-1_S_143	8.26	3.62	3.62	-2784	2059	2059	2.78	1.31	1.31	**6.61**	**0.900**	**0.904**	-138.2	116.8	Zircon_22Sep22_YD_ISU_2
BCG-1_S_119	~~6.47~~	~~2.58~~	~~2.58~~	~~**1358**~~	~~**502**~~	~~**502**~~	~~12.4~~	~~3.45~~	~~3.45~~	~~6.62~~	~~0.663~~	~~0.668~~	~~46.7~~	~~15.7~~	~~Zircon_22Sep22_YD_ISU_2~~
BCG-1_L_20	~~24.1~~	~~11.6~~	~~11.6~~	~~**2666**~~	~~**564**~~	~~**564**~~	~~25.8~~	~~10.1~~	~~10.1~~	~~6.62~~	~~1.34~~	~~1.34~~	~~74.3~~	~~11.3~~	~~Zircon_22Sep22_YD_ISU_1~~
BCG-1_S_131	13.2	4.71	4.73	266	1172	1172	7.43	3.90	3.90	**6.65**	**0.869**	**0.872**	10.4	48.5	Zircon_22Sep22_YD_ISU_2
BCG-1_S_144	7.72	2.09	2.10	846	741	741	9.77	3.61	3.62	**6.72**	**0.714**	**0.719**	31.2	26.5	Zircon_22Sep22_YD_ISU_2
BCG-1_M_37	17.1	5.47	5.51	-293	999	999	5.99	2.47	2.47	**6.75**	**0.901**	**0.905**	-12.8	48.9	Zircon_22Sep22_YD_ISU_1
BCG-1_M_40	~~8.42~~	~~2.14~~	~~2.16~~	~~**1369**~~	~~**683**~~	~~**683**~~	~~12.8~~	~~4.80~~	~~4.81~~	~~6.80~~	~~0.857~~	~~0.861~~	~~47.0~~	~~20.9~~	~~Zircon_22Sep22_YD_ISU_1~~
BCG-1_L_10	~~9.57~~	~~5.73~~	~~5.74~~	~~**1063**~~	~~**753**~~	~~**754**~~	~~11.0~~	~~4.27~~	~~4.27~~	~~6.80~~	~~0.743~~	~~0.747~~	~~38.1~~	~~24.9~~	~~Zircon_22Sep22_YD_ISU_1~~
BCG-1_M_59	~~8.00~~	~~2.81~~	~~2.82~~	~~**959**~~	~~**251**~~	~~**252**~~	~~10.5~~	~~1.71~~	~~1.71~~	~~6.82~~	~~0.739~~	~~0.743~~	~~34.9~~	~~12.7~~	~~Zircon_22Sep22_YD_ISU_1~~
BCG-1_S_106	7.41	2.22	2.24				1.88	1.08	1.08	**6.85**	**0.692**	**0.696**		213.1	Zircon_22Sep22_YD_ISU_1
BCG-1_S_121	6.83	1.80	1.81	-2527	1853	1853	3.06	1.34	1.35	**6.87**	**0.537**	**0.543**	-124.7	100.4	Zircon_22Sep22_YD_ISU_2
BCG-1_S_137	6.58	1.83	1.84	-1860	1312	1312	3.66	1.35	1.36	**6.94**	**0.558**	**0.564**	-89.7	71.9	Zircon_22Sep22_YD_ISU_2
BCG-1_M_64	10.8	3.57	3.59	866	878	878	10.2	4.47	4.47	**6.97**	**0.807**	**0.811**	31.9	30.8	Zircon_22Sep22_YD_ISU_1

Appendix B: LA-ICP-MS U-Pb Dates

Table S2. U-Pb isotope ratios and trace element concentrations by LA-ICP-MS: sample data															
							Dates (Ma)								
Analysis	208Pb/232Th	±2s (Ma)	±2s-sys (Ma)	207Pb/206Pb	±2s (Ma)	±2s-sys (Ma)	207Pb/235U	±2s (Ma)	±2s-sys (Ma)	**206Pb/238U**	±2s (Ma)	±2s-sys (Ma)	disc. (%)	±2s (%)	Experiment
BCG-1_M_56	~~10.8~~	~~2.18~~	~~2.22~~	**~~1602~~**	**~~336~~**	**~~336~~**	~~15.0~~	~~2.86~~	~~2.87~~	~~7.03~~	~~0.471~~	~~0.477~~	~~53.1~~	~~9.5~~	~~Zircon_22Sep22_YD_ISU_1~~
BCG-1_M_48	16.8	5.68	5.71	-28	1279	1280	6.94	3.80	3.80	**7.04**	**1.07**	**1.07**	-1.5	57.6	Zircon_22Sep22_YD_ISU_1
BCG-1_M_45	~~15.0~~	~~4.32~~	~~4.35~~	**~~2182~~**	**~~253~~**	**~~254~~**	~~20.8~~	~~3.79~~	~~3.80~~	~~7.09~~	~~0.797~~	~~0.801~~	~~65.9~~	~~7.3~~	~~Zircon_22Sep22_YD_ISU_1~~
BCG-1_S_120	8.16	2.66	2.67	446	473	473	8.68	1.97	1.98	**7.18**	**0.597**	**0.603**	17.2	20.1	Zircon_22Sep22_YD_ISU_2
BCG-1_S_145	~~18.8~~	~~6.08~~	~~6.10~~	**~~2205~~**	**~~476~~**	**~~476~~**	~~21.5~~	~~6.18~~	~~6.18~~	~~7.22~~	~~0.702~~	~~0.707~~	~~66.4~~	~~10.2~~	~~Zircon_22Sep22_YD_ISU_2~~
BCG-1_L_1	42.2	12.2	12.2	414	2494	2494	8.61	9.80	9.80	**7.23**	**1.78**	**1.78**	16.0	97.7	Zircon_22Sep22_YD_ISU_1
BCG-1_L_14	~~31.1~~	~~8.01~~	~~8.08~~	**~~3345~~**	**~~431~~**	**~~431~~**	~~43.3~~	~~13.5~~	~~13.5~~	~~7.36~~	~~1.18~~	~~1.18~~	~~83.0~~	~~6.0~~	~~Zircon_22Sep22_YD_ISU_1~~
BCG-1_M_50	~~36.9~~	~~12.8~~	~~12.9~~	**~~2095~~**	**~~1013~~**	**~~1013~~**	~~20.8~~	~~12.1~~	~~12.1~~	~~7.45~~	~~0.917~~	~~0.920~~	~~64.2~~	~~21.4~~	~~Zircon_22Sep22_YD_ISU_1~~
BCG-1_M_63	~~65.0~~	~~38.5~~	~~38.5~~	**~~3796~~**	**~~425~~**	**~~425~~**	~~58.5~~	~~20.6~~	~~20.6~~	~~7.47~~	~~1.70~~	~~1.70~~	~~87.2~~	~~5.3~~	~~Zircon_22Sep22_YD_ISU_1~~
BCG-1_S_118	~~12.1~~	~~4.54~~	~~4.55~~	**~~1855~~**	**~~655~~**	**~~655~~**	~~19.7~~	~~7.41~~	~~7.41~~	~~8.07~~	~~0.910~~	~~0.915~~	~~59.0~~	~~16.1~~	~~Zircon_22Sep22_YD_ISU_2~~
BCG-1_S_115	~~31.0~~	~~7.78~~	~~7.83~~	**~~3466~~**	**~~300~~**	**~~301~~**	~~62.3~~	~~14.2~~	~~14.2~~	~~9.88~~	~~1.31~~	~~1.32~~	~~84.1~~	~~4.2~~	~~Zircon_22Sep22_YD_ISU_2~~
BCG-1_S_142	~~93.3~~	~~34.6~~	~~34.7~~	**~~3512~~**	**~~490~~**	**~~490~~**	~~64.2~~	~~22.6~~	~~22.7~~	~~9.90~~	~~1.77~~	~~1.77~~	~~84.6~~	~~6.1~~	~~Zircon_22Sep22_YD_ISU_2~~
BCG-1_S_104	~~74.8~~	~~26.2~~	~~26.3~~	**~~3509~~**	**~~387~~**	**~~387~~**	~~68.5~~	~~19.4~~	~~19.4~~	~~10.6~~	~~1.61~~	~~1.61~~	~~84.5~~	~~5.0~~	~~Zircon_22Sep22_YD_ISU_1~~
BCG-1_S_128	~~44.5~~	~~10.5~~	~~10.6~~	**~~3674~~**	**~~358~~**	**~~358~~**	~~76.6~~	~~19.8~~	~~19.8~~	~~10.7~~	~~1.40~~	~~1.41~~	~~86.0~~	~~4.1~~	~~Zircon_22Sep22_YD_ISU_2~~
BCG-1_S_148	~~76.2~~	~~19.2~~	~~19.3~~	**~~4054~~**	**~~442~~**	**~~442~~**	~~134~~	~~50.3~~	~~50.3~~	~~15.0~~	~~4.01~~	~~4.02~~	~~88.8~~	~~5.1~~	~~Zircon_22Sep22_YD_ISU_2~~
BCG-1_M_33	~~205~~	~~81.9~~	~~82.2~~	**~~4502~~**	**~~192~~**	**~~193~~**	~~249~~	~~87.4~~	~~87.5~~	~~21.7~~	~~8.08~~	~~8.09~~	~~91.3~~	~~4.5~~	~~Zircon_22Sep22_YD_ISU_1~~
BCG-1_M_35	~~156~~	~~37.9~~	~~38.3~~	**~~4784~~**	**~~70.2~~**	**~~70.8~~**	~~371~~	~~84.5~~	~~84.6~~	~~28.3~~	~~7.56~~	~~7.56~~	~~92.4~~	~~2.7~~	~~Zircon_22Sep22_YD_ISU_1~~
BCG-273	**42.754171**	**112.021274**													
BCG-273_L_23	9.91	2.89	2.91	287	1128	1128	6.85	3.46	3.46	**6.08**	**0.714**	**0.718**	11.3	46.1	Zircon_22Sep22_YD_ISU_1
BCG-273_M_71	9.64	2.52	2.54	47.8	1062	1062	7.66	3.43	3.43	**7.53**	**0.494**	**0.501**	1.7	44.5	Zircon_22Sep22_YD_ISU_1
BCG-273_M_72	~~21.4~~	~~7.49~~	~~7.53~~	**~~1876~~**	**~~846~~**	**~~846~~**	~~24.3~~	~~11.6~~	~~11.6~~	~~9.87~~	~~1.13~~	~~1.14~~	~~59.4~~	~~19.9~~	~~Zircon_22Sep22_YD_ISU_1~~
BCG-273_S_161	494	14.4	19.6	425	60.4	61.5	466	11.9	12.8	**475**	**7.61**	**9.37**	-1.8	3.1	Zircon_22Sep22_YD_ISU_2
BCG-273_S_163	509	43.0	45.1	502	122	122	494	24.7	25.2	**492**	**14.5**	**15.5**	0.3	5.8	Zircon_22Sep22_YD_ISU_2
BCG-273_S_159	522	68.4	69.8	613	128	129	515	28.8	29.3	**493**	**18.8**	**19.6**	4.2	6.5	Zircon_22Sep22_YD_ISU_2
BCG-273_S_158	474	24.4	27.5	358	104	105	470	22.1	22.6	**493**	**17.2**	**18.1**	-4.9	6.1	Zircon_22Sep22_YD_ISU_2
BCG-273_S_162	477	29.5	32.2	372	154	154	475	28.5	29.0	**496**	**15.2**	**16.2**	-4.6	7.1	Zircon_22Sep22_YD_ISU_2
BCG-273_S_164	488	18.4	22.6	381	251	251	487	45.0	45.3	**511**	**16.1**	**17.1**	-4.7	10.2	Zircon_22Sep22_YD_ISU_2
BCG-273_S_160	~~658~~	~~84.5~~	~~86.4~~	**~~2426~~**	**~~53.9~~**	**~~54.6~~**	~~1282~~	~~125~~	~~126~~	~~713~~	~~114~~	~~115~~	~~44.4~~	~~10.4~~	~~Zircon_22Sep22_YD_ISU_2~~
BCG-30	**42.751736**	**112.021480**													
BCG-30_S_154	11.8	4.04	4.05	876	1472	1472	8.49	6.11	6.12	**5.75**	**0.761**	**0.764**	32.3	49.6	Zircon_22Sep22_YD_ISU_2
BCG-30_S_153	9.03	3.55	3.56	234	924	924	6.92	2.90	2.90	**6.28**	**0.796**	**0.799**	9.2	39.7	Zircon_22Sep22_YD_ISU_2
BCG-30_S_151	~~12.2~~	~~2.16~~	~~2.19~~	**~~1159~~**	**~~402~~**	**~~402~~**	~~11.6~~	~~2.62~~	~~2.62~~	~~6.82~~	~~0.707~~	~~0.712~~	~~41.0~~	~~14.7~~	~~Zircon_22Sep22_YD_ISU_2~~
BCG-30_L_21	~~9.87~~	~~2.61~~	~~2.64~~	**~~1521~~**	**~~846~~**	**~~846~~**	~~15.5~~	~~7.17~~	~~7.17~~	~~7.62~~	~~0.930~~	~~0.934~~	~~51.0~~	~~23.4~~	~~Zircon_22Sep22_YD_ISU_1~~
BCG-30_L_22	~~29.1~~	~~9.28~~	~~9.34~~	**~~2702~~**	**~~940~~**	**~~940~~**	~~30.5~~	~~18.2~~	~~18.2~~	~~7.68~~	~~1.61~~	~~1.61~~	~~74.8~~	~~16.0~~	~~Zircon_22Sep22_YD_ISU_1~~
BCG-30_M_70	24.6	9.95	9.99	816	952	952	11.1	5.35	5.35	**7.73**	**1.30**	**1.31**	30.2	35.7	Zircon_22Sep22_YD_ISU_1
BCG-30_M_69	~~23.0~~	~~8.29~~	~~8.33~~	**~~2722~~**	**~~539~~**	**~~539~~**	~~32.6~~	~~12.4~~	~~12.4~~	~~8.13~~	~~1.69~~	~~1.69~~	~~75.1~~	~~10.8~~	~~Zircon_22Sep22_YD_ISU_1~~
BCG-30_M_67	11.1	5.40	5.42	36.0	1059	1059	8.47	3.93	3.93	**8.37**	**1.23**	**1.24**	1.1	48.2	Zircon_22Sep22_YD_ISU_1
BCG-30_M_68	39.0	24.4	24.5	876	1153	1154	12.5	7.13	7.13	**8.51**	**1.11**	**1.11**	32.1	39.6	Zircon_22Sep22_YD_ISU_1
BCG-30_S_152	~~18.6~~	~~4.78~~	~~4.81~~	**~~923~~**	**~~739~~**	**~~739~~**	~~13.2~~	~~4.91~~	~~4.91~~	~~8.76~~	~~0.899~~	~~0.904~~	~~33.7~~	~~25.6~~	~~Zircon_22Sep22_YD_ISU_2~~
BCG-30_S_150	~~26.3~~	~~8.41~~	~~8.44~~	**~~1841~~**	**~~839~~**	**~~839~~**	~~23.5~~	~~11.2~~	~~11.2~~	~~9.73~~	~~1.30~~	~~1.31~~	~~58.6~~	~~20.5~~	~~Zircon_22Sep22_YD_ISU_2~~
BCG-30_S_157	463	48.0	49.6	235	234	234	434	37.8	38.1	**473**	**15.8**	**16.7**	-8.8	10.2	Zircon_22Sep22_YD_ISU_2
BCG-30_S_155	492	17.5	21.9	389	154	154	475	29.5	29.9	**493**	**17.5**	**18.4**	-3.8	7.4	Zircon_22Sep22_YD_ISU_2
BCG-30_S_156	495	32.5	35.2	441	181	182	486	34.1	34.5	**496**	**16.2**	**17.1**	-2.0	7.9	Zircon_22Sep22_YD_ISU_2
BCG-612	**42.765764**	**112.013782**													
BCG-612_S_178	~~7.32~~	~~2.63~~	~~2.64~~	**~~1386~~**	**~~608~~**	**~~608~~**	~~9.58~~	~~3.25~~	~~3.25~~	~~5.03~~	~~0.630~~	~~0.633~~	~~47.5~~	~~19.0~~	~~Zircon_22Sep22_YD_ISU_2~~

Appendix B: LA-ICP-MS U-Pb Dates

Table S2. U-Pb isotope ratios and trace element concentrations by LA-ICP-MS: sample data

	Dates (Ma)														
Analysis	208Pb/232Th	±2s (Ma)	±2s-sys (Ma)	207Pb/206Pb	±2s (Ma)	±2s-sys (Ma)	207Pb/235U	±2s (Ma)	±2s-sys (Ma)	**206Pb/238U**	±2s (Ma)	±2s-sys (Ma)	disc. (%)	±2s (%)	Experiment
BCG-612_L_27	~~14.4~~	~~5.00~~	~~5.03~~	~~**2246**~~	~~**521**~~	~~**521**~~	~~15.5~~	~~5.18~~	~~5.19~~	~~5.08~~	~~0.759~~	~~0.762~~	~~67.2~~	~~12.0~~	~~Zircon_22Sep22_YD_ISU_1~~
BCG-612_S_170	~~14.5~~	~~4.07~~	~~4.08~~	~~**1680**~~	~~**1262**~~	~~**1262**~~	~~11.6~~	~~8.00~~	~~8.01~~	~~5.20~~	~~0.680~~	~~0.682~~	~~55.1~~	~~31.6~~	~~Zircon_22Sep22_YD_ISU_2~~
BCG-612_S_176	5.18	1.15	1.16	-203	691	691	4.95	1.42	1.42	**5.39**	**0.423**	**0.428**	-8.8	32.3	Zircon_22Sep22_YD_ISU_2
BCG-612_S_185	6.48	2.41	2.41	813	1101	1101	7.77	4.12	4.12	**5.42**	**0.422**	**0.427**	30.2	37.4	Zircon_22Sep22_YD_ISU_2
BCG-612_S_169	9.59	4.29	4.30				0.877	0.436	0.436	**5.44**	**0.628**	**0.632**		316.5	Zircon_22Sep22_YD_ISU_2
BCG-612_L_32	~~12.8~~	~~5.21~~	~~5.23~~	~~**2143**~~	~~**740**~~	~~**740**~~	~~15.8~~	~~6.89~~	~~6.89~~	~~5.49~~	~~0.647~~	~~0.650~~	~~65.2~~	~~15.7~~	~~Zircon_22Sep22_YD_ISU_1~~
BCG-612_S_172	7.07	1.63	1.64	279	984	984	6.17	2.69	2.69	**5.49**	**0.452**	**0.457**	11.0	39.5	Zircon_22Sep22_YD_ISU_2
BCG-612_S_197	~~9.03~~	~~1.58~~	~~1.60~~	~~**1020**~~	~~**546**~~	~~**546**~~	~~8.81~~	~~2.63~~	~~2.64~~	~~5.56~~	~~0.738~~	~~0.741~~	~~36.9~~	~~20.7~~	~~Zircon_22Sep22_YD_ISU_2~~
BCG-612_M_77	~~14.6~~	~~6.30~~	~~6.32~~	~~**2081**~~	~~**957**~~	~~**957**~~	~~15.4~~	~~8.78~~	~~8.79~~	~~5.56~~	~~1.01~~	~~1.01~~	~~64.0~~	~~21.5~~	~~Zircon_22Sep22_YD_ISU_1~~
BCG-612_S_207	~~9.74~~	~~3.70~~	~~3.71~~	~~**1132**~~	~~**833**~~	~~**833**~~	~~9.32~~	~~4.04~~	~~4.04~~	~~5.57~~	~~0.658~~	~~0.661~~	~~40.3~~	~~26.8~~	~~Zircon_22Sep22_YD_ISU_2~~
BCG-612_M_84	8.94	2.53	2.55	655	609	610	7.43	2.16	2.16	**5.59**	**0.370**	**0.376**	24.8	22.4	Zircon_22Sep22_YD_ISU_1
BCG-612_S_194	8.92	2.69	2.70	130	1154	1154	5.89	2.97	2.97	**5.59**	**0.674**	**0.677**	5.1	49.1	Zircon_22Sep22_YD_ISU_2
BCG-612_M_90	~~5.30~~	~~1.81~~	~~1.82~~	~~**1768**~~	~~**544**~~	~~**544**~~	~~13.1~~	~~4.04~~	~~4.04~~	~~5.60~~	~~0.505~~	~~0.510~~	~~57.2~~	~~13.8~~	~~Zircon_22Sep22_YD_ISU_1~~
BCG-612_S_174	~~12.6~~	~~4.50~~	~~4.51~~	~~**1661**~~	~~**689**~~	~~**689**~~	~~12.3~~	~~4.86~~	~~4.86~~	~~5.60~~	~~0.760~~	~~0.762~~	~~54.6~~	~~18.9~~	~~Zircon_22Sep22_YD_ISU_2~~
BCG-612_S_184	8.43	4.13	4.14	-1790	2777	2777	3.03	2.38	2.38	**5.64**	**0.478**	**0.482**	-86.0	146.5	Zircon_22Sep22_YD_ISU_2
BCG-612_S_205	11.4	3.70	3.71	-251	1756	1756	5.10	3.58	3.58	**5.66**	**0.680**	**0.683**	-10.9	79.0	Zircon_22Sep22_YD_ISU_2
BCG-612_S_182	8.12	2.09	2.10	-332	1197	1197	4.98	2.41	2.41	**5.70**	**0.796**	**0.799**	-14.5	57.7	Zircon_22Sep22_YD_ISU_2
BCG-612_S_192	5.41	1.29	1.29	669	563	563	7.64	2.09	2.09	**5.71**	**0.459**	**0.463**	25.3	21.3	Zircon_22Sep22_YD_ISU_2
BCG-612_M_86	7.82	3.48	3.49	-2581	3207	3207	2.53	1.88	1.88	**5.75**	**0.494**	**0.498**	-127.6	170.5	Zircon_22Sep22_YD_ISU_1
BCG-612_L_26	9.05	2.62	2.64	189	997	997	6.21	2.73	2.73	**5.75**	**0.609**	**0.612**	7.4	41.9	Zircon_22Sep22_YD_ISU_1
BCG-612_M_79	7.50	2.58	2.60	310	767	767	6.57	2.32	2.32	**5.77**	**0.631**	**0.635**	12.2	32.5	Zircon_22Sep22_YD_ISU_1
BCG-612_S_195	7.19	1.86	1.87	-123	955	955	5.49	2.20	2.20	**5.79**	**0.607**	**0.611**	-5.4	43.6	Zircon_22Sep22_YD_ISU_2
BCG-612_M_78	~~9.81~~	~~3.52~~	~~3.53~~	~~**1417**~~	~~**695**~~	~~**695**~~	~~11.4~~	~~4.32~~	~~4.32~~	~~5.87~~	~~0.699~~	~~0.702~~	~~48.3~~	~~20.6~~	~~Zircon_22Sep22_YD_ISU_1~~
BCG-612_S_171	10.9	2.02	2.05	-1083	2439	2439	3.92	3.20	3.20	**5.87**	**0.820**	**0.823**	-49.9	124.4	Zircon_22Sep22_YD_ISU_2
BCG-612_M_89	~~14.2~~	~~5.42~~	~~5.44~~	~~**1605**~~	~~**532**~~	~~**532**~~	~~12.7~~	~~3.80~~	~~3.80~~	~~5.92~~	~~0.585~~	~~0.589~~	~~53.2~~	~~14.8~~	~~Zircon_22Sep22_YD_ISU_1~~
BCG-612_S_175	~~6.08~~	~~2.85~~	~~2.85~~	~~**1640**~~	~~**572**~~	~~**572**~~	~~12.9~~	~~4.26~~	~~4.26~~	~~5.93~~	~~0.726~~	~~0.729~~	~~54.1~~	~~16.1~~	~~Zircon_22Sep22_YD_ISU_2~~
BCG-612_S_209	10.4	3.28	3.29				1.43	0.906	0.906	**5.96**	**0.857**	**0.860**		269.7	Zircon_22Sep22_YD_ISU_2
BCG-612_S_188	6.46	2.30	2.31	-484	1296	1296	4.92	2.45	2.45	**5.97**	**0.587**	**0.591**	-21.4	61.5	Zircon_22Sep22_YD_ISU_2
BCG-612_S_199	~~9.83~~	~~2.51~~	~~2.53~~	~~**1387**~~	~~**687**~~	~~**687**~~	~~11.4~~	~~4.18~~	~~4.18~~	~~6.00~~	~~0.505~~	~~0.509~~	~~47.5~~	~~19.7~~	~~Zircon_22Sep22_YD_ISU_2~~
BCG-612_S_202	~~16.3~~	~~5.18~~	~~5.20~~	~~**2855**~~	~~**342**~~	~~**342**~~	~~26.2~~	~~6.18~~	~~6.19~~	~~6.00~~	~~0.681~~	~~0.685~~	~~77.1~~	~~6.0~~	~~Zircon_22Sep22_YD_ISU_2~~
BCG-612_S_198	7.21	2.00	2.01	-338	910	911	5.24	1.91	1.91	**6.02**	**0.548**	**0.552**	-14.8	43.1	Zircon_22Sep22_YD_ISU_2
BCG-612_L_25	~~8.44~~	~~3.16~~	~~3.17~~	~~**1143**~~	~~**630**~~	~~**630**~~	~~10.2~~	~~3.59~~	~~3.59~~	~~6.07~~	~~0.937~~	~~0.939~~	~~40.6~~	~~22.8~~	~~Zircon_22Sep22_YD_ISU_1~~
BCG-612_L_28	~~10.0~~	~~4.34~~	~~4.36~~	~~**1198**~~	~~**395**~~	~~**396**~~	~~10.5~~	~~2.36~~	~~2.37~~	~~6.09~~	~~0.625~~	~~0.629~~	~~42.2~~	~~14.2~~	~~Zircon_22Sep22_YD_ISU_1~~
BCG-612_S_206	6.27	1.32	1.33	-217	707	707	5.57	1.61	1.61	**6.10**	**0.418**	**0.424**	-9.5	32.5	Zircon_22Sep22_YD_ISU_2
BCG-612_S_180	6.34	1.31	1.32	-179	1208	1208	5.66	2.77	2.77	**6.10**	**0.479**	**0.485**	-7.8	53.4	Zircon_22Sep22_YD_ISU_2
BCG-612_L_29	11.3	3.30	3.33	381	687	687	7.17	2.24	2.24	**6.11**	**0.410**	**0.416**	14.9	27.2	Zircon_22Sep22_YD_ISU_1
BCG-612_M_75	12.3	3.63	3.65	-232	1286	1286	5.56	2.93	2.93	**6.13**	**0.839**	**0.842**	-10.1	59.9	Zircon_22Sep22_YD_ISU_1
BCG-612_S_200	8.09	2.00	2.01	902	1247	1247	9.17	5.60	5.60	**6.13**	**0.644**	**0.648**	33.1	41.5	Zircon_22Sep22_YD_ISU_2
BCG-612_M_80	~~8.62~~	~~3.42~~	~~3.43~~	~~**1168**~~	~~**658**~~	~~**658**~~	~~10.5~~	~~3.84~~	~~3.85~~	~~6.18~~	~~0.960~~	~~0.963~~	~~41.3~~	~~23.3~~	~~Zircon_22Sep22_YD_ISU_1~~
BCG-612_M_92	9.15	2.21	2.23	432	644	645	7.43	2.25	2.25	**6.19**	**0.572**	**0.576**	16.8	26.3	Zircon_22Sep22_YD_ISU_1
BCG-612_S_168	~~6.35~~	~~5.91~~	~~5.91~~	~~**2155**~~	~~**702**~~	~~**702**~~	~~17.9~~	~~7.38~~	~~7.38~~	~~6.20~~	~~0.638~~	~~0.642~~	~~65.4~~	~~14.7~~	~~Zircon_22Sep22_YD_ISU_2~~
BCG-612_S_173	~~8.27~~	~~1.40~~	~~1.42~~	~~**706**~~	~~**423**~~	~~**423**~~	~~8.47~~	~~1.76~~	~~1.77~~	~~6.22~~	~~0.404~~	~~0.411~~	~~26.6~~	~~16.0~~	~~Zircon_22Sep22_YD_ISU_2~~
BCG-612_M_73	12.1	4.43	4.45	332	1269	1269	7.18	4.07	4.07	**6.25**	**0.634**	**0.638**	13.0	50.1	Zircon_22Sep22_YD_ISU_1
BCG-612_S_177	~~7.74~~	~~3.33~~	~~3.34~~	~~**1839**~~	~~**686**~~	~~**686**~~	~~15.1~~	~~5.87~~	~~5.87~~	~~6.25~~	~~0.595~~	~~0.600~~	~~58.8~~	~~16.5~~	~~Zircon_22Sep22_YD_ISU_2~~
BCG-612_M_81	~~17.2~~	~~5.19~~	~~5.23~~	~~**1774**~~	~~**944**~~	~~**944**~~	~~14.8~~	~~7.82~~	~~7.82~~	~~6.34~~	~~0.753~~	~~0.756~~	~~57.3~~	~~23.1~~	~~Zircon_22Sep22_YD_ISU_1~~
BCG-612_M_82	6.80	3.02	3.03	492	726	726	7.85	2.80	2.80	**6.36**	**0.897**	**0.900**	19.0	31.1	Zircon_22Sep22_YD_ISU_1

Appendix B: LA-ICP-MS U-Pb Dates

Table S2. U-Pb isotope ratios and trace element concentrations by LA-ICP-MS: sample data

							Dates (Ma)								
Analysis	208Pb/232Th	±2s (Ma)	±2s-sys (Ma)	207Pb/206Pb	±2s (Ma)	±2s-sys (Ma)	207Pb/235U	±2s (Ma)	±2s-sys (Ma)	**206Pb/238U**	±2s (Ma)	±2s-sys (Ma)	disc. (%)	±2s (%)	Experiment
BCG-612_S_187	6.88	2.04	2.05	616	820	820	8.32	3.26	3.26	**6.37**	**0.644**	**0.648**	23.4	31.0	Zircon_22Sep22_YD_ISU_2
BCG-612_L_31	7.13	3.51	3.52	-1116	1636	1636	4.21	2.34	2.34	**6.38**	**0.907**	**0.910**	-51.6	86.9	Zircon_22Sep22_YD_ISU_1
BCG-612_M_76	7.18	2.75	2.76	-957	1700	1700	4.47	2.60	2.60	**6.43**	**0.392**	**0.399**	-43.7	84.0	Zircon_22Sep22_YD_ISU_1
BCG-612_S_186	6.29	1.58	1.58	92.9	398	398	6.67	1.25	1.25	**6.43**	**0.542**	**0.547**	3.5	19.8	Zircon_22Sep22_YD_ISU_2
BCG-612_M_85	~~6.46~~	~~1.52~~	~~1.54~~	~~**953**~~	~~**387**~~	~~**387**~~	~~9.88~~	~~2.07~~	~~2.08~~	~~6.45~~	~~0.602~~	~~0.607~~	~~34.7~~	~~15.0~~	~~Zircon_22Sep22_YD_ISU_1~~
BCG-612_L_30	~~9.28~~	~~3.79~~	~~3.81~~	~~**1536**~~	~~**641**~~	~~**641**~~	~~13.3~~	~~4.66~~	~~4.66~~	~~6.48~~	~~0.561~~	~~0.566~~	~~51.4~~	~~17.5~~	~~Zircon_22Sep22_YD_ISU_1~~
BCG-612_S_179	~~9.28~~	~~2.50~~	~~2.51~~	~~**1299**~~	~~**326**~~	~~**326**~~	~~11.8~~	~~2.13~~	~~2.13~~	~~6.49~~	~~0.451~~	~~0.457~~	~~45.1~~	~~10.6~~	~~Zircon_22Sep22_YD_ISU_2~~
BCG-612_S_167	~~11.4~~	~~1.40~~	~~1.44~~	~~**1772**~~	~~**317**~~	~~**318**~~	~~15.2~~	~~2.80~~	~~2.81~~	~~6.51~~	~~0.417~~	~~0.424~~	~~57.2~~	~~8.3~~	~~Zircon_22Sep22_YD_ISU_2~~
BCG-612_M_91	~~11.4~~	~~4.17~~	~~4.19~~	~~**2098**~~	~~**434**~~	~~**435**~~	~~18.3~~	~~4.76~~	~~4.76~~	~~6.55~~	~~0.561~~	~~0.566~~	~~64.3~~	~~9.8~~	~~Zircon_22Sep22_YD_ISU_1~~
BCG-612_S_193	~~19.6~~	~~6.58~~	~~6.60~~	~~**1793**~~	~~**1018**~~	~~**1018**~~	~~15.6~~	~~9.18~~	~~9.18~~	~~6.60~~	~~1.31~~	~~1.31~~	~~57.7~~	~~26.3~~	~~Zircon_22Sep22_YD_ISU_2~~
BCG-612_M_83	~~14.5~~	~~7.05~~	~~7.07~~	~~**1368**~~	~~**1064**~~	~~**1064**~~	~~12.5~~	~~7.17~~	~~7.17~~	~~6.63~~	~~1.10~~	~~1.10~~	~~47.0~~	~~31.6~~	~~Zircon_22Sep22_YD_ISU_1~~
BCG-612_L_24	~~12.8~~	~~3.12~~	~~3.15~~	~~**2024**~~	~~**586**~~	~~**587**~~	~~17.9~~	~~6.18~~	~~6.18~~	~~6.66~~	~~0.729~~	~~0.733~~	~~62.8~~	~~13.5~~	~~Zircon_22Sep22_YD_ISU_1~~
BCG-612_S_165	~~4.54~~	~~1.40~~	~~1.41~~	~~**1559**~~	~~**544**~~	~~**544**~~	~~13.9~~	~~4.36~~	~~4.36~~	~~6.68~~	~~0.826~~	~~0.830~~	~~52.0~~	~~16.2~~	~~Zircon_22Sep22_YD_ISU_2~~
BCG-612_M_87	~~36.0~~	~~11.1~~	~~11.2~~	~~**3062**~~	~~**487**~~	~~**487**~~	~~33.3~~	~~13.2~~	~~13.2~~	~~6.74~~	~~1.78~~	~~1.78~~	~~79.8~~	~~9.6~~	~~Zircon_22Sep22_YD_ISU_1~~
BCG-612_S_208	16.1	5.57	5.58	-4088	6602	6602	2.22	2.32	2.32	**6.76**	**0.697**	**0.701**	-203.7	318.2	Zircon_22Sep22_YD_ISU_2
BCG-612_S_166	11.5	3.14	3.15	683	800	800	9.12	3.52	3.52	**6.77**	**0.667**	**0.671**	25.8	29.5	Zircon_22Sep22_YD_ISU_2
BCG-612_S_190	~~15.1~~	~~2.58~~	~~2.61~~	~~**2060**~~	~~**385**~~	~~**385**~~	~~19.6~~	~~4.41~~	~~4.42~~	~~7.18~~	~~0.434~~	~~0.442~~	~~63.5~~	~~8.5~~	~~Zircon_22Sep22_YD_ISU_2~~
BCG-612_M_74	~~49.7~~	~~28.2~~	~~28.3~~	~~**1901**~~	~~**913**~~	~~**913**~~	~~18.0~~	~~9.96~~	~~9.96~~	~~7.18~~	~~1.66~~	~~1.66~~	~~60.1~~	~~23.9~~	~~Zircon_22Sep22_YD_ISU_1~~
BCG-612_M_88	~~11.9~~	~~3.40~~	~~3.43~~	~~**2623**~~	~~**424**~~	~~**424**~~	~~27.6~~	~~7.67~~	~~7.68~~	~~7.27~~	~~0.871~~	~~0.875~~	~~73.6~~	~~8.0~~	~~Zircon_22Sep22_YD_ISU_1~~
BCG-612_S_181	6.97	2.42	2.43	21.8	1381	1381	7.34	4.28	4.28	**7.30**	**0.783**	**0.788**	0.6	58.9	Zircon_22Sep22_YD_ISU_2
BCG-612_S_191	~~16.6~~	~~3.06~~	~~3.09~~	~~**2558**~~	~~**274**~~	~~**275**~~	~~26.6~~	~~4.91~~	~~4.92~~	~~7.30~~	~~0.656~~	~~0.661~~	~~72.6~~	~~5.6~~	~~Zircon_22Sep22_YD_ISU_2~~
BCG-612_S_183	~~26.5~~	~~9.81~~	~~9.83~~	~~**2735**~~	~~**512**~~	~~**512**~~	~~29.9~~	~~9.89~~	~~9.90~~	~~7.37~~	~~0.942~~	~~0.946~~	~~75.3~~	~~8.8~~	~~Zircon_22Sep22_YD_ISU_2~~
BCG-612_S_196	~~19.9~~	~~8.30~~	~~8.32~~	~~**2662**~~	~~**595**~~	~~**595**~~	~~29.1~~	~~12.3~~	~~12.3~~	~~7.51~~	~~1.76~~	~~1.76~~	~~74.2~~	~~12.5~~	~~Zircon_22Sep22_YD_ISU_2~~
BCG-612_S_203	~~24.3~~	~~7.71~~	~~7.74~~	~~**3375**~~	~~**440**~~	~~**440**~~	~~45.1~~	~~15.4~~	~~15.4~~	~~7.52~~	~~1.54~~	~~1.54~~	~~83.3~~	~~6.6~~	~~Zircon_22Sep22_YD_ISU_2~~
BCG-612_S_201	~~59.1~~	~~6.15~~	~~6.37~~	~~**4022**~~	~~**173**~~	~~**173**~~	~~94.7~~	~~13.6~~	~~13.6~~	~~10.6~~	~~1.01~~	~~1.01~~	~~88.8~~	~~1.9~~	~~Zircon_22Sep22_YD_ISU_2~~
BCG-612_S_189	~~231~~	~~120~~	~~120~~	~~**3138**~~	~~**518**~~	~~**518**~~	~~56.6~~	~~21.6~~	~~21.6~~	~~11.0~~	~~2.41~~	~~2.41~~	~~80.5~~	~~8.6~~	~~Zircon_22Sep22_YD_ISU_2~~
BCG-612_S_204	~~102~~	~~53.1~~	~~53.2~~	~~**3145**~~	~~**581**~~	~~**581**~~	~~62.7~~	~~30.9~~	~~30.9~~	~~12.2~~	~~4.31~~	~~4.31~~	~~80.5~~	~~11.8~~	~~Zircon_22Sep22_YD_ISU_2~~
BCG-612_S_210	~~107~~	~~27.3~~	~~27.5~~	~~**4469**~~	~~**188**~~	~~**189**~~	~~307~~	~~58.7~~	~~58.8~~	~~28.2~~	~~5.07~~	~~5.08~~	~~90.8~~	~~2.4~~	~~Zircon_22Sep22_YD_ISU_2~~
BCG-770	**42.751940**	**112.022740**													
BCG-770_S_215	4.58	0.937	0.946	438	392	392	7.12	1.33	1.34	**5.91**	**0.389**	**0.395**	17.0	16.5	Zircon_22Sep22_YD_ISU_2
BCG-770_S_219	21.3	6.87	6.90	**1727**	**1071**	**1071**	14.4	8.73	8.73	6.32	1.13	1.13	56.2	27.7	Zircon_22Sep22_YD_ISU_2
BCG-770_M_96	4.52	1.16	1.17	125	764	764	7.31	2.51	2.51	**6.95**	**0.809**	**0.813**	4.8	34.5	Zircon_22Sep22_YD_ISU_1
BCG-770_M_93	9.30	2.16	2.18	-53	642	642	6.99	1.90	1.90	**7.17**	**0.488**	**0.495**	-2.5	28.7	Zircon_22Sep22_YD_ISU_1
BCG-770_S_220	11.6	2.91	2.93	**1653**	**426**	**427**	16.3	4.08	4.09	7.46	0.761	0.766	54.3	12.3	Zircon_22Sep22_YD_ISU_2
BCG-770_M_97	8.95	2.84	2.86	**988**	**558**	**559**	11.6	3.41	3.41	7.47	0.793	0.798	35.8	20.0	Zircon_22Sep22_YD_ISU_1
BCG-770_S_217	10.7	3.36	3.37	549	1070	1070	9.51	4.81	4.81	**7.52**	**1.01**	**1.01**	21.0	41.3	Zircon_22Sep22_YD_ISU_2
BCG-770_S_218	10.4	2.56	2.57	703	647	647	10.2	3.26	3.27	**7.53**	**0.768**	**0.773**	26.4	24.6	Zircon_22Sep22_YD_ISU_2
BCG-770_S_222	9.48	2.79	2.80	-9	654	654	9.15	2.51	2.51	**9.22**	**0.444**	**0.457**	-0.8	28.0	Zircon_22Sep22_YD_ISU_2
BCG-770_S_226	26.3	10.7	10.8				2.64	1.97	1.97	**9.59**	**1.80**	**1.80**		279.4	Zircon_22Sep22_YD_ISU_2
BCG-770_M_94	14.9	5.63	5.65	**1561**	**649**	**649**	20.8	7.64	7.65	10.0	1.32	1.33	51.9	18.7	Zircon_22Sep22_YD_ISU_1
BCG-770_S_223	26.0	9.33	9.36	**2650**	**432**	**432**	42.5	13.3	13.3	11.1	2.07	2.08	73.9	9.5	Zircon_22Sep22_YD_ISU_2
BCG-770_S_229	18.3	7.24	7.26							**11.5**	**1.81**	**1.81**			Zircon_22Sep22_YD_ISU_2
BCG-770_S_211	13.9	4.49	4.51	-297	1213	1213	10.8	5.25	5.26	**12.2**	**1.46**	**1.47**	-13.2	56.8	Zircon_22Sep22_YD_ISU_2
BCG-770_S_225	48.0	23.1	23.2	**2047**	**713**	**713**	46.2	19.1	19.1	17.2	2.14	2.15	62.8	16.1	Zircon_22Sep22_YD_ISU_2
BCG-770_S_228	25.1	5.52	5.57	**1226**	**425**	**425**	59.5	13.6	13.6	34.7	3.17	3.19	41.7	14.3	Zircon_22Sep22_YD_ISU_2

Appendix B: LA-ICP-MS U-Pb Dates

Table S2. U-Pb isotope ratios and trace element concentrations by LA-ICP-MS: sample data

							Dates (Ma)								
Analysis	208Pb / 232Th	±2s (Ma)	±2s-sys (Ma)	207Pb / 206Pb	±2s (Ma)	±2s-sys (Ma)	207Pb / 235U	±2s (Ma)	±2s-sys (Ma)	**206Pb / 238U**	±2s (Ma)	±2s-sys (Ma)	disc. (%)	±2s (%)	Experiment
BCG-770_S_214	453	26.5	29.5	653	108	109	506	23.6	24.2	**474**	**14.3**	**15.3**	6.3	5.2	Zircon_22Sep22_YD_ISU_2
BCG-770_M_95	507	11.6	21.3	520	57.9	59.5	487	15.6	16.4	**480**	**14.1**	**15.1**	1.4	4.3	Zircon_22Sep22_YD_ISU_1
BCG-770_S_224	430	20.0	23.7	446	99.3	99.9	482	20.3	20.9	**490**	**13.3**	**14.4**	-1.6	5.1	Zircon_22Sep22_YD_ISU_2
BCG-770_S_216	473	17.1	21.8	555	62.5	63.5	502	14.9	15.8	**490**	**11.6**	**12.9**	2.3	3.7	Zircon_22Sep22_YD_ISU_2
BCG-770_M_98	513	12.6	22.0	403	61.9	63.4	480	15.2	16.0	**496**	**13.6**	**14.7**	-3.4	4.3	Zircon_22Sep22_YD_ISU_1
BCG-770_S_212	491	25.6	29.1	426	93.4	94.1	492	19.7	20.3	**506**	**13.7**	**14.9**	-2.9	5.0	Zircon_22Sep22_YD_ISU_2
BCG-770_S_221	855	78.0	81.8	1492	51.5	52.5	1393	50.6	51.5	**1329**	**73.2**	**74.6**	4.6	6.3	Zircon_22Sep22_YD_ISU_2
BCG-770_S_213	1316	38.7	53.4	1369	59.6	60.5	1399	32.8	34.3	**1419**	**38.4**	**41.3**	-1.4	3.6	Zircon_22Sep22_YD_ISU_2
BCG-770_S_227	1210	86.6	93.5	**1674**	**43.7**	**44.8**	1638	27.2	29.3	1611	33.8	38.1	1.7	2.6	Zircon_22Sep22_YD_ISU_2

Appendix C: LA-ICP-MS Trace Element Data

Table S2. U-Pb isotope ratios and trace element concentrations by LA-ICPMS: sample data

										Concentrations (ppm)													
	P	Ti	Y	Nb	La	Ce	Pr	Nd	Sm	Eu	Gd	Tb	Dy	Ho	Er	Tm	Yb	Lu	Hf	Ta	Th	U	Experiment
BCG-1	**42.802426**	**112.012556**																					
BCG-1_S_111	~~239~~	~~7.73~~	~~564~~	~~5.92~~	~~5.42~~	~~21.9~~	~~2.03~~	~~7.04~~	~~7.27~~	~~0.659~~	~~13.9~~	~~6.14~~	~~94.5~~	~~25.4~~	~~116~~	~~26.6~~	~~245~~	~~37.9~~	~~-50413~~	~~2.72~~	~~48.7~~	~~120~~	~~Zircon_22Sep22_YD_ISU_1~~
BCG-1_S_107	209	9.88	930	7.62	0.02	27.7	0.08	1.55	3.49	0.795	24.8	9.59	113	43.0	175	42.8	362	56.6	-47834	3.34	151	244	Zircon_22Sep22_YD_ISU_1
BCG-1_L_5	~~176~~	~~7.54~~	~~1355~~	~~7.28~~		~~13.3~~	~~0.255~~	~~4.43~~	~~10.2~~	~~1.72~~	~~56.0~~	~~17.2~~	~~198~~	~~66.6~~	~~255~~	~~56.2~~	~~457~~	~~64.8~~	~~-40434~~	~~3.10~~	~~112~~	~~199~~	~~Zircon_22Sep22_YD_ISU_1~~
BCG-1_S_127	332	8.68	1446	10.4		28.0	0.133	2.28	6.30	0.657	34.6	12.1	138	52.2	213	49.7	465	64.4	42873	4.09	150	262	Zircon_22Sep22_YD_ISU_2
BCG-1_L_12	229	6.81	1673	6.73		34.9	0.142	3.61	9.54	1.61	57.7	20.1	240	82.5	334	72.7	594	92.4	-47185	2.88	205	264	Zircon_22Sep22_YD_ISU_1
BCG-1_L_6	~~250~~	~~7.86~~	~~1068~~	~~12.3~~		~~31.9~~	~~0.068~~	~~2.08~~	~~5.24~~	~~0.604~~	~~32.7~~	~~11.0~~	~~137~~	~~51.8~~	~~210~~	~~51.0~~	~~443~~	~~66.8~~	~~-46576~~	~~5.09~~	~~171~~	~~283~~	~~Zircon_22Sep22_YD_ISU_1~~
BCG-1_L_4	~~179~~	~~8.78~~	~~1298~~	~~6.02~~	~~0.016~~	~~12.6~~	~~0.377~~	~~5.89~~	~~9.84~~	~~1.89~~	~~50.9~~	~~17.0~~	~~185~~	~~65.4~~	~~248~~	~~55.0~~	~~434~~	~~63.6~~	~~-40011~~	~~3.21~~	~~107~~	~~195~~	~~Zircon_22Sep22_YD_ISU_1~~
BCG-1_S_133	307	7.25	1287	11.2	0.01	32.3	0.036	1.59	3.72	0.687	26.3	10.0	126	46.4	193	46.9	434	60.3	46318	4.52	162	273	Zircon_22Sep22_YD_ISU_2
BCG-1_S_110	273	8.16	1305	13.5		36.6	0.124	2.64	6.39	0.858	38.5	13.6	169	60.9	252	59.1	493	76.2	-47784	5.14	183	299	Zircon_22Sep22_YD_ISU_1
BCG-1_S_149	~~344~~	~~8.13~~	~~1232~~	~~9.20~~		~~29.4~~	~~0.04~~	~~1.84~~	~~4.31~~	~~0.618~~	~~26.0~~	~~9.21~~	~~124~~	~~44.6~~	~~188~~	~~43.5~~	~~426~~	~~58.7~~	~~48477~~	~~4.04~~	~~167~~	~~270~~	~~Zircon_22Sep22_YD_ISU_2~~
BCG-1_S_134	359	8.28	2406	8.07	0.02	25.2	0.509	7.45	14.6	1.73	70.8	23.5	267	92.3	369	81.4	723	98.3	43232	3.33	236	350	Zircon_22Sep22_YD_ISU_2
BCG-1_S_129	~~293~~	~~6.96~~	~~1285~~	~~12.6~~		~~29.1~~	~~0.066~~	~~1.18~~	~~4.73~~	~~0.436~~	~~26.1~~	~~10.4~~	~~127~~	~~45.9~~	~~197~~	~~46.7~~	~~442~~	~~62.0~~	~~48601~~	~~4.92~~	~~159~~	~~295~~	~~Zircon_22Sep22_YD_ISU_2~~
BCG-1_S_125	311	7.22	1399	11.4		31.3	0.07	1.68	5.23	0.655	31.3	11.4	138	50.3	214	49.8	467	64.6	46580	4.34	163	285	Zircon_22Sep22_YD_ISU_2
BCG-1_L_17	~~208~~	~~6.99~~	~~1081~~	~~12.9~~		~~25.5~~	~~0.084~~	~~1.72~~	~~6.13~~	~~0.707~~	~~34.2~~	~~11.9~~	~~141~~	~~52.2~~	~~208~~	~~47.9~~	~~412~~	~~63.6~~	~~-47238~~	~~5.00~~	~~160~~	~~296~~	~~Zircon_22Sep22_YD_ISU_1~~
BCG-1_S_101	251	5.67	2440	10.7	0.030	34.4	0.217	5.34	12.4	1.03	78.6	27.2	316	118	471	106	863	131	-51437	4.92	379	562	Zircon_22Sep22_YD_ISU_1
BCG-1_M_62	185	6.16	736	11.4		22.0	0.020	0.860	3.49	0.223	19.6	7.33	89.1	36.5	147	36.0	315	47.9	-50474	4.52	107	228	Zircon_22Sep22_YD_ISU_1
BCG-1_L_11	~~193~~	~~6.24~~	~~841~~	~~11.9~~		~~24.0~~	~~0.03~~	~~1.50~~	~~3.48~~	~~0.308~~	~~22.6~~	~~8.81~~	~~109~~	~~40.7~~	~~169~~	~~40.1~~	~~347~~	~~54.3~~	~~-50705~~	~~4.34~~	~~116~~	~~253~~	~~Zircon_22Sep22_YD_ISU_1~~
BCG-1_L_3	~~178~~	~~7.23~~	~~861~~	~~10.3~~		~~23.9~~	~~0.039~~	~~1.46~~	~~3.77~~	~~0.445~~	~~22.2~~	~~8.70~~	~~106~~	~~39.6~~	~~170~~	~~39.4~~	~~353~~	~~53.7~~	~~-47059~~	~~4.33~~	~~118~~	~~234~~	~~Zircon_22Sep22_YD_ISU_1~~
BCG-1_L_13	~~176~~	~~7.42~~	~~928~~	~~9.99~~		~~16.4~~	~~0.142~~	~~2.48~~	~~6.13~~	~~0.560~~	~~30.5~~	~~10.1~~	~~121~~	~~45.1~~	~~180~~	~~40.3~~	~~340~~	~~52.1~~	~~-44205~~	~~4.20~~	~~118~~	~~226~~	~~Zircon_22Sep22_YD_ISU_1~~
BCG-1_L_8	~~185~~	~~6.96~~	~~930~~	~~11.7~~	~~0.136~~	~~22.2~~	~~0.109~~	~~1.78~~	~~4.75~~	~~0.368~~	~~29.1~~	~~9.74~~	~~115~~	~~44.7~~	~~179~~	~~41.8~~	~~356~~	~~54.1~~	~~-46295~~	~~4.39~~	~~132~~	~~251~~	~~Zircon_22Sep22_YD_ISU_1~~
BCG-1_L_2	~~149~~	~~6.24~~	~~732~~	~~8.86~~		~~13.6~~	~~0.060~~	~~1.07~~	~~3.77~~	~~0.525~~	~~25.3~~	~~7.80~~	~~94.3~~	~~34.6~~	~~142~~	~~32.4~~	~~269~~	~~40.0~~	~~-44048~~	~~3.29~~	~~73.6~~	~~164~~	~~Zircon_22Sep22_YD_ISU_1~~
BCG-1_S_140	341	7.72	1374	11.4		32.1	0.112	2.14	4.79	0.735	30.3	11.1	138	50.4	215	49.4	486	65.7	46763	4.47	181	311	Zircon_22Sep22_YD_ISU_2
BCG-1_S_105	~~297~~	~~6.06~~	~~2029~~	~~11.7~~	~~0.02~~	~~33.1~~	~~0.247~~	~~4.45~~	~~11.7~~	~~1.01~~	~~69.5~~	~~24.0~~	~~286~~	~~102~~	~~403~~	~~93.8~~	~~764~~	~~108~~	~~-49539~~	~~4.64~~	~~294~~	~~459~~	~~Zircon_22Sep22_YD_ISU_1~~
BCG-1_L_9	179	6.33	1291	8.54	0.0	15.4	0.246	5.35	8.98	1.12	50.8	15.4	178	64.6	246	53.7	443	64.2	-41754	3.63	123	231	Zircon_22Sep22_YD_ISU_1
BCG-1_M_49	200	6.69	989	12.0		24.5	0.068	1.73	5.02	0.614	29.7	10.4	126	47.5	199	47.8	388	59.5	-49818	5.16	136	270	Zircon_22Sep22_YD_ISU_1
BCG-1_S_116	345	10.1	2151	7.59	0.985	39.1	0.587	5.14	9.28	1.23	55.1	18.7	223	75.7	314	68.5	632	83.5	45837	3.13	207	287	Zircon_22Sep22_YD_ISU_2
BCG-1_M_57	~~198~~	~~8.03~~	~~1084~~	~~6.21~~		~~27.5~~	~~0.043~~	~~1.57~~	~~4.64~~	~~0.846~~	~~31.1~~	~~11.1~~	~~133~~	~~51.7~~	~~212~~	~~49.6~~	~~423~~	~~65.3~~	~~-46941~~	~~2.91~~	~~106~~	~~163~~	~~Zircon_22Sep22_YD_ISU_1~~
BCG-1_S_132	~~329~~	~~6.92~~	~~1564~~	~~14.2~~		~~29.2~~	~~0.070~~	~~1.94~~	~~6.31~~	~~0.561~~	~~37.2~~	~~12.4~~	~~158~~	~~57.8~~	~~237~~	~~56.3~~	~~521~~	~~69.4~~	~~48609~~	~~5.67~~	~~201~~	~~364~~	~~Zircon_22Sep22_YD_ISU_2~~
BCG-1_M_41	~~173~~	~~7.11~~	~~917~~	~~8.27~~	~~0.049~~	~~12.6~~	~~0.097~~	~~1.79~~	~~5.55~~	~~0.808~~	~~32.0~~	~~10.7~~	~~123~~	~~45.5~~	~~175~~	~~40.3~~	~~325~~	~~48.3~~	~~-41207~~	~~3.55~~	~~73.4~~	~~145~~	~~Zircon_22Sep22_YD_ISU_1~~
BCG-1_S_102	~~221~~	~~6.54~~	~~1132~~	~~8.53~~		~~25.0~~	~~0.102~~	~~2.19~~	~~6.03~~	~~0.712~~	~~35.3~~	~~12.0~~	~~145~~	~~56.0~~	~~220~~	~~52.5~~	~~463~~	~~67.6~~	~~-49956~~	~~4.13~~	~~135~~	~~239~~	~~Zircon_22Sep22_YD_ISU_1~~
BCG-1_S_146	311	10.1	2243	5.69	0.016	28.2	0.342	5.89	11.7	1.90	61.8	21.6	237	85.8	320	73.9	631	88.9	43175	2.56	258	317	Zircon_22Sep22_YD_ISU_2
BCG-1_S_124	443	8.54	1463	9.76		29.3	0.100	1.98	3.56	0.990	31.9	10.6	149	54.4	224	53.0	500	69.9	42554	4.02	123	200	Zircon_22Sep22_YD_ISU_2
BCG-1_L_15	~~178~~	~~9.02~~	~~985~~	~~8.37~~		~~14.4~~	~~0.102~~	~~2.88~~	~~5.98~~	~~1.00~~	~~35.0~~	~~12.4~~	~~138~~	~~47.2~~	~~187~~	~~43.7~~	~~352~~	~~54.7~~	~~-40273~~	~~3.40~~	~~106~~	~~203~~	~~Zircon_22Sep22_YD_ISU_1~~
BCG-1_M_43	~~311~~	~~7.59~~	~~1290~~	~~8.35~~		~~26.7~~	~~0.130~~	~~1.73~~	~~6.10~~	~~1.01~~	~~39.2~~	~~13.6~~	~~165~~	~~62.7~~	~~256~~	~~59.2~~	~~504~~	~~77.0~~	~~-46982~~	~~3.94~~	~~136~~	~~214~~	~~Zircon_22Sep22_YD_ISU_1~~
BCG-1_M_52	204	8.23	1328	8.41		30.9	0.139	2.85	7.62	1.31	40.9	14.9	173	63.5	256	59.4	503	75.6	-46838	3.34	167	227	Zircon_22Sep22_YD_ISU_1
BCG-1_L_16	257	7.41	1149	13.4	0.019	30.7	0.071	1.52	5.22	0.536	31.4	11.8	140	53.4	224	54.2	453	68.7	-48990	5.06	176	306	Zircon_22Sep22_YD_ISU_1
BCG-1_S_123	~~321~~	~~6.44~~	~~1362~~	~~13.2~~		~~28.8~~	~~0.090~~	~~1.96~~	~~3.88~~	~~0.455~~	~~28.8~~	~~10.7~~	~~133~~	~~48.5~~	~~207~~	~~51.0~~	~~468~~	~~64.5~~	~~48208~~	~~5.34~~	~~172~~	~~331~~	~~Zircon_22Sep22_YD_ISU_2~~
BCG-1_S_112	215	9.58	1341	6.53		30.5	0.212	4.13	8.39	2.08	48.7	15.9	178	64.5	250	58.9	487	73.8	-46077	2.95	140	189	Zircon_22Sep22_YD_ISU_1
BCG-1_M_55	~~185~~	~~6.56~~	~~785~~	~~9.17~~		~~18.8~~	~~0.07~~	~~0.770~~	~~3.77~~	~~0.477~~	~~20.3~~	~~8.05~~	~~97.0~~	~~37.2~~	~~159~~	~~37.2~~	~~320~~	~~49.3~~	~~-49611~~	~~3.54~~	~~95.8~~	~~206~~	~~Zircon_22Sep22_YD_ISU_1~~
BCG-1_S_114	~~200~~	~~6.28~~	~~913~~	~~12.6~~	~~0.024~~	~~26.3~~	~~0.059~~	~~1.06~~	~~3.14~~	~~0.428~~	~~24.5~~	~~8.86~~	~~110~~	~~42.2~~	~~176~~	~~42.1~~	~~365~~	~~53.4~~	~~-52248~~	~~4.64~~	~~129~~	~~261~~	~~Zircon_22Sep22_YD_ISU_1~~
BCG-1_S_113	~~217~~	~~8.79~~	~~1028~~	~~11.3~~		~~28.1~~	~~0.093~~	~~2.31~~	~~4.87~~	~~0.556~~	~~30.1~~	~~10.8~~	~~133~~	~~48.9~~	~~205~~	~~46.2~~	~~405~~	~~61.8~~	~~-48593~~	~~4.28~~	~~149~~	~~246~~	~~Zircon_22Sep22_YD_ISU_1~~

Appendix C: LA-ICP-MS Trace Element Data

Table S2. U-Pb isotope ratios and trace element concentrations by LA-ICPMS: sample data

										Concentrations (ppm)													
	P	Ti	Y	Nb	La	Ce	Pr	Nd	Sm	Eu	Gd	Tb	Dy	Ho	Er	Tm	Yb	Lu	Hf	Ta	Th	U	Experiment
BCG-1_S_126	441	8.34	2695	7.69		40.3	0.357	7.68	14.9	2.68	73.6	25.6	289	102	413	89.6	825	111	44100	3.75	306	368	Zircon_22Sep22_YD_ISU_2
BCG-1_S_108	202	7.09	1023	11.6		23.9	0.103	2.39	5.59	0.511	31.0	11.3	136	49.9	197	46.8	404	60.2	-46914	4.54	138	270	Zircon_22Sep22_YD_ISU_1
BCG-1_S_139	180	4.85	2077	7.31	0.01	17.0	0.390	7.66	11.8	2.12	65.0	20.7	236	80.6	306	65.2	564	73.8	36249	2.64	126	203	Zircon_22Sep22_YD_ISU_2
BCG-1_M_36	~~274~~	~~7.46~~	~~1446~~	~~24.2~~		~~36.1~~	~~0.089~~	~~1.82~~	~~6.41~~	~~0.529~~	~~38.3~~	~~15.4~~	~~188~~	~~72.9~~	~~297~~	~~67.5~~	~~571~~	~~87.4~~	~~-49456~~	~~8.79~~	~~373~~	~~614~~	~~Zircon_22Sep22_YD_ISU_1~~
BCG-1_S_100	199	7.85	897	11.6		26.7	0.044	1.40	4.24	0.465	25.2	9.82	111	41.6	185	41.6	364	56.9	-50297	4.28	126	236	Zircon_22Sep22_YD_ISU_1
BCG-1_M_66	~~187~~	~~7.11~~	~~825~~	~~9.38~~		~~20.5~~	~~0.046~~	~~0.938~~	~~2.75~~	~~0.422~~	~~22.7~~	~~7.98~~	~~101~~	~~39.0~~	~~162~~	~~39.5~~	~~332~~	~~55.2~~	~~-48345~~	~~4.40~~	~~90.8~~	~~169~~	~~Zircon_22Sep22_YD_ISU_1~~
BCG-1_S_99	~~210~~	~~7.13~~	~~1588~~	~~8.67~~	~~0.160~~	~~29.5~~	~~0.243~~	~~5.60~~	~~11.2~~	~~0.982~~	~~50.5~~	~~18.2~~	~~216~~	~~78.7~~	~~302~~	~~71.5~~	~~577~~	~~86.5~~	~~-49423~~	~~3.89~~	~~225~~	~~326~~	~~Zircon_22Sep22_YD_ISU_1~~
BCG-1_S_103	~~209~~	~~13.2~~	~~1162~~	~~7.59~~		~~25.2~~	~~0.104~~	~~1.95~~	~~5.29~~	~~1.32~~	~~35.7~~	~~12.4~~	~~148~~	~~54.6~~	~~220~~	~~52.4~~	~~449~~	~~67.3~~	~~-47711~~	~~3.06~~	~~142~~	~~211~~	~~Zircon_22Sep22_YD_ISU_1~~
BCG-1_S_138	651	9.43	5019	127	0.383	117	0.232	4.90	14.2	0.802	91.5	38.5	482	178	749	175	1539	200	50692	37.3	1586	2378	Zircon_22Sep22_YD_ISU_2
BCG-1_S_136	~~326~~	~~9.98~~	~~1088~~	~~10.8~~	~~0.302~~	~~27.6~~	~~0.172~~	~~2.15~~	~~3.22~~	~~0.542~~	~~22.8~~	~~8.78~~	~~109~~	~~40.7~~	~~173~~	~~42.8~~	~~390~~	~~53.3~~	~~45337~~	~~4.39~~	~~127~~	~~231~~	~~Zircon_22Sep22_YD_ISU_2~~
BCG-1_S_109	218	6.95	1119	13.3		30.1	0.106	2.02	5.67	0.457	31.6	11.2	138	52.6	212	51.8	434	66.4	-49063	5.30	164	300	Zircon_22Sep22_YD_ISU_1
BCG-1_S_147	~~699~~	~~7.81~~	~~962~~	~~9.10~~	~~20.9~~	~~58.5~~	~~5.91~~	~~28.0~~	~~9.76~~	~~0.895~~	~~29.6~~	~~9.43~~	~~106~~	~~36.6~~	~~153~~	~~34.6~~	~~321~~	~~43.3~~	~~41857~~	~~3.68~~	~~102~~	~~203~~	~~Zircon_22Sep22_YD_ISU_2~~
BCG-1_M_65	~~202~~	~~6.86~~	~~1010~~	~~12.4~~		~~26.7~~	~~0.067~~	~~1.11~~	~~4.76~~	~~0.560~~	~~28.5~~	~~10.1~~	~~130~~	~~47.7~~	~~197~~	~~45.6~~	~~405~~	~~62.9~~	~~-48901~~	~~5.07~~	~~158~~	~~288~~	~~Zircon_22Sep22_YD_ISU_1~~
BCG-1_M_60	~~141~~	~~6.13~~	~~509~~	~~7.39~~		~~15.5~~	~~0.023~~	~~0.572~~	~~2.15~~	~~0.206~~	~~12.3~~	~~4.53~~	~~59.7~~	~~23.5~~	~~100~~	~~26.2~~	~~225~~	~~35.3~~	~~-53153~~	~~3.48~~	~~54.4~~	~~133~~	~~Zircon_22Sep22_YD_ISU_1~~
BCG-1_M_51	~~236~~	~~7.07~~	~~1015~~	~~12.3~~		~~26.2~~	~~0.065~~	~~2.01~~	~~5.68~~	~~0.488~~	~~29.5~~	~~10.2~~	~~125~~	~~46.5~~	~~197~~	~~47.3~~	~~394~~	~~60.5~~	~~-45436~~	~~4.45~~	~~169~~	~~279~~	~~Zircon_22Sep22_YD_ISU_1~~
BCG-1_S_135	~~379~~	~~7.10~~	~~1269~~	~~11.5~~	~~11.0~~	~~42.3~~	~~3.13~~	~~15.2~~	~~8.31~~	~~0.883~~	~~34.2~~	~~10.9~~	~~135~~	~~47.7~~	~~195~~	~~44.6~~	~~395~~	~~54.8~~	~~45158~~	~~4.41~~	~~141~~	~~267~~	~~Zircon_22Sep22_YD_ISU_2~~
BCG-1_M_44	346	7.69	1059	10.6	2.04	33.3	0.673	5.90	7.47	0.745	34.8	11.5	142	50.6	206	48.2	415	63.1	-43953	4.12	155	266	Zircon_22Sep22_YD_ISU_1
BCG-1_M_58	228	8.85	900	8.65		27.7	0.063	1.51	4.01	0.585	23.3	8.40	111	39.8	174	42.6	367	55.7	-45792	4.04	104	169	Zircon_22Sep22_YD_ISU_1
BCG-1_M_39	248	10.4	1796	10.3	0.195	20.4	0.476	8.78	13.6	1.88	74.6	23.3	260	91.3	338	76.2	614	87.3	-41369	3.88	230	321	Zircon_22Sep22_YD_ISU_1
BCG-1_L_19	196	8.60	1086	10.9		17.6	0.127	2.51	6.99	1.11	38.9	12.8	145	50.6	205	47.8	393	56.2	-41706	4.16	136	261	Zircon_22Sep22_YD_ISU_1
BCG-1_L_18	188	6.97	1030	11.7		17.9	0.100	2.32	5.25	0.923	35.8	11.9	141	50.2	204	45.7	381	54.9	-44890	4.09	146	271	Zircon_22Sep22_YD_ISU_1
BCG-1_M_54	~~165~~	~~7.89~~	~~1532~~	~~5.13~~	~~0.04~~	~~12.8~~	~~0.468~~	~~8.00~~	~~14.3~~	~~2.24~~	~~66.8~~	~~20.4~~	~~219~~	~~75.3~~	~~279~~	~~59.4~~	~~474~~	~~69.8~~	~~-40210~~	~~2.58~~	~~109~~	~~193~~	~~Zircon_22Sep22_YD_ISU_1~~
BCG-1_L_7	~~165~~	~~6.21~~	~~1070~~	~~8.28~~	~~0.077~~	~~21.8~~	~~0.169~~	~~2.60~~	~~5.79~~	~~0.895~~	~~34.9~~	~~12.0~~	~~144~~	~~52.9~~	~~210~~	~~48.4~~	~~401~~	~~60.7~~	~~-45292~~	~~3.20~~	~~119~~	~~206~~	~~Zircon_22Sep22_YD_ISU_1~~
BCG-1_M_34	197	8.48	916	10.1		25.2	0.087	1.45	4.31	0.472	28.9	9.17	115	43.3	180	42.6	366	55.6	-46212	3.85	128	228	Zircon_22Sep22_YD_ISU_1
BCG-1_M_53	~~182~~	~~8.02~~	~~920~~	~~8.15~~	~~0.02~~	~~14.2~~	~~0.117~~	~~3.14~~	~~7.13~~	~~0.841~~	~~33.5~~	~~11.0~~	~~126~~	~~47.0~~	~~186~~	~~43.0~~	~~366~~	~~51.9~~	~~-39265~~	~~3.43~~	~~102~~	~~195~~	~~Zircon_22Sep22_YD_ISU_1~~
BCG-1_S_122	~~220~~	~~7.11~~	~~1107~~	~~7.35~~		~~21.5~~	~~0.041~~	~~0.642~~	~~3.14~~	~~0.401~~	~~21.4~~	~~8.24~~	~~98.9~~	~~40.5~~	~~174~~	~~40.7~~	~~392~~	~~54.0~~	~~47318~~	~~2.99~~	~~82.7~~	~~175~~	~~Zircon_22Sep22_YD_ISU_2~~
BCG-1_S_117	~~207~~	~~24.0~~	~~758~~	~~4.07~~	~~0.329~~	~~15.4~~	~~0.124~~	~~1.43~~	~~2.11~~	~~0.401~~	~~15.9~~	~~6.39~~	~~73.9~~	~~26.9~~	~~113~~	~~28.7~~	~~261~~	~~38.8~~	~~42824~~	~~1.78~~	~~54.5~~	~~99.2~~	~~Zircon_22Sep22_YD_ISU_2~~
BCG-1_M_61	163	7.11	640	7.31		30.1	0.026	0.871	2.18	0.327	14.6	5.82	77.7	29.6	127	32.4	290	46.3	-50596	3.64	143	238	Zircon_22Sep22_YD_ISU_1
BCG-1_M_46	~~393~~	~~7.27~~	~~1086~~	~~12.9~~	~~17.2~~	~~65.7~~	~~4.90~~	~~24.8~~	~~9.95~~	~~0.947~~	~~35.5~~	~~11.9~~	~~129~~	~~51.3~~	~~210~~	~~49.6~~	~~423~~	~~66.0~~	~~-47635~~	~~5.03~~	~~158~~	~~291~~	~~Zircon_22Sep22_YD_ISU_1~~
BCG-1_S_141	262	8.35	1482	11.1		18.3	0.179	3.51	6.39	0.847	38.8	13.6	159	55.5	231	50.8	449	60.8	41945	4.19	136	262	Zircon_22Sep22_YD_ISU_2
BCG-1_M_38	~~1185~~	~~8.61~~	~~1129~~	~~10.1~~	~~98.4~~	~~223~~	~~26.8~~	~~136~~	~~32.8~~	~~2.63~~	~~57.2~~	~~15.1~~	~~158~~	~~54.8~~	~~207~~	~~50.6~~	~~438~~	~~66.7~~	~~-46766~~	~~4.11~~	~~163~~	~~258~~	~~Zircon_22Sep22_YD_ISU_1~~
BCG-1_S_130	~~290~~	~~7.59~~	~~1925~~	~~6.64~~		~~31.5~~	~~0.131~~	~~2.86~~	~~8.41~~	~~1.42~~	~~47.1~~	~~16.7~~	~~198~~	~~71.4~~	~~284~~	~~65.1~~	~~578~~	~~80.2~~	~~45652~~	~~3.15~~	~~172~~	~~237~~	~~Zircon_22Sep22_YD_ISU_2~~
BCG-1_M_47	~~224~~	~~6.83~~	~~1129~~	~~11.8~~		~~32.0~~	~~0.068~~	~~2.02~~	~~5.33~~	~~0.653~~	~~35.6~~	~~12.6~~	~~146~~	~~56.9~~	~~226~~	~~55.2~~	~~466~~	~~69.4~~	~~-50115~~	~~4.71~~	~~163~~	~~279~~	~~Zircon_22Sep22_YD_ISU_1~~
BCG-1_M_42	~~154~~	~~6.14~~	~~1819~~	~~5.89~~		~~17.8~~	~~0.493~~	~~9.53~~	~~15.6~~	~~1.83~~	~~75.5~~	~~23.8~~	~~257~~	~~86.8~~	~~335~~	~~71.4~~	~~568~~	~~81.2~~	~~-42999~~	~~3.04~~	~~155~~	~~266~~	~~Zircon_22Sep22_YD_ISU_1~~
BCG-1_S_143	316	7.43	1332	10.5		26.4	0.069	1.95	5.43	0.667	28.7	10.5	130	48.4	197	46.8	441	62.3	49253	4.35	139	266	Zircon_22Sep22_YD_ISU_2
BCG-1_S_119	~~266~~	~~13.3~~	~~2043~~	~~4.38~~	~~0.051~~	~~17.1~~	~~0.309~~	~~6.63~~	~~11.4~~	~~1.74~~	~~62.2~~	~~19.1~~	~~221~~	~~77.6~~	~~302~~	~~67.0~~	~~624~~	~~84.8~~	~~41528~~	~~2.21~~	~~194~~	~~272~~	~~Zircon_22Sep22_YD_ISU_2~~
BCG-1_L_20	~~271~~	~~10.2~~	~~548~~	~~5.41~~	~~7.12~~	~~28.7~~	~~1.87~~	~~10.4~~	~~4.16~~	~~0.850~~	~~19.2~~	~~6.24~~	~~74.1~~	~~27.1~~	~~114~~	~~27.4~~	~~234~~	~~37.6~~	~~-41934~~	~~2.37~~	~~56.9~~	~~107~~	~~Zircon_22Sep22_YD_ISU_1~~
BCG-1_S_131	348	9.48	1340	9.94		25.8	0.109	2.12	5.25	0.828	29.9	11.2	133	47.4	202	46.8	431	60.2	41861	3.91	135	228	Zircon_22Sep22_YD_ISU_2
BCG-1_S_144	389	8.80	1519	10.3		36.2	0.091	2.41	6.01	1.06	33.7	12.9	155	54.3	226	55.0	492	71.1	43648	4.13	164	241	Zircon_22Sep22_YD_ISU_2
BCG-1_M_37	218	8.18	871	8.42		27.1	0.060	1.41	3.76	0.682	26.4	9.56	115	44.6	183	43.0	386	60.1	-48788	3.86	126	214	Zircon_22Sep22_YD_ISU_1
BCG-1_M_40	~~199~~	~~6.95~~	~~780~~	~~8.55~~		~~24.2~~	~~0.046~~	~~1.16~~	~~3.43~~	~~0.330~~	~~19.5~~	~~7.52~~	~~92.7~~	~~37.5~~	~~154~~	~~36.8~~	~~325~~	~~49.4~~	~~-49115~~	~~3.73~~	~~115~~	~~205~~	~~Zircon_22Sep22_YD_ISU_1~~
BCG-1_L_10	~~214~~	~~10.1~~	~~1540~~	~~5.93~~	~~0.011~~	~~35.1~~	~~0.130~~	~~3.88~~	~~9.03~~	~~2.06~~	~~54.4~~	~~18.4~~	~~206~~	~~74.2~~	~~294~~	~~67.4~~	~~553~~	~~83.3~~	~~-45746~~	~~3.12~~	~~156~~	~~194~~	~~Zircon_22Sep22_YD_ISU_1~~
BCG-1_M_59	~~170~~	~~6.96~~	~~1515~~	~~5.95~~	~~0.014~~	~~16.6~~	~~0.178~~	~~4.19~~	~~10.2~~	~~1.64~~	~~57.9~~	~~19.8~~	~~219~~	~~74.1~~	~~284~~	~~62.5~~	~~481~~	~~71.5~~	~~-42402~~	~~2.41~~	~~130~~	~~215~~	~~Zircon_22Sep22_YD_ISU_1~~

Appendix C: LA-ICP-MS Trace Element Data

Table S2. U-Pb isotope ratios and trace element concentrations by LA-ICPMS: sample data																							
									Concentrations (ppm)														
	P	Ti	Y	Nb	La	Ce	Pr	Nd	Sm	Eu	Gd	Tb	Dy	Ho	Er	Tm	Yb	Lu	Hf	Ta	Th	U	Experiment
BCG-1_S_106	287	6.90	1559	12.6		36.1	0.151	4.40	9.92	1.20	50.4	18.6	217	78.6	318	72.0	613	93.4	-49014	6.14	244	374	Zircon_22Sep22_YD_ISU_1
BCG-1_S_121	396	9.30	1901	8.11		33.2	0.170	3.53	9.17	1.64	45.6	16.6	200	68.7	286	66.3	608	78.9	43267	3.50	176	254	Zircon_22Sep22_YD_ISU_2
BCG-1_S_137	409	8.69	1762	14.0		43.8	0.175	2.56	6.26	1.10	39.3	14.8	173	64.8	266	62.5	572	80.9	45092	5.33	218	325	Zircon_22Sep22_YD_ISU_2
BCG-1_M_64	220	9.89	987	10.1	0.098	28.8	0.105	1.52	4.76	0.788	27.0	9.58	123	46.7	198	47.6	412	63.3	-49799	4.04	143	231	Zircon_22Sep22_YD_ISU_1
BCG-1_M_56	~~201~~	~~7.18~~	~~1428~~	~~7.85~~	~~0.04~~	~~32.2~~	~~0.126~~	~~1.50~~	~~6.75~~	~~0.820~~	~~44.9~~	~~15.6~~	~~186~~	~~68.2~~	~~279~~	~~64.1~~	~~532~~	~~77.6~~	~~-49246~~	~~3.32~~	~~189~~	~~278~~	~~Zircon_22Sep22_YD_ISU_1~~
BCG-1_M_48	135	6.33	1351	5.28		13.5	0.128	2.72	8.19	1.17	47.4	16.5	185	64.4	242	53.1	434	64.8	-42627	2.11	93.5	168	Zircon_22Sep22_YD_ISU_1
BCG-1_M_45	~~1188~~	~~7.25~~	~~1090~~	~~12.4~~	~~43.3~~	~~119~~	~~12.1~~	~~64.2~~	~~18.7~~	~~1.58~~	~~42.1~~	~~13.4~~	~~145~~	~~53.6~~	~~211~~	~~49.9~~	~~418~~	~~63.7~~	~~-47887~~	~~5.47~~	~~168~~	~~293~~	~~Zircon_22Sep22_YD_ISU_1~~
BCG-1_S_120	368	7.81	1809	17.5		33.6	0.149	2.72	6.26	0.940	42.0	14.8	183	65.0	283	64.4	587	75.8	47868	6.30	231	444	Zircon_22Sep22_YD_ISU_2
BCG-1_S_145	~~1975~~	~~8.81~~	~~1403~~	~~11.9~~	~~130~~	~~288~~	~~36.7~~	~~173~~	~~44.4~~	~~3.07~~	~~62.5~~	~~15.2~~	~~149~~	~~51.7~~	~~209~~	~~47.6~~	~~443~~	~~60.5~~	~~44958~~	~~4.13~~	~~169~~	~~275~~	~~Zircon_22Sep22_YD_ISU_2~~
BCG-1_L_1	92.1	10.2	890	1.79	0	4.55	0.329	5.87	9.57	4.42	41.9	12.8	128	44.4	164	35.8	288	44.8	-28442	0.762	34.1	54.3	Zircon_22Sep22_YD_ISU_1
BCG-1_L_14	~~2043~~	~~10.5~~	~~1391~~	~~3.98~~	~~151~~	~~321~~	~~38.3~~	~~219~~	~~56.5~~	~~5.53~~	~~99.5~~	~~22.9~~	~~229~~	~~71.3~~	~~261~~	~~55.7~~	~~456~~	~~66.2~~	~~-35379~~	~~1.54~~	~~74.3~~	~~126~~	~~Zircon_22Sep22_YD_ISU_1~~
BCG-1_M_50	~~113~~	~~7.18~~	~~373~~	~~6.06~~	~~0.054~~	~~14.7~~	~~0.027~~	~~0.420~~	~~1.18~~	~~0.193~~	~~7.79~~	~~3.69~~	~~43.0~~	~~18.7~~	~~80.2~~	~~19.8~~	~~181~~	~~29.1~~	~~-51139~~	~~2.60~~	~~41.2~~	~~113~~	~~Zircon_22Sep22_YD_ISU_1~~
BCG-1_M_63	~~152~~	~~19.7~~	~~1173~~	~~6.89~~	~~0.836~~	~~16.3~~	~~0.402~~	~~5.04~~	~~9.51~~	~~0.992~~	~~46.1~~	~~15.5~~	~~170~~	~~59.0~~	~~228~~	~~50.3~~	~~425~~	~~60.4~~	~~-41816~~	~~2.99~~	~~103~~	~~193~~	~~Zircon_22Sep22_YD_ISU_1~~
BCG-1_S_118	~~223~~	~~11.7~~	~~1040~~	~~9.36~~	~~0.244~~	~~27.6~~	~~0.143~~	~~1.23~~	~~3.17~~	~~0.541~~	~~19.3~~	~~8.04~~	~~107~~	~~38.7~~	~~162~~	~~37.8~~	~~364~~	~~52.7~~	~~46156~~	~~4.12~~	~~106~~	~~198~~	~~Zircon_22Sep22_YD_ISU_2~~
BCG-1_S_115	~~256~~	~~24.6~~	~~1286~~	~~7.86~~	~~0.907~~	~~24.1~~	~~0.288~~	~~2.29~~	~~4.35~~	~~0.723~~	~~30.6~~	~~10.2~~	~~124~~	~~44.7~~	~~193~~	~~44.5~~	~~412~~	~~59.0~~	~~46750~~	~~3.39~~	~~114~~	~~190~~	~~Zircon_22Sep22_YD_ISU_2~~
BCG-1_S_142	~~160~~	~~19.3~~	~~571~~	~~6.38~~	~~1.02~~	~~16.3~~	~~0.204~~	~~1.01~~	~~2.07~~	~~0.08~~	~~11.2~~	~~3.88~~	~~55.3~~	~~20.8~~	~~93.8~~	~~24.2~~	~~218~~	~~31.5~~	~~48301~~	~~2.76~~	~~50.0~~	~~125~~	~~Zircon_22Sep22_YD_ISU_2~~
BCG-1_S_104	~~171~~	~~10.7~~	~~601~~	~~7.98~~	~~10.0~~	~~25.8~~	~~1.19~~	~~5.60~~	~~3.06~~	~~0.342~~	~~15.4~~	~~5.71~~	~~68.8~~	~~27.9~~	~~117~~	~~28.7~~	~~263~~	~~40.5~~	~~-54253~~	~~3.75~~	~~64.2~~	~~155~~	~~Zircon_22Sep22_YD_ISU_1~~
BCG-1_S_128	~~11326~~	~~11.9~~	~~2234~~	~~9.99~~	~~726~~	~~1632~~	~~211~~	~~1034~~	~~230~~	~~15.2~~	~~253~~	~~42.7~~	~~323~~	~~88.2~~	~~299~~	~~62.0~~	~~543~~	~~73.1~~	~~45332~~	~~3.73~~	~~172~~	~~254~~	~~Zircon_22Sep22_YD_ISU_2~~
BCG-1_S_148	~~7938~~	~~9.94~~	~~1114~~	~~6.11~~	~~498~~	~~996~~	~~142~~	~~692~~	~~153~~	~~9.40~~	~~144~~	~~24.6~~	~~175~~	~~43.9~~	~~146~~	~~30.5~~	~~261~~	~~33.0~~	~~41039~~	~~2.30~~	~~76.8~~	~~116~~	~~Zircon_22Sep22_YD_ISU_2~~
BCG-1_M_33	~~146~~	~~47.7~~	~~494~~	~~7.33~~	~~2.69~~	~~18.1~~	~~0.541~~	~~3.51~~	~~2.32~~	~~0.369~~	~~13.8~~	~~5.26~~	~~67.8~~	~~24.7~~	~~107~~	~~25.4~~	~~218~~	~~33.8~~	~~-43468~~	~~2.48~~	~~55.9~~	~~109~~	~~Zircon_22Sep22_YD_ISU_1~~
BCG-1_M_35	~~186~~	~~160~~	~~1499~~	~~8.91~~	~~10.0~~	~~34.9~~	~~2.25~~	~~14.4~~	~~14.4~~	~~2.74~~	~~61.5~~	~~19.7~~	~~226~~	~~72.9~~	~~300~~	~~63.3~~	~~510~~	~~79.3~~	~~-26387~~	~~2.17~~	~~278~~	~~249~~	~~Zircon_22Sep22_YD_ISU_1~~
BCG-273	**42.754171**	**112.021274**																					
BCG-273_L_23	197	7.32	835	9.84		28.2	0.045	1.28	3.67	0.481	20.5	7.94	103	38.6	162	39.4	348	53.8	-49429	3.98	138	254	Zircon_22Sep22_YD_ISU_1
BCG-273_M_71	211	9.28	1012	11.4		29.7	0.098	1.92	4.16	0.371	27.5	9.58	119	47.3	198	47.6	414	63.6	-47794	5.35	242	406	Zircon_22Sep22_YD_ISU_1
BCG-273_M_72	~~165~~	~~17.1~~	~~503~~	~~4.11~~		~~11.1~~	~~0.041~~	~~0.724~~	~~2.52~~	~~0.233~~	~~14.4~~	~~4.62~~	~~59.1~~	~~23.3~~	~~97.7~~	~~24.5~~	~~209~~	~~33.6~~	~~-42840~~	~~1.74~~	~~61.5~~	~~101~~	~~Zircon_22Sep22_YD_ISU_1~~
BCG-273_S_16	168	4.30	2946	53.7	0.029	125	0.393	6.65	9.16	1.10	52.0	21.6	283	103	458	111	970	139	37034	13.0	410	387	Zircon_22Sep22_YD_ISU_2
BCG-273_S_16	190	11.6	766	6.48		17.7	0.076	2.32	4.76	1.07	24.0	7.11	82.2	27.8	105	26.2	231	30.2	39823	2.68	46.5	80.7	Zircon_22Sep22_YD_ISU_2
BCG-273_S_15	2516	29.3	763	3.52	68.7	139	19.9	93.7	24.5	4.14	43.9	10.5	98.9	30.3	107	23.9	205	29.3	33462	1.35	35.1	39.9	Zircon_22Sep22_YD_ISU_2
BCG-273_S_15	228	11.5	971	10.9		36.9	0.187	3.67	6.45	0.753	31.2	10.4	111	36.5	142	30.9	279	38.7	40750	4.87	78.2	112	Zircon_22Sep22_YD_ISU_2
BCG-273_S_16	201	14.9	615	6.70		20.1	0.067	1.56	3.48	1.04	17.2	5.79	70.3	23.5	92.7	21.6	198	27.0	39172	2.69	39.7	64.1	Zircon_22Sep22_YD_ISU_2
BCG-273_S_16	219	17.1	686	6.49	0.019	16.3	0.113	2.76	5.98	1.65	23.2	7.24	84.9	26.6	101	23.5	211	28.9	35813	2.88	47.9	78.8	Zircon_22Sep22_YD_ISU_2
BCG-273_S_16	~~5932~~	~~158~~	~~10164~~	~~164~~	~~33.5~~	~~287~~	~~52.4~~	~~421~~	~~377~~	~~267~~	~~740~~	~~212~~	~~1681~~	~~385~~	~~1080~~	~~217~~	~~1669~~	~~193~~	~~41884~~	~~11.4~~	~~893~~	~~2431~~	~~Zircon_22Sep22_YD_ISU_2~~
BCG-30	**42.751736**	**112.021480**																					
BCG-30_S_154	325	10.8	1933	5.89	0.019	33.0	0.223	4.09	9.01	2.10	61.1	18.9	224	74.5	303	67.0	595	78.2	42495	2.97	152	202	Zircon_22Sep22_YD_ISU_2
BCG-30_S_153	417	11.6	1578	8.37	1.89	38.7	0.773	4.58	9.08	1.74	40.9	13.6	172	57.1	238	55.0	494	67.9	42115	3.54	139	193	Zircon_22Sep22_YD_ISU_2
BCG-30_S_151	~~347~~	~~9.09~~	~~1265~~	~~10.5~~	~~0.03~~	~~31.4~~	~~0.092~~	~~1.66~~	~~5.67~~	~~1.14~~	~~32.4~~	~~11.8~~	~~136~~	~~48.4~~	~~206~~	~~46.8~~	~~429~~	~~58.6~~	~~42148~~	~~4.42~~	~~132~~	~~218~~	~~Zircon_22Sep22_YD_ISU_2~~
BCG-30_L_21	~~174~~	~~12.7~~	~~586~~	~~5.23~~		~~11.4~~	~~0.052~~	~~0.708~~	~~3.03~~	~~0.388~~	~~17.4~~	~~6.54~~	~~75.1~~	~~27.9~~	~~117~~	~~28.3~~	~~245~~	~~37.4~~	~~-45332~~	~~2.09~~	~~76.3~~	~~133~~	~~Zircon_22Sep22_YD_ISU_1~~
BCG-30_L_22	~~162~~	~~20.3~~	~~450~~	~~3.49~~		~~11.0~~	~~0.066~~	~~0.877~~	~~1.53~~	~~0.314~~	~~12.2~~	~~4.51~~	~~52.8~~	~~20.5~~	~~87.3~~	~~21.9~~	~~196~~	~~30.3~~	~~-42027~~	~~1.50~~	~~46.4~~	~~76.9~~	~~Zircon_22Sep22_YD_ISU_1~~
BCG-30_M_70	124	15.7	476	4.06	0.015	7.35	0.047	0.637	1.89	0.218	15.2	4.86	56.2	21.3	92.0	22.5	202	30.9	-43075	2.10	56.2	101	Zircon_22Sep22_YD_ISU_1
BCG-30_M_69	~~175~~	~~23.3~~	~~570~~	~~3.37~~		~~11.6~~	~~0.069~~	~~1.06~~	~~3.23~~	~~0.561~~	~~18.5~~	~~6.17~~	~~73.6~~	~~27.0~~	~~110~~	~~26.9~~	~~231~~	~~35.4~~	~~-42239~~	~~1.52~~	~~57.3~~	~~82.2~~	~~Zircon_22Sep22_YD_ISU_1~~
BCG-30_M_67	144	14.9	537	5.63	0.01	14.1	0.030	1.20	2.62	0.182	15.1	5.27	66.5	24.5	107	25.7	228	34.8	-44706	2.49	102	153	Zircon_22Sep22_YD_ISU_1
BCG-30_M_68	131	14.5	337	2.92		7.84	0.045	0.820	1.78	0.106	8.84	3.24	39.0	15.9	64.7	16.6	146	22.2	-44908	1.50	33.3	69.8	Zircon_22Sep22_YD_ISU_1
BCG-30_S_152	~~217~~	~~8.97~~	~~840~~	~~7.31~~		~~14.4~~	~~0.0~~	~~1.38~~	~~2.80~~	~~0.215~~	~~17.2~~	~~6.35~~	~~82.1~~	~~29.2~~	~~121~~	~~30.7~~	~~291~~	~~39.5~~	~~43283~~	~~3.30~~	~~128~~	~~242~~	~~Zircon_22Sep22_YD_ISU_2~~

Appendix C: LA-ICP-MS Trace Element Data

Table S2. U-Pb isotope ratios and trace element concentrations by LA-ICPMS: sample data																							
									Concentrations (ppm)														
	P	Ti	Y	Nb	La	Ce	Pr	Nd	Sm	Eu	Gd	Tb	Dy	Ho	Er	Tm	Yb	Lu	Hf	Ta	Th	U	Experiment
BCG-30_S_150	~~219~~	~~23.4~~	~~657~~	~~2.65~~	~~0.047~~	~~7.99~~	~~0.074~~	~~1.27~~	~~3.27~~	~~0.479~~	~~15.3~~	~~5.37~~	~~64.8~~	~~23.3~~	~~98.0~~	~~24.0~~	~~221~~	~~29.9~~	~~40973~~	~~1.12~~	~~58.8~~	~~98.5~~	~~Zircon_22Sep22_YD_ISU_2~~
BCG-30_S_157	195	27.3	588	7.59		23.6	0.093	1.98	3.98	0.731	19.2	6.44	66.5	22.7	89.5	20.4	184	26.0	36009	2.64	37.3	49.4	Zircon_22Sep22_YD_ISU_2
BCG-30_S_155	275	17.3	1929	8.32	0.076	25.0	0.783	12.7	22.4	7.60	95.5	26.2	264	78.9	279	56.7	494	61.7	34597	2.93	134	122	Zircon_22Sep22_YD_ISU_2
BCG-30_S_156	192	13.0	1023	5.39		11.7	0.306	4.97	9.03	1.95	37.1	11.7	121	39.6	145	32.5	275	37.2	35874	2.48	49.6	77.4	Zircon_22Sep22_YD_ISU_2
BCG-612	**42.765764**	**112.013782**																					
BCG-612_S_17	~~658~~	~~25.1~~	~~2559~~	~~12.3~~		~~66.7~~	~~0.248~~	~~4.94~~	~~8.62~~	~~1.09~~	~~53.4~~	~~19.5~~	~~242~~	~~89.1~~	~~373~~	~~91.0~~	~~879~~	~~120~~	~~98543~~	~~5.94~~	~~404~~	~~577~~	~~Zircon_22Sep22_YD_ISU_2~~
BCG-612_L_27	~~382~~	~~18.0~~	~~1945~~	~~17.0~~		~~62.7~~	~~0.02~~	~~3.05~~	~~8.08~~	~~1.01~~	~~51.4~~	~~18.9~~	~~239~~	~~89.5~~	~~368~~	~~90.5~~	~~811~~	~~121~~	~~-105548~~	~~8.11~~	~~263~~	~~436~~	~~Zircon_22Sep22_YD_ISU_1~~
BCG-612_S_17	~~592~~	~~27.2~~	~~2513~~	~~8.98~~		~~52.4~~	~~0.242~~	~~5.78~~	~~11.0~~	~~2.04~~	~~60.4~~	~~20.5~~	~~250~~	~~90.3~~	~~377~~	~~90.9~~	~~853~~	~~119~~	~~93967~~	~~4.81~~	~~265~~	~~388~~	~~Zircon_22Sep22_YD_ISU_2~~
BCG-612_S_17	887	20.8	3712	22.0	0.050	108	0.340	8.06	13.4	2.11	82.2	28.3	361	132	540	132	1246	173	96233	8.43	865	917	Zircon_22Sep22_YD_ISU_2
BCG-612_S_18	636	17.6	2710	18.6		80.2	0.182	3.98	8.36	1.34	51.1	19.9	247	98.2	411	99.5	958	136	108833	8.51	438	649	Zircon_22Sep22_YD_ISU_2
BCG-612_S_16	772	27.9	3725	9.06	0.04	55.7	0.785	11.6	24.4	3.82	108	35.3	398	140	565	130	1162	164	93110	4.93	407	503	Zircon_22Sep22_YD_ISU_2
BCG-612_L_32	~~361~~	~~15.8~~	~~1319~~	~~14.6~~		~~58.3~~	~~0.063~~	~~1.16~~	~~4.94~~	~~0.889~~	~~29.5~~	~~11.9~~	~~156~~	~~62.7~~	~~263~~	~~66.6~~	~~593~~	~~92.8~~	~~-109818~~	~~6.75~~	~~216~~	~~375~~	~~Zircon_22Sep22_YD_ISU_1~~
BCG-612_S_17	600	20.0	2639	20.0		88.7	0.129	2.78	8.68	1.36	54.1	20.7	252	92.4	396	99.0	965	132	104189	7.74	439	637	Zircon_22Sep22_YD_ISU_2
BCG-612_S_19	~~638~~	~~22.8~~	~~2557~~	~~15.8~~		~~70.3~~	~~0.159~~	~~4.04~~	~~8.80~~	~~1.34~~	~~53.7~~	~~21.5~~	~~251~~	~~93.2~~	~~400~~	~~94.3~~	~~907~~	~~127~~	~~94178~~	~~6.87~~	~~451~~	~~646~~	~~Zircon_22Sep22_YD_ISU_2~~
BCG-612_M_77	~~518~~	~~23.9~~	~~2481~~	~~9.78~~		~~57.3~~	~~0.330~~	~~6.37~~	~~16.4~~	~~2.37~~	~~76.1~~	~~25.2~~	~~303~~	~~112~~	~~461~~	~~109~~	~~893~~	~~137~~	~~-98870~~	~~4.37~~	~~328~~	~~398~~	~~Zircon_22Sep22_YD_ISU_1~~
BCG-612_S_20	~~596~~	~~21.8~~	~~2296~~	~~12.9~~		~~66.9~~	~~0.165~~	~~3.24~~	~~7.77~~	~~0.911~~	~~47.8~~	~~16.8~~	~~214~~	~~78.7~~	~~353~~	~~81.2~~	~~796~~	~~113~~	~~101871~~	~~5.87~~	~~324~~	~~506~~	~~Zircon_22Sep22_YD_ISU_2~~
BCG-612_M_84	496	15.6	2584	28.3	0.0	89.3	0.201	4.62	11.2	1.23	66.4	25.1	308	122	498	124	1038	161	-113476	11.3	515	792	Zircon_22Sep22_YD_ISU_1
BCG-612_S_19	483	13.8	1928	19.9		56.0	0.08	1.38	4.46	0.606	35.5	13.9	183	70.3	307	76.6	745	105	113685	8.75	298	542	Zircon_22Sep22_YD_ISU_2
BCG-612_M_90	~~474~~	~~13.4~~	~~3460~~	~~17.7~~		~~81.4~~	~~0.199~~	~~3.89~~	~~13.3~~	~~1.77~~	~~89.3~~	~~34.3~~	~~420~~	~~164~~	~~671~~	~~156~~	~~1319~~	~~204~~	~~-115211~~	~~7.96~~	~~588~~	~~827~~	~~Zircon_22Sep22_YD_ISU_1~~
BCG-612_S_17	~~545~~	~~25.5~~	~~2334~~	~~11.6~~		~~57.1~~	~~0.202~~	~~4.03~~	~~9.87~~	~~1.52~~	~~49.2~~	~~17.8~~	~~223~~	~~81.3~~	~~352~~	~~84.1~~	~~799~~	~~111~~	~~94961~~	~~4.87~~	~~256~~	~~379~~	~~Zircon_22Sep22_YD_ISU_2~~
BCG-612_S_18	687	21.4	2460	16.8	0.123	76.7	0.120	3.56	9.60	1.33	53.4	19.6	227	90.0	381	88.5	872	124	103420	6.27	426	591	Zircon_22Sep22_YD_ISU_2
BCG-612_S_20	1198	24.7	3187	9.46	11.0	70.5	3.73	22.2	17.9	2.83	79.3	27.0	320	115	479	110	1011	142	96751	5.22	314	423	Zircon_22Sep22_YD_ISU_2
BCG-612_S_18	705	21.9	2767	17.6		83.8	0.191	5.09	9.60	1.40	57.4	21.4	253	97.0	427	98.2	938	134	102821	7.82	494	658	Zircon_22Sep22_YD_ISU_2
BCG-612_S_19	920	12.9	5204	20.7	0.032	77.2	0.411	9.43	20.6	2.34	119	43.0	531	190	819	188	1702	233	109490	9.43	767	1063	Zircon_22Sep22_YD_ISU_2
BCG-612_M_86	481	28.5	1867	11.8		65.4	0.129	4.43	10.4	1.78	51.8	19.0	231	85.7	372	84.9	763	116	-97845	4.78	343	461	Zircon_22Sep22_YD_ISU_1
BCG-612_L_26	447	14.8	2089	26.9		74.1	0.186	2.88	8.72	1.06	54.5	20.5	254	97.3	414	104	912	138	-111875	10.7	453	729	Zircon_22Sep22_YD_ISU_1
BCG-612_M_79	398	14.2	1770	21.3		69.9	0.078	2.44	6.34	0.779	43.9	16.2	212	78.9	350	85.9	742	120	-110593	9.71	348	569	Zircon_22Sep22_YD_ISU_1
BCG-612_S_19	1321	19.0	5468	24.7	11.3	150	3.65	26.5	24.4	3.24	130	45.8	530	197	819	193	1727	240	99306	9.60	1048	1138	Zircon_22Sep22_YD_ISU_2
BCG-612_M_78	~~326~~	~~7.34~~	~~4526~~	~~22.8~~	~~2.62~~	~~67.7~~	~~1.88~~	~~26.4~~	~~42.2~~	~~2.79~~	~~197~~	~~62.9~~	~~676~~	~~237~~	~~886~~	~~193~~	~~1577~~	~~228~~	~~-86692~~	~~10.1~~	~~425~~	~~525~~	~~Zircon_22Sep22_YD_ISU_1~~
BCG-612_S_17	598	18.5	3017	13.9	0.012	75.7	0.197	6.66	12.3	2.03	64.5	24.2	296	108	465	107	1004	141	103181	6.68	403	534	Zircon_22Sep22_YD_ISU_2
BCG-612_M_89	~~753~~	~~11.9~~	~~2758~~	~~21.1~~		~~56.0~~	~~0.241~~	~~4.02~~	~~10.1~~	~~0.989~~	~~67.8~~	~~24.3~~	~~323~~	~~129~~	~~548~~	~~134~~	~~1126~~	~~180~~	~~-115336~~	~~9.40~~	~~404~~	~~734~~	~~Zircon_22Sep22_YD_ISU_1~~
BCG-612_S_17	~~648~~	~~26.1~~	~~2321~~	~~10.7~~		~~62.8~~	~~0.135~~	~~3.70~~	~~8.27~~	~~1.41~~	~~51.9~~	~~18.2~~	~~237~~	~~86.7~~	~~356~~	~~88.6~~	~~818~~	~~116~~	~~97860~~	~~5.49~~	~~343~~	~~484~~	~~Zircon_22Sep22_YD_ISU_2~~
BCG-612_S_20	510	21.5	2915	9.35		66.0	0.312	4.84	11.5	1.86	67.2	23.9	286	107	443	106	977	133	96980	4.25	350	452	Zircon_22Sep22_YD_ISU_2
BCG-612_S_18	666	27.9	3766	12.2		69.5	0.572	8.86	19.7	2.80	86.6	31.0	363	135	536	124	1151	159	97805	6.67	525	626	Zircon_22Sep22_YD_ISU_2
BCG-612_S_19	~~2247~~	~~18.7~~	~~5450~~	~~34.9~~	~~142~~	~~278~~	~~51.4~~	~~141~~	~~45.1~~	~~5.95~~	~~182~~	~~54.7~~	~~623~~	~~210~~	~~832~~	~~185~~	~~1628~~	~~219~~	~~95151~~	~~12.3~~	~~658~~	~~976~~	~~Zircon_22Sep22_YD_ISU_2~~
BCG-612_S_20	~~2208~~	~~32.5~~	~~2781~~	~~16.3~~	~~53.9~~	~~389~~	~~15.8~~	~~80.4~~	~~24.6~~	~~1.89~~	~~77.8~~	~~24.3~~	~~275~~	~~100~~	~~412~~	~~101~~	~~967~~	~~132~~	~~103270~~	~~6.51~~	~~382~~	~~559~~	~~Zircon_22Sep22_YD_ISU_2~~
BCG-612_S_19	2110	22.2	4020	22.6	12.2	245	4.36	98.4	36.8	3.11	105	33.9	402	149	609	143	1331	188	96498	8.72	925	951	Zircon_22Sep22_YD_ISU_2
BCG-612_L_25	~~706~~	~~18.7~~	~~2193~~	~~21.5~~	~~3.22~~	~~98.2~~	~~1.68~~	~~9.80~~	~~9.82~~	~~1.77~~	~~63.2~~	~~21.2~~	~~253~~	~~101~~	~~415~~	~~102~~	~~875~~	~~139~~	~~-107969~~	~~8.57~~	~~463~~	~~652~~	~~Zircon_22Sep22_YD_ISU_1~~
BCG-612_L_28	~~601~~	~~20.6~~	~~2428~~	~~24.2~~		~~58.0~~	~~0.273~~	~~4.97~~	~~10.7~~	~~1.39~~	~~71.3~~	~~25.0~~	~~315~~	~~117~~	~~481~~	~~117~~	~~980~~	~~151~~	~~-101579~~	~~10.1~~	~~324~~	~~559~~	~~Zircon_22Sep22_YD_ISU_1~~
BCG-612_S_20	772	11.5	4034	40.7		85.9	0.299	4.80	10.4	0.789	72.0	29.1	376	145	623	155	1386	194	111039	16.7	868	1473	Zircon_22Sep22_YD_ISU_2
BCG-612_S_18	2546	29.4	4579	18.1	79.1	251	21.4	108	43.0	4.31	125	40.5	470	165	673	158	1439	199	93068	7.60	844	839	Zircon_22Sep22_YD_ISU_2
BCG-612_L_29	402	17.1	1823	23.9		72.1	0.093	1.60	7.08	0.859	45.5	19.1	232	87.9	373	91.6	832	124	-112517	9.68	360	642	Zircon_22Sep22_YD_ISU_1
BCG-612_M_75	438	26.5	1817	11.7	0.06	50.1	0.160	3.72	9.51	1.36	52.7	17.8	218	82.0	351	87.1	746	123	-101613	5.90	266	393	Zircon_22Sep22_YD_ISU_1

Appendix C: LA-ICP-MS Trace Element Data

Table S2. U-Pb isotope ratios and trace element concentrations by LA-ICPMS: sample data

Concentrations (ppm)

	P	Ti	Y	Nb	La	Ce	Pr	Nd	Sm	Eu	Gd	Tb	Dy	Ho	Er	Tm	Yb	Lu	Hf	Ta	Th	U	Experiment
BCG-612_S_20	738	18.5	3421	20.0	0.009	72.7	0.251	5.00	10.9	1.92	69.9	26.9	336	121	507	118	1101	153	104340	8.71	440	703	Zircon_22Sep22_YD_ISU_2
BCG-612_M_80	~~484~~	~~15.1~~	~~2206~~	~~23.5~~		~~77.5~~	~~0.130~~	~~3.18~~	~~9.07~~	~~0.813~~	~~54.6~~	~~20.5~~	~~263~~	~~101~~	~~426~~	~~103~~	~~900~~	~~144~~	~~-110358~~	~~9.88~~	~~480~~	~~717~~	~~Zircon_22Sep22_YD_ISU_1~~
BCG-612_M_92	366	7.23	3180	109		80.0	0.128	4.99	13.0	0.489	86.4	34.1	425	158	627	138	1138	157	-106974	33.5	497	1153	Zircon_22Sep22_YD_ISU_1
BCG-612_S_16	~~521~~	~~19.6~~	~~1777~~	~~12.1~~		~~52.6~~	~~0.076~~	~~1.45~~	~~5.55~~	~~0.928~~	~~33.8~~	~~12.2~~	~~163~~	~~63.8~~	~~275~~	~~68.4~~	~~633~~	~~93.1~~	~~101886~~	~~5.94~~	~~193~~	~~333~~	~~Zircon_22Sep22_YD_ISU_2~~
BCG-612_S_17	~~2246~~	~~15.6~~	~~7284~~	~~16.2~~	~~20.8~~	~~136~~	~~6.00~~	~~41.3~~	~~35.2~~	~~6.04~~	~~197~~	~~66.9~~	~~764~~	~~264~~	~~1086~~	~~254~~	~~2329~~	~~324~~	~~87219~~	~~5.85~~	~~1867~~	~~2259~~	~~Zircon_22Sep22_YD_ISU_2~~
BCG-612_M_73	397	14.6	1443	17.8		60.0	0.06	2.22	5.71	0.755	34.7	12.7	163	68.9	269	71.2	623	100	-116955	8.56	269	453	Zircon_22Sep22_YD_ISU_1
BCG-612_S_17	~~466~~	~~17.1~~	~~2319~~	~~12.6~~	~~0.047~~	~~64.6~~	~~0.090~~	~~2.28~~	~~8.29~~	~~1.03~~	~~45.7~~	~~18.0~~	~~218~~	~~83.1~~	~~362~~	~~83.7~~	~~804~~	~~111~~	~~105490~~	~~6.32~~	~~275~~	~~398~~	~~Zircon_22Sep22_YD_ISU_2~~
BCG-612_M_81	~~676~~	~~35.2~~	~~1734~~	~~13.7~~	~~21.3~~	~~104~~	~~5.69~~	~~31.4~~	~~14.4~~	~~1.79~~	~~56.3~~	~~18.6~~	~~220~~	~~83.1~~	~~337~~	~~83.8~~	~~724~~	~~112~~	~~-99368~~	~~4.90~~	~~321~~	~~475~~	~~Zircon_22Sep22_YD_ISU_1~~
BCG-612_M_82	438	21.6	2858	8.82		64.2	0.347	7.95	18.5	2.62	95.6	31.7	371	140	550	128	1093	160	-103237	4.53	410	494	Zircon_22Sep22_YD_ISU_1
BCG-612_S_18	525	18.7	2252	19.8	0.03	79.9	0.162	2.74	6.05	1.05	44.7	16.8	214	76.7	338	84.6	810	115	104349	8.84	369	650	Zircon_22Sep22_YD_ISU_2
BCG-612_L_31	470	21.7	1934	15.0		71.6	0.113	4.49	11.6	1.35	52.5	19.7	240	88.8	381	92.4	801	124	-105704	6.54	376	540	Zircon_22Sep22_YD_ISU_1
BCG-612_M_76	468	13.3	2261	28.9		72.4	0.183	2.33	7.96	0.711	58.3	20.8	289	106	453	112	988	152	-110873	12.6	448	812	Zircon_22Sep22_YD_ISU_1
BCG-612_S_18	868	22.9	4695	19.7		101	0.731	13.3	21.7	2.58	111	37.7	460	169	702	163	1514	202	96723	7.68	803	910	Zircon_22Sep22_YD_ISU_2
BCG-612_M_85	~~623~~	~~12.1~~	~~3023~~	~~39.4~~		~~82.7~~	~~0.180~~	~~5.54~~	~~14.0~~	~~0.673~~	~~76.0~~	~~29.8~~	~~376~~	~~142~~	~~606~~	~~142~~	~~1282~~	~~193~~	~~-113199~~	~~15.9~~	~~799~~	~~1254~~	~~Zircon_22Sep22_YD_ISU_1~~
BCG-612_L_30	~~287~~	~~8.32~~	~~1959~~	~~45.4~~		~~54.0~~	~~0.139~~	~~4.00~~	~~9.69~~	~~0.396~~	~~59.7~~	~~21.0~~	~~252~~	~~94.8~~	~~398~~	~~90.4~~	~~764~~	~~113~~	~~-97444~~	~~14.7~~	~~246~~	~~545~~	~~Zircon_22Sep22_YD_ISU_1~~
BCG-612_S_17	~~2874~~	~~14.7~~	~~3450~~	~~29.7~~	~~150~~	~~378~~	~~41.7~~	~~197~~	~~52.7~~	~~3.00~~	~~106~~	~~30.8~~	~~348~~	~~124~~	~~506~~	~~126~~	~~1156~~	~~158~~	~~106467~~	~~11.8~~	~~654~~	~~1006~~	~~Zircon_22Sep22_YD_ISU_2~~
BCG-612_S_16	~~22431~~	~~15.8~~	~~8042~~	~~28.5~~	~~581~~	~~1325~~	~~160~~	~~761~~	~~187~~	~~11.5~~	~~320~~	~~83.9~~	~~911~~	~~300~~	~~1201~~	~~275~~	~~2436~~	~~327~~	~~101883~~	~~10.6~~	~~2050~~	~~2252~~	~~Zircon_22Sep22_YD_ISU_2~~
BCG-612_M_91	~~1653~~	~~24.5~~	~~3187~~	~~10.0~~	~~32.3~~	~~262~~	~~28.1~~	~~50.5~~	~~48.5~~	~~4.52~~	~~128~~	~~38.9~~	~~419~~	~~151~~	~~596~~	~~136~~	~~1130~~	~~171~~	~~-97733~~	~~5.46~~	~~444~~	~~518~~	~~Zircon_22Sep22_YD_ISU_1~~
BCG-612_S_19	~~861~~	~~53.2~~	~~2749~~	~~11.0~~	~~12.7~~	~~79.3~~	~~3.78~~	~~21.7~~	~~14.2~~	~~1.92~~	~~67.5~~	~~22.6~~	~~273~~	~~101~~	~~400~~	~~97.2~~	~~932~~	~~125~~	~~92799~~	~~5.31~~	~~322~~	~~420~~	~~Zircon_22Sep22_YD_ISU_2~~
BCG-612_M_83	~~458~~	~~22.1~~	~~1800~~	~~12.3~~		~~54.5~~	~~0.111~~	~~3.45~~	~~8.00~~	~~1.62~~	~~43.8~~	~~17.2~~	~~208~~	~~79.7~~	~~345~~	~~84.2~~	~~725~~	~~115~~	~~-103906~~	~~7.04~~	~~231~~	~~328~~	~~Zircon_22Sep22_YD_ISU_1~~
BCG-612_L_24	~~1594~~	~~32.1~~	~~1752~~	~~12.0~~	~~68.0~~	~~198~~	~~18.6~~	~~97.6~~	~~26.7~~	~~2.22~~	~~68.5~~	~~19.8~~	~~211~~	~~83.1~~	~~338~~	~~83.0~~	~~712~~	~~108~~	~~-96350~~	~~4.96~~	~~313~~	~~440~~	~~Zircon_22Sep22_YD_ISU_1~~
BCG-612_S_16	~~598~~	~~16.8~~	~~2565~~	~~23.5~~		~~63.5~~	~~0.108~~	~~2.52~~	~~8.56~~	~~0.743~~	~~53.2~~	~~20.0~~	~~258~~	~~91.0~~	~~395~~	~~92.4~~	~~918~~	~~130~~	~~104248~~	~~9.19~~	~~330~~	~~598~~	~~Zircon_22Sep22_YD_ISU_2~~
BCG-612_M_87	~~375~~	~~41.4~~	~~933~~	~~6.08~~		~~18.9~~	~~0.110~~	~~1.33~~	~~4.24~~	~~0.714~~	~~25.8~~	~~8.92~~	~~111~~	~~42.9~~	~~181~~	~~46.7~~	~~403~~	~~63.8~~	~~-97157~~	~~3.33~~	~~85.6~~	~~156~~	~~Zircon_22Sep22_YD_ISU_1~~
BCG-612_S_20	378	12.0	1167	16.3	0.042	32.3	0.074	0.577	2.27	0.310	19.3	7.74	112	42.5	191	48.4	485	69.2	106928	9.07	160	463	Zircon_22Sep22_YD_ISU_2
BCG-612_S_16	980	25.2	3200	23.5		88.9	0.191	4.29	9.94	1.21	69.1	25.1	310	115	496	117	1137	154	99302	9.11	411	656	Zircon_22Sep22_YD_ISU_2
BCG-612_S_19	~~4758~~	~~16.0~~	~~2471~~	~~16.9~~	~~150~~	~~416~~	~~44.8~~	~~208~~	~~48.8~~	~~2.40~~	~~80.1~~	~~22.8~~	~~246~~	~~85.5~~	~~360~~	~~88.0~~	~~873~~	~~120~~	~~111819~~	~~7.81~~	~~422~~	~~689~~	~~Zircon_22Sep22_YD_ISU_2~~
BCG-612_M_74	~~352~~	~~26.1~~	~~1344~~	~~17.7~~	~~1.31~~	~~53.9~~	~~0.318~~	~~3.13~~	~~4.60~~	~~0.887~~	~~32.9~~	~~11.2~~	~~160~~	~~63.5~~	~~278~~	~~69.7~~	~~617~~	~~97.7~~	~~-113653~~	~~8.12~~	~~217~~	~~414~~	~~Zircon_22Sep22_YD_ISU_1~~
BCG-612_M_88	~~821~~	~~35.1~~	~~2089~~	~~10.9~~	~~34.9~~	~~121~~	~~10.3~~	~~56.1~~	~~23.9~~	~~1.78~~	~~72.5~~	~~23.2~~	~~270~~	~~98.1~~	~~386~~	~~91.4~~	~~774~~	~~123~~	~~-101406~~	~~4.55~~	~~239~~	~~330~~	~~Zircon_22Sep22_YD_ISU_1~~
BCG-612_S_18	841	27.0	3593	10.6	0.107	76.4	0.535	9.66	22.7	2.84	94.7	32.1	379	138	578	129	1214	162	100406	4.76	430	516	Zircon_22Sep22_YD_ISU_2
BCG-612_S_19	~~7305~~	~~21.1~~	~~3894~~	~~33.9~~	~~387~~	~~910~~	~~113~~	~~538~~	~~123~~	~~5.40~~	~~179~~	~~41.3~~	~~423~~	~~140~~	~~562~~	~~134~~	~~1252~~	~~170~~	~~109967~~	~~13.2~~	~~830~~	~~1292~~	~~Zircon_22Sep22_YD_ISU_2~~
BCG-612_S_18	~~12099~~	~~33.6~~	~~3376~~	~~15.8~~	~~569~~	~~1291~~	~~160~~	~~781~~	~~160~~	~~10.4~~	~~198~~	~~39.9~~	~~400~~	~~123~~	~~488~~	~~113~~	~~1031~~	~~145~~	~~98095~~	~~6.12~~	~~480~~	~~627~~	~~Zircon_22Sep22_YD_ISU_2~~
BCG-612_S_19	~~600~~	~~46.1~~	~~2310~~	~~12.4~~	~~1.39~~	~~66.1~~	~~0.269~~	~~3.70~~	~~8.02~~	~~1.27~~	~~49.4~~	~~18.2~~	~~216~~	~~79.3~~	~~348~~	~~84.8~~	~~808~~	~~110~~	~~98523~~	~~5.71~~	~~310~~	~~455~~	~~Zircon_22Sep22_YD_ISU_2~~
BCG-612_S_20	~~1230~~	~~56.0~~	~~3144~~	~~38.7~~	~~20.4~~	~~2256~~	~~9.36~~	~~40.3~~	~~31.0~~	~~4.17~~	~~94.0~~	~~29.8~~	~~340~~	~~109~~	~~456~~	~~115~~	~~1013~~	~~132~~	~~102039~~	~~7.39~~	~~536~~	~~629~~	~~Zircon_22Sep22_YD_ISU_2~~
BCG-612_S_20	~~30619~~	~~27.3~~	~~4201~~	~~22.4~~	~~1844~~	~~4250~~	~~529~~	~~2538~~	~~552~~	~~23.1~~	~~541~~	~~90.0~~	~~614~~	~~154~~	~~539~~	~~112~~	~~991~~	~~131~~	~~104283~~	~~8.99~~	~~411~~	~~586~~	~~Zircon_22Sep22_YD_ISU_2~~
BCG-612_S_18	~~1101~~	~~27.8~~	~~5204~~	~~123~~	~~11.2~~	~~96.0~~	~~2.78~~	~~15.1~~	~~5.24~~	~~0.214~~	~~23.6~~	~~13.3~~	~~260~~	~~157~~	~~1060~~	~~354~~	~~4318~~	~~707~~	~~94051~~	~~97.4~~	~~7859~~	~~10724~~	~~Zircon_22Sep22_YD_ISU_2~~
BCG-612_S_20	~~405~~	~~59.4~~	~~1511~~	~~9.47~~	~~3.01~~	~~46.7~~	~~0.682~~	~~4.54~~	~~4.80~~	~~0.913~~	~~29.6~~	~~10.6~~	~~145~~	~~54.9~~	~~237~~	~~57.4~~	~~566~~	~~79.3~~	~~93643~~	~~4.92~~	~~168~~	~~298~~	~~Zircon_22Sep22_YD_ISU_2~~
BCG-612_S_21	~~706~~	~~230~~	~~2789~~	~~15.1~~	~~8.47~~	~~104~~	~~2.22~~	~~14.4~~	~~16.3~~	~~4.04~~	~~69.5~~	~~24.4~~	~~289~~	~~102~~	~~417~~	~~95.2~~	~~919~~	~~127~~	~~74289~~	~~5.64~~	~~360~~	~~296~~	~~Zircon_22Sep22_YD_ISU_2~~
BCG-770	**42.751940**	**112.022740**																					
BCG-770_S_21	351	5.65	1978	22.9	0.016	44.8	0.065	2.07	4.75	0.275	38.3	13.8	186	67.8	299	72.5	662	90.0	48550	9.02	580	894	Zircon_22Sep22_YD_ISU_2
BCG-770_S_21	225	14.2	591	4.02		13.5	0.038	0.634	2.14	0.335	12.7	4.48	57.2	21.1	90.9	22.5	215	30.2	42981	1.54	54.7	105	Zircon_22Sep22_YD_ISU_2
BCG-770_M_96	218	7.21	999	10.0		35.6	0.107	1.47	4.30	0.565	26.7	9.23	116	45.6	193	48.2	411	65.8	-50062	4.77	268	372	Zircon_22Sep22_YD_ISU_1
BCG-770_M_93	248	14.3	2338	4.22	0.104	16.2	0.570	9.90	20.9	2.94	99.7	32.0	334	116	456	103	825	122	-34979	2.08	348	358	Zircon_22Sep22_YD_ISU_1
BCG-770_S_22	4579	8.61	1567	13.0	244	550	74.1	363	80.3	3.75	104	20.6	193	58.8	230	51.6	474	65.1	47696	4.91	192	317	Zircon_22Sep22_YD_ISU_2

Appendix C: LA-ICP-MS Trace Element Data

Table S2. U-Pb isotope ratios and trace element concentrations by LA-ICPMS: sample data																							
									Concentrations (ppm)														
	P	Ti	Y	Nb	La	Ce	Pr	Nd	Sm	Eu	Gd	Tb	Dy	Ho	Er	Tm	Yb	Lu	Hf	Ta	Th	U	Experiment
BCG-770_M_97	202	8.20	881	9.73		30.9	0.070	1.01	3.29	0.293	24.5	8.87	108	41.5	177	43.5	377	59.1	-49927	4.02	210	347	Zircon_22Sep22_YD_ISU_1
BCG-770_S_21	200	9.24	719	8.08		11.0	0.04	1.19	2.05	0.256	15.8	5.92	74.6	26.7	113	26.9	247	34.9	46375	3.30	71.4	158	Zircon_22Sep22_YD_ISU_2
BCG-770_S_21	305	11.9	1707	5.77	0.03	17.5	0.257	5.45	10.6	1.22	47.6	15.6	184	63.1	249	57.8	505	67.9	41614	2.64	179	224	Zircon_22Sep22_YD_ISU_2
BCG-770_S_22	2365	11.2	1856	10.1	55.1	145	4.11	28.8	13.5	1.90	52.4	15.9	186	68.6	284	69.0	636	90.0	38262	3.85	372	781	Zircon_22Sep22_YD_ISU_2
BCG-770_S_22	258	23.0	748	2.67	0.068	7.39	0.148	1.67	4.18	0.604	20.0	6.74	79.8	27.4	115	25.7	243	35.7	38892	1.31	49.9	75.2	Zircon_22Sep22_YD_ISU_2
BCG-770_M_94	237	29.4	729	1.98	0.071	8.83	0.145	2.77	6.45	0.622	24.0	7.87	91.7	32.4	134	32.1	282	41.7	-34579	1.06	143	189	Zircon_22Sep22_YD_ISU_1
BCG-770_S_22	236	19.5	833	5.41	0.499	11.9	0.284	2.55	3.86	0.505	20.0	7.16	89.0	31.9	137	30.4	284	40.6	43079	2.61	112	153	Zircon_22Sep22_YD_ISU_2
BCG-770_S_22	236	20.4	609	2.79		8.78	0.06	1.24	2.43	0.361	14.8	5.35	59.6	22.4	94.6	22.2	204	30.2	41418	1.35	51.5	81.4	Zircon_22Sep22_YD_ISU_2
BCG-770_S_21	285	21.1	1771	2.52	0.119	5.39	0.477	7.79	11.9	2.84	59.6	17.8	205	63.9	239	55.8	482	65.2	35506	1.25	123	158	Zircon_22Sep22_YD_ISU_2
BCG-770_S_22	176	72.7	795	4.34	0.900	13.8	0.368	2.93	5.54	0.154	22.6	7.53	87.8	30.1	123	27.4	249	33.9	42638	1.63	124	207	Zircon_22Sep22_YD_ISU_2
BCG-770_S_22	314	13.4	1004	1.35	0.025	20.3	0.107	1.84	4.54	1.78	23.4	7.75	92.1	34.6	151	35.8	330	59.6	45499	0.436	102	89.3	Zircon_22Sep22_YD_ISU_2
BCG-770_S_21	182	21.6	923	4.81	0.023	41.5	0.328	5.61	8.87	2.27	34.8	10.9	113	35.5	136	30.9	277	37.8	37946	2.38	55.7	47.0	Zircon_22Sep22_YD_ISU_2
BCG-770_M_95	161	6.09	1578	95.0	0.198	179	0.280	3.38	5.82	0.898	32.0	14.1	183	73.0	309	74.7	631	96.7	-39622	21.2	611	501	Zircon_22Sep22_YD_ISU_1
BCG-770_S_22	265	11.1	1601	17.8	0.222	43.6	0.593	8.44	13.7	1.25	51.1	16.4	186	59.8	231	51.6	462	60.6	39682	7.33	157	196	Zircon_22Sep22_YD_ISU_2
BCG-770_S_21	137	4.84	1618	67.8	0.115	34.5	0.166	2.91	7.64	0.343	44.1	16.0	180	61.2	232	49.7	423	51.8	43128	20.4	238	481	Zircon_22Sep22_YD_ISU_2
BCG-770_M_98	118	5.14	2576	41.2	0	111	0.544	6.87	11.6	1.40	61.4	26.1	315	116	499	120	1016	146	-38770	10.7	377	333	Zircon_22Sep22_YD_ISU_1
BCG-770_S_21	236	5.16	1088	16.5	2.58	25.4	0.866	7.38	7.40	0.577	28.2	10.2	119	40.9	161	37.8	339	46.0	43368	6.82	110	214	Zircon_22Sep22_YD_ISU_2
BCG-770_S_22	262	11.7	594	4.29	0.025	11.7	0.118	1.18	2.61	0.639	13.3	4.66	57.0	20.8	90.4	24.0	256	37.3	42220	2.02	38.2	159	Zircon_22Sep22_YD_ISU_2
BCG-770_S_21	267	17.8	878	3.07		74.6	0.145	4.05	7.52	1.50	30.5	9.21	95.7	32.5	124	29.1	258	33.7	40098	1.15	124	122	Zircon_22Sep22_YD_ISU_2
BCG-770_S_22	895	11.3	2411	4.09	0.092	22.6	0.217	2.46	6.01	2.72	36.9	15.5	216	87.5	402	111	1125	171	46176	1.82	65.8	244	Zircon_22Sep22_YD_ISU_2

Appendix D: ID-TIMS Data

Table 1. Zircon IDTIMS U-Pb isotopic data

	Compositional Parameters						Radiogenic Isotope Ratios								Isotopic Ages					
Sample	$\frac{Th}{U}$	$^{206}Pb^*$ x10^{-13} mol	mol % $^{206}Pb^*$	$\frac{Pb^*}{Pb_c}$	Pb_c (pg)	$\frac{^{206}Pb}{^{204}Pb}$	$\frac{^{208}Pb}{^{206}Pb}$	$\frac{^{207}Pb}{^{206}Pb}$	% err	$\frac{^{207}Pb}{^{235}U}$	% err	$\frac{^{206}Pb}{^{238}U}$	% err	corr. coef.	$\frac{^{207}Pb}{^{206}Pb}$	±	$\frac{^{207}Pb}{^{235}U}$	±	$\frac{^{206}Pb}{^{238}U}$	±
(a)	(b)	(c)	(c)	(c)	(c)	(d)	(e)	(e)	(f)	(e)	(f)	(e)	(f)		(g)	(f)	(g)	(f)	(g)	(f)
BCG-612																				
z6	0.874	1.9587	0.999	347	0.15	18948	0.278	0.05071	0.1	0.18793	0.1	0.026890	0.073	0.949	225	2	174.86	0.21	171.14	0.12
z4	0.850	0.0162	0.383	0.21	2.16	29.3	0.277	0.05309	38.3	0.00681	39.9	0.000930	1.993	0.803	299	869	6.89	2.74	**6.082**	**0.121**
z7	0.735	0.0244	0.7	0.75	0.87	60.2	0.240	0.04618	12.2	0.00589	12.6	0.000925	0.584	0.806	-29	293	5.96	0.75	**6.046**	**0.035**
z3	0.752	0.0311	0.56	0.41	2.03	41.1	0.245	0.04943	17.6	0.00629	18.4	0.000923	0.982	0.906	133	410	6.37	1.17	**6.037**	**0.059**
z1	0.750	0.0204	0.649	1	0.91	51	0.244	0.04861	19.9	0.00616	20.3	0.000919	0.690	0.634	94	468	6.2	1.3	**6.010**	**0.041**
								weighted mean 206Pb/238U age = 6.032 ± 0.053 (0.053) [0.054] Ma; MSWD = 0.88 (n=4) (h)												
BCG-770																				
z2	0.966	0.0228	0.7415	0.97	0.66	69.8	0.313	0.04687	12.2	0.00979	12.6	0.001516	0.787	0.525	20	293	9.90	1.24	9.854	0.078
z8	0.593	0.0084	0.691	0.69	0.31	58.4	0.192	0.04492	45.6	0.00876	45.8	0.001415	1.020	0.199	-84	1112	8.86	4.04	9.201	0.094
z7	0.458	0.0452	0.394	0.19	5.75	30.3	0.149	0.04912	17.8	0.00887	18.7	0.001310	1.832	0.552	128	416	8.96	1.67	8.526	0.156
z3	0.609	0.0114	0.548	0.37	0.78	39.9	0.198	0.04596	40.2	0.00770	40.9	0.001215	1.818	0.377	-32	971	7.79	3.17	7.916	0.144
z5	0.606	0.0068	0.798	1.22	0.14	89.3	0.197	0.04913	28.5	0.00822	28.6	0.001215	0.639	0.200	127	666	8.32	2.37	7.913	0.051
z4	0.587	0.0103	0.595	0.45	0.58	44.5	0.191	0.04438	31.5	0.00707	32.1	0.001157	1.507	0.413	-119	773	7.16	2.29	7.538	0.114
z1	0.867	0.0235	0.466	0.29	2.23	33.8	0.282	0.05435	23.5	0.00866	25.2	0.001156	2.496	0.700	358	529	8.76	2.20	7.537	0.188
z6	0.640	0.0188	0.903	2.90	0.17	185	0.208	0.04777	4.5	0.00647	4.7	0.000983	0.277	0.695	55	107	6.55	0.30	6.421	0.018

(a) z1, z2 etc. are labels for single zircon grains or fragments annealed and chemically abraded after Mattinson (2005); bold indicates results used in weighted mean calculations.
(b) Model Th/U ratio iteratively calculated from the radiogenic 208Pb/206Pb ratio and 206Pb/238U age.
(c) Pb* and Pbc represent radiogenic and common Pb, respectively; mol % 206Pb* with respect to radiogenic, blank and initial common Pb.
(d) Measured ratio corrected for spike and fractionation only. Pb fractionation estimated at 0.17 +/- 0.03 %/a.m.u. for Daly analyses, based on analysis of ET2535-spiked samples run in the same analytical period.
(e) Corrected for fractionation, spike, and common Pb; all common Pb assigned the composition of the laboratory blank, which is similar to that of Snake River Plain silicic volcanics (Ellis et al. 2019): 206Pb/204Pb = 18.042 ± 0.61%; 207Pb/204Pb = 15.537 ± 0.52%; 208Pb/204Pb = 37.686 ± 0.63% (all uncertainties 1-sigma).
(f) Errors are 2-sigma, propagated using the algorithms of Schmitz and Schoene (2007).
(g) Calculations are based on the decay constants of Jaffey et al. (1971) and the natural 238U/235U ratio of Hiess et al. (2012). 206Pb/238U and 207Pb/206Pb dates corrected for initial disequilibrium in 230Th/238U using D(Th/U) = 0.2 ± 0.05.
(h) Age uncertainties reported at the 95% confidence interval, as ± analytical (+tracer) [+decay constant]; MSWD = mean squared weighted deviation. *The 95% confidence interval is computed as the internal standard deviation multiplied by the Student's t-distribution multiplier for a two-tailed 95% critical interval and n-1 degrees of freedom for MSWD < 1+2*sqrt[2/(n-1)] (Wendt and Carl, 1991), or expanded via multiplication by the sqrt(MSWD) when the MSWD ≥ 1+2*sqrt[2/(n-1)], in order to accommodate unknown sources of overdispersion.

Appendix E: Locations of Structural Measurements

Latitude	Longitude	Strike	Dip	Dip Direction	Unit
42.817642	112.056404	166	30	W	Ce
42.810574	112.064656	133	18	SW	Cbo
42.809274	112.064889	120	20	SW	Cbo
42.808552	112.066146	167	37	W	Cn
42.811708	112.067996	136	08	SW	Cbo
42.814543	112.068168	213	14	W	Cbo
42.819711	112.064189	198	13	W	Cbo
42.821201	112.065035	179	06	W	Cbo
42.822543	112.067318	202	20	W	Cbo
42.822801	112.067867	220	32	NW	Cn
42.825163	112.070741	278	24	N	Csw
42.826670	112.066827	193	24	W	Cbo
42.824523	112.063613	250	22	N	Cbo
42.823464	112.061135	214	20	W	Cbo
42.828385	112.052147	190	11	W	Ce
42.847273	112.075735	349	36	E	Cbo
42.832356	112.075392	323	15	NE	Csw
42.834022	112.076104	353	20	E	Csw
42.838601	112.076017	025	17	E	Csw
42.845589	112.079404	029	13	E	Cn
42.851279	112.073198	083	23	S	Ce
42.853734	112.063393	133	39	SW	Ce
42.857442	112.024087	037	14	SE	CZc
42.783001	112.039547	176	12	W	Os
42.792861	112.046935	179	22	W	Os
42.794830	112.046287	207	11	W	Og
42.797665	112.039971	078	26	SW	Ocsu
42.793350	112.029438	019	20	E	Csw
42.831003	112.061979	172	20	W	Ce
42.834330	112.063282	180	21	W	Ce
42.835880	112.061515	193	12	W	Ce
42.837166	112.046268	144	40	W	Cg
42.826650	112.008184	016	18	E	Cg
42.783583	112.096713	010	37	E	Og
42.784707	112.089038	009	26	E	Os
42.788060	112.089721	026	33	E	Os
42.773183	112.063945	109	17	S	Of
42.838754	112.123269	019	33	E	Cg
42.833409	112.124496	058	29	E	Ce/Cg
42.835310	112.117662	359	29	E	Cg

Latitude	Longitude	Strike	Dip	Dip Direction	Unit
42.779149	112.083681	005	28	E	Of
42.779766	112.081137	009	30	E	Of
42.779337	112.081117	013	24	E	Of
42.776960	112.078036	014	28	E	Of
42.786723	112.080436	355	34	E	Of
42.787974	112.081570	341	37	NE	Of
42.795424	112.084960	064	18	SE	Csw
42.798002	112.083953	033	33	E	Csw
42.797526	112.083181	012	20	E	Csw
42.795812	112.082782	036	15	SE	Csw
42.795061	112.082073	035	28	SE	Csw
42.793845	112.063165	054	19	SE	Sl
42.793558	112.063276	330	27	NE	Sl
42.793108	112.063094	060	16	SE	Sl
42.791665	112.062504	355	20	E	Sl
42.790710	112.062171	344	17	E	Sl
42.790388	112.060381	345	14	E	Sl
42.792324	112.057530	347	21	E	Sl
42.792441	112.057268	126	19	W	Sl
42.792778	112.055035	193	24	W	Of
42.796789	112.052480	269	27	NE	Os
42.791227	112.054893	204	09	NW	Of
42.791835	112.050836	337	31	NE	Of
42.790569	112.049068	168	11	W	Os
42.789116	112.054458	017	12	E	Of
42.793925	112.108374	018	35	E	Cbo
42.795432	112.110194	030	29	E	Cbo
42.796256	112.112177	010	13	E	Cbo
42.797452	112.113819	005	30	E	Ce
42.799531	112.114482	353	64	E	Ce
42.800503	112.115791	355	24	E	Ce
42.800391	112.117084	000	27	E	Ce
42.799075	112.119231	359	24	E	Ce
42.797389	112.119204	352	23	E	Ce
42.799002	112.121566	007	14	E	Ce
42.802030	112.123946	350	24	E	Ce
42.803450	112.122963	340	21	E	Ce
42.802027	112.119704	005	30	E	Ce
42.800992	112.118868	010	20	E	Ce
42.803224	112.117438	016	18	E	Ce

Appendix E: Locations of Structural Measurements

Latitude	Longitude	Strike	Dip	Dip Direction	Unit
42.834838	112.115683	345	33	E	Ce
42.829464	112.116116	341	39	E	Ce
42.829295	112.116838	339	37	E	Ce
42.808751	112.122281	350	23	E	Ce
42.809902	112.123557	002	40	E	Cg
42.814741	112.120811	333	18	E	Ce
42.816979	112.118422	350	48	E	Ce
42.817095	112.114932	355	37	E	Ce
42.816955	112.114131	343	34	E	Ce
42.818507	112.112299	327	26	E	Ce
42.820382	112.105091	343	27	E	Ce
42.817970	112.101852	350	20	E	Cbo
42.819531	112.103416	323	41	E	Cbo
42.820959	112.105448	326	33	E	Ce
42.822977	112.104114	330	46	E	Ce
42.823812	112.103392	332	46	E	Ce
42.83938	112.10848	357	39	E	Ce
42.852051	112.079138	101	13	S	Ce
42.850361	112.084440	228	03	NW	Ce
42.850467	112.085749	305	04	NE	Ce
42.850006	112.086787	141	05	SW	Ce
42.751940	112.022740	339	27	E	Ts
42.859360	112.078572	260	12	N	Ce
42.857294	112.077721	134	07	SW	Ce
42.854627	112.076681	138	09	SW	Ce
42.854377	112.078251	203	09	W	Ce
42.854283	112.075921	106	10	S	Ce
42.854378	112.071885	026	17	E	Ce
42.855041	112.068083	109	24	S	Ce
42.85215	112.01732	337	19	E	CZc
42.85917	112.01864	024	17	E	CZc
42.85554	112.02130	035	39	E	CZc
42.86363	112.02636	011	14	E	Zm
42.866953	112.044862	271	15	N	Zm
42.862013	112.040574	169	09	W	CZc
42.853656	112.029209	025	21	E	CZc
42.852778	112.025944	054	22	SE	CZc
42.851734	112.024354	034	17	E	CZc
42.856122	112.061701	116	33	SE	Cg
42.855332	112.063656	145	51	SW	Ce

Latitude	Longitude	Strike	Dip	Dip Direction	Unit
42.803528	112.118628	353	20	E	Ce
42.803446	112.114781	007	22	E	Ce
42.805025	112.114428	020	29	E	Ce
42.804546	112.112763	005	28	E	Ce
42.803833	112.111776	001	29	E	Ce
42.803114	112.111225	008	34	E	Cbo
42.800257	112.108009	355	33	E	Cn
42.800075	112.106992	357	55	E	Csw
42.799955	112.104395	004	24	E	Cn
42.799915	112.103341	004	54	E	Csw
42.796877	112.106417	345	54	E	Cbo
42.795837	112.107597	355	31	E	Cbo
42.792962	112.104870	031	19	SE	Cn
42.791939	112.097862	055	09	SE	Cbo
42.792425	112.096529	350	14	E	Csw
42.791176	112.107392	031	32	E	Cbo
42.769577	112.010979	044	16	SE	Csw
42.765316	112.006613	036	26	E	Ocs
42.827148	112.089962	310	32	E	Csw
42.833955	112.106620	335	31	E	Ce
42.756574	112.004938	005	17	E	Og
42.761517	112.005001	000	08	E	OCsu
42.765136	112.004972	015	25	E	Ocsu
42.765129	112.003689	055	26	SE	Og
42.765310	112.002242	080	18	S	Og
42.767159	112.002824	084	11	S	Og
42.863304	112.029296	352	27	E	CZc
42.791777	112.000813	342	23	E	Csw
42.794051	112.032554	168	23	W	Csw
42.796988	112.036320	169	20	W	Csw
42.794419	112.041118	171	16	W	OCs
42.794650	112.042058	173	23	W	Og
42.794626	112.042781	172	29	W	Og
42.800500	112.031366	097	38	S	OCs
42.800776	112.032172	107	27	S	OCs
42.804452	112.054328	172	20	W	Cbo
42.804644	112.056527	177	19	W	Cbo
42.805316	112.057179	202	19	W	Cbo
42.805901	112.056250	174	15	W	Cbo
42.807714	112.433047	029	41	SE	Cbo

Appendix E: Locations of Structural Measurements

Latitude	Longitude	Strike	Dip	Dip Direction	Unit
42.866406	112.037068	305	25	NE	Zm
42.868115	112.037275	002	30	E	Zm
42.868168	112.033936	297	12	NE	Zm
42.864077	112.034829	340	28	E	Zm
42.813495	112.110438	013	32	E	Cbo
42.811831	112.110112	035	45	E	Cbo
42.809246	112.107057	037	26	E	Cbo
42.808672	112.105921	008	41	E	Cn
42.810245	112.110514	013	22	E	Cbo
42.811178	112.111634	357	26	E	Cbo
42.812044	112.113501	350	48	E	Ce
42.812603	112.114165	357	29	E	Ce
42.811242	112.118704	355	30	E	Ce
42.811276	112.121008	303	54	E	Cg
42.812297	112.121444	320	29	E	Cg
42.813063	112.123298	325	37	E	Ce
42.814698	112.122708	338	29	E	Ce
42.818283	112.122267	308	35	NE	Ce
42.818939	112.121978	329	40	E	Ce
42.81833	112.12099	337	39	NE	Ce
42.819966	112.119820	326	38	E	Ce
42.81798	112.11957	336	32	NE	Ce
42.820447	112.118833	320	53	E	Ce
42.822001	112.120190	317	37	E	Ce
42.81769	112.11687	010	60	E	Ce
42.821992	112.118094	322	38	E	Ce
42.81824	112.14524	355	45	E	Ce
42.822831	112.116629	337	33	E	Ce
42.81906	112.11373	347	33	E	Ce
42.822064	112.115267	311	45	E	Ce
42.81987	112.11205	348	26	E	Ce
42.822892	112.110280	308	30	NE	Ce
42.827765	112.095021	338	35	E	Cn
42.829764	112.098863	346	38	E	Cbo
42.831154	112.101732	349	31	E	Cbo
42.831424	112.103794	348	40	E	Cbo
42.83130	112.10421	346	32	E	Cbo
42.834223	112.104814	331	47	E	Cbo
42.83191	112.10517	339	37	E	Ce
42.833245	112.107709	333	51	E	Ce

Latitude	Longitude	Strike	Dip	Dip Direction	Unit
42.808486	112.003564	024	50	SE	Cbo
42.807754	112.002156	009	41	E	Cbo
42.806097	112.002906	349	40	E	Cbo
42.803895	112.003275	003	36	E	Cbo
42.806267	112.004653	344	44	E	Cbo
42.781145	112.091322	344	07	NE	Os
42.784662	112.093703	344	23	NE	Os
42.792738	112.091131	031	22	SE	Csw
42.793616	112.091188	354	20	E	Csw
42.795585	112.093947	002	21	E	Csw
42.797103	112.094879	000	22	E	Csw
42.800403	112.099985	073	34	S	Csw
42.801897	112.101296	048	32	SE	Csw
42.806933	112.102836	020	37	E	Csw
42.804648	112.098383	325	35	E	Csw
42.802809	112.090792	052	33	SE	Csw
42.80218	112.09207	015	27	E	Csw
42.80136	112.09207	357	38	E	Csw
42.800756	112.088244	051	18	SE	Csw
42.79775	112.09103	009	32	E	Csw
42.799881	112.087972	048	23	SE	Csw
42.797230	112.086792	100	19	S	Csw
42.794325	112.087130	066	09	SE	Csw
42.789577	112.085967	351	39	E	Os
42.789385	112.084323	330	24	NE	Of
42.779782	112.090217	017	25	E	Os
42.768889	112.052283	142	17	W	Of
42.771771	112.055263	005	29	E	Of
42.771995	112.054891	295	5	NE	Of
42.771596	112.053644	118	7	S	Of
42.770639	112.054484	160	21	W	Of
42.773425	112.054433	091	15	S	Of
42.779672	112.053775	343	10	E	Of
42.778866	112.054262	035	12	E	Of
42.777770	112.054151	018	15	E	Of
42.777200	112.054729	015	14	E	Of
42.771251	112.046448	138	8	SW	Os
42.781120	112.046940	245	8	NW	Os
42.777715	112.049651	068	13	S	Of
42.776282	112.052908	037	9	SE	Of

Appendix E: Locations of Structural Measurements

Latitude	Longitude	Strike	Dip	Dip Direction	Unit
42.83260	112.10747	339	45	E	Ce
42.833171	112.109966	346	54	E	Ce
42.833997	112.110746	350	42	E	Ce
42.833325	112.111747	353	40	E	Ce
42.83179	112.11123	341	36	E	Ce
42.832473	112.115400	353	47	E	Ce
42.83122	112.14141	359	29	E	Ce
42.831297	112.117576	358	30	E	Ce
42.82994	112.11663	350	35	E	Ce
42.829928	112.120797	348	33	E	Ce
42.829780	112.121302	338	30	E	Cg
42.827957	112.121059	344	59	E	Cg
42.827300	112.118412	025	23	E	Cg
42.820321	112.108046	333	32	E	Ce
42.818404	112.106365	324	30	E	Ce
42.817417	112.108705	331	53	E	Ce
42.816981	112.110208	359	31	E	Ce
42.815134	112.110295	338	45	E	Ce
42.796725	112.055522	095	47	S	Os
42.794068	112.057147	320	21	E	Of
42.800856	112.063948	175	12	W	Cn
42.801336	112.063993	189	11	W	Cn
42.807656	112.056919	156	13	W	Cbo
42.803480	112.056960	174	20	W	Cbo
42.801654	112.055212	225	31	NW	Ce
42.874442	112.047585	171	35	W	Og
42.874504	112.047361	174	33	W	Og
42.875189	112.045256	185	36	W	Og
42.874232	112.041123	149	36	W	Og
42.873687	112.040514	177	24	W	Og
42.873588	112.037335	168	34	W	Og
42.874908	112.036150	151	55	W	Og
42.874451	112.035629	145	58	W	Og
42.873533	112.085420	141	39	SW	Og
42.874408	112.033284	136	46	SW	Og
42.876039	112.033913	170	28	W	Og
42.878020	112.034415	137	38	SW	Os
42.876368	112.033884	145	45	W	Og
42.873542	112.025285	316	29	NE	Zm
42.869168	112.033154	107	21	S	Zm

Latitude	Longitude	Strike	Dip	Dip Direction	Unit
42.847093	112.022222	064	13	SE	CZc
42.848392	112.019376	327	25	E	CZc
42.846123	112.022234	002	04	E	CZc
42.845604	112.021754	015	08	E	CZc
42.844480	112.018296	015	33	E	Cg
42.045334	112.012410	105	37	S	CZc
42.847387	112.042434	332	18	E	Cg
42.854597	112.031437	265	37	N	CZc
42.855391	112.031284	190	22	W	CZc
42.850783	112.030307	036	73	E	CZc
42.849891	112.022101	158	11	W	CZc
42.848971	112.023287	325	40	E	CZc
42.848687	112.024015	185	09	W	CZc
42.848151	112.026440	218	66	W	Cg
42.847856	112.029943	018	23	E	CZc
42.833997	112.053111	009	08	E	Cg
42.029151	112.039774	007	09	E	Cg
42.828184	112.039523	337	18	E	Cg
42.830183	112.036681	040	22	E	Cg
42.828939	112.027001	353	27	E	Cg
42.768257	112.098585	199	18	W	Os
42.766117	112.105040	350	45	E	Ce
42.765328	112.105122	355	38	E	Ce
42.764155	112.105631	334	36	E	Ce
42.763275	112.105663	343	42	E	Ce
42.761558	112.105691	348	49	E	Ce
42.759116	112.106109	347	35	E	Ce
42.757486	112.106487	328	30	E	Ce
42.755093	112.107109	358	44	E	Ce
42.752248	112.108369	325	29	E	Ce
42.753428	112.104857	353	26	E	Ce
42.753775	112.103464	340	32	E	Ce
42.753581	112.101670	344	53	E	Ce
42.753479	112.100559	340	56	E	Ce
42.752970	112.098590	329	82	E	Ce
42.753535	112.097740	345	70	E	Ce
42.762262	112.092776	343	23	E	Cbo
42.862778	112.054148	032	33	E	Cg
42.867444	112.056175	237	17	NW	CZc
42.870904	112.059083	254	18	NW	CZc

Appendix E: Locations of Structural Measurements

Latitude	Longitude	Strike	Dip	Dip Direction	Unit
42.870153	112.034467	097	26	S	Zm
42.86995	112.03710	044	16	SE	Zm
42.869973	112.037577	123	10	SW	Zm
42.870879	112.040745	161	23	W	Os
42.871570	112.040019	175	33	W	Og
42.841845	112.103876	005	28	E	Ce
42.842962	112.107058	001	42	E	Ce
42.842249	112.108002	015	30	E	Ce
42.842200	112.109248	355	25	E	Ce
42.842281	112.111247	009	37	E	Ce
42.841152	112.114988	346	44	E	Ce
42.840914	112.115549	356	42	E	Ce
42.842313	112.122486	335	30	E	Ce
42.847338	112.116572	336	35	E	Cg
42.847122	112.113636	338	37	E	Ce
42.826401	112.114419	348	35	E	Ce
42.825875	112.111251	356	39	E	Ce
42.824823	112.110331	329	42	E	Ce
42.825855	112.109689	346	35	E	Ce
42.826231	112.107270	350	26	E	Ce
42.825021	112.105864	329	45	E	Ce
42.826332	112.106339	327	32	E	Ce
42.827259	112.104685	334	54	E	Ce
42.827153	112.104259	337	73	E	Ce
42.825652	112.102559	315	51	E	Ce
42.825060	112.101233	320	57	E	Cbo
42.826424	112.097169	342	41	E	Cbo
42.825746	112.094753	327	26	E	Cn
42.825286	112.094260	322	23	E	Cn
42.825086	112.093531	320	28	E	Cn
42.825093	112.093163	322	20	E	Cn
42.825116	112.092874	318	44	E	Csw
42.826429	112.088300	323	26	E	Csw
42.827141	112.084891	312	28	E	Csw
42.861518	112.093676	319	28	NE	Cn
42.861137	112.093485	327	24	NE	Cn
42.790593	112.062537	018	21	E	Sl
42.801313	112.072989	286	26	N	Csw
42.795921	112.075843	108	14	S	Cbo
42.855152	112.005262	010	28	E	CZc

Latitude	Longitude	Strike	Dip	Dip Direction	Unit
42.873212	112.060721	250	14	NW	CZc
42.871783	112.057664	226	25	NW	CZc
42.863408	112.044289	180	22	W	CZc
42.860007	112.042434	326	06	SW	Cg
42.851541	112.043808	305	46	N	Cg
42.854355	112.044832	310	26	NE	Cg
42.865603	112.057953	088	24	S	Cg
42.757120	112.064138	173	40	W	Of
42.756895	112.051983	200	20	W	Os
42.755615	112.051921	170	29	W	Os
42.756513	112.048810	187	26	W	Os
42.754286	112.033720	207	13	W	Os
42.756727	112.035974	188	51	W	Os
42.756728	112.036900	172	19	W	Og
42.757234	112.035627	175	17	W	Og
42.761153	112.028869	265	6	NW	Og
42.761327	112.037661	235	18	NW	Og
42.760757	112.037908	235	8	NW	Og
42.762294	112.042737	170	18	W	Os
42.759324	112.063440	193	23	W	Of
42.751022	112.057906	182	33	W	Of
42.757318	112.060081	203	28	W	Os
42.765966	112.061232	206	19	W	Of
42.757577	112.065668	150	14	W	Of
42.751736	112.021480	019	20	E	Ts
42.751946	112.022731	343	27	E	Ts
42.752215	112.022731	348	14	E	Ts
42.751188	112.033249	188	31	W	Og
42.754988	112.062098	165	27	W	Of
42.753789	112.053457	176	24	W	Os
42.753961	112.048703	177	20	W	Os
42.753413	112.044981	212	11	W	Os
42.754311	112.040761	234	2	NW	Os
42.754466	112.035157	160	48	W	Og
42.756100	112.035441	164	22	W	Og
42.757629	112.035792	235	25	NW	Og
42.761038	112.038028	293	2	N	Og
42.761957	112.037668	202	4	W	Og
42.860536	112.122221	305	32	NE	Cg
42.858868	112.116617	332	39	E	Cg

Appendix E: Locations of Structural Measurements

Latitude	Longitude	Strike	Dip	Dip Direction	Unit
42.860394	112.003204	009	26	E	CZc
42.864562	112.010900	048	31	SE	Os
42.861584	112.018712	017	25	E	CZc
42.862034	112.018974	340	32	E	CZc
42.869910	112.024398	309	18	N	Zm
42.869661	112.026123	247	12	NW	Zm
42.870888	112.016863	330	55	NE	Os
42.870085	112.015978	145	33	SW	Os
42.765764	112.013782	016	12	E	Ts
42.765961	112.013863	151	18	SW	Ts
42.765879	112.008756	351	33	E	OCs
42.752959	112.005141	350	21	E	OCs
42.859793	112.019050	053	43	SE	CZc
42.057063	112.021721	036	36	E	CZc
42.856670	112.021706	032	45	E	CZc
42.860484	112.021198	037	26	E	CZc
42.863696	112.021254	350	24	E	CZc
42.863574	112.022699	032	16	E	Zm
42.869818	112.022908	120	52	SW	Zm
42.869963	112.023696	316	14	NE	Zm
42.869174	112.030555	075	30	S	Zm
42.866081	112.032558	007	21	E	CZc
42.864059	112.031833	013	07	E	CZc
42.849633	112.120017	042	16	SE	Cg
42.85114	112.11304	335	38	NE	Ce
42.854306	112.104448	336	44	NE	Cbo
42.854025	112.106806	330	45	NE	Ce
42.855316	112.108564	352	49	E	Ce
42.858338	112.108253	332	39	NE	Ce
42.858050	112.106433	325	29	NE	Cbo
42.843868	112.096540	359	27	E	Cbo
42.841701	112.097986	013	32	E	Cbo
42.841544	112.096522	019	40	E	Cbo
42.841654	112.095086	358	34	E	Cbo
42.841598	112.094726	351	45	E	Cn
42.841673	112.094382	358	26	E	Cn
42.841594	112.093619	355	30	E	Cn
42.841473	112.093346	348	30	E	Csw
42.840766	112.086653	355	26	E	Csw
42.840446	112.085090	358	15	E	Csw

Latitude	Longitude	Strike	Dip	Dip Direction	Unit
42.857746	112.115947	352	47	E	Cg
42.858553	112.114555	357	40	E	Ce
42.85782	112.11591	353	28	E	Ce
42.854245	112.114317	317	40	NE	Ce
42.764421	112.045347	150	22	W	Os
42.764329	112.042780	160	12	W	Os
42.763139	112.039125	167	28	W	Os
42.763345	112.037675	185	10	W	Og
42.763714	112.036320	218	7	W	Og
42.763253	112.035624	218	6	W	Og
42.765688	112.013510	346	13	E	Ts
42.764564	112.008132	017	18	E	Ocs
42.766680	112.008244	015	14	E	OCs
42.768653	112.010803	040	20	SE	Csw
42.767995	112.031842	340	12	E	Og
42.765492	112.036142	263	4	N	Og
42.766443	112.045941	182	10	W	Os
42.773545	112.057981	110	16	S	Sl
42.773121	112.057045	137	21	SW	Sl
42.772237	112.056614	145	12	SW	Sl
42.771592	112.055440	090	15	S	Of
42.771078	112.055170	032	21	E	Of
42.770335	112.054379	005	12	E	Of
42.769331	112.053332	163	10	W	Of
42.768539	112.051657	141	18	W	Of
42.769224	112.044993	333	6	E	Os
42.768028	112.044279	180	13	W	Os
42.777419	112.039127	148	8	W	Os
42.797249	112.073143	049	12	SE	Cn
42.797462	112.073080	091	23	SE	Cn
42.865833	112.095231	332	37	E	Csw
42.874445	112.092230	331	16	E	Ce
42.845232	112.075050	011	20	E	Csw
42.844184	112.077168	051	14	SE	Csw
42.844434	112.075623	035	24	E	Csw
42.843517	112.074830	014	32	E	Csw
42.832161	112.092363	338	39	NE	Csw
42.840983	112.090613	351	22	E	Csw
42.854689	112.079764	154	06	W	Cn
42.853842	112.086500	337	45	NE	Cn

Appendix E: Locations of Structural Measurements

Latitude	Longitude	Strike	Dip	Dip Direction	Unit
42.832239	112.079505	290	24	NE	Csw
42.830622	112.087410	345	30	NE	Csw
42.832905	112.095567	352	35	E	Csw
42.833614	112.095628	346	29	E	Csw
42.833952	112.096398	347	34	E	Cn
42.832360	112.098349	358	36	E	Cbo
42.850402	112.067754	113	04	SW	Ce
42.848930	112.066920	130	13	SW	Ce
42.850786	112.071118	156	23	W	Ce
42.848473	112.071874	010	20	E	Cbo
42.846938	112.072787	247	27	NW	Csw
42.843884	112.068257	192	09	W	Cbo
42.844830	112.068943	175	18	W	Cbo
42.836071	112.076087	347	27	E	Csw
42.833829	112.075427	341	21	E	Csw
42.839250	112.067726	293	23	NE	Cbo
42.838070	112.065903	190	10	W	Ce
42.838868	112.063855	233	11	NW	Ce
42.839442	112.064814	257	09	NW	Ce
42.846859	112.060920	175	18	W	Ce
42.849021	112.060790	174	13	W	Ce
42.873587	112.072204	287	37	N	Ce
42.874249	112.075404	293	33	N	Ce
42.875321	112.077187	315	17	NE	Ce
42.874661	112.077993	322	28	NE	Ce
42.873854	112.079871	317	16	NE	Ce
42.874872	112.082765	346	13	E	Ce
42.874175	112.083689	317	16	NE	Ce
42.874709	112.084930	331	12	E	Ce
42.873911	112.087510	339	35	E	Csw
42.873080	112.087195	329	41	E	Cn
42.872661	112.086779	290	33	N	Cn
42.871604	112.089988	335	33	E	Ce
42.872314	112.092220	335	26	E	Cn
42.870908	112.094816	342	20	E	Cn
42.871615	112.097749	343	21	E	Cbo
42.872804	112.101423	355	33	E	Cbo
42.874523	112.103296	347	30	E	Ce
42.873769	112.102460	348	41	E	Ce
42.863917	112.101288	352	16	E	Cn

Latitude	Longitude	Strike	Dip	Dip Direction	Unit
42.850267	112.095723	343	32	E	Cn
42.854111	112.079879	143	13	SW	Ce
42.852638	112.095775	348	33	E	Cn
42.853353	112.096206	344	42	E	Cn
42.853577	112.096959	338	36	NE	Cn
42.865378	112.102654	340	23	E	Cn
42.867064	112.102615	017	16	E	Cn
42.865378	112.102654	340	23	E	Cn
42.774236	112.113676	327	81	E	Ce
42.809364	112.005045	017	54	E	Cg
42.809086	112.003421	029	54	E	Cbo
42.810785	112.006697	010	33	E	Cg
42.812500	112.008633	355	32	E	Cg
42.814666	112.009787	355	36	E	Cg
42.819924	112.017946	355	18	E	Cg
42.819991	112.020658	354	19	E	Cg
42.819980	112.022738	005	26	E	Cg
42.821842	112.024841	020	28	E	Cg
42.817611	112.060755	157	44	SW	Ce
42.777889	112.093750	074	87	SE	Os
42.751986	112.002435	351	29	E	OCs
42.755740	112.004765	008	24	E	OCs
42.756905	112.005807	335	10	NE	OCs
42.759242	112.008899	001	23	E	OCs
42.759819	112.009815	333	29	NE	OCs
42.754261	112.021870	339	20	E	Ts
42.754171	112.021274	011	21	E	Ts
42.754449	112.006636	353	30	E	OCs
42.752252	112.005909	001	29	E	OCs
42.836255	112.029828	005	22	E	Cg
42.758568	112.115869	310	27	NE	Cg
42.796965	112.119218	330	24	NE	Cg
42.755421	112.118784	340	32	E	Cg
42.754452	112.118753	340	31	E	Cg
42.751668	112.118204	338	26	E	Cg
42.750929	112.118847	326	26	NE	Ce
42.750539	112.119862	348	43	E	Cg
42.753200	112.123027	356	30	E	Cg
42.757015	112.123459	005	28	E	Cg
42.758660	112.124136	349	52	E	Cg

Appendix E: Locations of Structural Measurements

Latitude	Longitude	Strike	Dip	Dip Direction	Unit
42.863644	112.101741	348	21	E	Cn
42.863227	112.101581	338	20	NE	Cn
42.861570	112.117492	332	28	NE	Cg
42.869372	112.122243	034	43	SE	Cg
42.869711	112.122622	019	33	E	Cg
42.873179	112.123527	355	66	E	Cg
42.872022	112.116760	354	43	E	Cg
42.869966	112.112999	356	23	E	Ce
42.872256	112.110680	352	33	E	Ce
42.870732	112.109365	359	33	E	Ce
42.868711	112.106779	013	31	E	Ce
42.868679	112.105377	356	44	E	Ce
42.868498	112.104818	007	27	E	Cbo
42.865969	112.101635	355	40	E	Csw
42.865774	112.107549	358	30	E	Ce
42.866351	112.108167	357	41	E	Ce
42.868191	112.111396	344	32	E	Ce
42.867787	112.113172	337	29	NE	Cg
42.867215	112.114728	147	32	W	Cg
42.868127	112.115399	338	88	NE	Cg
42.864321	112.115240	338	34	NE	Ce
42.850242	112.112343	04	15	E	Ce
42.855918	112.109978	338	36	NE	Ce
42.857859	112.111127	320	53	NE	Ce
42.859351	112.110965	339	54	E	Ce
42.859866	112.109825	331	47	NE	Ce
42.860107	112.104186	331	35	NE	Cbo
42.861534	112.104519	340	51	E	Cbo
42.858728	112.104031	339	42	E	Cbo
42.856680	112.101971	342	48	E	Cbo
42.854754	112.100765	337	37	NE	Cbo
42.853795	112.099062	339	41	E	Cbo
42.852651	112.095127	342	46	E	Csw
42.854765	112.088963	313	48	NE	Csw
42.848650	112.091820	349	23	E	Csw
42.850926	112.099899	352	32	E	Cbo
42.850620	112.103884	344	43	E	Ce
42.788158	112.069929	006	43	E	Of
42.795959	112.075916	098	19	S	Cbo
42.798253	112.075982	035	29	SE	Cn

Latitude	Longitude	Strike	Dip	Dip Direction	Unit
42.764892	112.123936	340	32	E	Cg
42.767240	112.120475	202	41	NW	Cg
42.770026	112.113505	299	31	N	Ce
42.760238	112.114972	330	19	NE	Cg
42.759118	112.120190	340	27	NE	Cg
42.763779	112.118682	317	30	NE	Cg
42.763956	112.118186	334	26	NE	Cg
42.764084	112.117630	330	45	E	Cg
42.764906	112.116898	338	55	E	Cg
42.770447	112.006028	041	11	SE	OCs
42.768001	112.003134	075	18	S	OCs
42.768698	112.004617	044	15	SE	OCs
42.773143	112.007358	327	40	E	OCs
42.773317	112.007715	359	15	E	OCs
42.773534	112.006518	317	17	NE	OCs
42.775211	112.041877	255	8	N	Os
42.777816	112.042682	115	7	S	Os
42.776017	112.050898	346	14	E	Of
42.768685	112.037702	155	9	W	Os
42.780432	112.065258	059	7	SE	Sl
42.781547	112.064347	016	7	E	Sl
42.780762	112.062744	348	21	E	Sl
42.780153	112.061087	037	13	E	Sl
42.763398	112.057238	137	12	SW	Of
42.846185	112.025342	011	35	E	Cg
42.844573	112.037125	115	17	S	Cg
42.851964	112.047227	280	22	N	Cg
42.853556	112.050547	309	25	NE	Cg
42.836103	112.052528	143	08	W	Cg
42.780072	112.064730	129	15	W	Sl
42.763398	112.057238	137	12	SW	Of
42.846185	112.025342	011	35	E	Cg
42.8470265	112.023085	175	58	W	CZc
42.844573	112.037125	115	17	S	Cg
42.753984	112.093801	012	37	E	Cbo
42.851964	112.047227	280	22	N	Cg
42.853556	112.050547	309	25	NE	Cg
42.836103	112.052528	143	08	W	Cg
42.791817	112.063481	356	15	E	Sl
42.770447	112.006028	041	11	SE	OCs

Appendix E: Locations of Structural Measurements

Latitude	Longitude	Strike	Dip	Dip Direction	Unit
42.798899	112.075562	165	23	W	Cn
42.799385	112.076773	163	43	W	Cn
42.800367	112.077730	191	24	W	Cbo
42.800889	112.079847	009	24	E	Csw
42.802145	112.080555	335	33	NE	Csw
42.803374	112.082298	320	19	NE	Cn
42.805747	112.084562	334	14	NE	Csw
42.809445	112.088561	013	18	E	Csw
42.801498	112.080774	007	25	E	Csw
42.804129	112.070525	119	07	SW	OCs
42.807527	112.067498	129	25	SW	Cn
42.804865	112.065207	126	22	SW	Cn
42.803520	112.063841	123	13	SW	Cn
42.802214	112.063956	160	21	W	Cn
42.804626	112.068198	155	20	W	Csw
42.808320	112.072903	178	27	W	OCs
42.798184	112.071609	120	07	SW	Cbo
42.792412	112.070881	012	47	E	Of
42.791526	112.070556	027	32	SE	Of
42.816136	112.062598	161	17	W	Cbo
42.817029	112.063741	182	28	W	Cbo
42.817384	112.065389	157	38	W	Cbo
42.822103	112.067649	230	15	NW	Cn
42.823361	112.068310	231	32	NW	Csw
42.823360	112.069035	340	20	E	Csw
42.822206	112.070399	224	16	SE	Csw
42.821156	112.072934	335	12	SW	Csw
42.819411	112.082533	356	11	E	Csw
42.813321	112.085978	354	08	E	Cn
42.811634	112.077541	037	16	SE	Csw
42.812850	112.076871	330	31	NE	Csw
42.815029	112.074904	005	14	E	Csw
42.822155	112.075496	320	24	NE	Csw
42.823218	112.074554	320	25	NE	Csw
42.823859	112.069973	314	18	NE	Csw
42.824573	112.067636	329	14	NE	Cn
42.825524	112.066422	247	20	NW	Cn
42.825654	112.066240	225	21	NW	Cbo
42.822398	112.066187	222	10	NW	Cbo
42.829121	112.055073	070	16	SE	Ce

Latitude	Longitude	Strike	Dip	Dip Direction	Unit
42.768001	112.003134	075	18	S	OCs
42.768698	112.004617	044	15	SE	OCs
42.773143	112.007358	327	40	E	OCs
42.773317	112.007715	359	15	E	OCs
42.773534	112.006518	317	17	NE	OCs
42.775211	112.041877	255	8	N	Os
42.777816	112.042682	115	7	S	Os
42.776017	112.050898	346	14	E	Of
42.768685	112.037702	155	9	W	Os
42.780432	112.065258	059	7	SE	Sl
42.781547	112.064347	016	7	E	Sl
42.780762	112.062744	348	21	E	Sl
42.780153	112.061087	037	13	E	Sl
42.802426	112.012556	033	20	E	Ts
42.754570	112.123372	335	331	E	Cg
42.753345	112.062956	178	35	W	Of
42.754525	112.060977	199	31	W	Of
42.858611	112.123353	353	55	E	Cg
42.752832	112.081447	325	46	E	Os
42.767686	112.035085	298	15	N	Og
42.773588	112.053658	063	15	S	Of
42.844629	112.044499	332	23	E	Cg
42.847772	112.031813	357	54	E	CZc
42.841517	112.076865	339	44	E	Csw
42.845048	112.078824	039	09	E	Cn
42.812431	112.079431	007	09	E	Csw
42.812548	112.082503	007	07	E	Csw
42.814359	112.084866	325	11	NE	Csw
42.793910	112.064262	337	16	NE	Sl
42.793425	112.065564	133	16	SW	Sl
42.793833	112.068523	126	14	SW	Of
42.792901	112.065963	131	22	SW	Sl
42.791262	112.064806	010	23	E	Of
42.789350	112.063541	003	31	E	Sl
42.788074	112.062903	023	11	E	Of
42.786943	112.061806	006	11	E	Of
42.848824	112.056864	131	28	SW	Ce
42.851882	112.058862	106	28	S	Ce
42.852427	112.060393	118	45	SW	Ce
42.851577	112.062132	144	22	SW	Ce

Appendix E: Locations of Structural Measurements

Latitude	Longitude	Strike	Dip	Dip Direction	Unit
42.827795	112.056707	160	16	W	Ce
42.828449	112.057487	172	13	W	Ce
42.827802	112.058896	160	10	W	Ce
42.828411	112.060236	158	22	W	Ce
42.828128	112.062739	150	19	W	Cbo
42.829731	112.062167	160	23	W	Ce
42.826374	112.063834	217	07	NW	Cbo
42.825081	112.061229	197	13	W	Cbo
42.824742	112.057939	200	13	W	Ce
42.825017	112.053134	156	18	SW	Ce
42.826782	112.048893	171	14	W	Cg
42.751902	112.080977	327	71	NE	Os
42.777018	112.072238	064	11	SE	Of
42.776116	112.073116	085	18	S	Of
42.771387	112.078753	042	29	SE	Of
42.772040	112.080873	051	37	SE	Of
42.773824	112.081135	053	24	SE	Of
42.777872	112.088573	010	25	E	Os
42.779843	112.059534	070	9	S	Sl
42.778758	112.060025	015	20	E	Sl
42.775871	112.060060	350	4	E	Of
42.773466	112.056144	128	27	SW	Of

Latitude	Longitude	Strike	Dip	Dip Direction	Unit
42.850190	112.061675	177	09	W	Ce
42.850042	112.064287	157	06	W	Ce
42.849634	112.065085	138	09	Sw	Ce
42.848054	112.064277	110	05	S	Ce
42.848148	112.058357	177	13	W	Ce
42.838466	112.063265	213	11	W	Ce
42.837991	112.062301	201	13	W	Ce
42.838860	112.053065	158	29	W	Ce
42.854149	112.059017	112	40	S	Ce
42.852906	112.057048	135	35	SW	Ce
42.850573	112.055352	166	49	W	Ce
42.866964	112.048775	160	14	W	Zm
42.867639	112.053286	211	22	W	CZc
42.868779	112.050513	183	21	W	Zm
42.753116	112.096652	348	64	E	Cbo
42.777089	112.061346	038	15	SE	Of
42.778825	112.065911	045	20	SE	Sl
42.779885	112.057529	053	9	SE	Sl
42.780713	112.054421	045	10	SE	Sl
42.781892	112.055019	120	11	SW	Sl
42.781408	112.058201	070	7	S	Sl
42.781613	112.059024	301	6	NE	Sl

Appendix F: Locations of samples

Sample	Latitude	Longitude	Strike	Dip	Dip Direction
BCG-1	42.802426	-112.012556	037	18	E
BCG-30	42.751736	-112.021480	019	20	E
BCG-31	42.751946	-112.022731	343	27	E
BCG-62	42.765688	-112.013510	346	13	E
BCG-63	42.765678	-112.013574			
BCG-273	42.754171	-112.021274	011	21	E
BCG-612	42.765764	-112.013782	016	12	E
BCG-770	42.751940	-112.022740	339	27	E

BCG-1

Appendix F: Cathodoluminescence Images of LA-ICP-MS spot analyses

Appendix F: Cathodoluminescence Images of LA-ICP-MS spot analyses

BCG-30

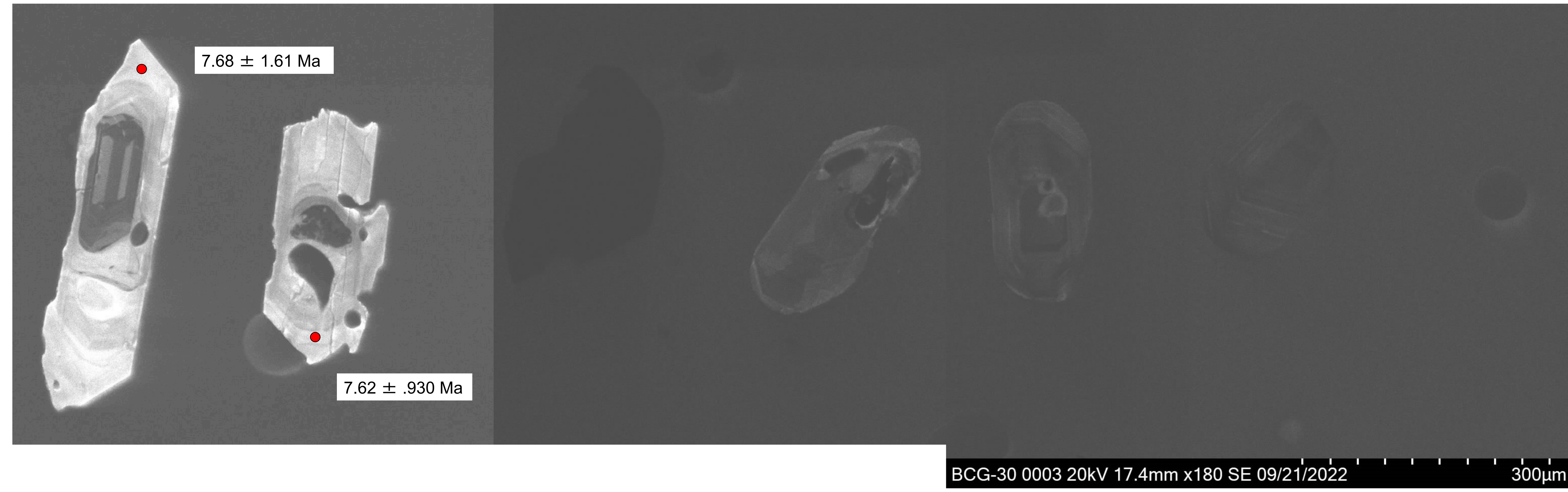

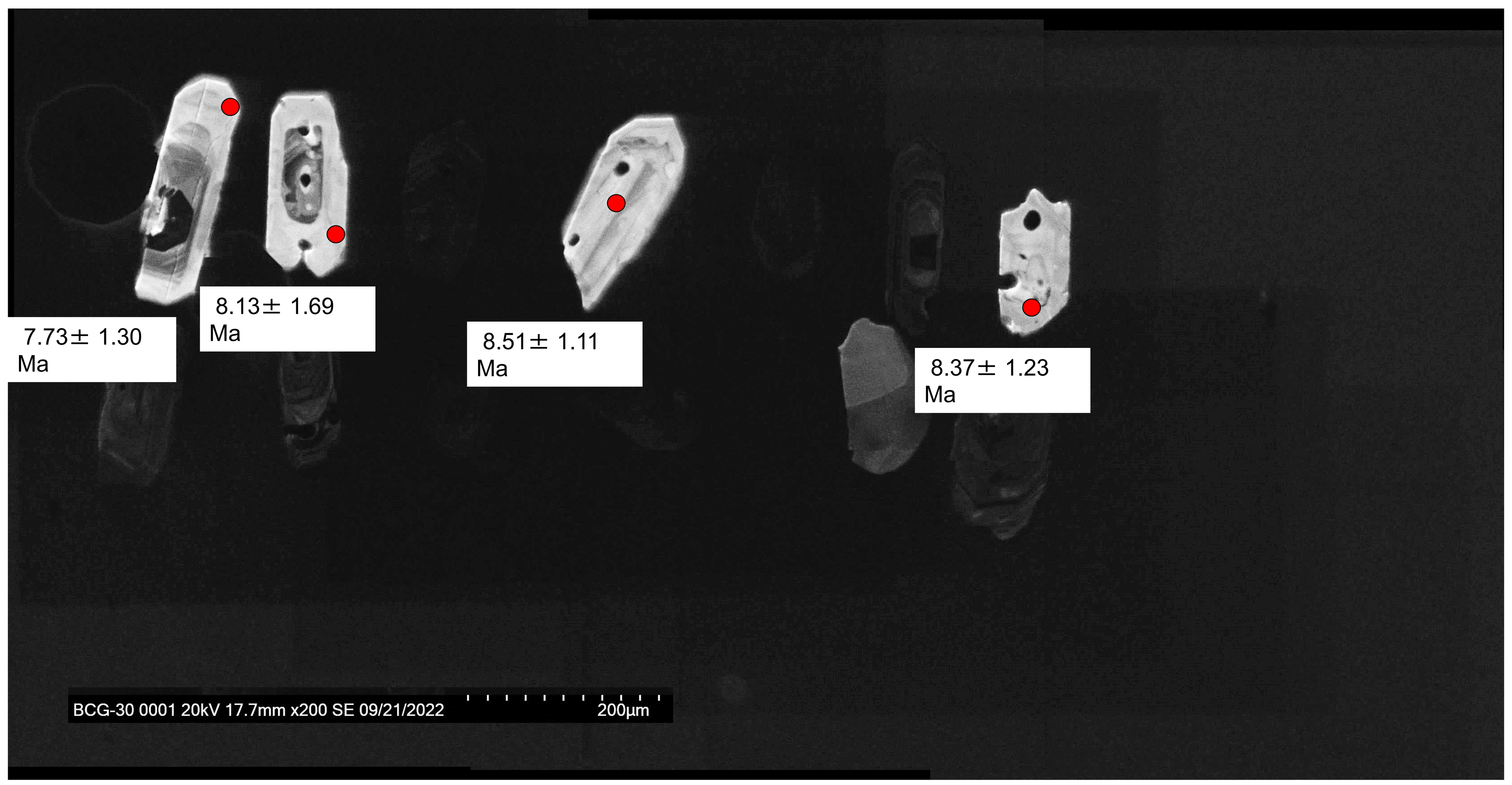

Appendix F: Cathodoluminescence Images of LA-ICP-MS spot analyses

BCG-273

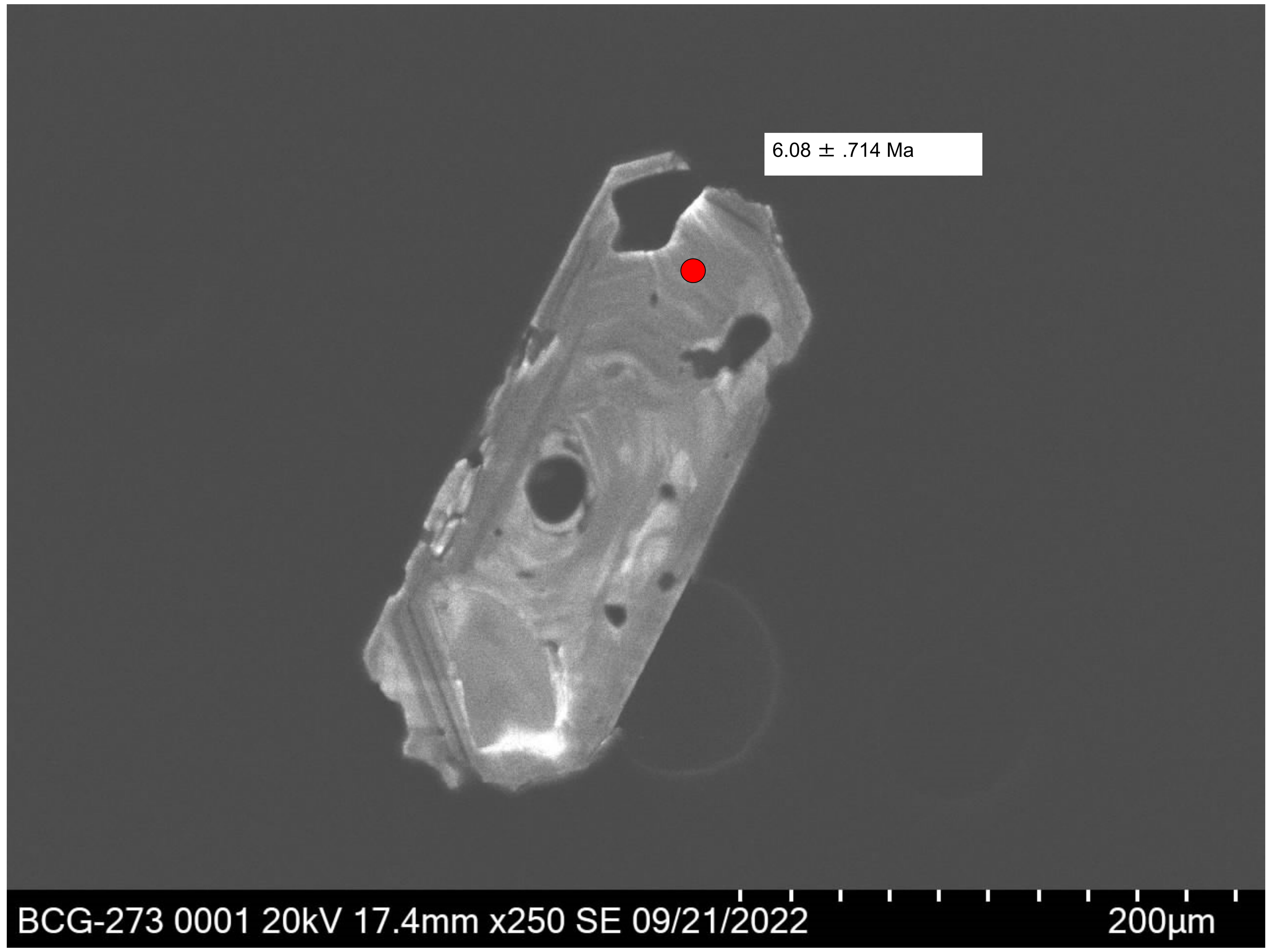

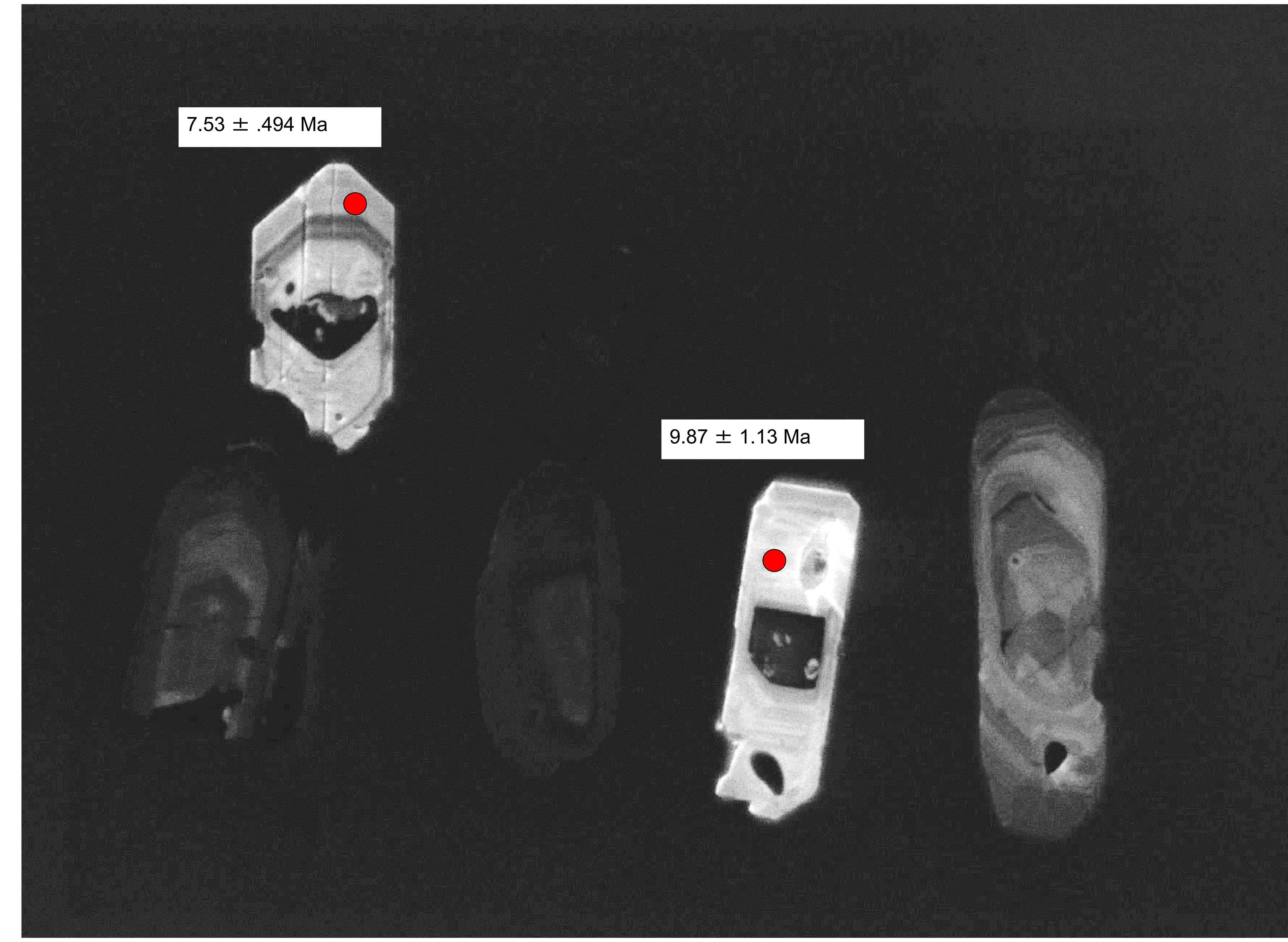

Appendix F: Cathodoluminescence Images of LA-ICP-MS spot analyses

Appendix F: Cathodoluminescence Images of LA-ICP-MS spot analyses